TECHNISCHE UNIVERSITÄT MÜNCHEN

Max-Planck-Institut für Physik
(Werner-Heisenberg-Institut)

Development of thin sensors and a novel interconnection technology for the upgrade of the ATLAS pixel system

Michael Beimforde

Vollständiger Abdruck der von der Fakultät für Physik der Technischen Universität München zur Erlangung des akademischen Grades eines

Doktors der Naturwissenschaften (Dr. rer. nat.)

genehmigten Dissertation.

Vorsitzender:	Univ.-Prof. Dr. A. J. Buras
Prüfer der Dissertation:	
1.	Hon.-Prof. Dr. S. Bethke
2.	Univ.-Prof. Dr. St. Paul

Die Dissertation wurde am 22.06.2010 bei der Technischen Universität München eingereicht und durch die Fakultät für Physik am 19.07.2010 angenommen.

Abstract

To extend the discovery potential of the experiments at the LHC accelerator a two phase luminosity upgrade towards the super LHC (sLHC) with a maximum instantaneous luminosity of $10^{35}\,/\mathrm{cm}^2\mathrm{s}^1$ is planned. Retaining the reconstruction efficiency and spatial resolution of the ATLAS tracking detector at the sLHC, new pixel modules have to be developed that have a higher granularity, can be placed closer to the interaction point, and allow for a cost-efficient coverage of a larger pixel detector volume compared to the present one. The reduced distance to the interaction point calls for more compact modules that have to be radiation hard to supply a sufficient charge collection efficiency up to an integrated particle fluence equivalent to that of $(1-2)\cdot 10^{16}$ 1 MeV-neutrons per square centimeter ($\mathrm{n_{eq}}/\mathrm{cm}^2$).

Within this thesis a new module concept was partially realised and evaluated for the operation within an ATLAS pixel detector at the sLHC. This module concept utilizes a novel thin sensor production process for thin n-in-p silicon sensors which potentially allow for a higher radiation hardness at a reduced cost. Furthermore, the new 3D-integration technology ICV-SLID is explored which will allow for increasing the active area of the modules from 71% to about 90% and hence, for employing the modules in the innermost layer of the upgraded ATLAS pixel detector.

A semiconductor simulation and measurements of irradiated test sensors are used to optimize the implantation parameters for the inter-pixel isolation of the thin sensors. These reduce the crosstalk between the pixel channels and should allow for operating the sensors during the whole runtime of the experiment without causing junction breakdowns. The characterization of the first production of sensors with active thicknesses of 75 μm and 150 μm proved that thin pixel sensors can be successfully produced with the new process technology. Thin pad sensors with a reduced inactive edge demonstrate that the active sensor area fraction can be increased to fulfill the requirements for the detector upgrades. A subset of sensors, irradiated up to the fluence expected at the sLHC demonstrated that thin sensors show a higher charge collection efficiency than expected from current radiation damage models. First thin diodes equipped with the SLID metallization and first test structures that were connected with SLID indicate that this novel interconnection as part of the ICV-SLID technology could be a suitable replacement for the present bump-bonding technology. Finally, a new calibration algorithm for the ATLAS pixel readout chips is presented which is used to lower the discriminator threshold from 4000 electrons to 2000 electrons, to account for the reduction of the signal size due to radiation damage and the reduced sensor thickness.

Keywords:
ATLAS, Pixel detector, sLHC, 3D-integration, Radiation damage

Zusammenfassung

Um das Entdeckungspotenzial der Experimente am LHC zu erweitern, ist ein mehrstufiger Ausbau des Beschleunigers zum super LHC (sLHC) mit einer maximalen instantanen Luminosität von $10^{35}\,/\mathrm{cm}^2\mathrm{s}^1$ geplant. Zur Erhaltung der Rekonstruktionseffizienz und der Ortsauflösung des ATLAS Spurdetektors am sLHC müssen neue Pixelmodule entwickelt werden, die im Vergleich zu den derzeitigen eine höhere Granularität aufweisen, dichter am Wechselwirkungspunkt installiert werden können und ein größeres Volumen kosteneffizient abdecken. Der geringe Abstand zum Wechselwirkungspunkt erzwingt den Bau von kompakteren Modulen, die bis zu einem integrierten Teilchenfluss äquivalent zu dem von $(1-2)\cdot 10^{16}$ 1 MeV-Neutronen pro Quadratzentimeter ($\mathrm{n_{eq}}/\mathrm{cm}^2$) eine ausreichende Signalausbeute gewähleisten.

Im Rahmen der vorliegenden Arbeit wird ein neues Modulkonzept in Teilen verwirklicht und für den Einsatz im ATLAS Pixeldetektor am sLHC evaluiert. Dieses umfasst mit einem neuartigen Prozess hergestellte gedünnte n-in-p Siliziumsensoren, die eine höhere Strahlenresistenz bei geringeren Herstellungskosten erwarten lassen. Desweiteren wird das neue 3D-Integrationsverfahren ICV-SLID eingesetzt mit dessen Hilfe der aktive Flächenanteil der Module von 71% auf ca. 90% erhöht werden kann, um den Einsatz in der innersten Lage des zukünftigen Pixeldetektors zu ermöglichen.

Eine Halbleitersimulation und Messungen an bestrahlten Sensoren werden dazu eingesetzt, um die Implantationsparameter der Zwischenpixel-Isolation für die dünnen Sensoren zu optimieren. Diese soll das Übersprechen zwischen den Pixelkanälen und die Entstehung von elektrischen Durchbrüchen während der gesamten Laufzeit des Experiments verhindern. Die Charakterisierung der ersten Produktion von Sensoren mit aktiven Dicken von 75 μm und 150 μm belegt, dass dünne Pixelsensoren mit dem neuen Verfahren erfolgreich hergestellt werden können. Dünne Dioden mit reduzierten inaktiven Randbereichen zeigen, dass der aktive Flächenanteil der Sensoren vergrößert werden kann, um sich für die zukünftigen Detektoren zu qualifizieren. Die Untersuchung einer Teilmenge der Sensoren, die bis zu dem am sLHC erwarteten integrierten Teilchenfluss bestrahlt wurden, zeigt, dass die dünnen Sensoren eine höhere Signalausbeute ermöglichen als es derzeitige Modelle für Strahlenschäden vorhersagen. Desweiteren wird mit einer ersten Produktion von dünnen Dioden, die mit der SLID-Metalisierung versehen wurden, und ersten SLID-Verbindungen gezeigt, dass die neuartige Verbindungstechnologie des ICV-SLID Integrationsverfahrens einen Ersatz für das derzeitige Bump-Bonding darstellen könnte. Zuletzt wird ein optimierter Kalibrationsalgorithmus des ATLAS Auslesechips vorgestellt, der dazu verwendet wird, die Diskriminatorschwelle von 4000 Elektronen auf 2000 Elektronen zu senken, um die Auslesechips an die durch die Strahlenschäden und die verringerte Sensordicke reduzierten Signalgrößen anzupassen.

Schlagwörter:
ATLAS, Pixeldetektor, sLHC, 3D-Integration, Strahlenschäden

Contents

Overview

The Large Hadron Collider (LHC) will reach a maximum instantaneous luminosity of $10^{34}/\mathrm{cm}^2\mathrm{s}$ leading to an average of 25 proton-proton collisions per bunch crossing and creating a total of around 1000 tracks in the ATLAS inner detector every 25 ns. Already before the start of the LHC, the planning for a two phase luminosity-upgrade program had been started targeting a peak luminosity of $2.3{\cdot}10^{34}/\mathrm{cm}^2\mathrm{s}$ after the phase 1 and up to $10^{35}/\mathrm{cm}^2\mathrm{s}$ after the phase 2 upgrade to the super LHC (sLHC). For both collider upgrade phases, also upgrades of the ATLAS pixel detector are needed to allow for efficient tracking despite the increased track multiplicity and the radiation damage caused by secondary particles.

For the phase 1 upgrade an additional innermost pixel layer will be inserted into the present pixel detector which will have suffered from radiation damage. With a reduced instrumentation radius and pixel size of the new layer, the full tracking performance of the present device is planned to be recovered. For the phase 2 upgrade, the complete ATLAS inner detector is planned to be replaced with a new silicon tracking detector also covering the volume of the present gas-based transition radiation tracker. In this scenario the pixel detector will have a smaller inner- and a larger outer radius compared to the present layout. This calls for very compact and also inexpensive pixel modules to efficiently populate the whole foreseen pixel detector volume at affordable cost.

Especially in the innermost tracking layers of the pixel detector, where the track density is very high, the interaction of high energetic particles with the silicon sensors leads to a considerable damaging of the crystal lattice structure. Normalized to the radiation damage of 1 MeV neutrons ($\mathrm{n_{eq}}$), modules of the innermost layer of the ATLAS pixel detector at the sLHC will be exposed to an integrated radiation dose of $(1-2)\cdot 10^{16}\,\mathrm{n_{eq}}/\mathrm{cm}^2$. The resulting radiation damage in the pixel sensors leads to high leakage currents and a reduction of the signal size. The most demanding challenge of the module upgrades is to develop sensors and readout electronics that allow for an operation with a high signal efficiency in this extreme environment.

Within this thesis, the development towards a novel ATLAS pixel module is presented that is proposed by the Max-Planck-Institut für Physik (MPP). The module will include the new 3D-interconnection technology ICV-SLID and a reduced guard-ring structure for the sensors to reach a higher active fraction and compactness to fulfill the criteria

for the innermost pixel layer of the upgrades of the pixel detector. To still use the more efficient electron readout, the sensors will use the n-in-p doping concept while allowing to reduce the number of processing steps during the sensors fabrication compared to the present n-in-n sensors. This will lower the production costs to allow for large area detectors. Furthermore, the sensors will be produced with a new production process for thin sensors which was developed at the semiconductor laboratory HLL of the Max-Planck-Gesellschaft (MPG). Thin sensors are expected to deliver a higher signal after large irradiation doses compared to sensors of standard thickness due to their different electric field configurations. Nevertheless, the signal sizes of the sensors at the sLHC are expected to decrease due to the radiations damage. Therefore, to allow for successful module operation at high signal to noise ratios, the threshold of the pixel readout chips has to be lowered.

This thesis is organized as follows: Chapter 1 gives a short summary of the physics prospects of the sLHC and introduces the phase 1 and phase 2 upgrade plans of the LHC collider. Chapter 2 describes the basic functionality of semiconductor sensors as well as the processes leading to radiation damage and highlights the benefits of the novel MPP module concept for the operation at the sLHC. In Chap. 3, the results from a semiconductor simulation and measurements of pre-production sensors are presented that have been conducted to define the most promising implant parameters applied for the main thin sensor production. The characterization of the first thin pixel and strip sensors from the main production is shown and especially the results of measurements of the signal size before and after proton irradiation are presented. Measurements of diodes with a reduced guard-ring structure indicate that a decrease of the inactive edge to less than 500 μm can be achieved. Chapter 4 summarizes the results obtained so far towards the use of the ICV-SLID 3D-integration technology. A proof of principle for the compatibility of this technology with semiconductor sensors is given and the interconnection efficiency is characterized with test structures. Future steps of the ongoing R&D are outlined. Chapter 5 recapitulates the most important results on the optimization of the discriminator threshold of the present ATLAS readout chips with a modified calibration algorithm. At the end, a summary concludes the results of this thesis.

Chapter 1

Luminosity upgrade plans for the Large Hadron Collider

"What I cannot create, I do not understand."

R. Feynman,
written at his blackboard at the
time of his death in 1988 [1]

The Large Hadron Collider (LHC), located at the Conseil Européen pour la Recherche Nucléaire (CERN) [2] near Geneva, is the largest and most powerful proton collider in existence today. Colliding protons at a foreseen center of mass energy of 14 TeV, elementary particles are created and used to study the physics of the fundamental building blocks of nature and their interactions. In an alternative operation mode the LHC accelerator can also be used for lead-lead heavy ion collisions at an energy of 2.76 TeV per nucleon or 574 TeV per ion, surpassing the energies reached at the Relativistic Heavy Ion Collider (RHIC) [3] at the Brookhaven National Laboratory by almost a factor of 30. Detailed reviews of the physics opportunities at the LHC can be e.g. found in [4, 5].

With a nominal luminosity of $10^{34}\,/\mathrm{cm}^2\mathrm{s}^1$ the LHC will surpass the peak luminosity of the Tevatron collider at the Fermilab by over a factor of 30 [6]. The luminosity integrated over the first 5 years of LHC operation time is expected to reach $300\,\mathrm{fb}^{-1}$ [7], compared to the $8\,\mathrm{fb}^{-1}$ produced during the Tevatron Run-II so far [8]. Nevertheless, an upgrade of the LHC luminosity is currently being planned, targeting a peak value of $10^{35}\,/\mathrm{cm}^2\mathrm{s}^1$ and an integrated luminosity of up to $3000\,\mathrm{fb}^{-1}$ [7] at the so called Super LHC or sLHC. The motivation behind this upgrade is to extend the measurement precision of particle parameters as well as the discovery potential for physics beyond the Standard Model (SM) of elementary particle physics. As major hardware upgrades of the accelerator and detectors have to be carried out to increase the luminosity by a factor of ten, a prolonged operation shutdown period is needed. This is planned to

coincide with the mandatory shutdown after about 10 years of data taking at the nominal luminosity which is needed to replace detector components and focussing magnets which will suffer from radiation damage [9].

In this chapter, Sec. 1.1 gives a short introduction to the physics cases that can be investigated with a ten-fold luminosity at the sLHC. Section 1.2 introduces the LHC accelerator complex and possible scenarios for reaching the targeted peak luminosity in a two step upgrade. In Sec. 1.3, the ATLAS detector is briefly introduced with an explicit focus on the sLHC upgrade strategies for the different sub-detector components. Finally, Sec. 1.4 gives an overview of the pixel module concept proposed by the Max-Planck-Institut für Physik (MPP) for use in the ATLAS detector during the sLHC operation. This novel module concept, being the main research target of the presented thesis, is expected to allow for the production of radiation hard, very compact, and cost-effective pixel modules for large scale tracking detectors.

1.1 Physics motivation

There are several physics cases that call for a luminosity upgrade of the present LHC accelerator. Some of them are already foreseeable at this point in time, while others depend much on the physics actually realized in nature and probed by the LHC. In general, the discovery reach of the experiments at the sLHC accelerator can be extended to higher particle masses by $(20 - 30)\%$, and the statistical error halving time, which will have reached around 5 years at the time of the foreseen upgrade, can be reduced with the increased luminosity [9]. More specific examples of measurements which profit from the higher luminosity at the sLHC are listed in the following.

1.1.1 Measuring the parameters of the SM Higgs boson

The Higgs boson was proposed in 1964 [10, 11, 12] to explain the origin of the masses of the W and Z bosons via the Higgs-Mechanism. Also the massive fermions of the SM could acquire their mass by coupling to the Higgs field via the Yukawa coupling. The Higgs boson is the last particle of the SM which has not been discovered yet. The current upper limit for the Higgs boson mass in the SM, deduced from precision measurements of the W-boson and top quark masses, is $m_{\mathrm{H}} \leq 157\,\mathrm{GeV}/c^2$ at 95% CL [13]. By direct searches for the Higgs boson, the LEP experiments have set a lower limit of $m_{\mathrm{H}} \geq 114.4\,\mathrm{GeV}/c^2$ on the Higgs mass also at 95% CL. Recently the mass range of $163\,\mathrm{GeV}/c^2 < m_{\mathrm{H}} < 166\,\mathrm{GeV}/c^2$ was excluded at a 95% CL by experiments conducted at the Tevatron [14]. Taking into account the exclusion limits from the direct searches, the upper limit for a SM Higgs is currently $m_{\mathrm{H}} \leq 186\,\mathrm{GeV}/c^2$ [13].

For the multi-purpose experiments ATLAS [15, 16] and CMS [17] at the LHC, search strategies have been established over the last years to be sensitive to Higgs boson sig-

natures over a large mass range up to $m_{\mathrm{H}} = 1\,\mathrm{TeV}/c^2$, also covering the mass range predicted for a supersymmetric Higgs boson [18, 19]. If the Higgs boson has been discovered, its parameters have to be precisely measured. These include the mass, the spin, the CP-quantum numbers, and the couplings to itself as well as to other fermions and bosons. The Higgs boson mass can be measured over a wide mass range using the electromagnetic $\gamma\gamma$ or 4-lepton final states. The spin and the CP quantum numbers can be deduced by the angular distribution of the four leptons in the decay $\mathrm{H} \rightarrow \mathrm{ZZ} \rightarrow 4\mathrm{l}$ [20]. Since the coupling strengths cannot be measured directly, the couplings to bosons and fermions will be normalized to the $\mathrm{H} \rightarrow \mathrm{WW} \rightarrow \mathrm{l}\nu\mathrm{l}\nu$ rates [21]. At the sLHC the relative couplings of fermions and bosons to the Higgs are expected to be measured at an accuracy of $(10 - 20)\%$, an improvement by a factor of two compared to the LHC [9]. Furthermore, new rare decay channels will become accessible including $\mathrm{H} \rightarrow \mu\mu$ and $\mathrm{H} \rightarrow \mathrm{Z}\gamma$ [22].

To fully prove or disprove the Higgs mechanism, the Higgs self-coupling strength λ_{HHH} has to be measured to deduce the shape of the Higgs potential. Due to the limited production rates, measuring the Higgs self-coupling is not possible at the LHC. The self-coupling strength enters in the Higgs pair-production and it has been suggested to look for $\mathrm{HH} \rightarrow \mathrm{WW\,WW}$ decays at the sLHC if $m_{\mathrm{H}} > 140\,\mathrm{GeV}$ [23].

1.1.2 Precision measurements of Standard Model parameters

At the end of the LHC operation, most measurements of SM parameters will not be limited by the statistical uncertainties, but rather by the systematic uncertainties of the Monte Carlo simulations, the detector performance, and the physics models. However, there are measurements of rare processes in the SM that benefit from the increased statistics collected at the sLHC. One example are the rare top quark decays which are mostly believed to be beyond the reach of the LHC. There is a class of theories beyond the SM that predicts branching ratios of top quark decays by flavor changing neutral currents ($\mathrm{t} \rightarrow \mathrm{q}\gamma$, $\mathrm{t} \rightarrow \mathrm{qZ}$, and $\mathrm{t} \rightarrow \mathrm{qg}$ where $\mathrm{q} = \mathrm{u}, \mathrm{c}$) of $10^{-5} - 10^{-6}$ [22]. Especially for the decay process $\mathrm{t} \rightarrow \mathrm{qZ}$, the sensitivity depends almost linearly on the luminosity and therefore can be improved significantly at the sLHC. Nevertheless, to reach this enhanced sensitivity the performance of identifying b-quarks, i.e. the b-tagging, must be kept at the same level as for the present detectors. This poses a strong challenge to the future detectors which will have to cope with a much higher track density.

1.1.3 Physics beyond the Standard Model

The LHC will be the first accelerator to probe physics processes at energies well above the electroweak symmetry breaking scale. Several Beyond-the-Standard-Model (BSM) models exist that could already be probed at the LHC. These are for example SUper SYmmetry (SUSY), extra dimensions, technicolor and leptoquarks. Reviews can be

found, e.g. in [24, 25, 26, 27] and references therein. The physics case of the sLHC strongly depends on the physics discovered at the LHC, but the sLHC will in general be able to extend the discovery potential for the given models to higher masses. Furthermore, the sensitivity of the rate-limited processes will be increased giving excess to higher precision measurements at the highest energies.

If for example SUSY is discovered at the LHC, the masses and the model parameters will have to be measured. Depending on the energy scale where SUSY will reveal itself, this will not be possible at the LHC. The precise measurement of SUSY particles requires in most cases the selection of exclusive decay modes containing leptons or b-jets, being in some cases rate-limited. For these, the sLHC will provide an improvement in the statistical uncertainties if the detector, especially the trackers will show the same tracking performance as the present ones. In the case of no observation of SUSY particles at the LHC, the upgrade to the sLHC can extend the discovery reach by about 0.5 TeV up to 3.0 TeV [9].

1.2 The LHC accelerator and the luminosity upgrade plans

The present accelerator complex of the LHC is shown in Fig. 1.1. Only one of the two LINear ACcelerators (LINACs) can be used at a time to either introduce protons or heavy ions into the accelerator system. In the case of using the LHC as a proton accelerator, the LINAC2 accelerates the protons up to an kinetic energy of 50 MeV and injects them into the accelerator chain of the Proton Synchrotron Booster (PSB, 1.4 GeV), the Proton Synchrotron (PS, 26 GeV), and the Super Proton Synchrotron (SPS, 450 GeV). From the SPS the protons are injected into the main LHC accelerator. Here, for the first time they are circulating in opposing directions and thus, can be collided at the four interaction points at the experiments ATLAS, CMS, ALICE [28], and LHCb [29]. In the heavy ion runs, the linear accelerator LINAC3 is used to inject the lead atoms with an energy of 4.2 MeV per nucleon into the Low Energy Ion Ring (LEIR). From here, they follow the same acceleration process through the PS and SPS into the LHC which they enter with an initial energy of 177 GeV per nucleon.

1.2.1 The first LHC collision runs

After the first LHC startup in late 2008 and the following shutdown due to a technical failure, the collider was successfully repaired and restarted in 2009. Starting with first injection tests in October of that year, the LHC circulated first proton beams in November when also first collisions were seen. On the 30^{th} of November, both proton beams were accelerated to 1.18 TeV setting a new world record for proton accelerators. The first collisions at this record energy were initiated in December and first collision data

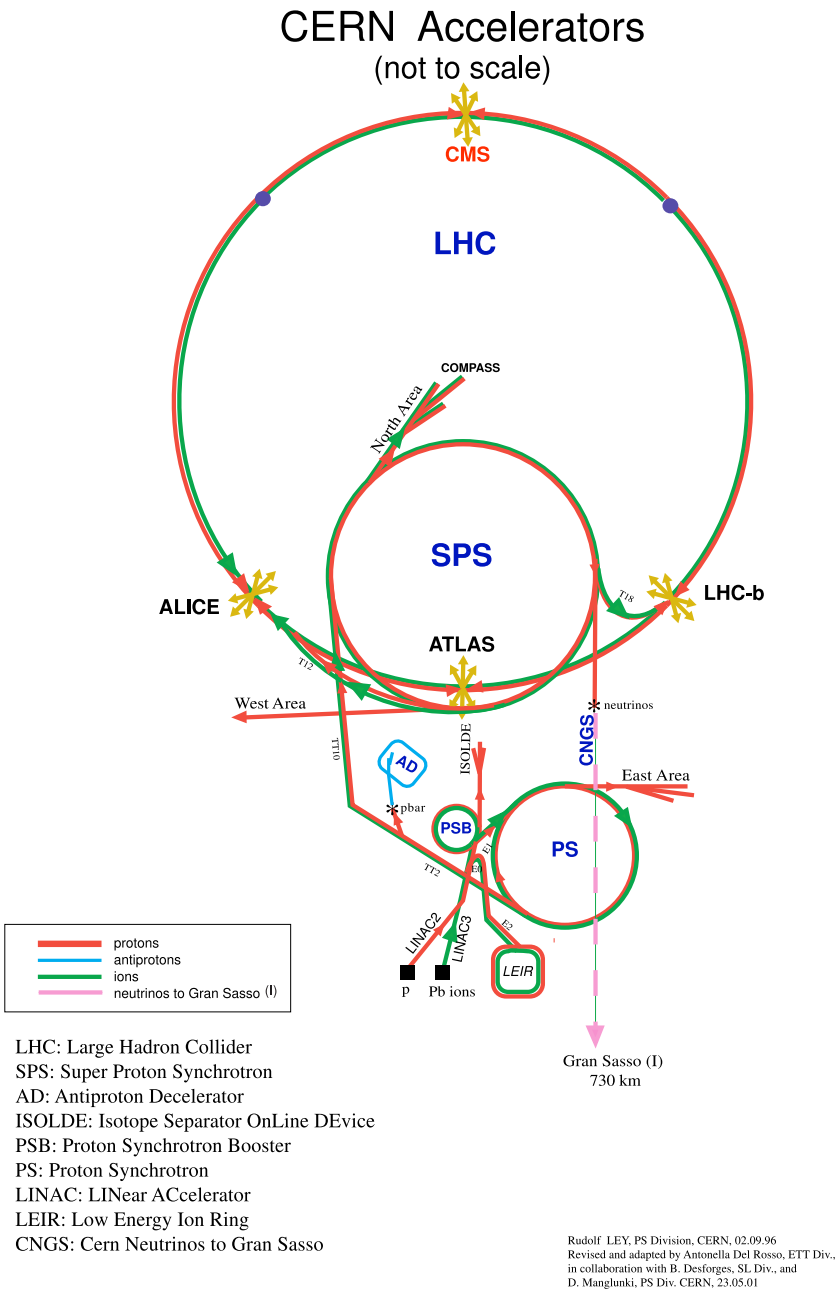

Figure 1.1: The LHC accelerator complex [2].

was taken by all four main experiments. From early 2010, a long physics run has started collecting the first $1\,\mathrm{fb}^{-1}$ with a beam energy of 3.5 TeV. On the 30^{th} of March, the first collisions and successful physics data taking of all four main experiments at this new record energy set the start of this run which is planned to last up to the end of 2011. After this, a shutdown will follow to prepare the accelerator for the nominal beam energy of 7 TeV. At this energy it is planned to reach a maximum instantaneous luminosity of $10^{34}\,/\mathrm{cm}^2\mathrm{s}^1$. The LHC will be operated with these parameters for several years, until an integrated luminosity of about $100\,\mathrm{fb}^{-1}$ is collected in 2014 to 2015 [30]. At this point, a first longer shutdown is planned to start with the first of the two luminosity upgrade phases.

1.2.2 Upgrade phase 1 - the LINAC4

The maximum luminosity for ideal head-on collision L_{head} of the LHC accelerator depends on the beam current I, the beam brightness B, and the beam geometry at the interaction point:

$$L_{\mathrm{head}} = \frac{\gamma}{4\pi\beta^*} \cdot B \cdot I, \quad \text{with } \gamma = \frac{1}{\sqrt{1-\beta^2}} \quad \text{and } \beta = v/c. \tag{1.1}$$

Here v is the particle velocity, c the vacuum speed of light, and β^* is the beta function at the interaction point [31]. The brightness

$$B = \frac{N_{\mathrm{b}}}{\epsilon_{\mathrm{n}}} \tag{1.2}$$

depends on the number of protons per bunch N_{b}, and the normalized transverse emittance $\epsilon_{\mathrm{n}} = \beta\gamma\epsilon$. The beam current

$$I = N_{\mathrm{b}} \cdot n_{\mathrm{b}} \cdot f_{\mathrm{rev}} \tag{1.3}$$

also depends on the number of protons per bunch, the number of bunches per beam n_{b}, and the revolving frequency f_{rev} of the protons. At the Interaction Points (IPs) located within in the detectors, ideal head-on collisions are not possible, due to the crossing-angle θ_{c} between the beams. This introduces a geometric reduction F of the maximum luminosity leading to

$$L = L_{\mathrm{head}} \cdot F = L_{\mathrm{head}} \cdot \frac{1}{\sqrt{1+\frac{\theta_{\mathrm{c}}\sigma_z}{2\sigma^*}}}. \tag{1.4}$$

Here, $\sigma^* = \sqrt{\epsilon\beta^*}$ is the RMS of the transverse beam size and σ_z is the RMS of the bunch length.

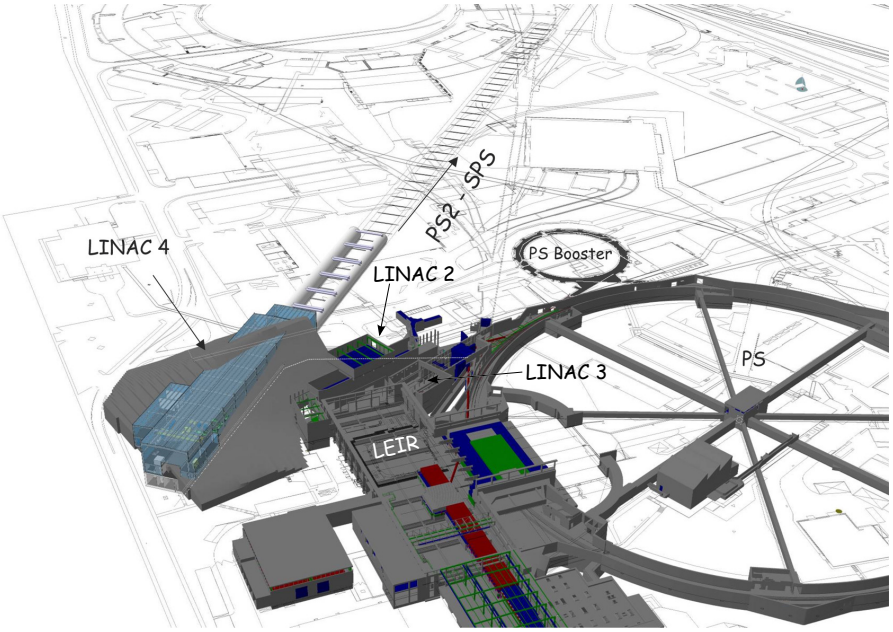

Figure 1.2: The new LINAC4 injector and the present PSB-PS accelerator system [33].

For the planned luminosity upgrades, several of these parameters will be optimized. In the first phase to extend the physics reach of the LHC, the luminosity is going to be increased by replacing the LINAC2 with a new proton injector. This approach is followed since the main bottleneck for the current luminosity is the beam brightness, which is limited by space charge effects at the injection of protons from the LINAC2 into the PSB [30]. Figure 1.2 shows the schematics and the location of the new LINAC4 [32], already being under construction to overcome this problem. It is 100 m long and injects the protons through a transfer line into the PSB. The orientation of the LINAC4 is chosen to allow for a future upgrade to higher energies and direct proton injections into the SPS accelerator.

The LINAC4 will accelerate negatively charged H^--ions instead of protons to a kinetic energy of 160 MeV. Before the protons are injected into the first ring accelerator, a stripping foil is used to remove the electrons. With this well proven technology and the increased energy, protons can be accumulated in the accelerators at smaller transverse emittances ϵ_n. For the same number of protons per bunch the LINAC4 will be able to deliver an improvement of the brightness, and thus the luminosity, by a factor of two. With additional optimizations of the focussing magnets at the experiments, leading to a reduction of β^*, a maximum luminosity of $2.3 \cdot 10^{34}\,/\mathrm{cm}^2\mathrm{s}^1$ is planned to be reached with this phase 1 upgrade [9]. Current planning foresees the finishing of the LINAC4 construction and the first delivered protons in 2014 or 2015.

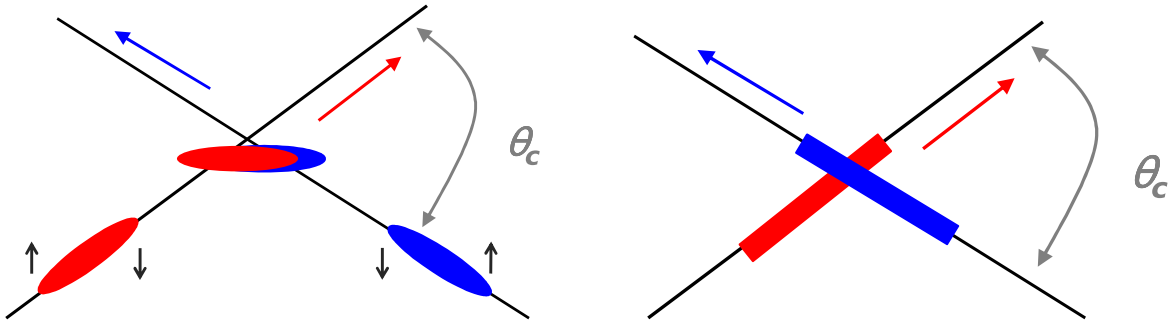

(a) FCC (b) LPA

Figure 1.3: The *Full Crab Crossing* (FCC) scheme and the *Large Piwinski Angle* (LPA) approach [30].

1.2.3 Upgrade phase 2 - the sLHC

The second upgrade phase towards the sLHC is expected to be carried after around ten years of physics data taking. The primary goal of this upgrade is to increase the luminosity to the maximum value reachable, targeting a ten-fold increase to 10^{35} /cm^{2}s^1. This will involve major changes to the beam- and IP parameters. However these have not been finalized so far, since only after gaining experience from the present accelerator operation the best upgrade approach can be assessed.

Nevertheless, two alternative upgrade scenarios are already thought of. Figure 1.3 shows the schematics of these two very different approaches. The first (Fig. 1.3(a)) will involve installing crab cavities [34, 35] close to the IPs. These reduce the effective crossing angle of the bunches to allow for almost head-on collisions, i.e. an effective reduction of θ_c and hence, an increase of the geometric reduction factor F closer to 1. The second approach (Fig. 1.3(b)) does not try to decrease the crossing angle, but rather to increase the number of protons per bunch at a constant ϵ_n. Here it is planned, to increase N_b proportional to $1/F$ so that the product $B \cdot F$ remains constant. Since N_b also enters in I, it follows $L \propto N_b$.

Both of these scenarios involve major rework, especially of the focussing magnets but could be realized with the new LINAC4 injector scheme presented above.

1.3 The ATLAS detector at the Super LHC

With a length of 44 m, a height of 25 m, and a mass of 7000 t, the ATLAS[1] detector (see e.g. [36] and references therein) is the largest detector ever built at a particle collider.

[1] ATLAS: A Toroidal LHC ApparatuS

In Fig. 1.4(a) the main detector components of ATLAS are presented. Each of them is centered around the IP and consists of a cylindrical barrel section with endcaps on each side. Emerging from the collisions in the center of the detector, the secondary particles first pass the different sub-detectors of the inner detector (ID) [37, 38] (Fig. 1.4(b)) residing in a 2 T solenoidal magnetic field. These are the semiconductor pixel detector [39], the SemiConductor Tracker (SCT) (e.g. [40] and references therein), and the Transition Radiation Tracker (TRT) [41]. Both, the pixel detector and the SCT consist of an arrangement of many detector modules, mounted on barrel and endcap support structures. Each of the modules consists of a patterned silicon sensor with attached readout electronics. The detection principle is based on the collection of electron-hole pairs created by ionizing particles in depleted silicon. The TRT consists of straw tubes with a diameter of 4 mm containing a gas mixture and a central gold plated tungsten anode wire. Penetrating particles ionize the gas atoms and the radial electric field configuration is used to amplify the drifting charges via avalanche multiplication. Between the straws a polypropylene-polyethylene fiber radiator is placed to cause the emission of transition radiation by penetrating particles. This is mainly used to discriminate between electrons and pions. A total of up to 47 hits are created by charged particles interacting with the ID detector components, most of them in the TRT. They can be assigned to one or several readout channels of the detectors and from this, the initial vertex as well as the momentum of the particles can be reconstructed. The pseudo-rapidity

$$\eta = -\log\left(\frac{\theta}{2}\right) \tag{1.5}$$

with θ being the angle between the beam-axis and the particle momentum, is covered by the ID over a range up to $|\eta| < 2.5$.

Outside of the solenoid magnet, the electromagnetic and hadronic sampling calorimeters follow [42]. The electromagnetic calorimeter is used to detect particle showers from electromagnetically interacting particles. The active material of the electromagnetic calorimeter is liquid argon which is interleaved with lead, used as the absorber material, in an accordion arrangement. The hadronic calorimeter follows the same principle but uses scintillating tiles and iron absorbers in the barrel part. Liquid argon and copper as well as tungsten absorbers are used in the endcap region. The hadronic calorimeter is designed to measure showers from strongly interacting particles, which are generally not stopped in the electromagnetic calorimeter. From the shape of the showers in both calorimeters the energy of the initial incident particle can be determined.

Surrounding the calorimeters, the ATLAS muon spectrometer follows [43]. It is enclosed in a 4 T toroidal magnetic field, giving ATLAS its name, which is used to bend the trajectories of the muons, usually not stopped in the calorimeters. The muon spectrometer comprises the Monitored Drift Tubes (MDTs) and the Cathode Strip Chambers (CSCs) for precision muon tracking. Resistive Plate Chambers (RPC) and Thin Gap Chambers (TGP) are used for triggering and the later also to gain additional tracking

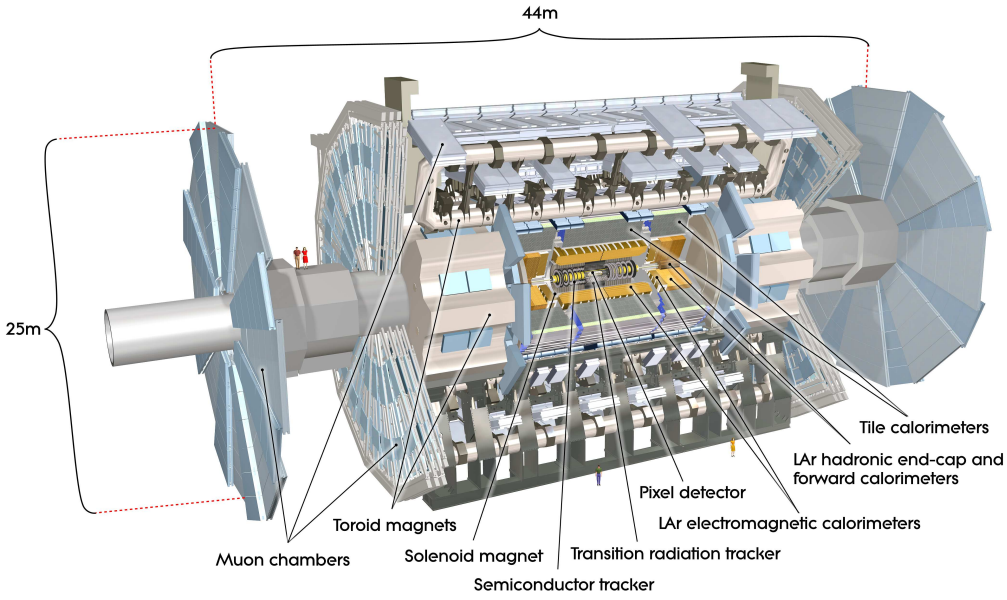

(a)

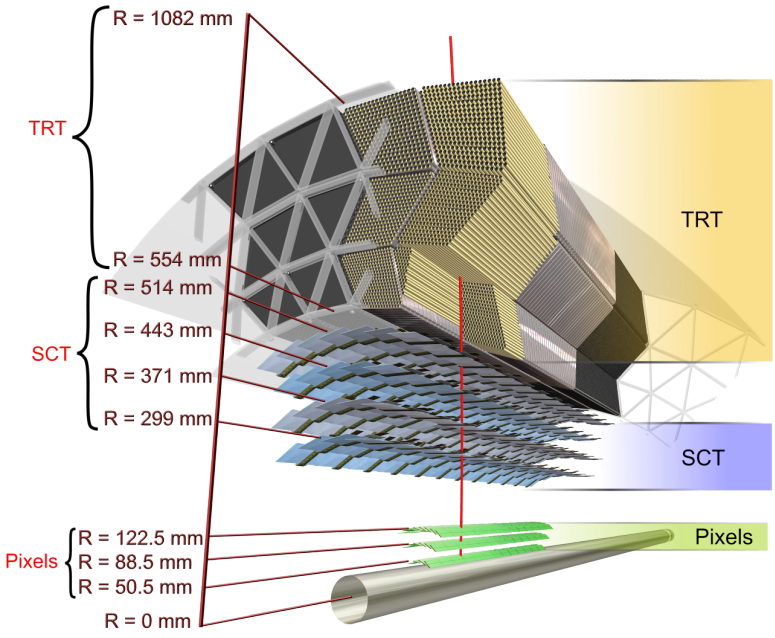

(b)

Figure 1.4: The ATLAS detector (a) and the barrel part of inner detector (b), both from [16].

information in the forward region. The aluminum MDTs with a radius of 30 mm are gas filled and contain a central anode wire to create a radial electric field. Similar to the TRT detection principle, penetrating muons ionize the gas atoms and the generated charges are separated and eventually multiplied close to the anode wire. To increase the spatial resolution of the tubes also the drift time of the charges is determined.

Combining the results from all sub-detector components, most of the particles created in the collisions can be identified and their initial vertex and energy can be measured. From the presently known particles, neutrinos which are solely weakly interacting manifest as missing energy.

1.3.1 Upgrades of the ATLAS detector components

Increasing the luminosity of the LHC accelerator inevitably leads to additional requirements for some of the ATLAS sub-detectors. In general, the occupancy of all sub-detectors increases and especially for detectors with very high hit rates, i.e. those located close to the IP and in the high η regions, radiation damage will deteriorate the detector performance. The following discusses the planned upgrades of the individual detector components for the phase 2 upgrade. For the innermost pixel layer, even after the phase 1 upgrade, changes to the pixel detector are foreseen.

Muon system

Most parts of the muon system are far away from the interaction point and thus, are not expected to suffer from radiation damage. However, due to the comparably large area of the readout channels and their dead-time of at least 200 ns, the occupancy can reach more than 30% in most MDTs and CSCs [44]. This high occupancy is mainly caused by the large neutron and photon background stemming from secondary interactions in the calorimeter systems. To reduce the high occupancy in the most affected areas, i.e. especially in the forward direction close to the interaction point, a replacement of the present MDTs and some of the CSCs is planned, using aluminum tubes with a reduced radius of 15 mm. This shortens the maximum drift time from 700 ns to 200 ns and allows for an increase of the maximum hit rate per area by a factor of three. Instead of a three layer-design the thin tubes allow for a six-layer design, doubling the redundancy for reconstructing the muon tracks.

Calorimeters

As for the muon spectrometer, most components of the calorimeter system will not suffer from radiation damage. The scintillator tiles in the barrel region of the hadronic calorimeter are sufficiently far away from the IP and the liquid argon calorimeters are intrinsically radiation hard. However, especially in the forward region, the radiation

level will be significant and might cause a deterioration of the cold electronics in the Hadronic Endcap Calorimeter (HEC). Therefore, investigations to evaluate the radiation hardness of the electronics as well as research and development towards their upgrade are carried out [45]. Furthermore, especially the liquid argon Forward CALorimeter (FCAL), covering the pseudo-rapidity range of $3.1 < |\eta| < 5.0$ at low z, faces two challenges. The first is the increased build-up of space charges in the active medium leading to a modification of the measured signal size. Even though the gap size between the absorbers filled with the active medium is only $250\,\mu$m, current developments aim at reducing this gap size down to $100\,\mu$m to decrease the build-up of space charges.

The second challenge, provoked by a ten-fold increase of luminosity is the increased heat load caused by the energy absorbed in the calorimeters. Current simulations foresee a power dissipation of $400\,\mathrm{W/m^2}$ which would lead to temperatures above the boiling point of the liquid argon, considering the current cooling system and operating parameters [46]. Replacing the forward calorimeter modules represents a serious logistical challenge, since it would involve opening the endcap cryostats. Including the re-assembly, this would take up to three years [47], being too long for the anticipated upgrade shutdown. Therefore, new strategies are investigated that involve installing a new calorimeter, which does not need to be cooled, between the IP and the present forward calorimeter. It could be used for additional energy measurements and as a radiation shield, avoiding major upgrades of the present system. However, still under discussion is the availability of space and the impact of such a calorimeter on the ID in terms of increasing occupancy due to back-scattering.

Inner detector

For the sLHC, the upgrade of the ID will pose the highest technical challenge in terms of data processing, track discrimination power, and radiation damage. Already in the early phase of the planning towards the phase 2 LHC upgrade it was evident, that the gas-based TRT cannot cope with a ten-fold increase of the hit rate. Therefore, it was decided by the upgrade steering group [48], that during a complete upgrade of the ID, the TRT will be replaced by silicon based detectors with a much higher granularity.

An initial layout of the new ID has been proposed which is called the strawman, being a flexible and rearrangeable first approach. Several iterations of this layout have led to the current version shown in Fig. 1.5, which might still be subject to changes. The outer part consists of a large volume n-in-p silicon strip detector with modules on five layers in the barrel region and five endcap discs at each side. In the barrel region, the outer two layers, spanning over a radial range of $74.3\,\mathrm{cm} < R < 100.0\,\mathrm{cm}$, will comprise long-strip sensors with an approximate cell size of $80\,\mu\mathrm{m} \times 10\,\mathrm{cm}$. The inner three layers of short-strip sensors with a cell size of $80\,\mu\mathrm{m} \times 2.5\,\mathrm{cm}$ will populate the volume within $38.0\,\mathrm{cm} < R < 62.2\,\mathrm{cm}$. Each of the modules consists of two sandwiched single-sided sensors with a small stereo angle to improve on the resolution along the strip direction.

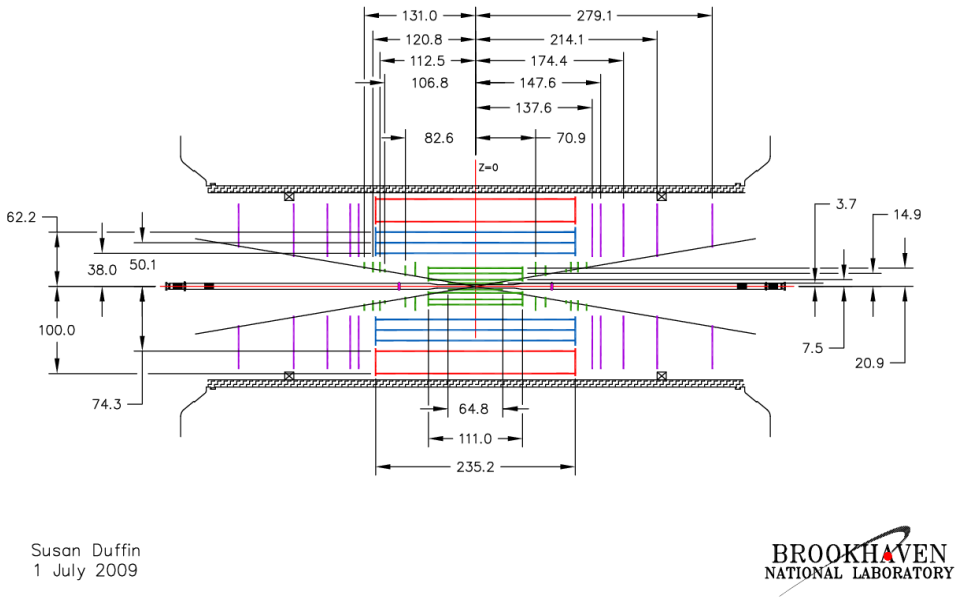

Figure 1.5: The present strawman layout [48] of the inner detector for the ATLAS detector at the sLHC.

Encompassed by the strip detector, the pixel detector with four barrel layers with radii of $3.7\,\text{cm} < R < 20.9\,\text{cm}$ and five endcap discs is located. The outer two layers will have a pixel cell size of $50 \times 250\,\mu\text{m}^2$ and the inner two of $50\times \leq 200\,\mu\text{m}^2$ for improved resolution and decreased hit occupancy. Like for the present ID, the strawman layout covers the pseudorapidity range up to $|\eta| = 2.5$.

With the replacement of the TRT by silicon sensors and the reduction of the pixel size in the innermost layers, the occupancy can be lowered to allow for efficient operation at the sLHC. However, especially the innermost pixel layers also face radiation damage that will accumulate during the LHC, and even faster, during the sLHC operation. For this reason already coinciding with the LHC phase 1 upgrade, an upgrade of the ATLAS pixel detector is planned. At this point in time the radiation damage is expected to impair the signal efficiency of the sensors in the innermost pixel layer, i.e. the so called b-layer. The shutdown for the LHC phase 1 upgrade is planned to last less than one year, forbidding a complete exchange of the present pixel detector. Therefore, only a new b-layer will be build, that is going to be mounted directly onto a new slimmer beam-pipe and will be slided into the present b-layer [49]. The foreseen mean sensor radius of the new b-layer is $R = 3.2\,\text{cm}$. This phase 1 ATLAS pixel detector upgrade is commonly referred to as the Insertable B-Layer or IBL upgrade.

In both upgrade phases the innermost pixel detector layer will be closer to the IP than the present b-layer, and the luminosity will be higher than the design luminosity

of the LHC. Therefore, the new pixel modules will have to be optimized for radiation hardness, and compactness to achieve a large live-fraction, i.e. a large ratio of active sensor area to the total area of the modules. In addition, the material budget of the modules has to be reduced as much as possible since the effect of multiple scattering close to the IP significantly decreases the tracking performance. There are several research projects ongoing that try to develop pixel modules that meet the requirements for the IBL and sLHC upgrades. In the following, the pixel module concept developed at the MPP will be presented.

1.4 The novel MPP pixel module concept

In this section the requirements for the pixel modules for the upgrade scenarios and the approach of the MPP to meet these requirements are discussed. The target detector of this research is the ATLAS pixel detector for the sLHC, however, also a sensor production for the IBL upgrade is anticipated. The individual components of the new MPP module concept are described in the following.

1.4.1 Requirements for a new pixel module

Presently, the requirements for a pixel detector at the sLHC are only partly known since some of the effects of high luminosity operation can only be estimated after running the present device at the LHC for some time. One of the key ingredients to a pixel detector close to the IP is the radiation hardness, i.e. the resistance to damages caused by high energetic particles penetrating the detector. Current estimations of the expected integrated fluence Φ_{eq}, scaled to the radiation damage of 1 MeV neutrons per square centimeter ($\mathrm{n_{eq}/cm^2}$), are extracted from a Monte-Carlo simulation [47]. This is presented in Fig. 1.6, as a function of the radial distance from the IP for different values of $|z|$ (measured along the beam-axis with the IP located at $z = 0$), and assuming an integrated luminosity of $3000\,\mathrm{fb}^{-1}$. Since the innermost pixel layer will likely be placed at a radius of $3\,\mathrm{cm} < R < 4\,\mathrm{cm}$, it will be exposed to an equivalent fluence of $\Phi_{\mathrm{eq}} \approx (1-2)\cdot 10^{16}\,\mathrm{n_{eq}/cm^2}$, depending on the safety factors multiplied to the simulation results.

Apart from the requirements with respect to radiation hardness, the smaller radius of the innermost pixel, compared to the present ATLAS pixel detector also leads to additional requirements for the module arrangement. While the layout of the ID for the sLHC is not fixed yet, the one for the IBL upgrade is strongly restricted due to the already present pixel detector. The foreseen radius envelope of the new b-layer is so small that shingling in z, i.e. an overlap of the modules in the direction along the beam-axis, like in the present detector, is not possible. This restriction is also expected to hold for the detector for the phase 2 upgrade. If shingling along this direction is

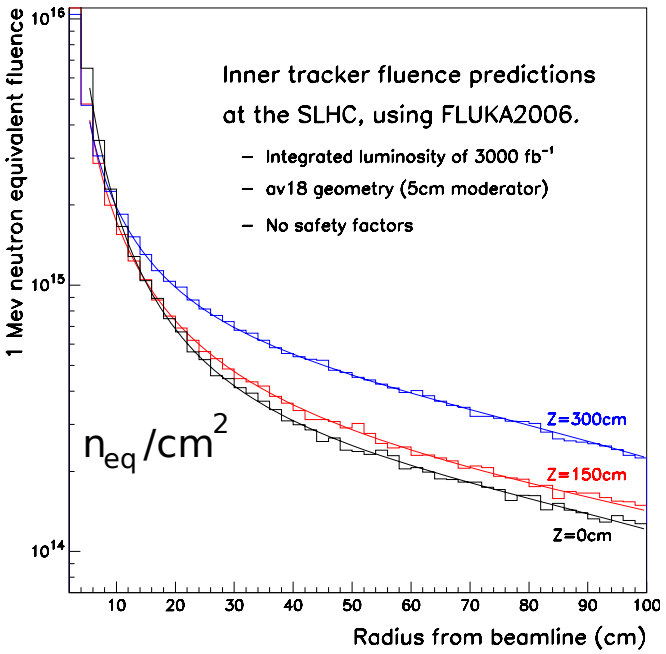

Figure 1.6: Expected equivalent fluences Φ_{eq} (in $\mathrm{n_{eq}/cm^2}$) in the tracking detector at the sLHC as a function of the radial distance from the beam-line [47].

not possible, the active area of the pixel sensors has to extend as far as possible to the module edges perpendicular to the z-axis. The target value for the width of the inactive edge on these two sides is $(450 - 500)\,\mu$m [50], being a reduction of 50% compared to the current sensors.

Another goal that is followed is the reduction of the material budget of the detectors. Since multiple scattering causes a deterioration of the tracking performance especially in the innermost layers, it is planned to reduce the material budget of the pixel module support structures, the cooling system, and also the detector modules. Apart from the physics requirements, also the monetary aspect has to be considered for such a large scale semiconductor detector. Therefore, a cost optimization is much desired.

1.4.2 Improvement of the present module concept

The present ATLAS pixel module (Fig. 1.7) consists of three layers of active components and has an area footprint of about $2.0 \times 6.3\,\mathrm{cm}^2$. A $250\,\mu$m thick n-in-n silicon pixel sensor forms the central layer of the module in which the penetrating charged particles generate the signals. Bump-bonding is used to connect the contact pads of the individual pixel cells of $50 \times 400\,\mu\mathrm{m}^2$ to the 46080 input pads of 16 FE-I3 ATLAS readout electronics chips [51]. In the readout electronics the signals are amplified, digitized, and via wire-

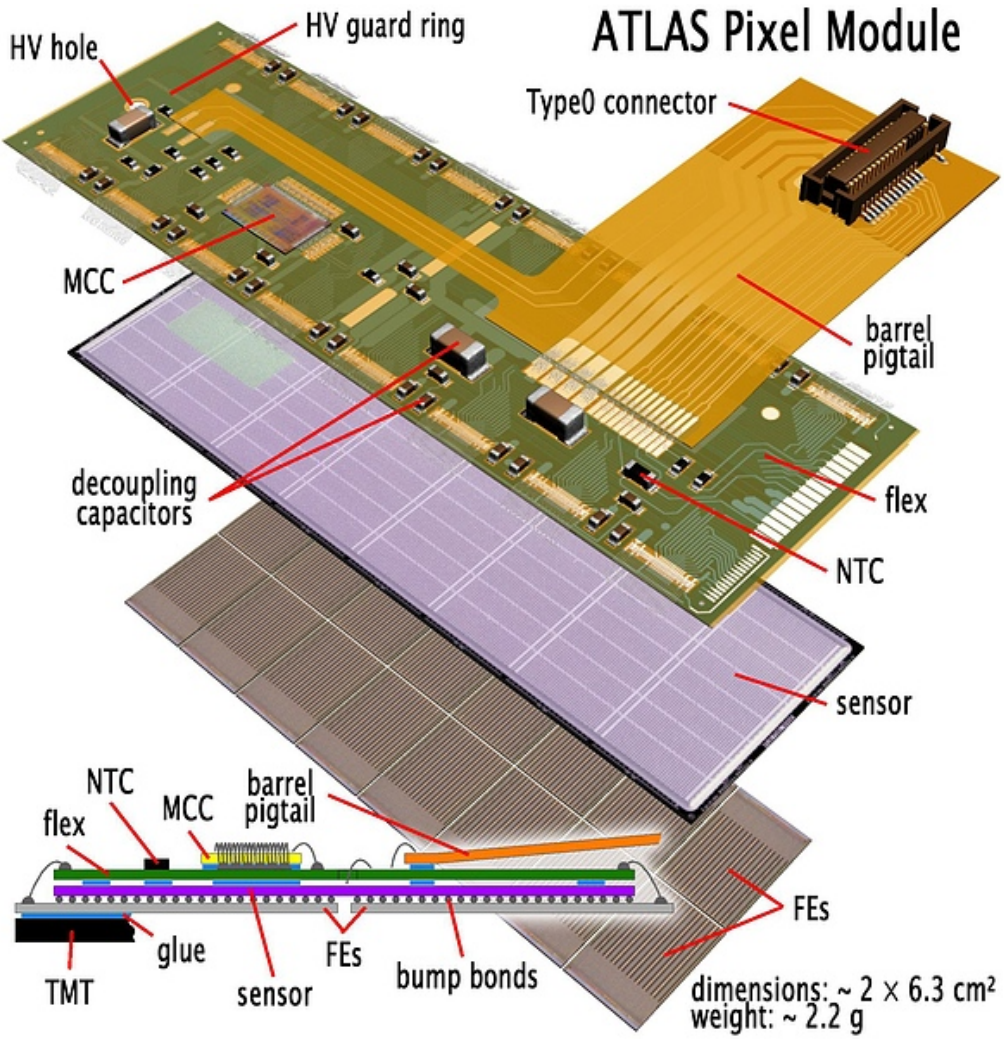

Figure 1.7: Technical drawing of the ATLAS pixel module [16].

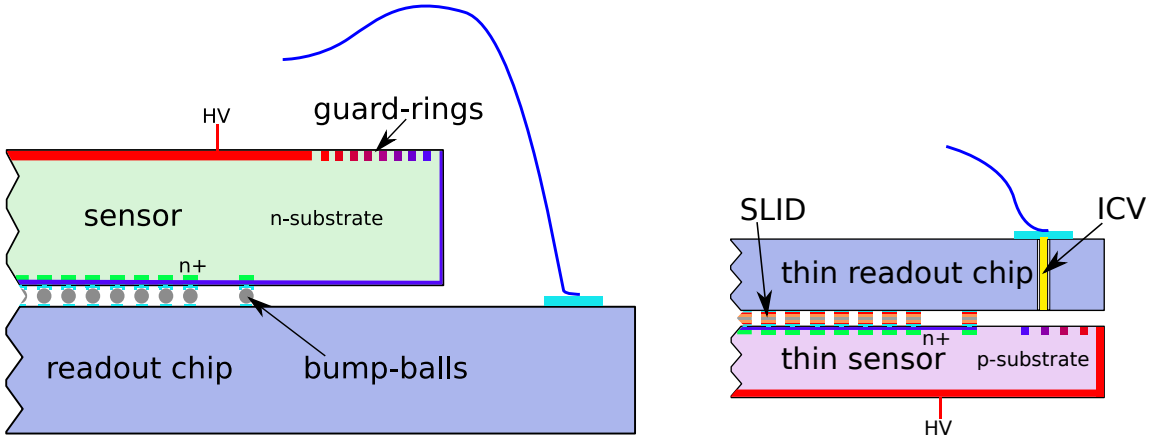

Figure 1.8: A schematic view of the present ATLAS pixel module concept (a) in comparison to the proposed MPP concept (b).

bonds on the cantilever, running along the long side of the modules, transmitted to the uppermost module layer (side-view in Fig. 1.7). The top layer flexible printed circuit board (flex) is glued to the sensor and contains next to several surface mounted devices (SMDs) also the Module Control Chip (MCC), which collects the data from the 16 FE-I3 chips. Over the so called pigtail the data from the MCC is transmitted to the off-detector data acquisition system.

A schematic side view of the long edge of the present ATLAS pixel module is shown in Fig. 1.8(a). Compared to this, the MPP pixel module proposed [52] for the ATLAS pixel detector sLHC is shown in Fig. 1.8(b). It contains several new technologies and optimizations for a higher compactness and increased radiation hardness to meet the requirements for operation at the sLHC:

- **Thin sensors:** Particle irradiation induces crystal defects in silicon sensors that lead to a reduction of the signal and an increase of the noise contribution. Sensors with a thickness of less than the standard 250 μm are expected to be less affected by the signal reduction processes and therefore more radiation hard. In addition, since the radiation length of the sensors is proportional to their thickness, thin sensors reduce multiple scattering. To explore these advantages of thin sensors, a novel thinning technology, developed at the semiconductor laboratory HLL [53] of the MPG, is used to produce sensors with a thickness, which can be optimized for a maximum signal to noise ratio at the expected fluences. The preparations preceding the production and the results of the first thin pixel sensor production are presented in Chapter 3.

- **N-in-p sensor design:** The use of an n-in-p sensor design is foreseen (Fig. 1.8(b)). This allows for less processing steps during the sensor production compared to the present ATLAS n-in-n design since the sensors only need a structured processing on one side. This should lead to a cost reduction, since the processing cost dominates the total sensor cost. Furthermore, in contrast to the equally complex p-in-n design, electrons instead of holes are the main charge carriers collected by the readout electronics. This leads to higher signals, especially after irradiation with high integrated fluences.

- **Reduced guard-rings:** The live-fraction of the pixel sensors can be optimized by the reduction of the inactive sensor edges. For the IBL upgrade the inactive edge, comprising the guard-ring structure and a safety margin towards the cutting edge of the sensors, has to be smaller than $(450 - 500)\,\mu$m. To estimate the feasibility of fulfilling this requirement, pad sensors with various guard-ring structures of reduced size were produced and tested. The results are presented in Sec. 3.4.2.

- **3D-integration:** To further increase the live-fraction of the ATLAS pixel module [54] from the present 71% to more than 90%, a new 3D-integration technology is planned to be used. It replaces the current bump-bonding interconnection with the Solid Liquid InterDiffusion (SLID) process and introduces vertical InterChip Vias (ICVs) in thinned readout chips. With this ICV-SLID technology, the cantilever needed for wire-bonding (Fig. 1.8(a)) can be avoided since the digitized signals are routed vertically through the readout chips (Fig. 1.8(b)). In addition, the ICV-SLID technology allows for stacking of several sensor and electronics layers which can be explored for future, even more integrated pixel modules. Since less processing steps are needed for the SLID processing in comparison to the bump-bonding interconnection, a cost reduction might be achieved, once the SLID technology enters the industrial main stream market. Chapter 4, gives a more detailed introduction to the ICV-SLID processing and presents the first results on SLID connections for diodes and structures that resemble the ATLAS pixel sensor geometry.

- **Low threshold readout electronics:** As mentioned above, the introduction of crystal defects in silicon sensors leads to a reduction of the signal. To be able to detect the signals from highly irradiated sensors the readout electronics has to be optimized to reach lower thresholds. This can be done by calibration algorithms changing the operation parameters of the readout chip. An introduction to the ATLAS FE-I3 readout chip and the results of a threshold optimization are shown in Chap. 5.

Chapter 2

Pixel sensors and radiation damage

Since the invention of pixel sensors [55], CMOS sensors [56], and CCDs [57], patterned semiconductor sensors have been used in many applications in science and industry. For particle detectors in high energy physics semiconductor pixel sensors with a high granularity are mostly used as tracking detectors reconstructing the trajectories of charged particles passing through the sensors.

The signal generation in semiconductor sensors is based on free charge carriers drifting in an electric field. As opposed to gaseous ionization chambers the active volume in which the charges are generated is a semiconductor whose surfaces are structured by photo lithographic processes. This allows for much smaller readout cells and hence a better resolution reaching for example less than $15\,\mu$m in the $\mathrm{R}-\phi-$direction of the present ATLAS pixel detector [39]. Details about the working principles of semiconductor sensors are introduced in Sec. 2.1 with an emphasis on n-in-p sensors, being the main sensor type investigated in this work.

At high luminosity hadron colliders, especially at the LHC and its proposed luminosity upgrades to the sLHC, semiconductor sensors are exposed to intense high energy particle fluences. Next to the high signal rates which demand enormous data transport and processing capabilities the vast amount of secondary particles also introduces defects in the semiconductor crystals leading to a deterioration of the sensor performance. The different defects and their implications are presented in Sec. 2.2.

The need for radiation hard high granularity tracking detectors has triggered intensive research towards new sensor concepts. Within this thesis a novel detector module concept containing thinned pixel sensors for increased radiation tolerance is investigated. The beneficial properties of thin sensors and alternative approaches are introduced in Sec. 2.3.

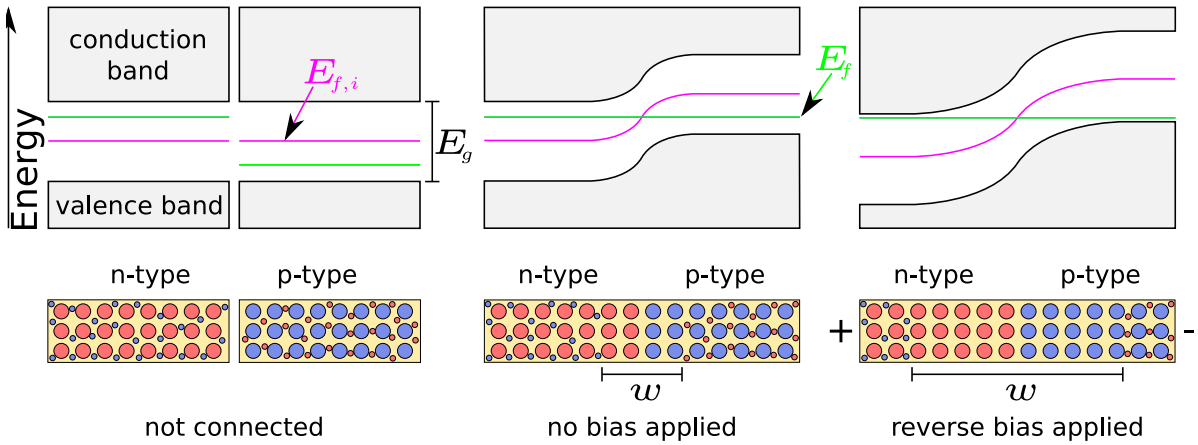

Figure 2.1: Working principle of the pn-junction. The upper images show the energy band structure in the n- and p-type silicon. The lower images visualize the acceptors, donors, electrons, and holes (large blue, large red, small blue, and small red circles, respectively) in the doped silicon materials. The width of the depletion zone is denoted by w.

2.1 Working principles of silicon pixel sensors

While for single atoms electrons are confined to discrete energy levels, in condensed matter the electron wave functions of many atoms overlap, leading to continuous but possibly separated energy bands of phase-space states. The uppermost completely filled band is referred to as valence band while the lowest partially or not occupied band is called conduction band (see left side of Fig. 2.1). The probability f_e that a phase-space state of energy E is occupied by an electron can be described by the Fermi-Dirac statistics [58]:

$$f_\mathrm{e}(E) = \frac{1}{e^{(E-E_\mathrm{f})/kT}+1}. \tag{2.1}$$

Here k is the Boltzmann constant and E_f is the Fermi energy at which

$$f_\mathrm{e}(E_\mathrm{f}) = \frac{1}{2}. \tag{2.2}$$

The temperature T determines the width in energy of the transition region between $f_\mathrm{e}(E) \approx 0$ and $f_\mathrm{e}(E) \approx 1$. Depending on the band gap E_g between the valence and conduction band and the position of E_f, condensed matter can be classified into insulators, conductors, and semiconductors. The latter are defined as having a band gap of $0\,\mathrm{eV} < E_\mathrm{g} \lesssim 3\,\mathrm{eV}$ which contains E_f. Hence, at $T \to 0\,\mathrm{K}$ all phase-space states in the valence band are occupied, whereas the conduction band is empty. Since no electron

in the valence band can change to a state with a different momentum, a current is not possible.

The energy supplied by ionizing particles can lift electrons from the valence band into the conduction band, where they can move through the crystal. In a semiconductor sensor, these free charge carriers are propagated towards attached readout electronics in an electric field, created by applying different potentials at opposing sensor surfaces. This induces a time dependent current $I_{\mathrm{e}}(t)$ in the electronics that forms part of the measured signal. At the same time the empty phase-space state in the valence band can be occupied by a neighboring valence electron. Hence, the empty space, usually interpreted as a positively charged particle called hole, is - compared to the electrons - propagating in the opposite direction and generates an additional hole current $I_{\mathrm{h}}(t)$[1].

Silicon is the most prominent example of all semiconductor detector materials and it is used for the sensors relevant for the presented work. On average for each 3.6 eV energy lost or 12.5 nm travelled in silicon a minimum ionizing particle (MIP) lifts an electron from the valence band into the conduction band, i.e. creates an electron-hole pair. This leads to an average collectable charge corresponding to 8000 electrons (8 ke) per 100 μm of sensor thickness.

However, intrinsic silicon is not suitable as a sensor material, since at usual working temperatures many electrons occupy phase-space states in the conduction band and would cause a large current in the electric field. This leakage current would be far larger than the current induced by the electron-hole pairs created by penetrating MIPs. To reduce the leakage current and to create a sensor volume with very few free charge carriers, the rectifying properties of a junction between two extrinsic silicon materials is exploited.

2.1.1 The pn-junction

To create sensors with very low leakage currents and a low free carrier concentration, a combination of n-type and p-type silicon is used (Fig. 2.1). In the lattice of these materials, silicon atoms are replaced with dopant atoms having different electron configurations. For n-type silicon atoms with 5 valence electrons (e.g. phosphorus) are used to introduce almost free electrons while for p-type silicon atoms with 3 valence electrons (e.g. boron) are implanted to enrich the material with loosely bound holes. These additional electrons and holes become the majority charge carriers of the respective extrinsic silicon material. In both cases the Fermi energy E_{f} is changed from the intrinsic value $E_{\mathrm{f,i}}$ and moves closer towards the valence band or the conduction band for n- and p-type silicon, respectively. Joining these two silicon types the majority charge carriers recombine at the pn-junction between them until the Fermi energy is

[1] The Hall effect in semiconductors shows, that the concept of positively charged holes is more than a simple trick to ease the mathematical description of semiconductors. It rather is a consequence of the quantum mechanical properties of electrons in a crystal lattice (e.g. [59])

equal throughout the crystal (middle section of Fig. 2.1). Remaining in this so called depletion zone are the immobile positively charged donor atoms in the n-type and the negatively charged acceptor atoms in the p-type silicon also called the space charges. The width w of the depletion zone can be increased by an externally applied reverse bias voltage $U = U_{\mathrm{p-type}} - U_{\mathrm{n-type}} < 0$ over the pn-junction (right side of Fig. 2.1):

$$w(U) = \sqrt{\frac{2\epsilon_{\mathrm{Si}}\epsilon_0 \left(N_{\mathrm{A}} + N_{\mathrm{D}}\right)}{qN_{\mathrm{A}}N_{\mathrm{D}}} \left(U_{\mathrm{bi}} - U\right)}. \tag{2.3}$$

Here q is the elementary charge, N_{A} and N_{D} are the concentrations of acceptor atoms in the p-type and donor atoms in the n-type silicon and $\epsilon_{\mathrm{Si}}, \epsilon_0$ are the permittivities for silicon and the vacuum. The built-in voltage U_{bi} is generated by the ionized donor and acceptor atoms and determines the width of the depletion zone when no external voltage is applied. Ideally within the depletion zone no free charge carriers are present and hence, a current only flows when additional electron-hole pairs are created by ionization. However, small leakage currents can be measured also under reverse bias, since the thermal generation rate of carriers at finite temperatures is not zero, and charge carriers diffuse from the un-depleted volume into the depletion zone.

The voltage U_{fd} needed to deplete the full detector thickness $d = w(U_{\mathrm{fd}})$ is naturally referred to as full depletion voltage. To collect the full charge generated by ionizing particles in the sensor volume, it is needed to apply a bias voltage of $U \geq U_{\mathrm{fd}}$. Depending on the silicon material properties, for example after heavy irradiation (see Sec. 2.2), U_{fd} can reach several kilo-volts for a typical 250 μm thick sensor, since the effective doping concentration strongly increases. Such high voltages can exceed the maximum operating voltage of the sensors above which the pn-junction will show a junction break-down. A junction break-down is characterized by a strong increase of the leakage current by several orders of magnitude rendering the pn-junction unusable for particle detection. Three effects are responsible for break-downs:

- **Thermal instability**: As the power dissipation increases for higher voltages the device heats up. This leads to an increased thermal generation rate of free charge carriers and hence a higher leakage current. Larger currents again cause a higher power dissipation resulting in a positive feedback situation and quickly evolving towards very high currents.

- **Tunneling**: As higher bias voltages are applied the band structure (Fig. 2.1) is more and more deformed until the valence band energy of the p-type silicon is far above the lowest energy of the conduction band of the n-type silicon. The potential barrier of forbidden states between them decreases and consequently the chance for band-to-band tunneling strongly increases.

- **Avalanche multiplication**: If the electric field at the pn-junction reaches very high values, the free charge carriers are strongly accelerated. Above a critical field

Parameter	$1.75 \cdot 10^5 \leq \mathcal{E}/(\mathrm{V/cm}) \leq 4.0 \cdot 10^5$	$4.0 \cdot 10^5 \leq \mathcal{E}/(\mathrm{V/cm}) \leq 6.0 \cdot 10^5$
$\alpha_{\infty_\mathrm{e}}$ $[10^6\,1/\mathrm{cm}]$	0.703	0.703
b_e $[10^6\,\mathrm{V/cm}]$	1.231	1.231
$\alpha_{\infty_\mathrm{h}}$ $[10^6\,1/\mathrm{cm}]$	1.582	0.671
b_h $[10^6\,\mathrm{V/cm}]$	2.036	1.693

Table 2.1: Parameters for the multiplication rate in high electric fields as listed in [61].

strength the energy gained by a charge carrier between two scattering interactions is enough to create more charge carriers by ionization. The latter generate further electron-hole pairs and so on, leading to an avalanche of charge carriers.

The avalanche process is the most important breakdown mechanism, imposing an upper limit on the reverse bias for most sensors. However, this mechanism can also be used in a controlled way to amplify the signal within the sensor itself. This approach is followed with the so called avalanche photo-diodes and silicon photo-multipliers (see for example [60]).

A parameterization of the multiplication rate $\alpha(\mathcal{E})$, i.e. the number of newly created electron-hole pairs per drift length is formulated in [61] and depends on the electric field $\mathcal{E}$:

$$\alpha_{\mathrm{e,h}}(\mathcal{E}) = \alpha_{\infty_{\mathrm{e,h}}} e^{-b_{\mathrm{e,h}}/|\mathcal{E}|}. \tag{2.4}$$

The corresponding parameters for electrons (e) and holes (h) can be found in Tab.2.1.

2.1.2 N-in-p pixel sensors

Silicon pixel sensors are usually based on a structured grid of shallow p(n)-type implants in an n(p)-type doped silicon bulk to form *p-in-n*(*n-in-p*) sensors with many individual pn-junctions. For the present ATLAS pixel sensors a third option, the n-in-n design, is chosen which uses an additional p-type back side implantation to form the pn-junction. The doping concentrations of the pixel implants are usually a factor of $10^7 - 10^8$ higher than the bulk doping resulting in strongly asymmetric pn-junctions, i.e. a depletion zone developing from the shallow implants into the bulk. Typical pitches of the pixel cells are between $(50 - 500)\,\mu$m and, depending on the instrumented volume, up to several million channels are used for modern pixel detectors in high energy physics experiments. In the ATLAS pixel detector 1744 sensors with over $80 \cdot 10^6$ pixel cells of $50 \times 400\,\mu\mathrm{m}^2$ result in an active area of about $1.7\,\mathrm{m}^2$ [62]. The typical thickness of pixel sensors is between $250\,\mu$m and $300\,\mu$m.

Figure 2.2 depicts the schematics of an n-in-p sensor which is the most promising sensor design for radiation tolerant large area pixel sensors [54] and the main sensor type investigated within the presented work. N-type pixel implants collect electrons which

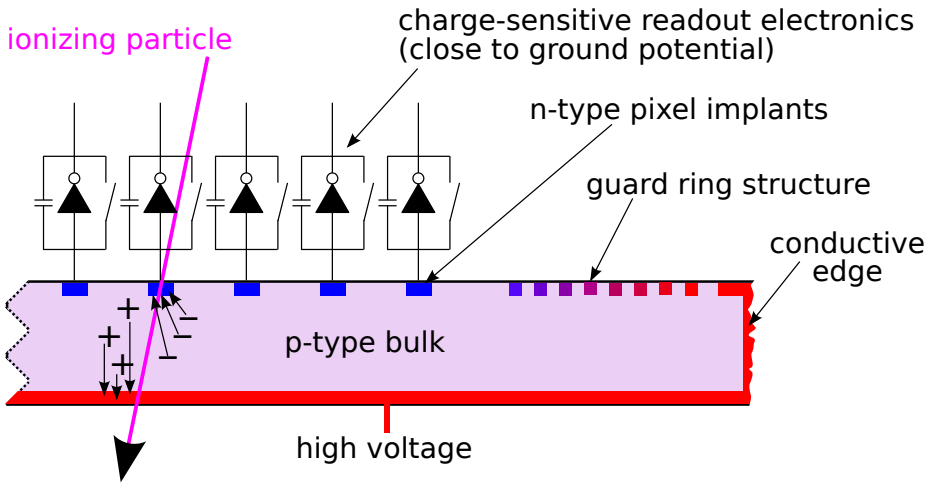

Figure 2.2: Schematics of an n-in-p pixel sensor with attached readout electronics.

have a higher mobility than holes and are less affected by radiation induced charge trapping (cf. Sec. 2.2.2). Hence, the signal size after irradiation is larger in sensors with n-type pixel implants compared to those with p-type pixels. With respect to n-in-n sensors the n-in-p design has the advantage that only single sided structured processing is needed during the production. The back-side has a homogeneous p-type implantation, demanding less handling and processing steps, i.e. lower production costs.

The individual n-type pixel implants are connected to the readout electronics which are usually kept at ground potential. To the back-side of the sensor a reverse bias voltage is applied to increase the depletion zone developing from the pixel implants. Since the cutting edge (right side of Fig. 2.2) is usually conductive the back side potential is forwarded to the front side. To avoid a short with the pixel implants an additional guard-ring implant structure has to be implemented enclosing the active area to allow for a smooth decrease of the potential to ground. Since the volume below the guard-rings is not part of the active sensor volume, their extension should be minimized.

Inter-pixel isolation

To reduce crosstalk, i.e. charges moving from one n-type implant to its neighbors and possibly yielding a false signal, p-type implants are introduced between the pixel implants to create an electrically insulating double n-p-n junction. Choosing the isolation geometry and the implant parameters involves a compromise between a strong isolation and a low electric field strength. The higher the isolation implant doping concentration, the stronger is the isolation. However, this leads to pn-junctions with many space charges generating high electric field peaks which may cause junction break-downs if the

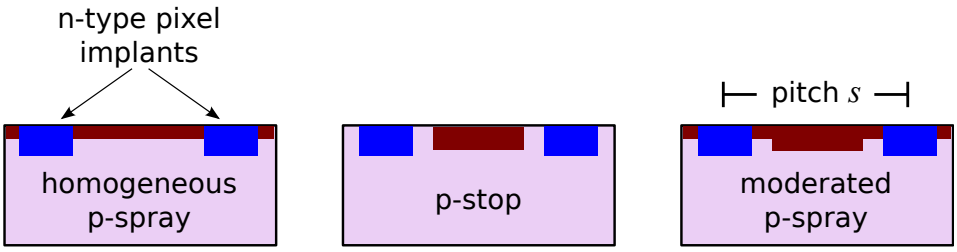

Figure 2.3: Three common forms of inter-pixel isolations for n-in-p sensors. The homogeneous p-spray (red) is implanted over the whole sensor including the n-type pixel implants (blue). For the p-stop and moderated p-spray additional masks have to be used to structure the p-type implant. The distance between the pixel implant centers is referred to as pitch s.

electric field reaches about 300 kV/cm [63].

Figure 2.3 shows the three common geometry options for the p-type isolation implant. The homogeneous p-spray option uses a unstructured implant with a relatively low concentration over the whole sensor area. This has the advantage of the smallest processing needs during the sensor production, but leads to a direct contact between the n-type pixel and the p-spray implant. Choosing a too high doping concentration, the electric field at this pn-junction can lead to break-downs during normal sensor operation. A p-stop isolation needs extra processing, as an additional mask for implant structuring has to be used. Furthermore, very good process alignment is needed to ensure that the p-implant, having a higher doping concentration as the homogeneous p-spray, resides in the center between the pixel implants without a direct contact to them. Here the largest differences in the doping concentration, i.e. the highest electric field is found between the p-stop implant and the lower doping concentration of the p-type sensor. The moderated p-spray option has the same processing demands as the p-stop isolation, but combines advantages of the other two designs. In the center a higher implant concentration is used which is surrounded by a lower moderated one. To achieve an equivalent isolation to either of the other options, the implant concentration in the center can be chosen lower than the one in the p-stop isolation, and the implant concentration of the moderated part can be chosen lower than in the homogeneous p-spray implant [63]. This leads to lower electric fields at the boundary between different implant concentrations. However, the implant parameters have to be carefully chosen since changes of the sensor properties caused by a high irradiation fluence can deteriorate the isolation properties.

Signal and noise in pixel detectors

As described before electrons and holes generated by ionizing particles passing through the depleted volume are separated by the electric field within the sensor and induce a

Parameter	parameterization	at $T = 294\,\mathrm{K}$
μ_e $[\mathrm{cm}^2/\mathrm{Vs}]$	$1.51 \cdot 10^9 \cdot (T/[\mathrm{K}])^{-2.42}$	1605.4
μ_h $[\mathrm{cm}^2/\mathrm{Vs}]$	$1.31 \cdot 10^8 \cdot (T/[\mathrm{K}])^{-2.2}$	486.3
$v_{\mathrm{sat_e}}$ $[\mathrm{cm/s}]$	$1.53 \cdot 10^9 \cdot (T/[\mathrm{K}])^{-0.87}$	$1.09 \cdot 10^7$
$v_{\mathrm{sat_h}}$ $[\mathrm{cm/s}]$	$1.62 \cdot 10^8 \cdot (T/[\mathrm{K}])^{-0.52}$	$0.84 \cdot 10^7$
β_e	$2.57 \cdot 10^{-2} \cdot (T/[\mathrm{K}])^{0.66}$	1.09
β_h	$0.46 \cdot (T/[\mathrm{K}])^{0.17}$	1.21

Table 2.2: Parameters for the drift velocity relation in silicon.

signal current in one or more nearby readout channels. Depending on the signal sizes in the individual readout channels the position of the particle penetration is reconstructed. The signal current $I_{j_\mathrm{e,h}}(t)$ induced in a pixel channel j from a number $N_\mathrm{e,h}$ of charge carriers generated in the sensor at a single position $x_\mathrm{e,h}(0)$ is described by Ramo's theorem [64]:

$$I_{j_\mathrm{e,h}}(t) = \pm q N_\mathrm{e,h}(t) v_{\mathrm{dr_{e,h}}}(x_\mathrm{e,h}(t)) \mathcal{E}_{\mathrm{w},j}(x_\mathrm{e,h}(t)). \tag{2.5}$$

Here, $\mathcal{E}_{\mathrm{w},j}(x_\mathrm{e,h}(t))$ is the weighting field for the j-th pixel channel, and $v_{\mathrm{dr_{e,h}}}$ is the drift velocity of the charge carriers. The weighting field solely depends on the sensor and implant geometry and is calculated by applying a unit potential to channel j while leaving all others at 0 V. The drift velocities depend on the electric field $\mathcal{E}$, the mobilities $\mu_\mathrm{e,h}$ of electrons and holes and their trajectories $x_\mathrm{e,h}(t)$:

$$\begin{aligned} v_{\mathrm{dr_e}}(x_\mathrm{e}(t)) &= -\mu_\mathrm{e} \mathcal{E}(x_\mathrm{e}(t)) \\ v_{\mathrm{dr_h}}(x_\mathrm{h}(t)) &= \mu_\mathrm{h} \mathcal{E}(x_\mathrm{h}(t)). \end{aligned} \tag{2.6}$$

This linear relation is valid for fields small enough that the velocity change due to acceleration by the electric field is small with respect to the thermal velocity. For higher electric fields a saturation of the drift velocities is measured. A common interpolation between the linear relation and the saturation velocity is given in [65] and reads:

$$v_{\mathrm{dr_{e,h}}}(x_\mathrm{e,h}(t)) = \frac{\mu_\mathrm{e,h} \mathcal{E}(x_\mathrm{e}(t))}{\left(1 + \left(\frac{\mu_\mathrm{e,h} \mathcal{E}(x_\mathrm{e}(t))}{v_{\mathrm{sat_{e,h}}}}\right)^\beta\right)^{\frac{1}{\beta}}} \tag{2.7}$$

The parameters to be used in Eq. 2.7 are given in Tab. 2.2

There are several sources for noise for readout electronics, based on charge-sensitive amplifiers with a field effect transistor (FET) as first input stage. The total quadratic equivalent noise charge (ENC^2) is the quadratic sum of the ENCs of the shot noise, the thermal noise (Johnson noise), the white noise, the flicker noise ($1/f$-noise), and the

transistor channel thermal noise [66]:

$$\mathrm{ENC}^2 = \frac{e^2\tau_{\mathrm{shape}}I}{4q} + \frac{e^2kTC^2}{3g_mq^2\tau_{\mathrm{shape}}} + \frac{e^2\tau_{\mathrm{shape}}kT}{2q^2R_{\mathrm{p}}} + \frac{e^2kTR_{\mathrm{s}}C^2}{q^2\tau_{\mathrm{shape}}} + \frac{e^2K_{\mathrm{f}}C^2}{2C_{\mathrm{ox}}WLq^2}, \tag{2.8}$$

with

$$\begin{aligned} e &: \text{Euler constant} \\ g_m &: \text{forward transductance of the FET} \\ \tau_{\mathrm{shape}} &: \text{shaping time of the FET} \\ R_{\mathrm{p}} &: \text{parallel resistance of the sensor} \\ R_{\mathrm{s}} &: \text{serial resistance of the sensor} \\ C &: \text{total input capacitance} \\ I &: \text{leakage current} \\ K_{\mathrm{f}} &: \text{flicker noise coefficient} \\ C_{\mathrm{ox}} &: \text{oxide capacitance per unit area} \\ W &: \text{FET channel width} \\ L &: \text{FET channel length} \end{aligned} \tag{2.9}$$

For the charge sensitive amplifier used in the Beetle chip for the Alibava system (Sec. 3.5.3) the two main contributions from serial noise (last three terms of Eq. 2.8) and shot noise can be parameterized with

$$\mathrm{ENC}_{serial} = a + b \cdot C \tag{2.10}$$

and

$$\mathrm{ENC}_{shot} = \sqrt{B \cdot I} \tag{2.11}$$

with $a = 497\,\mathrm{e}$, $b = 48.3\,\mathrm{e/pF}$ [67], and $B = 169\,\mathrm{e}^2\mathrm{/nA}$ [68].

2.2 Crystal defects from irradiation and their implications

Next to the ionizing energy loss caused by interactions with the valence electrons, particles penetrating the sensors are also subject to non ionizing energy loss through scattering off the lattice atoms. Both effects are taking place not only in the silicon bulk but also in the SiO_2, used to electrically passivate the sensor surface. Surface and bulk defects have to be considered separately since the impact of the defects on the device performance, as well as the time scales of the defect formation, are very different.

2.2.1 Surface defects

To electrically passivate the surface of silicon sensors a layer of several 100 nm of SiO_2 is grown onto the silicon wafers in a high temperature oxygen atmosphere. Through this layer two kinds of crystal defects are introduced in the sensor surface region:

- **Defects within the volume of the SiO_2 layer:** Due to the growing process, the crystal lattice of the SiO_2 has many imperfections, which are mostly positively charged. The most important defects are tri-valent silicon (positively charged), non-bridging oxygen (negatively charged), and interstitial oxygen (positively charged). As the defects worsen the quality of the SiO_2 layer, annealing techniques are used to passivate the defects during the sensor production. This is done by the diffusion of H^+ and OH^- ions into the oxide to pair-up with and neutralize the defect charges [69].

- **Defects at the interface between the silicon and the SiO_2:** As the lattices of silicon and SiO_2 are not identical there are unpaired, positively charged dangling bonds at the interface plane forming the interface defects. Also for these defects a controlled annealing with H^+ ions diffused into the silicon is used to passivate the dangling bonds by forming neutral $Si - H$ bonds [70].

Radiation penetrating the sensors, reactivates the passivated defects in the SiO_2 volume and the interface plane. The positive charge in the SiO_2 volume is built up mainly due to the reaction of radiation and the tri-valent silicon as well as the interstitial oxygen [71]:

$$\equiv \mathrm{Si} \cdot + \mathrm{rad} \longrightarrow \equiv \mathrm{Si}^+ + \mathrm{e}^- \tag{2.12}$$

$$\mathrm{O_i} + \mathrm{rad}(+) \longrightarrow \mathrm{O_i^+} \tag{2.13}$$

But also hydrogen ions from the annealing processes can be released from the SiO_2 layer [72] via

$$\mathrm{SiOH} + \mathrm{exciton} \rightarrow \mathrm{SiO}^- + \mathrm{H}^+. \tag{2.14}$$

Experiments and calculations have shown that the H^+ ions propagate through the SiO_2 as described by dispersive transport models [73]. Hence, in an electric field, as it is present under reverse bias, they drift towards the interface plane, where they can react with the passivated dangling bonds to depassivate them again (see Fig. 2.4 and [74]). After the reaction of

$$\mathrm{SiOH} + \mathrm{H}^+ \rightarrow \mathrm{SiO}^+ + \mathrm{H_2}, \tag{2.15}$$

a positively charged dangling bond is remaining at the interface, while the neutral hydrogen molecule can leave the crystal.

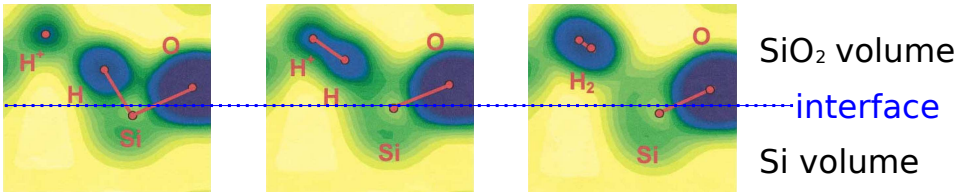

Figure 2.4: Simulated depassivation of a passivated interface bond [74]. The hydrogen ion arrives at the passivated SiOH interface complex and forms a hydrogen molecule. Remaining is the positively charged interface defect, i.e. dangling bond.

Implications of surface defects

Both kinds of surface defects after irradiation lead to a positive charge density of the sensor surface which attracts electrons from the silicon bulk. This leads to a partial compensation of the p-type doping between the pixel implants and consequently to a reduction of the isolation capability. For a homogeneous p-spray implant the lower doping concentration results in a decreased electric field, while for a p-stop isolation the electric field is increased due to the overcompensation of the acceptors in the p-type bulk [63]. In the moderated p-spray option, during irradiation the location of the highest field region can move from the transition between pixel- and moderated p-implants towards the transition between moderated and not moderated p-implant during irradiation (see Sec. 3.2.3).

Since both, the defects in the SiO_2 layer as well as those in the interface plane, are only reactivated, their amount is limited to the initial number of defects generated during the sensor production. As a consequence, a saturation of the number of surface defects is expected. This has been measured to happen after an integrated fluence of around $10^{14}\,n_{eq}/cm^2$. Hence, already for the LHC, 90% of the b-layer operation will be done with a saturated surface charge which increases from an initial value of $(1-5)\cdot 10^{11}\,/cm^2$ to a saturated charge density of $(2-3)\cdot 10^{12}\,/cm^2$ [63, 69].

2.2.2 Bulk defects

Strong head on collisions of high energetic particles with silicon atoms can lead to atom displacements if the energy transferred is larger than about 25 eV [75]. These primary knock-on atoms (PKA) can either come to rest at a close-by interstitial position to form a Frenkel pair together with the vacant lattice site, or trigger further displacements, i.e. point-like crystal defects, along their trajectory if their energy is sufficient. As the scattering cross section increases with decreasing particle energy, an increased scattering rate and energy loss can develop at the end of the trajectories leading to a dense volume of defects called terminal cluster or cluster defect (see Fig. 2.5 and [76]).

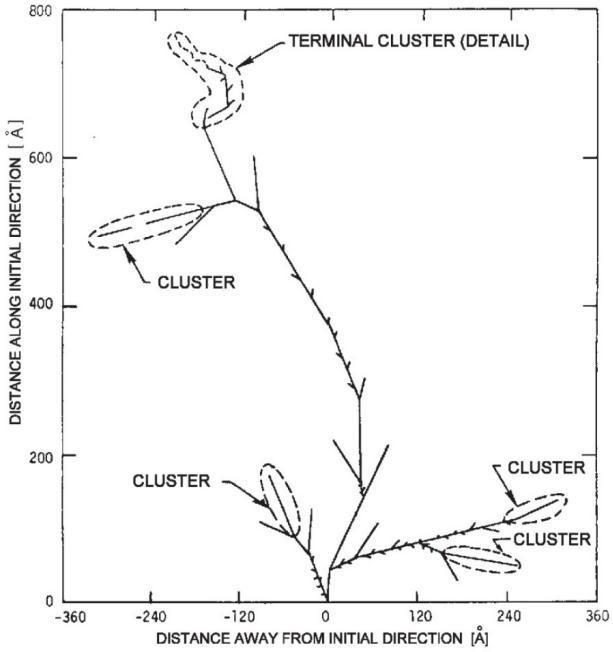

Figure 2.5: Monte Carlo simulation of the interaction of a PKA with an initial energy of 50 keV in silicon [75]. The PKA initially travels in the vertical direction upwards, starting from the origin. At the ends of the trajectories of the displaced atoms, clusters of defects are generated.

Next to the above mentioned displacement of the PKA also atoms other then silicon can be introduced at lattice positions or in-between those, forming point defects. These impurity defects are usually enclosed during the production or processing of the silicon material. Naturally, the deliberate n- and p-type doping atoms also constitute this kind of impurities. In general, three types of point defects can be differentiated: interstitials, substitutionals, and vacancies. Figure 2.6 shows a classification of different point defects in silicon sensors. Furthermore, combinations of these are classified as they reveal additional properties [77].

A model for cluster defects [78] was initially introduced to explain the very high hole recombination rate in n-type semiconductors after irradiation with fast neutrons, not seen after irradiation with fast electrons or slow neutrons. Spherical p-type clusters of $(15 - 20)$ nm radius with encircling pn-junctions were considered in n-type silicon, to act as wells or sinks for minority carriers. The model was able to explain at least qualitatively the strong difference in hole recombination rates, however, quantitative consistency with preceding experiments [79] could not be reached. Still until today, there have been only few experiments spreading light on the formation and structure of

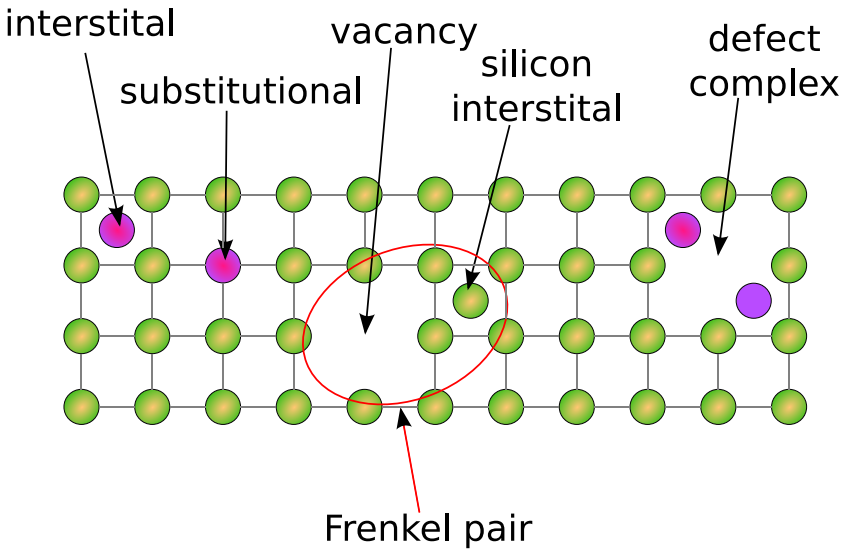

Figure 2.6: Schematic representation of some point defects in a square lattice. Silicon atoms are shown in green, other atoms in purple.

cluster defects. More detailed explanations, improved models, and simulations can be found in [80, 81, 82, 83].

Implications of bulk defects

In general, any defects in the silicon crystal disturbing the periodicity can lead to additional energy levels in the band gap region. These energy levels act as donors or acceptors, hence constitute an effective doping, and thereby change the properties of the semiconductor sensor. A detailed review of effects from bulk defects is e.g. given in [76] and partly summarized here:

- **Generation**: Especially defects close to the middle of the band gap lead to increased thermal generation rates as the band gap can be overcome by two smaller steps in energy. The closer the defects to the mid-gap position the higher is the generation rate. This leads to large leakage currents in the devices proportional to the received irradiation fluence.

- **Recombination**: Some lattice defects can capture charge carriers of both polarities at the same time, leading to an increased recombination of electrons and holes after irradiation. The free carrier lifetime and drift length are reduced and hence the signal size decreases. This effect depends on the density of these recombination center defects, their energy levels, and the capture cross-sections for both carrier types.

- **Trapping**: Especially shallow defect levels close to one of the bands can temporarily trap charges after an effective trapping time $\tau_{\mathrm{eff}_{\mathrm{e,h}}}$. After large irradiation doses $\tau_{\mathrm{eff}_{\mathrm{e,h}}}$ decreases and many charges are trapped within the readout time window of the readout electronics, which leads to a reduction of the signal size as $N_{\mathrm{e,h}}(t)$ in Eq. 2.5 exponentially decays:

$$N_{\mathrm{e,h}}(t) = N_{\mathrm{e,h}}(0) \cdot \exp\left(-\frac{t}{\tau_{\mathrm{eff}_{\mathrm{e,h}}}}\right). \tag{2.16}$$

  The effective trapping time is inversely proportional to the received equivalent fluence Φ_{eq}:

$$\frac{1}{\tau_{\mathrm{eff}_{\mathrm{e,h}}}} = \beta_{\mathrm{e,h}}\Phi_{\mathrm{eq}}, \tag{2.17}$$

  where

$$\begin{aligned} \beta_{\mathrm{e}} &= 5.7 \cdot 10^{-16}\,\mathrm{cm}^2/\mathrm{ns} \\ \beta_{\mathrm{h}} &= 7.7 \cdot 10^{-16}\,\mathrm{cm}^2/\mathrm{ns} \end{aligned}$$

  are determined by measurements [84]. After fluences as expected at the sLHC, charge trapping is the dominating effect for reduced charge collection efficiencies (CCEs).

- **Scattering**: Radiation induced defects can act as scattering centers which reduce the mobility of electrons and holes. Hence, for the same voltages applied, the drift velocity of the charge carriers is lower, reducing the induced signal current (cf. Eq. 2.6).

- **Change of effective doping concentration**: Most bulk defects in irradiated silicon exhibit acceptor like behavior and compensate the donors present in the sensors. Hence, the effective doping concentration $N_{\mathrm{eff}} = N_{\mathrm{D}} - N_{\mathrm{A}}$ decreases. The change of the effective doping concentration as a function of the equivalent fluence Φ_{eq} can be parameterized as an exponential reduction of donors and a linear introduction of acceptors [85]:

$$N_{\mathrm{eff}}(\Phi_{\mathrm{eq}}) = N_{\mathrm{D}} \cdot e^{-a\Phi_{\mathrm{eq}}} - N_{\mathrm{A}} - b\Phi_{\mathrm{eq}}, \tag{2.18}$$

  with

$$\begin{aligned} a &= (3.54 \pm 0.16) \cdot 10^{-13}\mathrm{cm}^2 \\ b &= (7.94 \pm 0.64) \cdot 10^{-2}/\mathrm{cm}^1. \end{aligned}$$

  For n-type silicon the radiation induced decrease of the effective doping concentration can lead to a full compensation of donors and a space charge sign inversion (SCSI) into a p-type bulk. For the present ATLAS n-in-n pixel sensors this

is expected to happen at around $(1-3)\cdot 10^{13}\,\mathrm{n_{eq}/cm^2}$ [86], i.e. already in the early operation phase. After the SCSI the depletion zone develops from the front n-implant like in an n-in-p sensor, while before, it develops from the back side p-implant.

The continuous increase of the acceptor concentration leads to an increase of the full depletion voltage U_{fd}. This can be derived using Eq. 2.3. e.g. for the case of a p-type bulk with highly doped n-type pixel implants ($N_{\mathrm{A}} \ll N_{\mathrm{D}}$), and setting $w(U_{\mathrm{fd}}) = d$

$$d = \sqrt{\frac{2\epsilon_{\mathrm{Si}}\epsilon_0}{qN_{\mathrm{A}}}\,(U_{\mathrm{bi}} - U_{\mathrm{fd}})}. \tag{2.19}$$

With the substitution of $N_{\mathrm{A}} \rightarrow |N_{\mathrm{eff}}(\Phi_{\mathrm{eq}})|$, neglecting U_{bi} since it is usually smaller than 1 V, and solving for U_{fd} the result is

$$U_{\mathrm{fd}} = \frac{q}{2\epsilon_{\mathrm{Si}}\epsilon_0}\,|N_{\mathrm{eff}}(\Phi_{\mathrm{eq}})|\,d^2. \tag{2.20}$$

It is expected that U_{fd} in the ATLAS pixel b-layer will reach 600 V after around 5 years of operation [39]. For the envisaged sLHC the U_{fd} for a 250 μm thick planar silicon sensor will reach several kV. Therefore, the sensors will have to be operated partly depleted, since the needed power supplies and cooling infrastructure are not in place. This leads to a decrease of the signal size.

- **Poole-Frenkel effect**: After high irradiation doses the effectiveness of thermal carrier creation is enhanced in high electric field regions [87]. This is known as the Poole-Frenkel effect and is a source for additional leakage current.

In summary, the presence of defects caused by radiation leads to higher leakage currents and a reduced charge collection efficiency (CCE). Higher leakage currents result in increased noise and thus the signal to noise ratio decreases significantly. Furthermore, the leakage currents lead to a larger power dissipation. This needs to be compensated, if possible, by more powerful cooling systems, that may introduce additional inactive material into the detector system.

2.2.3 The NIEL scaling hypothesis

The previous section qualitatively introduced the different displacement-defects created by non ionizing energy loss (NIEL) of penetrating particles. However, the amount of damage varies widely with the type of incident particles and their energy. Low energy protons for example mainly interact by coulomb interactions with the electrons and nuclei. Low energy neutrons only interact by elastic scattering with the lattice nuclei. For energies above several MeV for both, protons and neutrons, nuclear interactions begin to be the dominating effects for energy loss.

The NIEL scaling hypothesis correlates the amount of displacement-damage to the incident particle type and energy. This is done by assuming that the displacement-damage $D(E)$ scales linearly with the amount of energy imparted in displacing collisions [77].

$$D(E) = \frac{A}{n_\mathrm{A}} \frac{dE}{dx}(E)\bigg|_{\mathrm{non-ionizing}} \tag{2.21}$$

Here E is the energy of the incident particle, dE/dx is the specific energy loss, A is the gram atomic weight of the target material and n_A is the Avogadro constant. The damage function $D(E)$ can be calculated from the sum over all possible particle interactions ν with the lattice atoms

$$D(E) = \sum_\nu \sigma_\nu(E) \cdot \int_0^{E_\mathrm{R}^\mathrm{max}} f_\nu(E, E_\mathrm{R}) P(E_\mathrm{R}) dE_\mathrm{R}. \tag{2.22}$$

Each of the possible interactions ν has an associated cross-section $\sigma_\nu(E)$ and a probability $f_\nu(E, E_\mathrm{R})$ that a particle with initial energy E will generate a PKA with a recoil energy E_R. The relation between recoil energy and displacement-damage is given by the Lindhard partition function $P(E_\mathrm{R})$ [88, 89]. The maximum transferable energy $E_\mathrm{R}^\mathrm{max}$ depends on the impact particle mass m and energy, the mass of the silicon atom m_Si, and is given in the non-relativistic approximation by:

$$E_\mathrm{R}^\mathrm{max} = 4E \frac{m\, m_\mathrm{Si}}{(m + m_\mathrm{Si})^2}. \tag{2.23}$$

With the help of the damage function 2.22 the measured damage values can be very well understood on the basis of known interactions. Figure 2.7 shows the calculated damage functions for protons, neutrons, pions, and electrons over a wide range of energies. Details about the individual contributions to the calculations can be found in [91].

The NIEL scaling hypothesis is used to scale the radiation damage to the equivalent damage of 1 MeV neutrons to allow for comparisons of irradiations at the various irradiation facilities. The damage constant or hardness factor κ for a certain irradiation type and energy can be calculated as

$$\kappa = \frac{\int D(E)\phi(E)dE}{\int D(E_\mathrm{n} = 1\,\mathrm{MeV})\phi(E)dE} = \frac{\int D(E)\phi(E)dE}{D(E_\mathrm{n} = 1\,\mathrm{MeV}) \cdot \Phi} \tag{2.24}$$

leading to an equivalent fluence

$$\Phi_\mathrm{eq} := \frac{\int D(E)\phi(E)dE}{D(E_\mathrm{n} = 1\,\mathrm{MeV})} = \kappa\Phi \tag{2.25}$$

for the actual received energy spectrum $\phi(E)$.

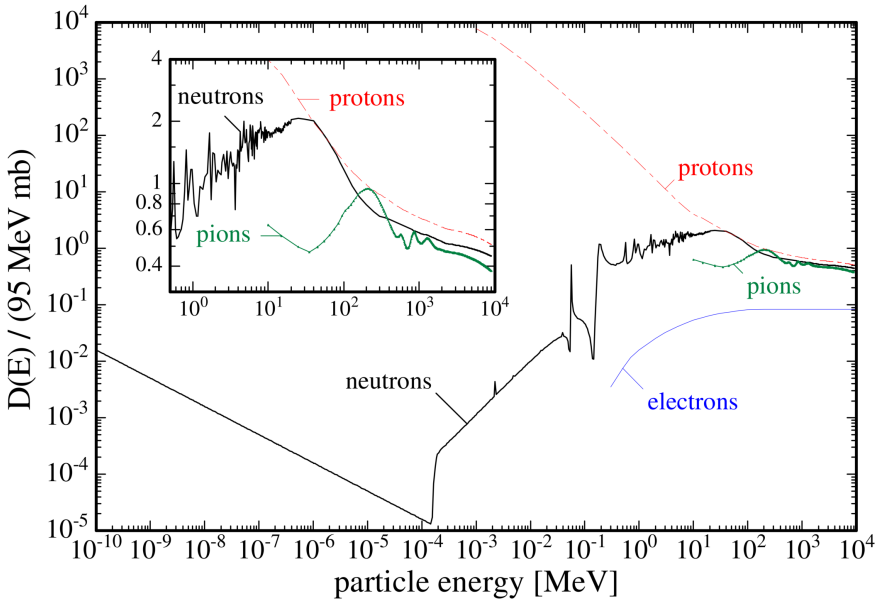

Figure 2.7: Summary of the displacement damage functions $D(E)$ for protons, neutrons, electrons, and pions [77]. The normalization of the ordinate to 95 MeV mb represents the damage equivalent to 1 MeV neutrons [90].

2.2.4 Defect annealing

Not all defects generated by NIEL are stationary and permanent. Some are mobile even at room temperature and interact with other defects in the silicon material. These interactions are in generally referred to as annealing and are often classified into beneficial and reverse annealing (Fig. 2.8) as they lead to a decrease or increase of the effective doping concentration. The annealing mechanisms can roughly be classified into three categories [93]:

- **Migration**: The mobility of some defects strongly depends on the temperature as they are loosely bound to certain lattice positions. Above a certain activation energy which can be supplied by thermal excitations, these defects become quasi free and start to migrate until they are trapped by deep potential sinks from other crystal defects or the temperature is decreased again.

- **Complex formation**: The migrating defects can form new complexes. These can either result in larger stable defects like the formation of a double vacancy or result in defect recombination e.g. of Frenkel pairs. In the latter case the lattice locally returns into its undisturbed state recovering from the crystal damage.

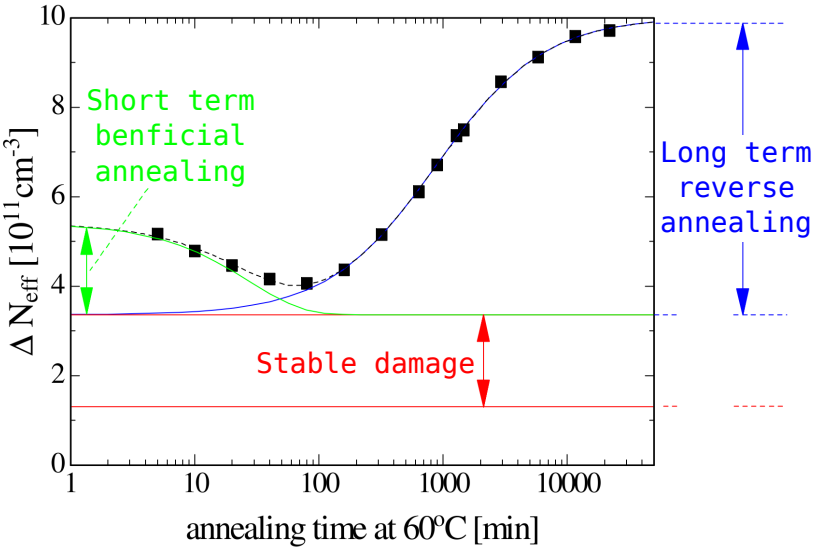

Figure 2.8: Measured change of the effective doping concentration as a function of the time during controlled annealing at 60 °C with fitted contributions of short term beneficial annealing, long term reverse annealing, and stable damage [92].

- **Dissociation**: A larger complex of defects can dissociate into smaller defects if the energy supplied is above a corresponding dissociation energy. After this, the complex defect acts as separated defects usually showing different properties.

In all cases of defect annealing a certain activation energy needs to be supplied usually via thermal excitations. Depending on the activation energy for each annealing process an annealing temperature can be defined as described in [77]. With knowledge of the annealing temperature and corresponding annealing times it is possible to perform a controlled beneficial annealing of some of the bulk defects. Because permanently damaging reverse annealing processes dominate after long exposure to high temperatures (Fig. 2.8) the annealing parameters have to be chosen carefully.

2.3 Approaches towards more radiation tolerant pixel sensors

Several attempts to increase the collected charge and decrease the noise of irradiated pixel sensors have been investigated in the past and are being carried out at present, especially in the framework of the CERN RD50 collaboration [94]. These include variations of the sensor material, new implant design options, and variations of the silicon production and processing.

Already successfully implemented in the present ATLAS pixel detector is the diffusion of oxygen into n-bulk silicon sensors. This deliberate introduction of defects has been shown to increase the sensor performance after charged irradiation, since it compensates some of the defects being produced during operation in high fluence environments [95]. Furthermore, silicon sensors produced in magnetic Czochralski or epitaxial processes rather than in the standard float-zone technique are investigated for their radiation hardness and defect development [96, 97].

Another pursuit followed by the CERN RD42 collaboration [98] is to investigate sensors made of diamond. The advantages of diamond sensors are the large band gap of $E_g = 5.48\,\text{eV}$ leading to a very low leakage current even after irradiations, and the lower permittivity which reduces the sensor capacitance. Both these properties lead to a reduction of the sensor noise (cf. Eq. 2.8). However, since the mean ionization energy is more than a factor of 3.5 higher than in silicon [99], the signals from penetrating charged particles are lower than for silicon sensors of equal thickness. Another disadvantage is that the procurement of single crystal diamonds is difficult and financially demanding. Hence, research is primarily focussed on cheaper polycrystalline diamonds produced by chemical vapor deposition (CVD) resulting in lower CCEs. A summary of recent results on diamond sensors can be found in [100].

A new silicon processing technology is investigated to produce the so-called 3D silicon sensors [101]. Instead of surface pixel implantations, columns are etched with deep reactive ion etching into the sensor and filled with doped silicon, grown from silane gas mixed with the appropriate doping atoms in the form of diborane or phosphine. The advantage of 3D sensors is the decoupling of the sensor thickness and the distance between the electrodes. This allows for thick sensors, i.e. the creation of many electron-hole pairs, while retaining short collection distances that lead to high CCEs. Furthermore, the three dimensional processing allows for doped sensor edges, increasing the live-fraction of the sensors. On the other hand a lot of non-standard processing is involved to fabricate 3D sensors, leading to high cost and lower device yield. Hence, in the foreseeable future only small area detectors can be realized. Also the thickness cannot be increased much, since multiple scattering would increase, deteriorating the spatial resolution. Minimizing the material budget is one of the key design goals for an upgraded ATLAS pixel detector. Further details and present progress on 3D sensors are reported in [102].

2.3.1 Thin planar sensors

Increasing the collected charge after irradiations with low material budget and standard implant processing could be realized with thin planar sensors [52] and is the main research activity presented within this thesis.

Standard sensors used in present silicon pixel detectors have thicknesses in the range $(250 - 300)\,\mu\text{m}^2$ since high resistivity wafers are industrially produced with these thick-

nesses. A technology for wafer thinning developed at the HLL of the MPG and described in the next section, gives access to thin sensors using the thickness as a free parameter. In thin sensors less charge carriers are generated by traversing ionizing particles leading to smaller signals in not irradiated sensors. However, after intense irradiation as expected at the sLHC the electric field configuration in thin sensors should allow for an enhanced signal and a better signal to noise ratio compared to thick sensors.

As introduced in Sec. 2.2.2, the full depletion voltage increases due to crystal defects so that thick sensors cannot be fully depleted after the fluence expected at the sLHC. For a given fluence and the highest achievable bias voltage, the maximum depth of the depletion zone can be estimated beforehand (cf. Eq. 2.20). With the above mentioned thinning technique, the sensor thickness can be optimized for these conditions, realizing an optimal compromise between signal size and material budget. Furthermore, producing even thinner sensors allows for operation in an over-depleted mode. This should be advantageous as soon as charge trapping dominates the reduction of the CCE. In this case not all charges can be collected even though the sensor is fully depleted. In the over-depleted operation mode, a higher electric field is present in the sensors, which can lead to several effects that are beneficial for the CCE.

- **Increased drift velocity**: The high electric field can lead to an increased drift velocity and therefore potentially higher signals (cf. Eq. 2.5). Even though the drift velocity saturates already at moderate values, especially the low field regions of a sensor will profit from this (see Sec. 3.5.2 and [103]).

- **Detrapping**: Trapped charges are released after a certain characteristic trapping time. A high electric field might lead to a reduction of the detrapping time as a consequence of the Poole-Frenkel effect. Measurements in GaAs detectors have shown a decrease of the detrapping time at bias voltages above the full depletion voltage [104].

- **Charge Multiplication**: Recently charge measurements of irradiated thin sensors have been published, exhibiting a CCE above 100% after integrated fluences expected at the sLHC [105]. This is interpreted as caused by charge multiplication effects close to the pn-junction, consistent with edge-TCT measurements from other groups [106].

The production and evaluation of the first thin pixel and strip sensors produced with the HLL technology is the subject of the following section.

Chapter 3

Production and evaluation of thin sensors

As motivated in the last section, compared to planar sensors of standard thicknesses thinned silicon sensors have a decreased material budget and are expected to show improved signal sizes after the intense integrated fluence received at a future sLHC collider. The development, production, and testing of thin sensors is one of the main research activities carried out and presented within this thesis.

The main technology to produce thin silicon sensors is the novel production process developed by the semiconductor laboratory HLL of the Max-Planck-Institute. It can be used to produce high-resistivity wafers with arbitrary thicknesses down to about $50\,\mu$m. With this technology the main prototype sensor production of twelve 6-inch float-zone (FZ) wafers with a thinned active volume was carried out. A second smaller production of sensors with a thin active volume was fabricated in the framework of the RD50 collaboration by standard epitaxial silicon growing. An introduction to the HLL process as well as an overview of the two thin sensor productions and the devices implemented is given in Sec. 3.1.

Ahead of the production of the thin sensors, a semiconductor simulation series was carried out to define suitable implant parameters for the p-spray isolation, ensuring safe sensor operation before and during irradiation. Section 3.2 gives an overview of the simulation programs and presents the parameters found to provide the most promising p-spray options for the actual sensor production. In addition to the simulation, inter-strip resistance measurements were carried out on a pre-production of n-in-p strip sensors before and after X-ray-irradiation. The X-ray-irradiation is used to saturate the surface defects which cause a deterioration of the inter-strip isolation as expected during the future detector operation. The results presented in Sec. 3.3 were used together with those from the simulation to define the final sets of implantation parameters for the p-spray isolation.

With these parameters the thin sensor production was finished and the produced

sensors were electrically characterized. Afterwards, some of the sensors were irradiated with 26 MeV protons up to $\Phi_{eq} = 10^{16}\,n_{eq}/cm^2$ and characterized again to investigate the effects induced by radiation damage. The results of the electrical characterizations of the FZ and the epitaxial sensors are presented and discussed in Sec. 3.4.

The Alibava [107] readout system is used to measure the signal and noise of strip sensors included in the main thin sensor production before and after irradiation. Signal charges are created in the sensors by ionizing electrons from a ^{90}Sr source, and scintillators are used to trigger the readout. The readout system and the performance of the thin sensors before and after irradiation are presented in Sec. 3.5.

3.1 Production of thin sensors

The typical thickness of sensor wafers cut from a silicon ingot ranges between 250 μm and 300 μm. Thinner sensors are usually not available as the wafer processing and handling would be very difficult due to the risk of breaking. For the work presented two technologies are used to produce sensors with a thin active volume on top of a low resistivity handling substrate, allowing for standard handling and processing. The first, used for the main thin sensor production, is the novel HLL technology applied to high resistivity sensor grade FZ wafers. The second, used for a smaller production of mainly strip sensors, is the industrially available epitaxial silicon growing technology. In the following, both technologies are introduced and the wafer content of the productions is shown.

3.1.1 The HLL thin sensor production process

Thinning of low resistivity wafers used for CMOS electronics is a commonly used technique in the micro-electronics industries. These devices however are not fully depleted and usually do not have an electrically active back-side implantation. Hence, thinning is usually performed as one of the latest processing steps after the front side implantations are finished. For sensors with active implants on both sides of the wafers this is not feasible because after thinning very fragile wafers would have to be handled and back-side implanted.

To allow thinning and processing of wafers with implants on both sides, a new technology [108] has been developed at the HLL. It uses two oxidized wafers of standard thickness, one low resistivity handle wafer and one high resistivity sensor wafer. In a first step the back-side implantation of the sensor wafer is performed as shown in Fig. 3.1 (1.). This step can be performed at the HLL or at an industrial company, because the wafers still have their initial thickness. The sensor wafer and the handle wafer are then bonded directly onto each other through oxide bonding (Fig. 3.1 (2.)). This is done at temperatures above 1000°C to form stable $Si-O-Si$ bonds [109]. The third step is the

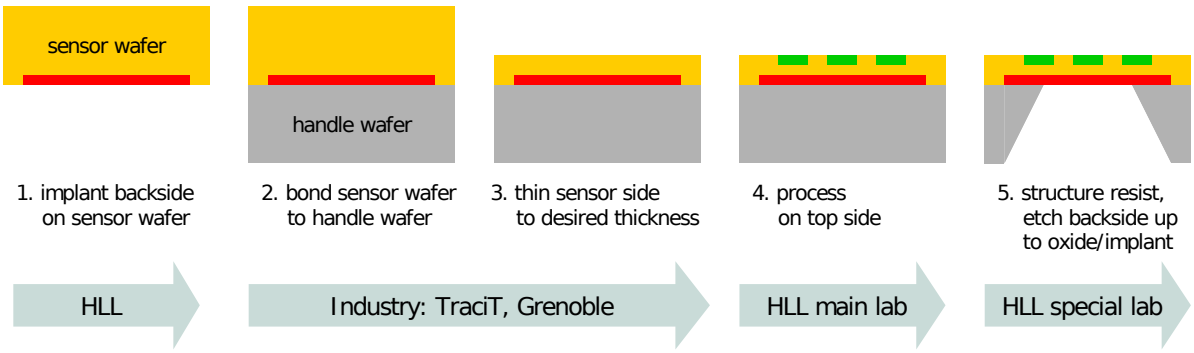

Figure 3.1: The thin sensor production process [53].

wafer thinning from the front-side of the sensor wafer to the desired thickness by standard chemical mechanical polishing (CMP). The wafer bonding and thinning is performed in industry [110]. The resulting stack of the thick handle wafer and the thinned sensor wafer can be processed just as a standard wafer in terms of stability and handling. The sensitive back-side implantations are well protected during the remaining processing. Furthermore, during the oxide bonding, oxygen is diffused into the silicon sensors. This is known to enhance the radiation hardness of silicon sensors as mentioned before. In a fourth step (Fig. 3.1 (4.)), the front-side implantations are performed, e.g. the pixel and strip implants. Figure 3.1 (5.) finally shows how the handle wafer is removed by deep anisotropic wet etching. For this tetramethyl ammonium hydroxide (TMAH) is used, which has a much higher etch rate in the (100) crystal direction than in the (111) direction, allowing for deep etching with well-defined boundaries. This is needed to only remove certain parts of the handle wafer and using the remaining frame as a mechanical support structure for the thin active sensors. During the etching process the buried oxide layer between the two wafers acts as a very efficient etch-stop, protecting the sensor wafer. For n-in-n sensors, to be able to contact the back-side implantation, openings in the oxide and metal structuring demand for two more lithographic masks and processing steps. As the n-in-p sensors have a homogeneous back-side implantation, which does not need to be contacted at a dedicated position, the contact to the back-side implant can also be applied through the low resistivity handle wafer.

With the novel sensor production technology described above, it is possible to produce thin and mechanically stable sensors. During the processing the handle wafer supplies the same stability as known from standard wafers. After the anisotropic etching the remaining frame structure still allows for careful handling and suppresses deformations of large area thin structures. Prototypes up to a size of $10 \times 1.2\,\mathrm{cm}^2$ and a thickness of $50\,\mu\mathrm{m}$ have been produced and showed good handling stability as seen in Fig. 3.2.

Figure 3.2: A large size mechanical dummy sensor, with the sensor wafer thinned to 50 μm with a stabilizing frame structure from the handle wafer.

3.1.2 Thin FZ sensor production overview

The main production of thin sensors was carried out on twelve 6-inch (15 cm diameter) FZ wafers procured by Soitec [111]. Eight wafers are based on a p-type silicon bulk (n-in-p) with a specified resistivity of $\rho \geq 2\,\mathrm{k\Omega cm}$, while the other four follow the present ATLAS pixel n-in-n approach with $\rho = 360\,\Omega\mathrm{cm}$. A high resistivity for the p-type wafers is favorable since it leads to lower depletion voltages before and during irradiation. The resistivity of the n-type wafers was chosen such that for testing purposes, the sensors before irradiation are fully depleted at moderate voltages of about 50 V. Apart from this, it is beneficial for n-in-n sensors if the initial resistivity is low, i.e. the donor concentration is high, since during the irradiation mainly acceptor like defects are created which compensate the donors in the silicon bulk. A high initial donor concentration prolongs the time until large amounts of acceptors dominate the effective doping, causing an increase of U_{fd}. The active sensor thicknesses after thinning were chosen to be 75 μm and 150 μm as given in Tab. 3.1.

From the eight n-in-p wafers produced, four were used for sensor testing including electrical characterizations of all structures and CCE measurements before and after irradiation of a subset of strip sensors. The remaining four wafers were dedicated for connecting the pixel sensors to pixel readout electronics, using the novel SLID interconnection technology to arrive at single chip demonstrator modules, explained in Chap. 4. The last column of Tab. 3.1 contains information about the p-spray isolation between the n-type implants. Two different isolation options called high and low were chosen

Name	bulk type	thickness [μm]	p-spray
1	p	75	high
2	p	75	high
D1	p	75	low
4	p	75	low
5	n	75	high
6	n	75	high
7	n	75	low
8	n	75	low
D3	p	150	low
10	p	150	high
11	p	150	low
12	p	150	low

Table 3.1: List of FZ wafers of the main thin sensors production. Wafer names starting with a "D" are backup wafers replacing wafers 3 and 9, which were damaged during the sensor production.

based on simulations and measurements of test structures presented in the following sections.

The last step of the thinning procedure, i.e. partially removing the handle wafer, has not yet been carried out since in the early R&D phase extensive manual handling is needed for the characterization of the sensors. The feasibility of the back-side etching on diodes has already been demonstrated [108]. As a consequence, only the n-in-p wafers could be tested at this point in time. Hence, all measurements presented in this thesis were performed on these sensors, which are the preferred choice to be investigated for the proposed detector upgrade. Characterizing the n-in-n sensors and evaluating their performance for a future sLHC pixel detector will be carried out later.

Figure 3.3(a) shows the layout of the wafers designed at the MPP. Each wafer incorporates many different structures including diodes, strip and pixel sensors, as well as further test devices to control the quality of the wafer processing. The implemented sensors relevant to the presented results are given in Tab. 3.2, including their multiplicity and information about the implant structures. The footprint of the large-size multi-chip pixel sensor (red outline in Fig. 3.3(a)) is identical to the one used in the present ATLAS pixel module. This sensor was included to rebuild full-size ATLAS pixel modules using the standard bump-bonding technology [112] to connect 16 ATLAS readout chips with the thin sensor. The ten single-chip pixel sensors (yellow outline) are also compatible with the ATLAS readout chip. From 4 of the 8 n-in-p wafers each of these sensors will be connected to a single chip. Figure 3.3(b) shows a close-up of some on the $50 \times 400\,\mu\text{m}^2$

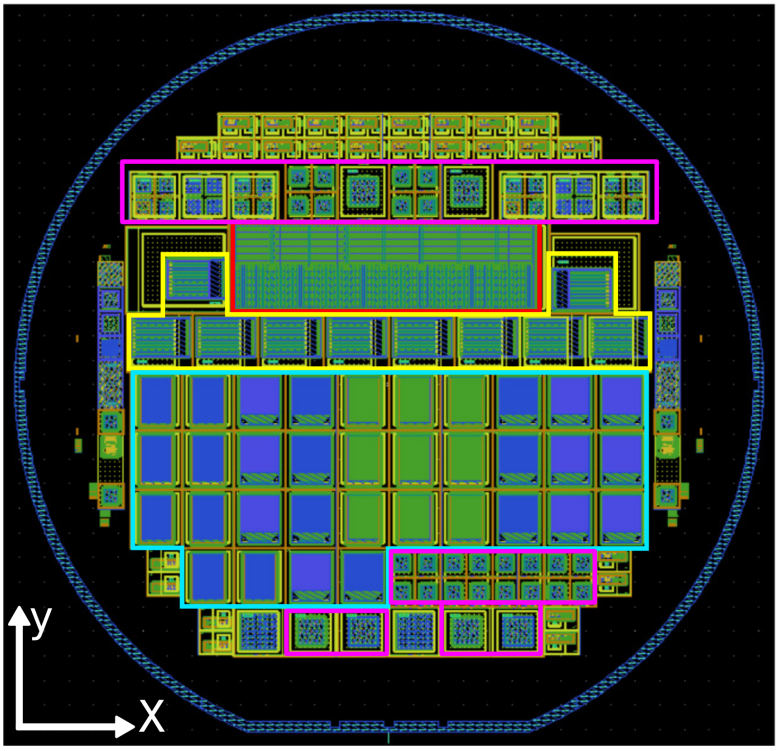

(a) Full wafer map

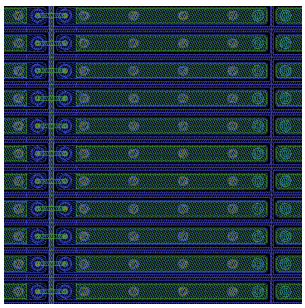

(b) Part of a pixel sensor

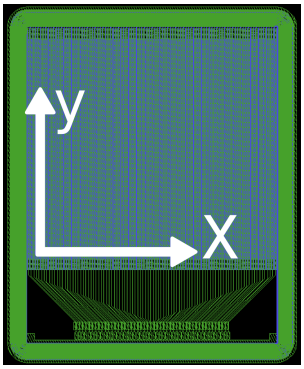

(c) Strip sensor

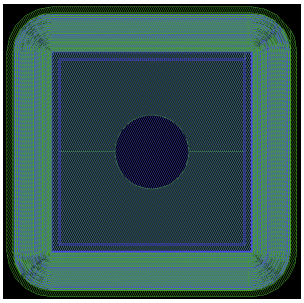

(d) Diode

Figure 3.3: Overview of the main thin sensor production on 6-inch float-zone wafers (a). The contents of the colored boxes are given in the text. In (b) a column of pixel cells is shown with the vertical bias line and the adjoined punch through structures. The full strip sensor (c) and the diode (d) are not to scale to the other pictures.

Device	multiplicity	cell size [μm^2]	# of cells
multi-chip pixel module	1	50 x 400	47232
single-chip pixel sensor	10	50 x 400	2880
strip sensors 80 μm pitch	17	80 x 7400	96
strip sensors 50 μm pitch	17	50 x 9000	96
small diodes	40	2500 x 2500	1
large diodes	6	5000 x 5000	1

Table 3.2: Sensor structures implemented per 6-inch wafer of the main production of thin sensors.

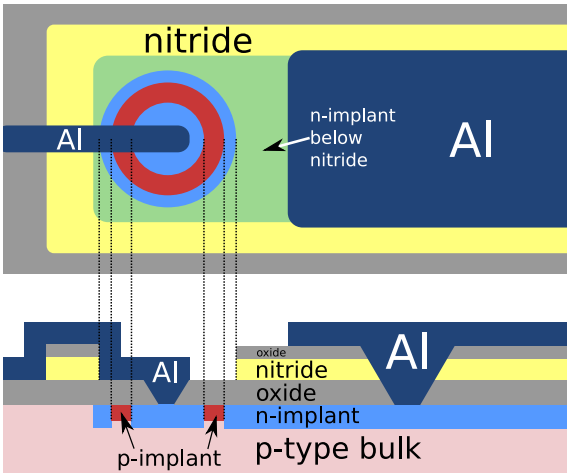

Figure 3.4: Layout of the punch-through biasing structure.

pixel cells of such a sensor. Towards the left side the punch-through structures and the bias grid are visible.

The punch-through structures, implemented in all pixel and strip sensors, are used to distribute a common ground potential to all pixel- and strip implants. This is only needed during electrical characterizations when no readout chip is attached, or if some of the connections between sensor and chip are broken. In both circumstances, the ground potential cannot be supplied by the readout electronics, but only through the bias grid, which has an additional contact pad put to ground potential outside of the active area.

Figure 3.4 depicts a schematic representation of the punch-through structure. Within the n-type pixel implants a ring-shaped implant void is placed close to one of the short edges. Since no n-type implantation is introduced in this area the uniform p-spray implanted over the whole wafer will be the dominating implant type. While the outer part of the punch-through belongs to the pixel implant, the central implantation is connected

via an aluminum line to a bias grid on the sensor. When a reverse bias voltage is applied to the back-side implant and the bias grid is grounded the leakage current generated in the bulk will draw the potential of the pixel implants towards the back-side potential. In this situation the punch-through structure acts as an n-channel Metal-Oxide-Semiconductor Field-Effect Transistor (MOSFET) which is depleted, i.e. not conductive, and has different potentials applied to its source (the pixel-implant) and drain (the inner implant connected to the bias grid). Two mechanisms can cause a flow of current between the bias grid and the pixel-implant that will bring the potential of the latter closer to the ground potential. The first one is the punch-through current, caused by thermally generated charge carriers in the depleted bulk below the punch-through structure [113]. Because of the dependence of this current on the potential difference between the source and the drain, it will always adapt to the leakage current collected by the respective pixel. In this equilibrium state the pixel-potential reaches the punch-through potential U_{PT}. A second source of current is generated if the potential difference between the source and the drain is larger than the threshold potential U_{th} of the MOSFET. In this case an electron channel (inversion layer) is formed below the aluminum line in the p-spray implant which opens the contact between the source and the gate. This leads to currents that draw the pixel-potential closer to the one of the bias grid until the potential difference is smaller than U_{th}.

The strip sensors, shown in Fig. 3.3(c) and the blue outline in Fig. 3.3(a) have electrical properties comparable to those of the single-chip pixel sensors. Their size and complexity is similar, and they also contain the punch-through structures at one end of the strip implants. However, the strip implants are much longer and span over the whole active area in the y-direction and are only segmented in x. This allows for connecting all strip implants to readout electronics via wire bonding from one end of the strips. Therefore, next to the electrical characterization, strip sensors can also be used for CCE and noise measurements with strip readout systems like Alibava (see Sec. 3.5.3). The similar functionality compared to pixel sensors, combined with the convenience of signal-readout via simple wire bonds, motivates the high abundance of strip sensors in most prototype pixel sensor productions.

The diodes in Fig. 3.3(d) and the pink outline in Fig. 3.3(a) are mainly used to measure leakage currents and capacitances of large size pn-junctions to investigate silicon bulk properties. Furthermore, within the presented work, diodes with different size guard-ring structures are included to investigate a possible way to increase the active area of planar silicon sensors (see Sec. 3.4.2).

3.1.3 Epitaxial thin sensor production

A second production of thin n-in-p sensors on a handling substrate was carried out by CiS [114] for the CERN RD50 collaboration to obtain a set of identical sensors distributed to the different member groups to conduct comparable measurements. In-

Name	active thickness [μm]	handle wafer thickness [μm]	resistivity [Ωcm]
1-6	50 ± 5	525 ± 25	120 - 180
7-12	75 ± 7.5	525 ± 25	250 - 350

Table 3.3: List of the produced epitaxial wafers.

Structure	multiplicity	cell size [μm^2]	# of cells
strip sensors 80 μm pitch	16	80 x 7400	96
strip sensors 50 μm pitch	14	50 x 9000	96
small diodes	26	2500 x 2500	1
large diodes	4	5000 x 5000	1

Table 3.4: List of strip sensors and diodes per wafer included in the 4-inch epitaxial production.

stead of the wafer processing technology described above, an industrial epitaxial growth process was used to produce twelve 4-inch (10 cm diameter) wafers. The active thicknesses were 50 μm and 75 μm, on 525 μm thick, low resistivity (100) handling wafers (cf. Tab. 3.3). The grown epitaxial layers have the same crystal orientation, adopted from the handling wafers during the growing process.

The epitaxial silicon growing is done with a chemical vapor deposition. Two gasses, for silicon usually silicon tetrachlorine ($SiCl_4$) and hydrogen (H_2), are mixed at around 1200°C and react on a seed material like the low resistivity handle wafer to form solid silicon and hydrochloric acid

$$SiCl_{4(g)} + 2H_{2(g)} \longrightarrow Si_{(s)} + 4HCl_{(g)}. \tag{3.1}$$

Controlling the mixtures of these two gases allows for changing the speed of the growing process. The faster the process is conducted, the more crystal defects are expected leading to low resistivity silicon not suitable for fully depleted sensors. Growing high resistivity epitaxial silicon wafers, needed for sensors, is therefore time consuming and difficult. Hence, for producing thin sensors with resistivities of several kΩcm, the HLL process is currently a preferable technology.

The epitaxial wafers (Fig. 3.5) contain mainly diodes and strip sensors of 50 μm and 80 μm pitch with different options of inter-strip isolations. Table 3.4 lists the diodes and strip sensors implemented on the epitaxial wafers.

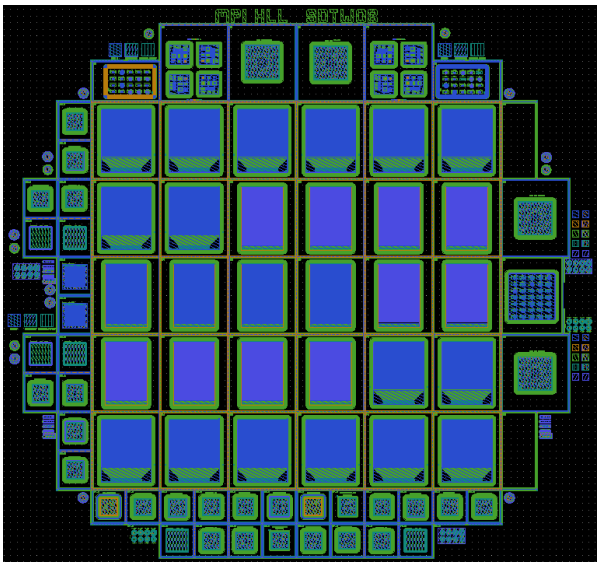

Figure 3.5: Wafer map of the 4-inch epitaxial thin sensor production. In the central region 30 strip sensors are placed surrounded by diodes and other test structures.

3.2 Simulations of p-spray implant parameters

The performance of pixel and strip sensors exposed to high integrated particle fluences strongly depends on the choice of the implant parameters. Especially a radiation resistant isolation between the individual pixel cells is needed to prevent electrical shorts, crosstalk, and high electric field strengths causing junction break-downs before and during irradiation. For n-in-p and n-in-n sensors the isolation is reached by a p-type implant between the pixel n-type implants to form an isolating n-p-n junction as described in Sec. 2.1.2. Different p-type implant geometries and parameters, i.e. implant energy and the area dose, lead to different potential distributions within the sensors. High potential differences in the n-p-n junction lead to a good isolation but also to high electric field regions. As the latter can cause junction break-downs, a compromise between a strong isolation and acceptable field values has to be found.

During the irradiation, the variation of the sensor material also has to be taken into account since the fluences of high-energetic particles will alter the silicon material properties. As described before, this is on the one side caused by the introduction of defects changing the effective doping concentration of the bulk and on the other side by the formation of surface defects in the form of positive oxide charges and dangling bonds. Especially the surface defects have a strong influence on the inter-pixel isolation since the introduced positive surface charges attract electrons which lead to a compensation of the p-type implants. Hence, the implant parameters have to be chosen such that they ensure

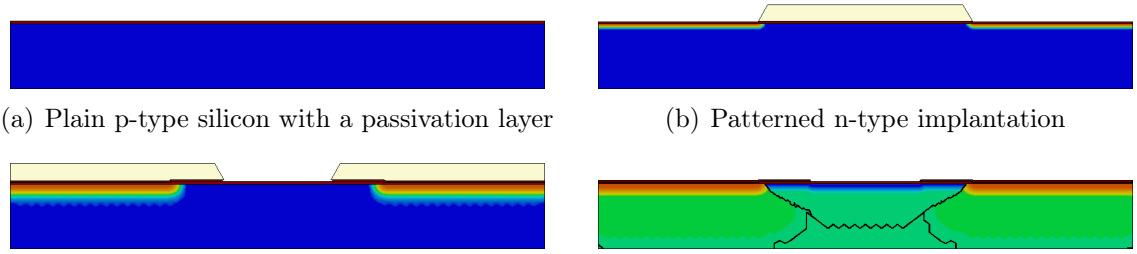

(a) Plain p-type silicon with a passivation layer

(b) Patterned n-type implantation

(c) Opening of the nitride layer for sensors with a moderated p-spray isolation

(d) Final distribution of the doping concentrations

Figure 3.6: Different steps of the DIOS device simulation towards a 2-dimensional doping profile. In each picture, the colors always range from red, marking the highest donor concentrations, over green to blue, symbolizing the highest acceptor concentrations.

successful operation before irradiation for testing purposes, and even more important during various levels of irradiation, because most of the actual detector operation will be performed in this condition.

Since the implant parameters and their variations under irradiation cannot be calculated analytically, numerical simulations were carried out to arrive at the desired implant parameters. These simulations consist of two consecutive steps, a simulation of the implanting process to arrive at a 2-dimensional doping profile of the devices, followed by numerical discrete solving of the partial differential equations that describe the potential, the electric field, the charge carriers, and the currents within the sensors.

3.2.1 Semiconductor device simulations with DIOS

The simulation of the implant process is carried out with DIOS [115], a commercial device simulation package that uses Monte Carlo and finite element techniques. In DIOS, a 2-dimensional cross-section is modelled for the implant formation in the surface region of a silicon wafer. The two dimensions are spanned by the vector orthogonal to the sensor surface (z-direction) and one vector within the surface plane. Naturally, the latter one is chosen to be orthogonal to the long side of the strip or pixel implants (x-direction in Fig. 3.3(c)) to arrive at the cross-section of the n-p-n implant structure. The thickness of the simulation cross-section is chosen to be $z \leq 6\,\mu$m, since the surface implants do not penetrate deeper into the bulk. The width in x corresponds to the pitch of the strip or pixel and the endpoints of the simulation region in x are chosen to reach from the middle of one n-type implant to the middle of the neighboring one with the p-spray region enclosed in-between. Employing periodic boundary conditions in this direction allows to simulate a full cell as if it would be part of an infinite array of identical cells.

For modelling pixel and strip sensor implants in DIOS a set of simulation parameters has to be supplied. They control the final implant profile of the sensor and can be best introduced by explaining the individual simulation steps. Since during the time of the simulation the final thicknesses of the surface layers of the actual production were not known yet, the simulation was carried out with standard values given in the next paragraphs. The final choice of the p-spray implant parameters is based on an additional simulation performed for the actual surface parameters as they became known. However, they cannot be disclosed within this thesis.

Figure 3.6(a) shows the initial sensor cross-section with a passivated (oxidized) but otherwise untreated p-type silicon wafer. For this, the dimensions of the 2-D simulation volume have to be given as described above. The thickness of the oxide layer used for the surface passivation is 230 nm. Furthermore, the crystal orientation has to be specified and is defined to be (100) corresponding to the actual wafers.

The next processing step is to apply a patterned mask on the sensor surface, corresponding to the photo-resist (Fig. 3.6(b)). A virtual etching process is performed which removes 190 nm of the oxide layer on the uncovered sensor area followed by an implantation of phosphorus with an area dose of 10^{15} /cm^2 and an implant energy of 180 keV. This forms the structured n-type implants in the silicon since the doping atoms do not pass the photo-resist. After removing the resist, a heating of the wafer to 1000°C for 180 minutes is simulated which diffuses the implanted donor atoms as seen in the difference of Figs. 3.6(b) and 3.6(c).

A homogeneous 90 nm thick layer of nitride is added to the surface which will be used as a further moderator to stop some of the p-spray implant atoms used for the isolation. On top of this a 30 nm layer of a low temperature oxide (LTO) is added. Up to here the processing is identical for all isolation schemes used. The next step depends on the desired implant geometry being a homogeneous or a moderated p-spray. No p-stop implant isolations were used in the main production since they show an increased maximum electric field strength after irradiation [63]. In the case of a moderated p-spray isolation a new structured resist mask is applied which has an opening in the center between the n-implants (Fig. 3.6(c)). The 30 nm of LTO are etched away and the resist mask is removed. Another etching is performed which only affects the nitride, being only opened in the area where there is no LTO on top. In the other case of the homogeneous p-spray isolation there is no opening in the oxide and consequently also no opening can be etched in the nitride layer.

The following implantation with boron atoms is used to form the isolating p-type implant. Here the difference between the homogeneous and moderated p-spray becomes apparent. In the former case the whole silicon sensor is homogeneously doped as the oxide and nitride layers have the same thickness all over the sensor surface. For the moderated p-spray the opening in the oxide and nitride leads to a lower moderation of

Name	pitch s [μm]	contact width [μm]	nitride opening [μm]
503010	50	30	10
503606	50	36	6
503006	50	30	6
502410	50	24	10
802024	80	20	24
803024	80	30	24
802000	80	20	-

Table 3.5: Implant geometries simulated with DIOS.

the incident boron atoms, i.e. a higher doping concentration in the silicon bulk[1]. As the dose of the p-type implant is around three orders of magnitude lower than that of the n-type implant, the compensating effect of the p-type doping in the n-type implants is negligible.

The last step is an additional heating to 900°C for 60 minutes to diffuse the implanted boron atoms. The resulting simulation cross-section (Fig. 3.6(d)) now contains the profile of the implant doping concentrations as expected from a real production run and can be used as an input to the TeSCA finite element solver.

The above device simulation procedure was carried out for a number of different implant geometries which are included on the wafers of the main thin sensor production. The designs have different pitches s and widths of the n-type implantations combined with various options for the opening in the nitride. A list of the simulated geometries is presented in Tab. 3.5. They contain various moderated p-spray options since the behavior of these is more complex than of the homogeneous p-spray geometries. The simulated homogeneous p-spray option represents the one where the highest electric field strength is expected and thus gives an upper limit for the sensors with a homogeneous p-spray isolation.

Furthermore, a total of 18 different combinations of boron implant energies from 100 keV to 130 keV and area doses from $3 \cdot 10^{12}$ /cm^2 to $5 \cdot 10^{12}$ /cm^2 were simulated and are listed in Tab. 3.6. Added in the last two columns are the effective area densities of boron acceptors in the moderated part (labeled "M") of the p-spray and below the central opening (labeled "O") of the nitride. These are the key parameters that determine the isolation characteristics of a given geometry.

[1] It is noteworthy that in the above-mentioned definition the term moderated p-spray only refers to different levels of moderation. The homogeneous p-spray isolation has also a moderated but uniform p-spray implantation over the whole sensor area.

Isolation ID	energy [keV]	dose [10^{12}/cm^2]	M [10^{12}/cm^2]	O [10^{12}/cm^2]
00	100	3.0	0.5	2.8
01	105	3.0	0.6	2.8
02	110	3.0	0.8	2.8
03	120	3.0	1.4	2.8
04	100	4.0	0.6	3.7
05	105	4.0	0.8	3.7
06	110	4.0	1.1	3.7
07	120	4.0	1.8	3.7
08	100	5.0	0.8	4.6
09	105	5.0	1.1	4.6
10	110	5.0	1.4	4.7
11	120	5.0	2.3	4.7
12	125	3.0	1.6	2.9
13	130	3.0	1.8	2.9
14	125	4.0	2.2	3.8
15	130	4.0	2.4	3.9
16	125	5.0	2.7	4.8
17	130	5.0	3.0	4.9

Table 3.6: Boron isolation parameters used in the DIOS simulations. Listed are the isolation identifier and the boron implant energy and dose. Also listed are the integrated effective dose in the moderated area (M) and the integrated dose below the nitride opening (O). The uncertainties of the effective doses calculated by DIOS are expected to be below 10% [116].

3.2.2 Simulation of the potential and electric field distribution

To simulate the distribution of the electric field and potential in the silicon sensor, the program TeSCA [117] is used for solving a set of semiconductor equations on a 2-dimensional grid. Setting up a simulation problem to be solved by TeSCA involves several steps. As a first step the simulation area has to be created with respect to the aforementioned simulation coordinate system. This is done via a steering file containing a number of defined edges that form the 2-dimensional sensor cross-section, this time for the whole thickness of the sensor to also simulate the behavior of the bulk. For numerical reasons the cross-section is divided into several sub-areas, each receiving additional parameters that control the desired accuracy of the simulation. The outermost edges of the simulation area have to be defined in terms of their functionality. Possible choices are contact edges, as the n-type implants and the back-side p-type implant, gate edges, i.e. the edges above the isolation implant, and finally internal edges which connect the simulated area to its periodical neighbor cells. With these inputs the simulation area is well defined as shown in Fig. 3.7(a).

In a next step the program `gridgen` [118] is used to divide the simulation area in finite triangular elements based on the Delaunay triangulation method [119]. For this, `gridgen` first defines the needed granularity of each simulation area by considering the information given by the edge types and the parameters in the aforementioned steering file. Within the simulation area several ten thousand knots, i.e. points in the 2-D coordinate system, are generated. Finally, a corresponding number of triangles is defined with the knots as corner points, forming the mathematical basis of the discretized semiconductor equations. The output of `gridgen` is a file containing the full compilation of knots and triangles which constitute the designed simulation area shown in Fig. 3.7(b).

In an additional steering file, serving as input for TeSCA the generated grid of the simulation area, the implantation profile simulated with DIOS, and further parameters are defined. The latter include the doping concentration of the bulk material, the doping profile of the back-side implantation, and the effective oxide charges above the p-spray isolation. Furthermore, the boundary conditions for the contact edges, i.e. the applied bias voltages to the sensor implants are defined.

From the input given, TeSCA solves the coupled differential system of the Poisson equation and the continuity equations for electrons and holes, which are defined on the discretized simulation area [120]. Poisson equation:

$$(\epsilon \cdot \nabla U) = q \cdot (N_0 + p - n), \tag{3.2}$$

continuity equations:

$$q \cdot \frac{dn}{dt} - \nabla J_{\mathrm{e}}(n, \mu_{\mathrm{e}}, U, n_{\mathrm{i}}) = q \cdot (G - R), \tag{3.3}$$

$$q \cdot \frac{dp}{dt} - \nabla J_{\mathrm{h}}(p, \mu_{\mathrm{h}}, U, n_{\mathrm{i}}) = q \cdot (G - R). \tag{3.4}$$

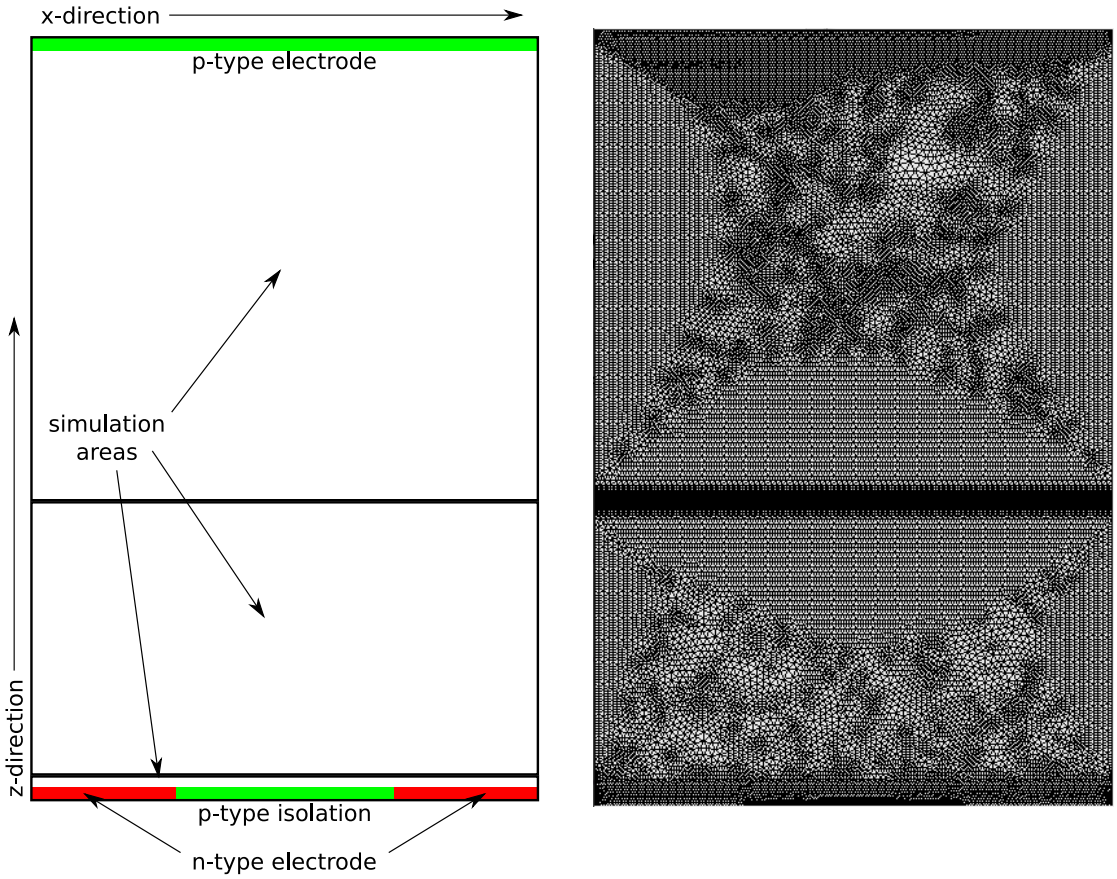

Figure 3.7: Schematics of the simulation area of the TeSCA program. Shown are (a) the different implant structures and (b) the discretization into a triangular finite element grid.

In these equations the variables are defined as follows:

$$
\begin{aligned}
U &: \text{potential} \\
n_{\mathrm{i}} &: \text{intrinsic doping concentration} \\
n, p &: \text{concentration of electrons and holes} \\
N_0 = N_{\mathrm{D}} - N_{\mathrm{A}} &: \text{net concentration of doping atoms} \\
q &: \text{elementary charge} \\
\mu_{\mathrm{e}}, \mu_{\mathrm{h}} &: \text{electron and hole mobilities} \\
\epsilon &: \text{dielectric constant of the sensor} \\
J_{\mathrm{e}}, J_{\mathrm{h}} &: \text{electron and hole currents} \\
G, R &: \text{generation and recombination rates.}
\end{aligned}
$$

Given in these equations are the initial donor and acceptor concentrations (N_D, N_A) throughout the sensor corresponding to the expected values at a particular fluence, the applied potential at the n-type and back-side p-type implants, and all constants. The boundary conditions needed for solving the equations are taken from the definition of the input grid. All contact implants are treated as Dirichlet boundaries with fixed values, whereas the p-spray implantation edge is treated as a gate boundary condition, i.e. a floating edge influenced by a surface (oxide) charge. The periodic edges to the neighboring simulation cells are treated as Neumann boundary conditions, characterized by a vanishing gradient orthogonal to the edge. The output variables of interest are the charge carrier concentrations ($n(x, z)$ and $p(x, z)$) to acquire information about the depletion behavior, and the potential distribution $U(x, z)$ with the derived electric field $\mathcal{E}(x, z) = \nabla U(x, z)$.

Figure 3.8 shows an example of a potential distribution within the simulation cross-section, being the numerical solution of the equation system 3.2 - 3.4 for a given set of input parameters. In the presented example, the n-implants are kept a ground potential while the back side is set to $-20\,\mathrm{V}$. Clearly visible is the drop of the potential between the n-type implants and the p-spray isolation. The more abrupt this transition between the n-type and p-type potential is, the stronger is the electric field in this region.

3.2.3 Simulation results

The pixel and strip geometries introduced in Tab. 3.5 and the boron implantation parameters from Tab. 3.6, were simulated for various bulk doping concentrations and surface charge densities q_{s}. This accounts for the properties of p-type and n-type silicon sensors after different received irradiation fluences. A list of the simulated values is given in Tab. 3.7. They correspond to the initially planned wafer resistivities of $360\,\Omega\mathrm{cm}$ for the n-type and $5\,\mathrm{k}\Omega\mathrm{cm}$ for the p-type wafers. Both options were simulated before and after

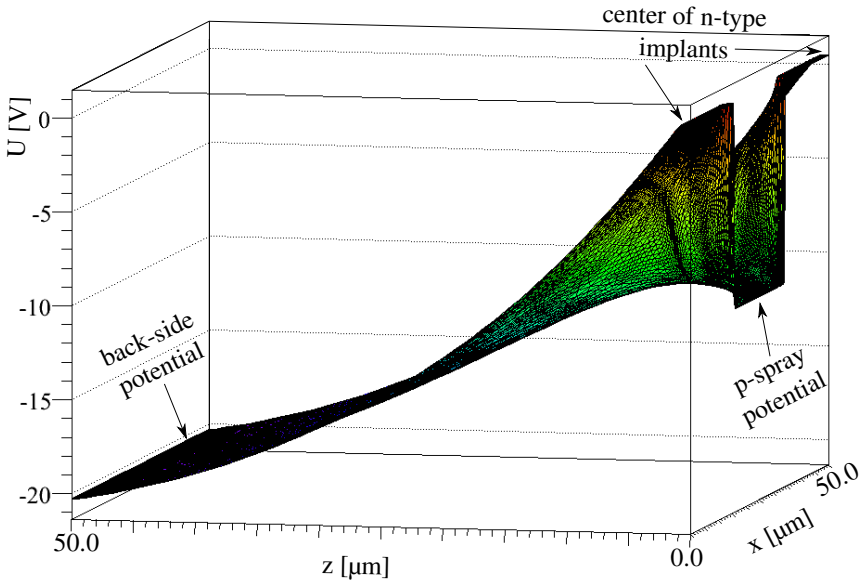

Figure 3.8: Exemplary potential distribution within a simulation area with a thickness $d = 50\,\mu$m and a pitch of $s = 50\,\mu$m.

the saturation of q_s (similar to [63]) and also for higher levels of bulk damage corresponding to a high acceptor concentration. For the n-in-n sensors which undergo the SCSI to n-in-p sensors also a bulk doping concentration close to the type inversion was simulated.

The largest electric field strength in the n-p-n implantation structure is expected before irradiation ($q_s = 2 \cdot 10^{11}/\text{cm}^2$). The lowest isolation potential, i.e. minimum potential difference between the n-type and p-type implants, leading to the lowest resistance between the n-implants, is expected after the surface charge saturation. For higher irradiation doses, causing larger acceptor concentrations, the maximum field strength and the isolation potential have intermediate values. Therefore, the two cases before and after surface charge saturation are the most interesting for finding suitable isolation implant parameters.

The thickness of the simulated sensor is 75 μm, being the thinner of the two options of the main thin sensor production. Simulating thin sensors has the advantage of reaching the same electric field and potential configurations with lower bias voltages as compared to thicker sensors. Therefore, with voltages of up to 200 V a full depletion of all simulated sensors could be reached (cf. Tab. 3.7). The voltages are applied iteratively increasing from 0 V in small steps with intermediate simulations to allow for better convergence of

Description	bulk doping concentration c [1/cm^3]	surface charge density q_s [1/cm^2]	U_{fd} [V]
n-type	$1.3 \cdot 10^{13}$	$2 \cdot 10^{11}$	55.6
+ surface charge	$1.3 \cdot 10^{13}$	$2 \cdot 10^{12}$	55.6
close to type inversion	$1.5 \cdot 10^{12}$	$2 \cdot 10^{12}$	6.4
p-type	$-2.8 \cdot 10^{12}$	$2 \cdot 10^{11}$	12.0
+ surface charge	$-2.8 \cdot 10^{12}$	$2 \cdot 10^{12}$	12.0
LHC fluence	$-4.0 \cdot 10^{13}$	$2 \cdot 10^{12}$	171.1

Table 3.7: Simulation parameters used to account for the different silicon bulk types and irradiation stages. Negative values for the bulk doping concentration stand for p-type material, positive values for n-type material.

the TeSCA finite element solver.

As an example of the effects of the surface damage and the working principle of the p-spray isolation, two sub-sets will be introduced in more detail. The first is a simulation of an n-in-p sensor with a pitch of $s = 50\,\mu$m, a contact width of $30\,\mu$m, and a nitride opening of $10\,\mu$m, corresponding to the moderated p-spray geometry of the present ATLAS pixel sensor. Figure 3.9 shows the isolation potential and the maximum lateral electric field strength of this structure with some of the different isolation options, before and after the introduction of surface defects. The lateral electric field is the field component in the x-direction, and its maximum value is the figure of merit for predicting junction break-downs which are expected above 300 kV/cm. In all four diagrams, the shape of the data-point markers denote the isolation implant dose, whereas their colors indicate the implant energy (cf. Tab. 3.6). Figures 3.9(a) and 3.9(c) show the isolation potential before and after the surface charge saturation. In both cases it is increasing with the applied voltage. Before the surface charge saturation, the isolation potential does not vary strongly for different boron implantation parameters. After the saturation, the results in Fig. 3.9(c) show a slight decrease of the isolation potential which is more pronounced for the isolation options with the lowest boron doses (square markers) but is almost independent of the implant energy. This can be explained by variation of the effective doping concentration in the p-spray isolation. In the moderated part of the isolation the effective doping concentration is strongly depending on the implant energy since low energy boron atoms are stopped more likely in the nitride and oxide layers. Below the nitride opening the effective doping concentration is almost independent of the energy because nearly all the implant atoms reach the silicon. The general decrease of the isolation potential can be explained by the compensation of the p-spray in the moderated area. The insensitivity of the graphs to the energy is a consequence of the fact that the boron concentration below the nitride opening, giving the major contribution

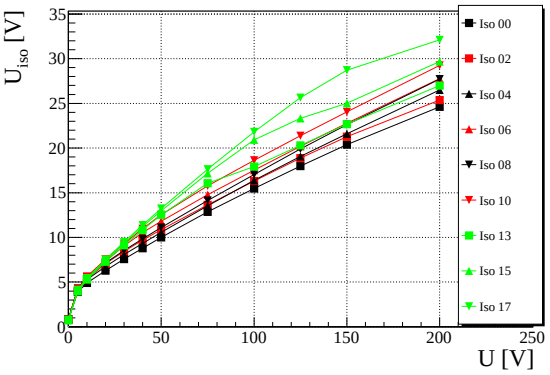

(a) Isolation potential, $q_s = 2 \cdot 10^{11}\,/\mathrm{cm}^2$

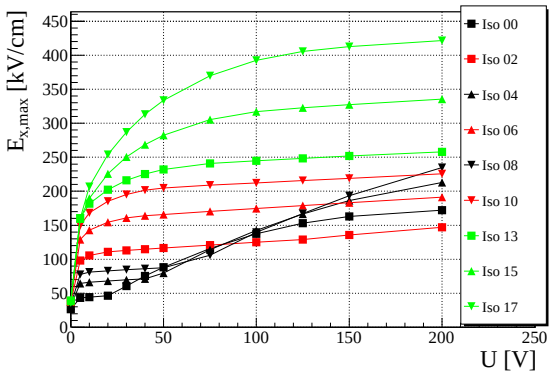

(b) Max. lat. electric field, $q_s = 2 \cdot 10^{11}\,/\mathrm{cm}^2$

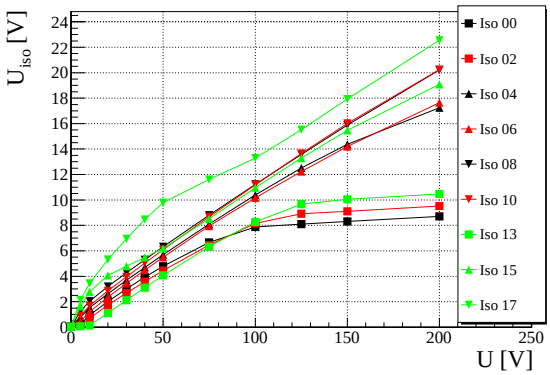

(c) Isolation potential, $q_s = 2 \cdot 10^{12}\,/\mathrm{cm}^2$

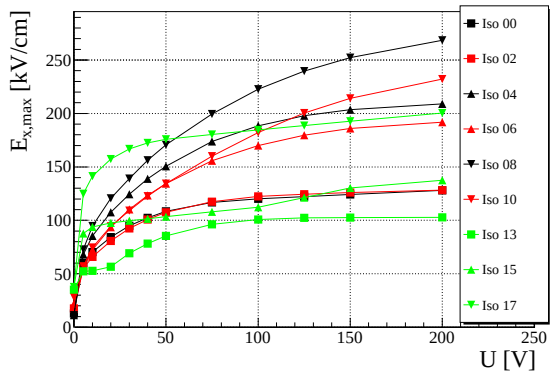

(d) Max. lat. electric field, $q_s = 2 \cdot 10^{12}\,/\mathrm{cm}^2$

Figure 3.9: Isolation potentials and maximum lateral electric fields as functions of the applied bias voltage. The curves are shown for a subset of simulation parameters for a sensor with $s = 50\,\mu\mathrm{m}$ and $d = 75\,\mu\mathrm{m}$.

to the isolation after the surface charge saturation, is also almost independent of the energy. Only the isolations with the lowest implant doses of $3 \cdot 10^{12}$ /cm^2, i.e. not much higher than the final surface charge, are significantly weakened in the area below the nitride opening.

The corresponding maximum electric field strength before irradiation show a wide spread (Fig. 3.9(b)) reaching maximum field strengths of more then 400 kV/cm at 200 V for the highest implantation energies. These options should not be used for the sensor production, because only values below 300 kV/cm are considered to be safe for operation [63]. After the saturation of surface charges the maximum electric field strength for these isolations decreases, whereas for the other isolation options it stays similar or even slightly increases. All of the selected options stay below the critical 300 kV/cm.

The variations of the maximum of the electric field strengths can also be explained by the change of the effective doping concentrations in the silicon. The largest field values are expected in the regions where the doping concentrations change abruptly. This is at the pn-junction between n-type and p-spray implants, and also at the border between the moderated and not moderated p-spray implant. For high implant energies the difference between the doping concentration in the moderated part and below the nitride opening is higher than for low implant energies. Therefore, before irradiation the highest field values are at the pn-junction for the implant options with high energies, whereas in the case of low energy implantations, they are at the border between the moderated and un-moderated p-spray implants.

The saturation of surface charges compensates significant parts of the p-spray isolation in the moderated area and hence, this leads to a lower electric field at the pn-junction and a higher one below the edge of the nitride opening. Depending on the initial field distribution the overall maximum can either decrease, stay about constant, or even increase. To visualize this, Fig. 3.10 shows the electric field distributions for $0\,\mu\text{m} \leq z \leq 1\,\mu\text{m}$ of a sensor with isolation option 06 biased at 200 V. Clearly visible are the four field peaks of the moderated p-spray isolation; the opposing polarities denote the different lateral drift directions for the charge carriers in the left and right part of the sensor. The inner two peaks are caused by the transition between the moderated and not moderated p-spray implantations, whereas the outer two peaks are caused by the transition between the p-spray and the n-type implant.

Before irradiation, the highest field regions are found at the transition between the p-type and and n-type implants, still staying below 150 kV/cm (Fig. 3.10(a)). After the saturation of the surface charges the moderated part of the p-implant is almost completely compensated leading to very little change in the potential and hence low electric fields at the pn-junction (Fig. 3.10(b)). The high concentration implant below the nitride opening on the other hand is not compensated. Consequently the highest electric field strengths are now observed at the transition between the moderated and unmoderated parts of the p-spray implant.

A second example is shown in Fig. 3.11, containing the same diagrams as in Fig. 3.9

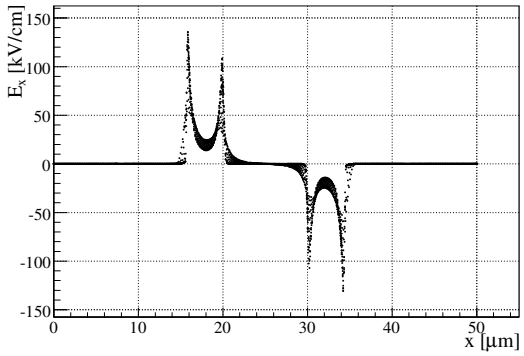

(a) $q_s = 2 \cdot 10^{11}\,/\mathrm{cm}^2$

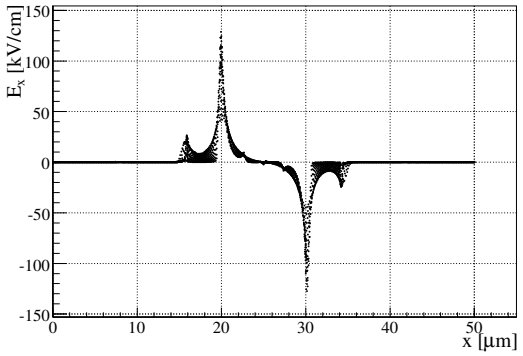

(b) $q_s = 2 \cdot 10^{12}\,/\mathrm{cm}^2$

Figure 3.10: Variation of the electric field caused by surface damage through irradiation. Shown are the values of the distribution with $0\,\mu\mathrm{m} \leq z \leq 1\,\mu\mathrm{m}$.

but this time for an n-in-p sensor with 80 μm pitch, 20 μm contact width, and no opening in the nitride. In terms of the implant geometry this sensor with a homogeneous p-spray isolation is very different to the one presented before, and hence, exhibits other characteristics. From all structures with homogeneous p-spray implants of the thin sensor production, this geometry is expected to have the highest isolation potential and electric field strengths. The isolation potential in Fig. 3.11(a) shows a strong dependence on the implant energy and is in general lower than for the sensor with the moderated p-spray in Fig. 3.9. This is expected since there is no opening in the nitride and hence, the effective doping concentration is equal to the lowest doping concentration of the moderated structures. The strong dependence on the implant energy again shows that the nitride layer is an effective moderator for low energy boron atoms. Strongly correlated to the isolation potential is the maximum electric field strength with the initial surface charge concentration (Fig. 3.11(b)). This can be explained by the simple implant geometry only having a change in the doping concentration at the pn-junction.

After the saturation of surface charges, for almost all isolation options, the homogeneous p-spray shows a strong compensation (Fig. 3.11(c)). Only the highest implantation parameters lead to sufficient isolation potentials, whereas the others yield $U_{\mathrm{iso}} \approx 0\,\mathrm{V}$. This can be explained by the small effective doping concentration below the nitride, listed in column "M" of Tab. 3.6 which is mostly less than $2 \cdot 10^{12}\,/\mathrm{cm}^2$, i.e. the final value of the surface charges. Hence, all implanted acceptors seem to be compensated by the electrons attracted from the surface charges. Consequently, also the maximum electric field strength decreases significantly down to a minimum of 20 kV/cm at 200 V for isolation 00 (Fig. 3.11(d)).

Summarizing the simulations, Fig. 3.12 gives an overview of the minimum isolation

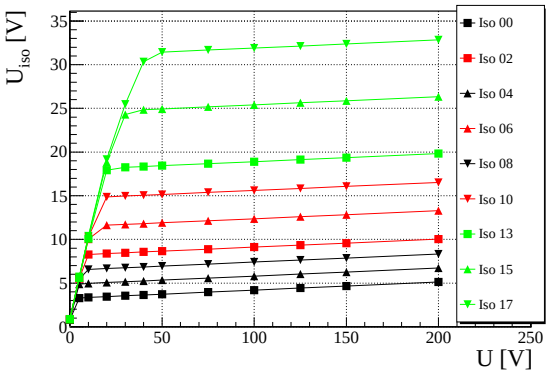

(a) Isolation potential, $q_s = 2 \cdot 10^{11}\,/\mathrm{cm}^2$

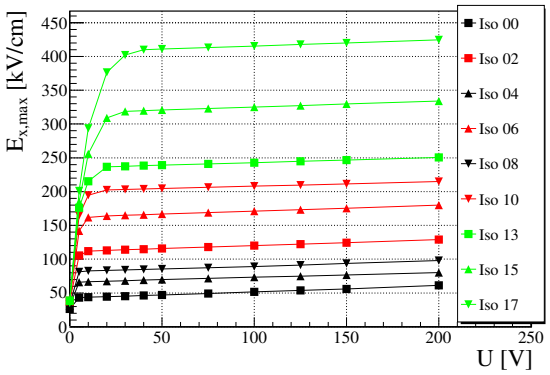

(b) Max. lat. electric field, $q_s = 2 \cdot 10^{11}\,/\mathrm{cm}^2$

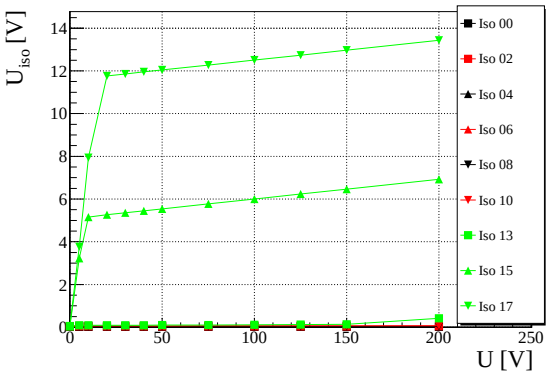

(c) Isolation potential, $q_s = 2 \cdot 10^{12}\,/\mathrm{cm}^2$

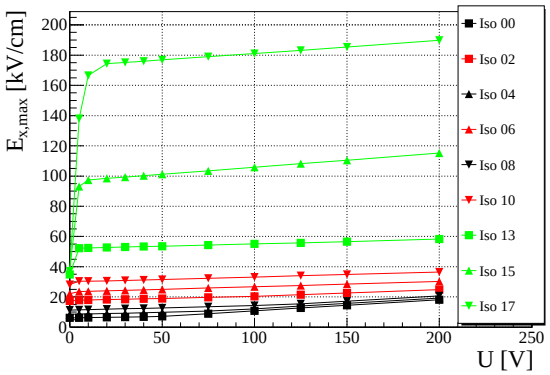

(d) Max. lat. electric field, $q_s = 2 \cdot 10^{12}\,/\mathrm{cm}^2$

Figure 3.11: Isolation potentials and maximum lateral electric fields as functions of the applied bias voltage. The curves are shown for a subset of simulation parameters for a sensor with $s = 80\,\mu\mathrm{m}$ and $d = 75\,\mu\mathrm{m}$.

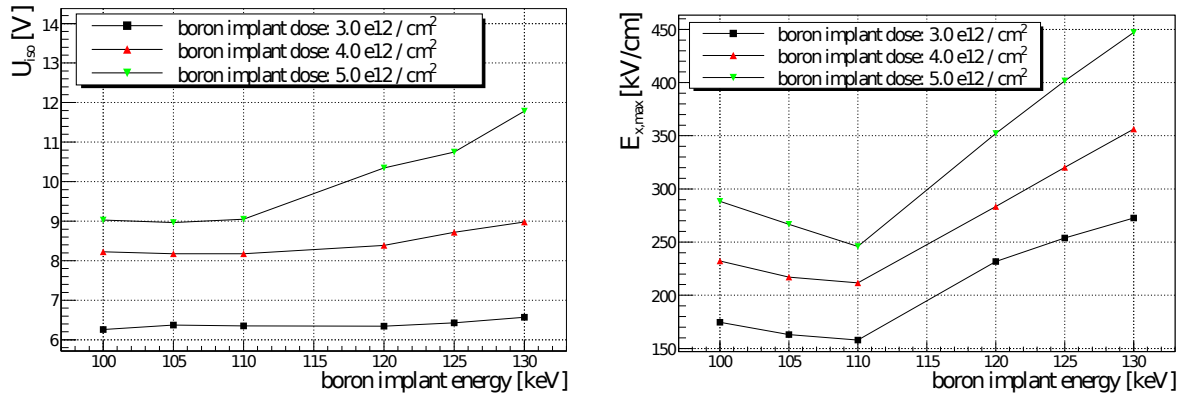

(a) Minimum isolation potential

(b) Maximum lateral electric field

Figure 3.12: Summary of all moderated structures with an applied bias voltage of 200 V. In (a) the minimum isolation potential is given, whereas (b) shows the maximum lateral electric field.

potential and the maximum lateral electric field of all moderated structures at 200 V. This includes all combinations of geometries (Tab. 3.5), bulk dopings, surface charges (Tab. 3.7), and isolation options (Tab. 3.6). Taking into account the critical values of the electric field strength of 300 kV/cm, and a minimum requirement on the isolation potential of about 5 V, which should ensure a sufficient inter-pixel and inter-strip resistance, many of the simulated isolations would be acceptable. However, the most favorable are those with boron doses between $3.0 \cdot 10^{12}$ /cm^2 and $4.0 \cdot 10^{12}$ /cm^2 and implant energies between 100 keV and 110 keV. The simulation of the structures with the homogeneous p-spray isolation shows a full compensation of the implanted boron due to the surface charges for many of the implant parameters. To arrive at suitable p-spray isolations also for the homogeneous options, measurements of inter-strip isolations were carried out before and after saturated surface charges. These measurements were performed on a pre-production of strip sensors which were irradiated with X-rays to introduce the surface charges.

3.3 Measurements of low dose inter-strip isolations

The simulation of the last section has shown that for sensors with a homogeneous p-spray implant, high boron implant energies are needed to achieve an acceptable isolation between the n-type implants. On the other hand, too high doping concentrations lead to critical electric fields in the pn-junction, especially before irradiation (cf. Fig. 3.11(b)). Therefore, strip sensors with moderated and homogeneous p-spray isolations with a

low doping concentration below the nitride were used to experimentally measure the inter-strip resistance before and after the saturation of surface charges. The latter were introduced by generating surface defects with an X-ray source.

3.3.1 Sensors under test

For the p-spray isolation studies two n-in-p sensors with 80 μm pitch and 30 μm contact width were used. These sensors were produced in an earlier CiS production run (STWD07), and are made from (100) FZ wafers with a standard thickness of 285 μm. One of them had a homogeneous p-spray implant, while for the other a moderated p-spray option with a nitride opening of 10 μm was used. The boron implant parameters correspond to isolation 08 with an implant energy of 100 keV and an area dose of $5 \cdot 10^{12}$ /cm^2 (cf. Tab. 3.6). Due to slightly different thicknesses of the oxide and nitride layers in this production the resulting effective area charge concentration are expected to be $7.4 \cdot 10^{11}$ /cm^2 below the moderated part of the p-spray, and $4.2 \cdot 10^{12}$ /cm^2 in the area below the nitride opening, both calculated with the DIOS simulation program. Hence, the homogeneous p-spray sensor has an effective charge density in the whole implant area which is less than the expected saturated surface charge of $q_s = 2 \cdot 10^{12}$ /cm^2. The strip length of 7.4 mm and the strip count of 96 are identical to the strip sensors with 80 μm pitch from the main thin sensor production. Therefore, the strip sensors of both productions should give comparable results.

3.3.2 Experimental setup

High energy photons like X-rays are known to introduce only surface defects via the processes described in Sec. 2.2.1. The energy transfer to the lattice atoms is usually not sufficient to create bulk defects. Therefore X-ray sources can be used to selectively introduce surface charges.

For the irradiation presented here, the X-ray setup of the Karlsruhe Irradiation Center [121] was used. It consists of a 2 kW tungsten X-ray tube with an accelerating voltage of up to 60 kV enclosed in a steel casing (Fig. 3.13). For the irradiation of the sensors the full acceleration voltage was used, delivering a most probable photon energy of 35 keV, at an average dose rate of 125 krad/h. Irradiation times of $\sim$ 8.0 h led to a total received dose of 910 krad for the sensor with the moderated p-spray isolation and 1 Mrad for the sensor with the homogeneous p-spray isolation. The difference is due to a power interruption of the setup.

For the irradiation, the sensors were glued on special brass mounting plates with electrical contact pins (Fig. 3.14). Wire bonds from two of the pins to the bias grid and the back-side are used to bias the strip sensors during irradiation (red and black lines). Six additional wire bonds (green and blue lines) are connected to two triplets

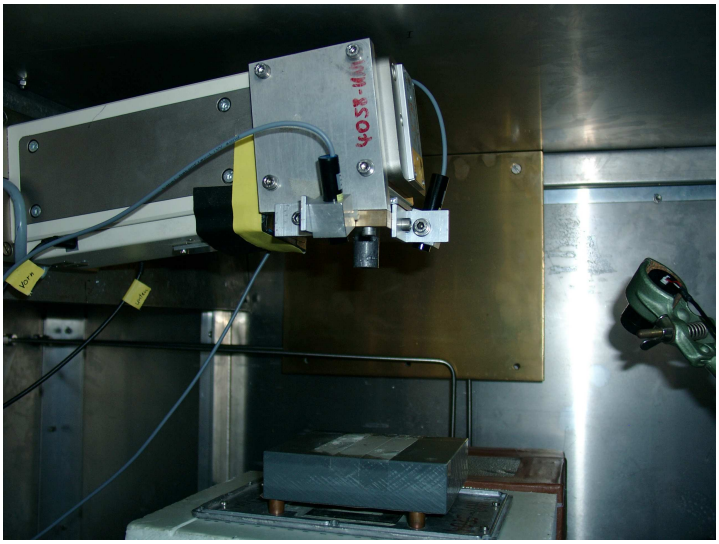

Figure 3.13: The X-ray tube of the Karlsruhe setup [121]. The tube and the probe holder at the bottom of the image are enclosed in a steel casing.

of neighboring strips to measure the inter-strip capacitance and resistance. The backsides of the pins are connected to a PCB with cables attached. The latter are routed to the outside of the irradiation chamber, thereby allowing for permanent biasing and continuous measurements during the irradiation.

3.3.3 Inter-strip isolation before and after X-ray irradiation

The goal of the X-ray irradiation is to reach a saturated concentration of surface defects and hence, of q_s. This can be monitored during the irradiation by measuring the inter-strip capacitance of the biased sensor. In this setup the n-p-n structure of the strip-implants and the isolation acts as a capacitor with the p-spray implant as the dielectric. The p-implant is electrically insulated from the rest of the sensor since the bulk and also the pn-junctions to the neighboring n-implants are at least partially depleted. The holes within the p-implant are however mobile and cause a high polarizability of the p-spray volume. Since surface charges are forming during the irradiation the positive potential causes an additional depletion from the top of the p-spray implant, reducing the amount of free charge carriers. Hence, the capacity decreases. Figure 3.15 shows the measured capacitances per strip length for both sensors during irradiation. The measurements indeed show the expected decrease of the capacitances up to X-ray doses of $(50 - 100)\,\mathrm{krad}$ for the homogeneous p-spray isolation, and up to $350\,\mathrm{krad}$ for the moderated p-spray option, containing the higher doping concentration in the central part of the p-implant. Above these irradiation doses, the capacitances are constant in

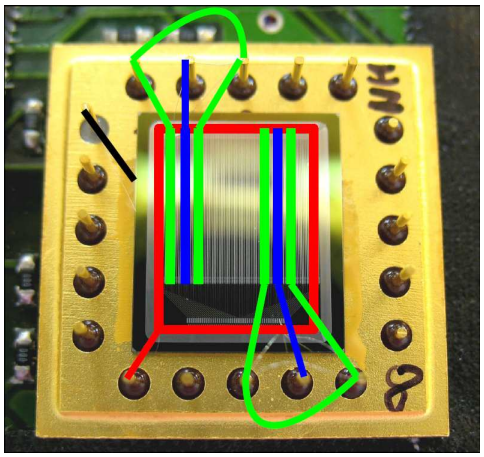

Figure 3.14: A sensor glued to a brass mounting plate with surrounding pins. Eight of the pins are connected with wire bonds to the sensor and via the PCB and attached cables to the measurement devices.

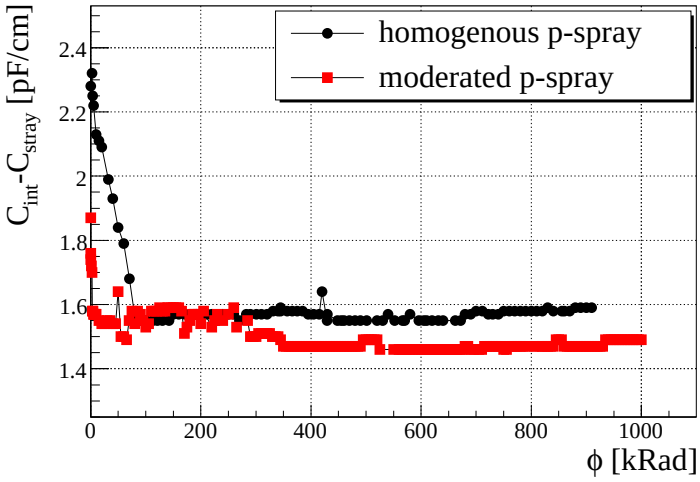

Figure 3.15: Inter-strip capacitance as a function of the received dose, measured with a bias potential of $-40\,\mathrm{V}$ and at a frequency of $100\,\mathrm{kHz}$. The stray capacitance C_{stray} is the capacitance of the measurement setup without a sensor attached.

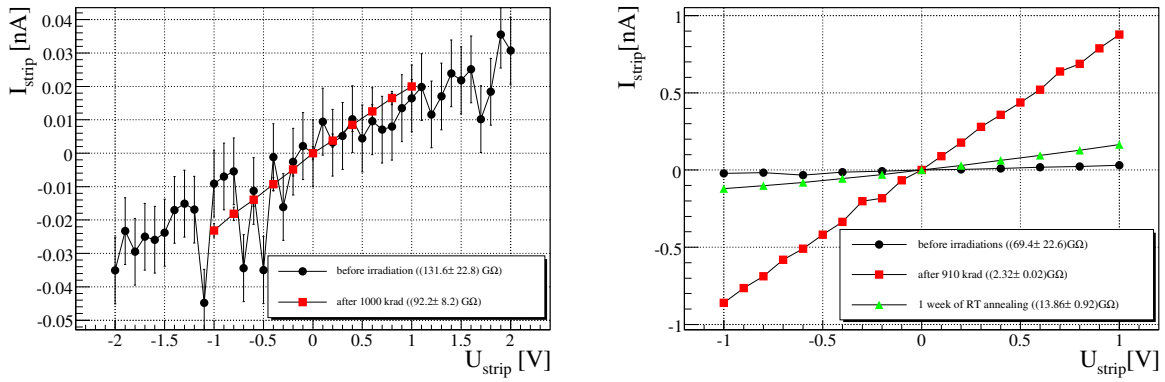

(a) moderated p-spray (b) homogeneous p-spray

Figure 3.16: Variation of the inter-strip current as a function of the applied inter-strip voltage before and after irradiation and after annealing.

both cases, signaling a saturation of the surface charges. This measurement proves that for both sensors a complete saturation of the surface charges was reached.

Direct measurements of the inter-strip resistance before and after the irradiation are presented in Fig. 3.16. For these a bias voltage of $-40\,\mathrm{V}$ was applied to the back-side, while the strip implants were fixed to ground potential via the punch-through structures. A varying voltage U_{strip} of $-1\,\mathrm{V} \leq U_{\mathrm{strip}} \leq +1\,\mathrm{V}$ was applied to the central strip of one of the triplets. From the current I_{strip} flowing between the central strip and the outer ones at ground, for a given U_{strip} the inter-strip resistance R_{int} can be calculated with Ohm's law

$$R_{\mathrm{int}} = \frac{2U_{\mathrm{strip}}}{I_{\mathrm{strip}}}. \tag{3.5}$$

The factor of 2 is introduced since two resistive isolations are measured in parallel. The current of the sensor with the moderated p-spray isolation (Fig. 3.16(a)) showed considerable fluctuations of unknown origin before the irradiation. Increasing the applied voltage U_{strip} up to $\pm 2\,\mathrm{V}$ led to a linear fit with reduced fluctuations. From the inverse value of the slope, an inter-strip resistance before irradiation of $(132 \pm 23)\,\mathrm{G\Omega}$ was calculated, which decreases after the introduction of surface charges to $(92 \pm 8)\,\mathrm{G\Omega}$, where the uncertainties are derived from the statistical uncertainty of the slope parameter. The currents measured between the strips with the homogeneous p-spray isolation (Fig. 3.16(b)) are in general higher corresponding to a resistance of $(69 \pm 23)\,\mathrm{G\Omega}$ before and $(2.3 \pm 0.1)\,\mathrm{G\Omega}$ after the X-ray irradiation. The third set of measurements was performed after 1 week of room temperature (RT) annealing, after which some of the introduced defects seemed to be cured since the resistance increased to $(13.9 \pm 1.0)\,\mathrm{G\Omega}$.

Naturally it is expected that the homogeneous p-spray implant leads to a smaller

resistance because the effective boron implant dose in the silicon is lower. Also the larger change in resistance before and after irradiation is expected since for the moderated p-spray option the isolation below the nitride opening is by far not compensated. The relative change in this region is much lower. For the homogeneous p-spray isolation in all areas of the isolation the p-implant is almost compensated leading to a stronger decrease in R_{int}. But even this very low dose isolation with a simulated area charge density of $7.4 \cdot 10^{11}\,/\text{cm}^2$ shows always resistances in the GΩ range, which should in any case ensure a good inter-pixel isolation. This seems to contradict the results of the simulation presented above, where a compensation of the p-spray implants by the positive surface charges was seen. However, not considered in the simulation was the possibility of electron trapping at the $\text{Si} - \text{SiO}_2$ interface of the sensor [122]. Depending on the bias voltage applied during the irradiation, this can lead to a permanent accumulation of negative interface charges which in turn compensate some of the usually positive surface charges. This is the case for n-in-p sensors with a negative voltage applied to the back-side and positive surface charges acting from the front side. Hence, the effective dose of $7.4 \cdot 10^{11}\,/\text{cm}^2$ can indeed provide a sufficient isolation before and during the irradiation. The results obtained from the simulation in any case give a conservative lower limit for the isolation potential.

3.3.4 Final choice of production parameters

For the main sensor production two sets of parameters for the p-spray implantation were planned to be implemented. To decide for these two sets the results from the simulation as well as the measurements on the irradiated strip sensors were taken into account. From Figs. 3.12(a) and 3.12(b) it is visible that the best isolation option for the moderated p-spray isolation, leading to the lowest electric field strength at a sufficient isolation potential, uses a boron implant energy of 110 keV with an area dose of $3.0 \cdot 10^{12}\,/\text{cm}^2$ (isolation 02 in Tab. 3.6). The measurements presented in the last section show that for the sensors with the homogeneous p-spray isolation an integrated boron dose of $0.74 \cdot 10^{12}\,/\text{cm}^2$ is sufficient to reach the desired inter-strip isolation. Hence, also for the sensors with a moderated p-spray implant, isolation 02 is a promising option. However, the final surface parameters of the wafers that were procured are slightly different with respect to those that were simulated. To adapt to the actual parameters, which cannot be disclosed within this work, the simulations for some of the parameters had to be repeated.

Since the isolation potential and the maximum electric field strength depends solely on the effective boron doping in the silicon, and for this the target values are elaborated with the TeSCA simulation, only the DIOS simulation had to be repeated. For isolation 02 in Tab. 3.6 the integrated doses are $0.84 \cdot 10^{12}\,/\text{cm}^2$ in the moderated area ("M") and $2.8 \cdot 10^{12}\,/\text{cm}^2$ below the nitride opening ("O"). To add a safety margin for the isolation potential, it was decided that the minimum effective dose should be $1 \cdot 10^{12}\,/\text{cm}^2$. Taking

Isolation	energy [keV]	dose [10^{12}/cm^2]	M [10^{12}/cm^2]	O [10^{12}/cm^2]
high	100	3.2	0.95	3.0
low	140	1.4	1.1	1.4

Table 3.8: Final isolation parameters. See Tab. 3.6 for the column definitions.

these considerations into account and adapting the simulation to the surface parameters of the actual production, a new set of boron implant parameters was derived with DIOS. Closely corresponding to isolation 02 a boron implant energy of 100 keV with an area dose of $3.2 \cdot 10^{12}$ /cm^2 leads to an effective doping concentration of $0.95 \cdot 10^{12}$ /cm^2 in the moderated area and $3.0 \cdot 10^{12}$ /cm^2 below the nitride opening.

The second set of parameters was chosen to be more aggressive. For this also the area below the nitride opening should have a lower effective doping concentration, while the moderated part should again be above $1 \cdot 10^{12}$ /cm^2. This was achieved with a lower implant area dose but higher energy. With 140 keV and $1.4 \cdot 10^{12}$ /cm^2 as implantation parameters the resulting doses are $1.1 \cdot 10^{12}$ /cm^2 in the moderated area and $1.4 \cdot 10^{12}$ /cm^2 below the nitride opening. These values should lead to a considerably lower electric field strength but, as the measurements showed, still reach a sufficient inter-strip and inter-pixel isolation. The final two sets of parameters from now on referred to as "high" and "low" are also summarized in Tab. 3.8.

3.4 Electrical characterization of thin sensors

With the p-spray implantation parameters finalized through the simulation and measurements, the main production of the twelve 6-inch sensor wafers was finished. It is resembling the first production containing n-in-p pixel sensors envisaged to be used in the upgrade of the ATLAS pixel detector. Furthermore, it represents the first production of thin pixel and strip sensors using the HLL process. Therefore, the performance of these sensors is of very high interest for future thin sensor productions beyond the research presented within this thesis. To evaluate the performance of the sensors, in a first step an electrical characterization of the implemented sensors was carried out. The eight n-in-p wafers (cf. Tab. 3.1), which have a homogeneous back-side implant contain the main sensors to be investigated and were characterized directly at wafer level. The sensors of the n-in-n wafers will be examined once the handling substrate is opened from the back-side.

The initial characterization that was carried out, consists of measuring the capacitance and the leakage current as a function of the applied voltage. These provide information about the general silicon properties which may deteriorate during the processing. In a second step, the current-voltage characteristics of all pixel sensors were

measured to determine the leakage currents per unit area I/A and the break-down voltages U_{bd}. On the basis of these measurements, four wafers containing those pixel sensors having the highest U_{bd} were selected to be used for the envisaged production of single chip pixel modules (see Sec. 4.4). The other four wafers were cut and used for further electrical characterizations of the contained devices.

The diodes under investigation employ different guard-ring structures, some of them with a much reduced number of guard-rings designed to investigate the possibility of increasing the active area of silicon sensors. A subset of the devices was irradiated with protons up to an equivalent integrated fluence of $10^{16}\,\mathrm{n_{eq}/cm^2}$, i.e. the one expected during the sLHC operation, and afterwards characterized again to determine their electric functionality.

Next to the sensors of the main production, also the epitaxial sensors were characterized. In these, junction break-downs were seen at relatively low voltages before irradiation. The cause for this problem could be understood by infrared emission analysis complemented with simulations.

3.4.1 Initial characterization

During the production of thin sensors, several processing steps could lead to the introduction of defects into the silicon bulk or its surfaces. These defects can be caused by the introduction of atoms other than silicon into the wafers, but also by mechanical damage during the wafer handling or the thinning process. They would lead to an increase of the sensor leakage current or an increased U_{fd}. Both should be as low as possible to ensure full functionality at low voltages and with low leakage currents.

Diodes

To characterize the global silicon bulk properties after all processing steps, diodes with an active area of $2.5 \times 2.5\mathrm{mm}^2$ are used to measure the leakage currents and the diode capacitances between the front- and back-side implants. From the change of the capacitance C with the applied bias voltage, U_{fd} can be measured. The squared inverse capacitance $1/C^2$ of these diodes with an active thickness of 75 μm and 150 μm is shown in Fig. 3.17(a). Since the depletion depth w (Eq. 2.3) up to $w = d$ depends on the square root of the applied voltage, and the capacity C for an ideal diode is inversely proportional to w, a linear behavior of $1/C^2$ for $U < U_{\mathrm{fd}}$ is expected. For $U > U_{\mathrm{fd}}$, i.e. in a fully depleted diode, the capacitance is expected to stay constant. Both behaviors are visible in Fig. 3.17(a) and the value of U_{fd} is approximated by the intersection of two linear fits: one for the linear slope and the other for the constant part of the diagram. From the full depletion voltage, the effective doping concentration N_{eff} of the bulk material is calculated (cf. Eq. 2.20). The low values obtained for U_{fd} and N_{eff} (Tab. 3.9) show that the sensors can be efficiently operated at low voltages. The uncertainties are

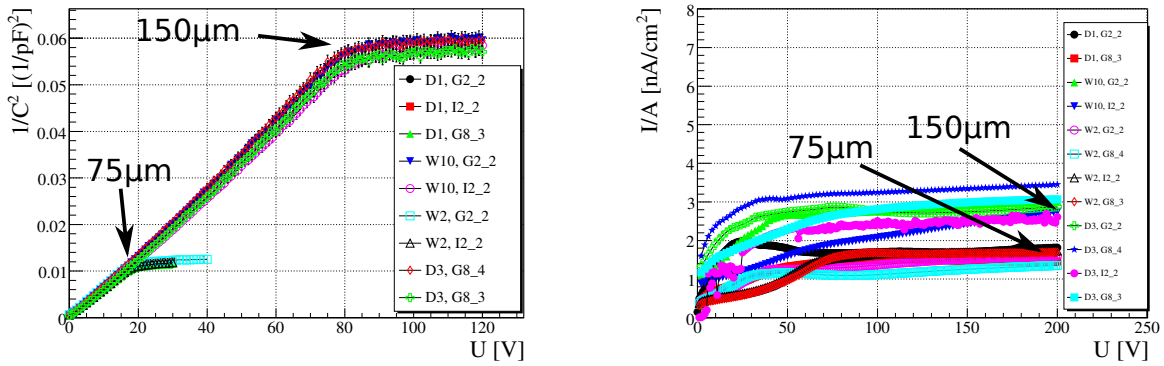

(a) (b)

Figure 3.17: Measurements of the inverse squared capacitance (a) and the leakage current of diodes (b) both as a function of the bias voltage. The position of the change from the linear increase of $1/C^2$ to the plateau marks U_{fd}.

thickness $d\,[\mu\text{m}]$	U_{fd} [V]	$N_{\text{eff}}\,[10^{12}/\text{cm}^3]$	$\rho\,[\text{k}\Omega\text{cm}]$
75	18 ± 5	4.2 ± 0.3	3.1 ± 0.2
150	82 ± 6	4.6 ± 0.1	2.8 ± 0.1

Table 3.9: Characteristics of n-in-p diodes. Listed are the measured full depletion voltage and the deduced effective doping concentration and resistivity.

calculated from the uncertainties of the fits and the variations for the different diodes measured. The quadratic dependence of U_{fd} on d is clearly visible and the specified minimum resistivity of $\rho \geq 2\,\text{k}\Omega$ is even surpassed by 50%.

Figure 3.17(b) shows the leakage currents normalized to area I/A up to 200V, i.e. far above the full depletion voltage. They are $(1.6 \pm 0.2)\text{nA/cm}^2$ for the 75 μm thick diodes and $(2.8 \pm 0.3)\text{nA/cm}^2$ for the 150 μm thick diodes, showing a roughly linear increase with the diode thickness. Together with the low U_{fd}, the low currents show that the thin sensor production was successful and the initially good silicon bulk parameters are preserved.

Pixel sensors

The most important structures of the thin sensor production for the construction of pixel modules, are naturally the ten pixel sensors of each wafer. Therefore, for all the 80 n-in-p pixel devices, the current-voltage characteristic was measured to evaluate I/A and U_{bd}. Figure 3.18 shows the leakage currents of the sensors grouped by the wafer number.

On each wafer, two pixel sensors have a moderated p-spray isolation (marked with ● and ■) while for the other a homogeneous p-spray implant between the pixel implants is used. A complete legend for the measurements of the different pixel structures in Fig. 3.18 can be found in 3.19. In general, I/A of the pixel sensors is higher than for the diodes. This is expected since the implant structures are much more complicated, leading to larger electric fields which generate leakage current. Still, all pixel devices with a homogeneous p-spray implant (P3-P10) and the pixel devices with the low dose moderated p-spray isolation (P1 and P2 of wafers D1, 4, D3, 11, 12) have currents in the plateau region mostly below $10\,\mathrm{nA/cm^2}$. The pixel devices with the high dose moderated p-spray implant show a faster increase in their leakage currents, reaching around $(10-12)\,\mathrm{nA/cm^2}$ at 100 V.

From a subset of sensors, U_{fd} was measured as described above to be $(30\pm5)\,\mathrm{V}$ and $(105\pm5)\,\mathrm{V}$ for the 75 μm and 150 μm thick sensors where the uncertainties are only statistical. The break-down voltages mostly range between 250 V and 750 V, showing that most of the structures can be operated well over-depleted. The devices with the high dose moderated p-spray implant, show an earlier break-down and higher I/A, but also these surpass their U_{fd}. Only pixel device P6 of wafer 12 (□ in Fig. 3.18(h)) with a homogeneous p-spray implant exhibits an unusual early break-down, and must be considered not functioning. The ratio $U_{\mathrm{bd}}/U_{\mathrm{fd}}$, relating the maximum operating voltage of the devices to the full depletion voltage ranges from 3.7 ± 1.0 for wafer 4 and 15 ± 2 for wafer 2. Since the absolute break-down voltage of thin and thick sensors in general is similar before irradiation, the thin sensors can be operated in stronger over-depletion.

The device yield of $79/80\approx98.8\%$ and the low leakage currents show that this production run of thin pixel sensors was very successful. The simulated implant parameters seem to be a safe choice since most of the pixel devices show a very good break-down performance ($U_{\mathrm{bd}}\gg U_{\mathrm{fd}}$). This gives the first proof of principle that the HLL thinning process can be used to produce thin pixel sensors without deteriorating the sensor properties. From the eight n-in-p wafers, two 75 μm and two 150 μm thick wafers (1, 4, D3, 11 - all marked in red in Fig. 3.18) were chosen to supply the pixel sensors for the single chip demonstrator pixel modules. Consequently, none of the devices of these wafers can be used for further testing since the sensors cannot be singularized before the end of the module production. The structures of the remaining four wafers are used for all further measurements.

Strip sensors

The strip sensors are used for the majority of the thin sensor tests. They were characterized at wafer level and after the singularization, not showing any degradation due to this step. A subset of the measurements is shown in Fig. 3.20, containing data from wafer 2, having an active thickness of 75 μm and comprising the high dose p-spray option, and wafer 12 which has an active thickness of 150 μm and uses the low p-spray option. In

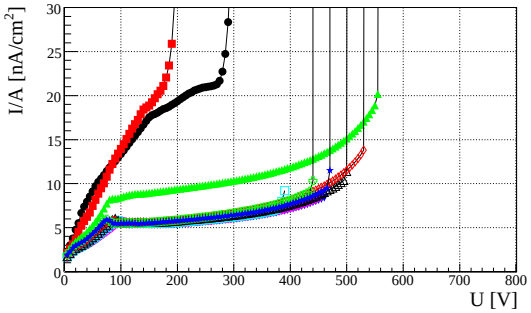

(a) Wafer 1, $d = 75\,\mu$m, high p-spray

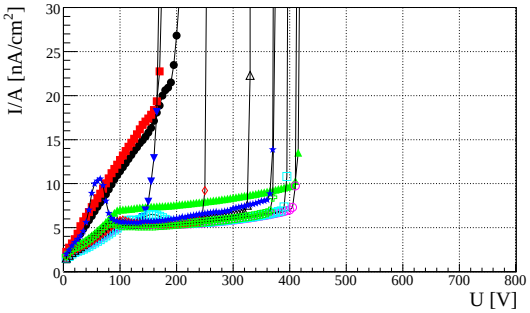

(b) Wafer 2, $d = 75\,\mu$m, high p-spray

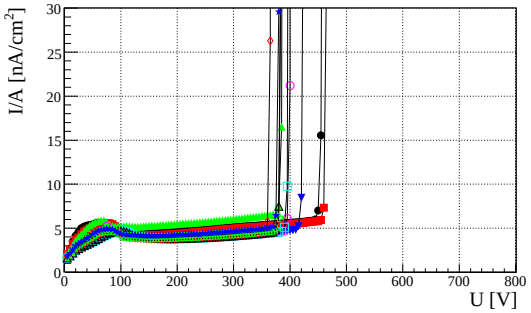

(c) Wafer D1, $d = 75\,\mu$m, low p-spray

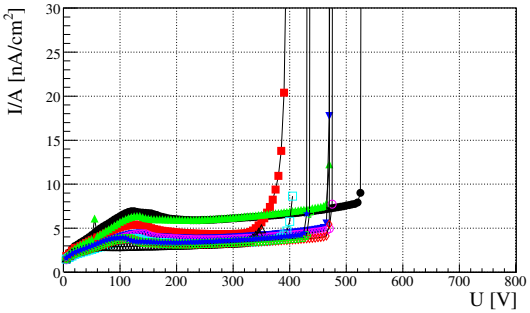

(d) Wafer 4, $d = 75\,\mu$m, low p-spray

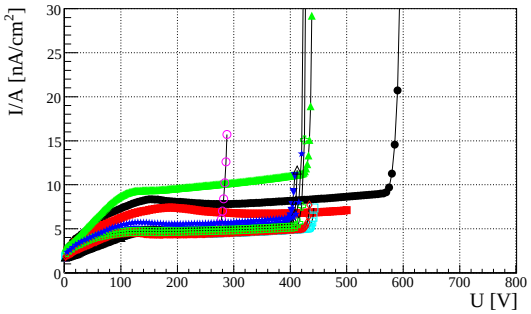

(e) Wafer D3, $d = 150\,\mu$m, low p-spray

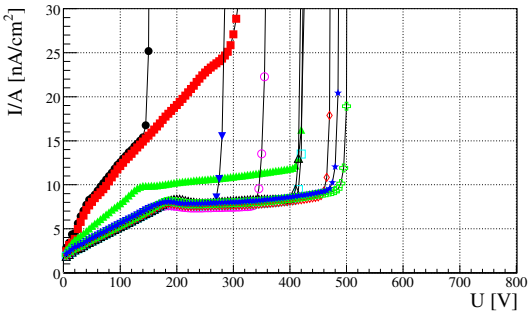

(f) Wafer 10, $d = 150\,\mu$m, high p-spray

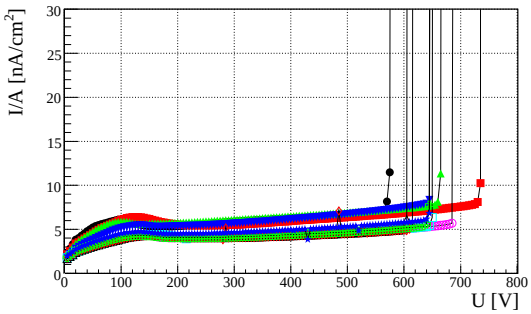

(g) Wafer 11, $d = 150\,\mu$m, low p-spray

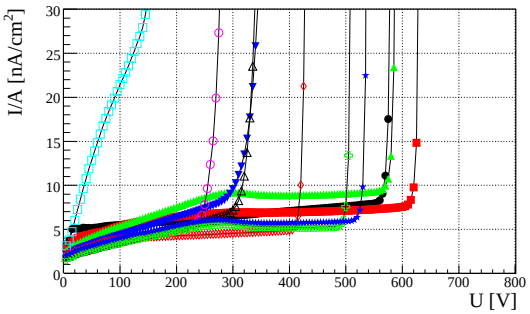

(h) Wafer 12, $d = 150\,\mu$m, low p-spray

Figure 3.18: I/A-U characteristics of all pixel sensors ($A = 0.87\,\text{cm}^2$). The legend of the wafers is given in Fig. 3.19. Apart from pixel sensors P6 from wafer 12, all sensors can be fully depleted.

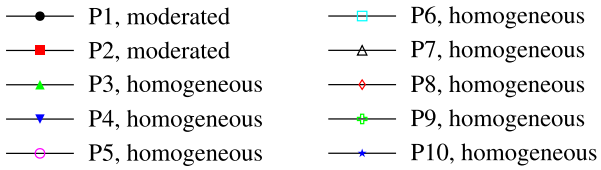

Figure 3.19: Legend for Fig. 3.18, denoting the pixel sensor number and the p-spray isolation geometry.

terms of leakage current and break-down voltage these represent the two most different strip sensors measured. In both cases, current characteristics of strip sensors with a pitch of 50 μm and 80 μm, and homogeneous as well as moderated p-spray options are presented.

The leakage currents per area of the strip sensors are comparable to those of the pixel sensors and mostly less than 10 nA/cm^2. Similar to the measurements shown above, the sensors with the moderated high dose p-spray show higher leakage currents and a lower U_{bd}. The break-down voltages of all strip sensors is in the approximate range of 100 V to 450 V. Here the sensors with the 50 μm pitch (Figs. 3.20(a) and 3.20(c)) show a higher U_{bd} than the sensors with 80 μm pitch (Figs. 3.20(b) and 3.20(d)). Even though U_{bd} is in most cases lower than for the pixel sensors, all of them can be fully depleted. Due to their p-spray isolation, the sensors are expected to show an increased U_{bd} after particle irradiation.

Infrared emission analysis

In view of possible sensor optimizations of future thin sensor productions, it is very important to understand where the weakest point, i.e. the location of the junction break-down, of the sensors is. This can be achieved with an emission microscope setup which was used to accurately pin-point regions of high electric currents in the sensors.

The Hamamatsu [123] PHEMOS-1000 emission microscope is a wafer probe-station in a dark-box equipped with an infrared-sensitive CCD camera (Fig. 3.21). It is used to locate failures in semiconductor devices which lead to increased leakage currents. For this the device under test (DUT) is placed on a chuck where it can be visually inspected with a microscope providing an optical magnification factor of up to 100. Of a selected area two pictures are taken with a very low-noise CCD camera, cooled to -50°C with a Peltier cooling element. The first image is a regular photograph of the area of the DUT which is illuminated by the light source of the microscope. A second image is taken of the same area but without the external light source. The DUT is operated slightly above its maximum operation voltage, i.e. when the junction break-down starts to develop and large leakage currents flow through the device. This leads to the emission of infrared

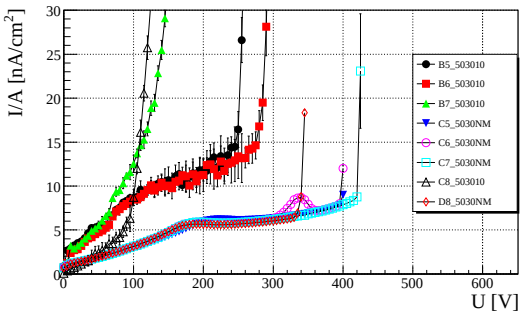

(a) Wafer 2, 50 μm pitch

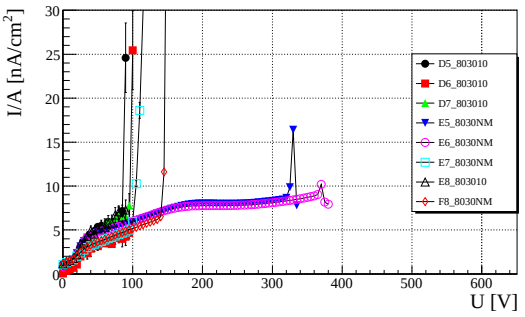

(b) Wafer 2, 80 μm pitch

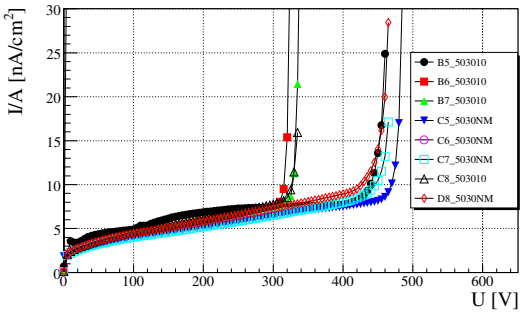

(c) Wafer 12, 50 μm pitch

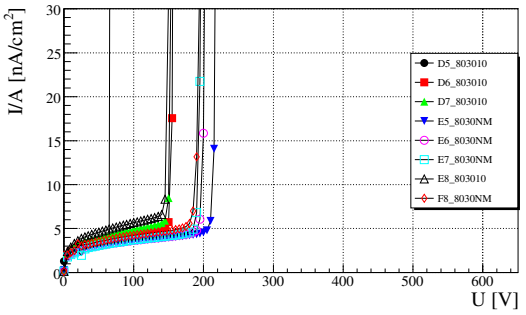

(d) Wafer 12, 80 μm pitch

Figure 3.20: I/A-U characteristics of a subset of strip sensors. The area of the sensors with 50 μm pitch is 0.63 cm^2, for the 80 μm pitch sensors it is 0.75 cm^2.

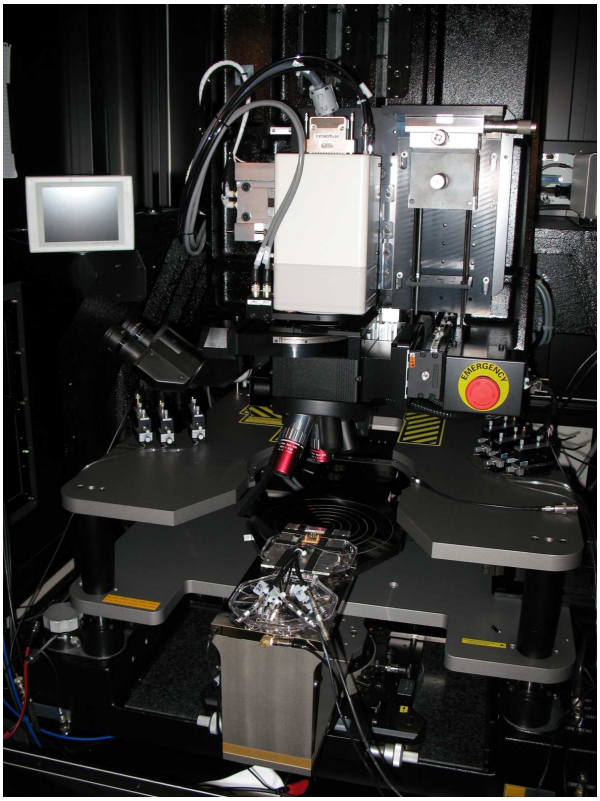

Figure 3.21: The PHEMOS-1000 emission microscope.

light which is collected by the CCD. The emission is mainly caused by the large amounts of flowing charge carriers in regions with junction break-downs in the devices. These charge carriers emit photons from bremsstrahlung or recombination with charge carriers of the opposite charge. The optical and infrared images are overlayed to locate the position and intensity of the light-emittance within the DUT.

A set of images of strip and pixel sensors was taken with the PHEMOS setup to locate the point of the junction break-down. Figures 3.22(a) to 3.22(d) show four images from strip and pixel sensors. They reveal the two main locations in which the junction break-downs occur in almost all of the investigated devices. Figure 3.22(a) depicts a complete strip sensor with vertically oriented strips with a pitch of 50 μm. Clearly visible are a large number of hot spots, i.e. light emitting regions, along a row in the upper part of the image and a single large hot spot at the lower left side. While the upper spots are contained within the punch-through biasing structures, the single hot spot in the lower region is located in the guard-ring structure. Figure 3.22(b) presents a close-up view of the punch-through region of a strip sensor with a pitch of 80 μm. Again in this sensor, a number of hot spots point to large leakage currents within the punch-through

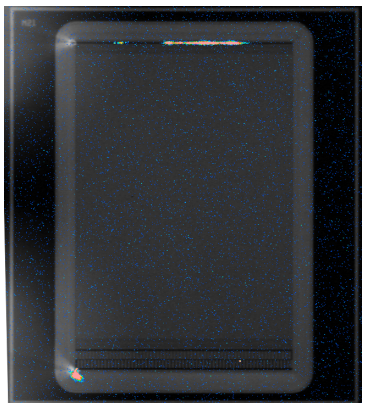

(a) A full strip sensor with $s = 50\,\mu$m

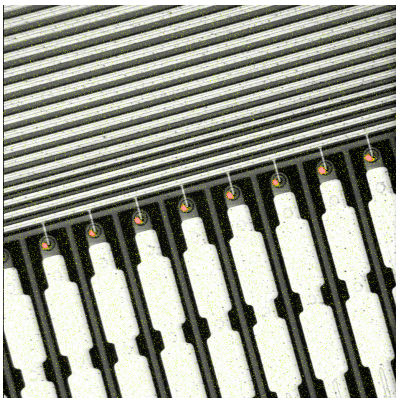

(b) Punch-through region of a strip sensor with $s = 80\,\mu$m.

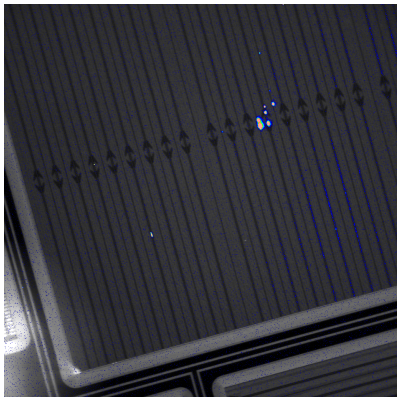

(c) Punch-through region of a pixel sensor.

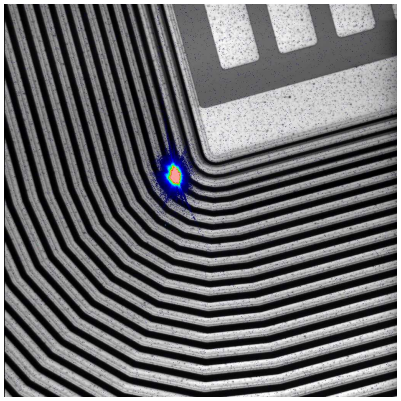

(d) Lower left corner of the guard-ring structure.

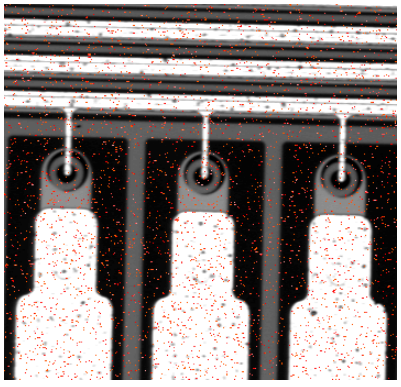

(e) Possible misalignment.

Figure 3.22: PHEMOS images of strip and pixel sensors. In both devices the breakdown could be confined to two positions: the punch-through structures and the lower left corner of the guard-rings.

structures. A similar image from identical punch-through structures of a pixel sensor is shown in Fig. 3.22(c). Even though, not easily spotted, many of the biasing structures emit light, again pointing to a junction break-down. Figure 3.22(d) shows the lower left side of the guard-ring structure of a strip sensor. At exactly the same position as for the sensor in Fig. 3.22(a), i.e. between the third and the fourth guard-ring, a large hot spot is seen.

Even though the location of the observed break-downs could be pin-pointed to two critical areas of the strip and pixel sensors, the cause for these remains subject to speculations. The most likely explanation however, seems to be a small misalignment of the different lithographic masks during the production. Figure 3.22(e) gives a close-up view of three punch-trough structures. Comparing this image to the schematics presented in Fig. 3.4, reveals that the ring shaped p-spray implant seems to be not centered with respect to the circular opening in the nitride and the tip of the aluminum line. Such a constellation is only possible, if the n-type implant is shifted with respect to the rest of the layers. This in turn can lead to a deformation of the p-spray implantation since it might be partially covered by the nitride layer, leading to a local reduction of the implant dose. A reduced implant dose could lead to a direct conduction channel through the p-spray and hence cause an early junction break-down. Assuming this shift of the n-type implant layer could also explain the second hot spot in the area of the guard-rings. It is always found between the same two guard-rings and always in the lower left corner. From the images in Fig. 3.22(b) and 3.22(e) also the lower left side of the punch-through structure seems to be the origin of the junction break-down. So, a likely explanation is that the n-type implant layer is slightly misaligned towards the lower left side leading to unfavorable doping geometries.

3.4.2 Slim guard-ring studies

In Sec. 1.3.1 it was motivated that for the upgrade of the ATLAS pixel modules a larger live-fraction is targeted. Especially for the innermost layers, space is scarce and the modules need to efficiently use as much as possible of this. For the insertion of the new b-layer, it is already decided that shingling of the pixel modules along the direction of the beam pipe is not allowed. Very likely, this will also apply to the innermost layer of the new ATLAS pixel detector that will be operated at the sLHC. To still reach an acceptable coverage along this direction, the inactive area at the edges of the sensors has to be minimized. The present target value for the IBL upgrade is to achieve an inactive area fraction of less than 2.5% corresponding to $(450 - 500)\,\mu$m of inactive edge. This is a reduction by a factor of 2 compared to the present ATLAS pixel sensors.

There are two handles that can be utilized to reduce the inactive edge and arrive at slimmer edges. The first is reducing the width of the guard-ring structures, while the second is moving the cutting line of the sensors closer to the outermost guard-ring. Within the presented main thin sensor production, diodes were implemented

that followed the first of the two approaches. The second approach of cutting the sensors closer to the outermost guard-ring and thereby reducing the safety margin is followed up within the ATLAS Planar Pixel Sensor collaboration [124], and results on first successful trials are summarized for example in [125]. For the future a combination of both approaches will likely be the most promising solution.

The diodes to investigate the slim guard-ring structures have an active area of $2.5 \times 2.5\,\mathrm{mm}^2$, active thicknesses of $75\,\mu\mathrm{m}$ and $150\,\mu\mathrm{m}$, and use the low and the high p-spray implantation doses. The guard-rings of these diodes differ by their general design concerning the width and distances of the individual rings as well as the width of the metalization above each ring. There are three options (HOM I, HOM II, and HOM III) which have a homogeneous p-spray isolation between the n-type implants of the guards rings, and one option (MOD) which has moderated p-spray implants. Each of the above-mentioned designs exists as a 21 and 10 guard-ring option. The 21 guard-ring option, exemplary shown in Fig. 3.23(a), has a total width of $610\,\mu\mathrm{m}$ and represents the standard guard-ring design of the strip and pixel sensors for this production. Together with the safety margin of $300\,\mu\mathrm{m}$ to the cutting edge of the sensors, the total inactive edge from the outermost part of the active area is $910\,\mu\mathrm{m}$. This is already a little less than the total inactive edge of the present ATLAS pixel sensors, spanning over $995\,\mu\mathrm{m}$ and containing 16 guard-rings. The second option of each diode has an identical design for the innermost 10 guard-rings, but the outer 11 are not implemented at all (Fig. 3.23(b)). The width of this reduced guard-ring structure is only $220\,\mu\mathrm{m}$ and hence presents a possible reduction of $390\,\mu\mathrm{m}$. Even though the width of the guard-ring structures is different, the total inactive edge of $910\,\mu\mathrm{m}$ is the same for both types of diodes. Diodes with a reduced guard-ring structure and a lower safety margin to the cutting line are already implemented in a next production currently ongoing.

To evaluate the functioning of the different guard-ring designs, the current-voltage characteristic was measured for all diodes of different thicknesses and p-spray implant options. Table 3.10 summarizes the measurements, giving the relative change of U_{bd} due to the reduction of the guard-ring structure, and in parentheses the ratio of minimum break-down voltage $U_{\mathrm{bd,min}}$ of the 21 and 10 guard-ring diode and U_{fd}. In the case of a clear junction break-down, U_{bd} was defined as the intersection of two linear fits in the plateau and the break-down region and could be measured to an accuracy of 10 V. For soft break-downs, where these two regions were not distinguishable, U_{bd} was defined with a single linear fit spanning over ten consecutive measurements (50 V). The fit window was shifted from low to high voltages, and once the fit had an inclination of $0.01\,\mathrm{nA/V}$ the lowest voltage of the fit-window was defined to be U_{bd} with a measurement accuracy of 20 V. Comparisons where one of the diodes surpassed the maximum measurable U_{bd} of 1000 V are indicated by upper or lower limits in Tab. 3.10. Negative values indicate a higher U_{bd} for the diode with the 10 guard-ring option.

In general all diodes with the reduced guard-ring structure still had a very high U_{bd}, i.e. could be well over-depleted, and showed similar leakage currents as the ones with the

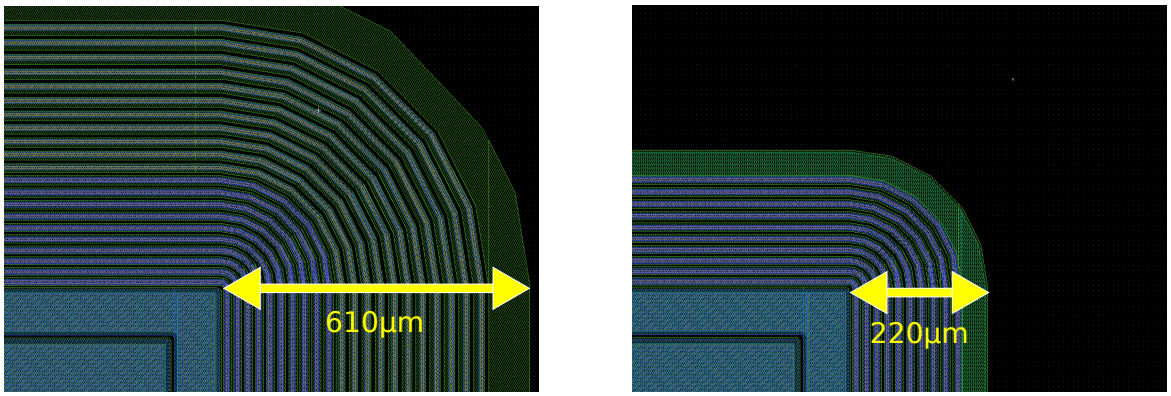

(a) 21 guard-rings (b) 10 guard-rings

Figure 3.23: Comparison of standard and reduced guard-ring designs. In both cases the distance from the active area to the cutting line is 910 μm.

	ΔU_{bd} [%] ($U_{\mathrm{bd,min}}/U_{\mathrm{fd}}$)			
	high p-spray dose		low p-spray dose	
isolation	75 μm	150 μm	75 μm	150 μm
HOM I	13 ± 3 (40 ± 11)	< -12 (11 ± 1)	1 ± 3 (52 ± 14)	< -18 (10 ± 1)
HOM II	37 ± 2 (28 ± 8)	> 36 (8 ± 1)	1 ± 3 (51 ± 14)	> 20 (10 ± 1)
HOM III	-4 ± 4 (22 ± 6)	-1 ± 4 (5 ± 1)	-3 ± 4 (20 ± 6)	0 ± 3 (6 ± 1)
MOD	78 ± 2 (6 ± 2)	30 ± 5 (3 ± 1)	15 ± 2 (28 ± 8)	-4 ± 3 (7 ± 1)

Table 3.10: Change of U_{bd} for a reduction of the guard ring size for different thicknesses, p-spray options, and guard ring designs.

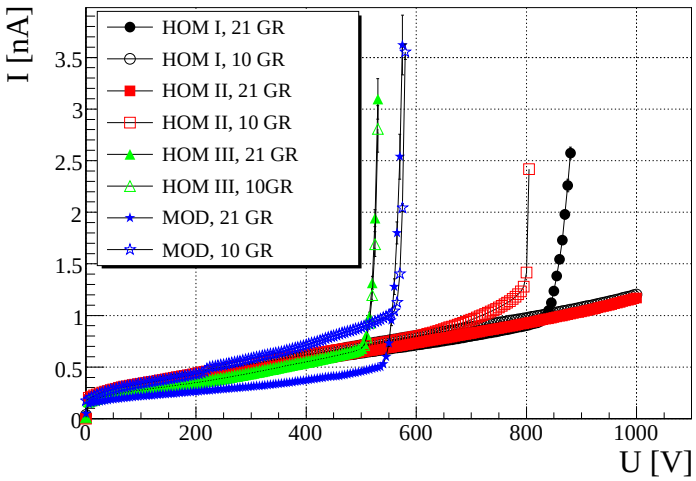

Figure 3.24: Current-voltage characteristics of diodes of Wafer 12 with standard and slim guard-ring designs.

full guard-ring structure. The changes in U_{bd} were smallest for the design option HOM III, and the highest over-depletion was reached with the options HOM I and HOM II for the diodes with an active thickness of 75 μm. Comparing the high- and low dose p-spray implants, the decrease of U_{bd} was most significant for the sooner, especially for the moderated guard-ring design MOD with $\Delta U_{\mathrm{bd}} = 78\%$. These results show, like for the characterization of the pixel sensors, that the homogeneous p-spray design with the low implant parameters lead to the most preferable properties for the 75 μm and 150 μm sensors. Therefore, this option will be primarily used for the follow-up production of thin pixel sensors.

Figure 3.24 exemplary shows the results of diodes from wafer 12, having an active thickness of 150 μm and the low p-spray implantation dose (rightmost column in Tab. 3.10). In this particular case, the guard-ring options HOM I and HOM II yield the highest U_{bd} but larger differences between the 21 and 10 guard-ring diodes. Similar to the diodes with the high p-spray implant dose, U_{bd} even increases for HOM I in the 10 guard-ring version, indicating that the break-down for the 21 guard-ring design likely occurs in the outer guard-rings. The options HOM III and MOD perform almost identically for the 21 and 10 guard-ring options.

Summarizing the results, a reduction of the guard-rings by almost 400 μm does not decrease U_{bd} to values close to U_{fd}, or increase the leakage currents. Especially for the diodes with the low p-spray option and the HOM III guard-ring design, which is planned to be implemented in the next thin sensor production, the differences between the 21 and 10 guard-ring versions are very small and allow for high U_{bd}. Together with the results on reducing the safety margin performed by other groups [125], it should be

possible to reduce the total inactive edge around the pixel sensor to less than 500 μm, reaching the design value for the upcoming pixel detector upgrade.

3.4.3 Characteristics of irradiated thin sensors

One of the main goals of the presented research on thin sensors, is to evaluate their performance after irradiation with large particle fluences. For prototyping purposes this irradiation can be supplied by nuclear reactors or particle accelerators. The different irradiations, carried out within this project, were performed at the Karlsruhe Irradiation Center [121] with the proton cyclotron operated by the ZAG Zyklotron AG [126]. A set of diodes, strip-, and pixel sensors was irradiated with protons having a kinetic energy of 25 MeV with a hardness factor of $\kappa = 1.85$ (cf. Sec. 2.2.3). Two irradiation runs were performed: the first up to an integrated fluence of $\Phi_{\mathrm{eq}} = 10^{15}\,\mathrm{n_{eq}/cm^2}$, contained diodes, strip-, and pixel sensors; the second with fluences of up to $\Phi_{\mathrm{eq}} = 10^{16}\,\mathrm{n_{eq}/cm^2}$ only contained strip sensors. The strong focus on strip sensors for the second irradiation, receiving the integrated fluence expected at the sLHC, is motivated by the fact that only a limited amount of sensors could be irradiated, and that the strip sensors present the most interesting devices since they can be more easily used for CCE measurements as presented below.

The first irradiation run was divided into three fluence groups of $10^{14}\,\mathrm{n_{eq}/cm^2}$, $5 \cdot 10^{14}\,\mathrm{n_{eq}/cm^2}$, and $10^{15}\,\mathrm{n_{eq}/cm^2}$ to study the procedural change of the sensor performance. The two groups with lower fluences contained only diodes and pixel sensors, while the group with the highest fluence also contained a large number of strip sensors for CCE measurements. Figure 3.25 gives a representative overview of the electrical characterization of the devices after these irradiations. As expected from preceding investigations, the currents of the sensors (Figs. 3.25(a) and 3.25(b)) linearly increase with the received dose. At the same time, already anticipated from the simulations, U_{bd} increases due to the accumulation of positive surface charges, and values up to 800 V are observed. The electric field after irradiation is larger in the thinner option, leading to values of U_{bd} that are about $(100 - 200)$ V lower than for the thicker sensors. Furthermore, in both cases with increasing fluences the break-down becomes less abrupt and occurs as a so called soft break-down.

Figure 3.25(c) depicts the full depletion voltage of diodes as a function of the received fluence before and after controlled beneficial annealing. Starting from the values before irradiation, U_{fd} reaches around 100 V and 360 V for the diodes with active thicknesses of 75 μm and 150 μm after an integrated fluence of $10^{15}\,\mathrm{n_{eq}/cm^2}$. Hence, also after the irradiation, U_{fd} is much smaller than U_{bd}. Even taking into account the slightly larger U_{fd} of the more complicated strip- and pixel sensors, it is clear that after $\Phi_{\mathrm{eq}} = 10^{15}\,\mathrm{n_{eq}/cm^2}$, the devices can still be fully depleted. In addition, U_{fd} can be lowered by a controlled beneficial annealing as described in Sec. 2.2.4. For this, the diodes were heated to a temperature of 60°C for 80 minutes, being the well established parameters that lead

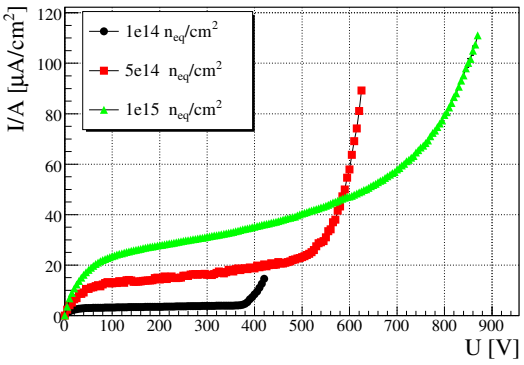

(a) Pixel sensors, $d = 75\,\mu$m

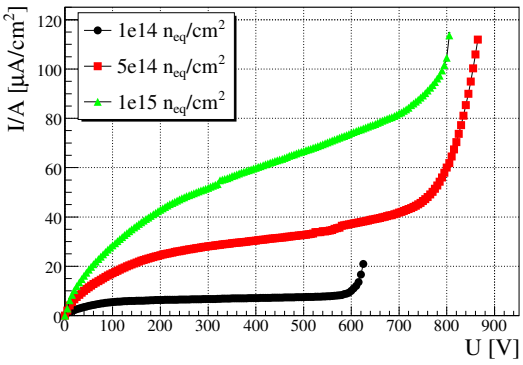

(b) Pixel sensors, $d = 150\,\mu$m

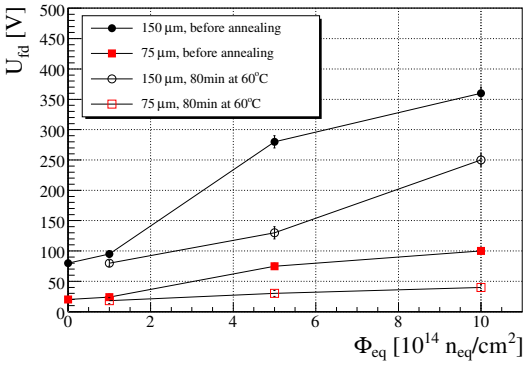

(c) U_{fd} of diodes

Figure 3.25: Current voltage characteristics of pixel sensors at a temperature of $-10°$C are shown in (a) and (b). The full depletion voltages as a function of the received integrated fluence are shown for diodes in (c). The capacitance, used to determine the full depletion voltage, was measured at 5 kHz and at a temperature of 0°C.

to the highest benefit from the annealing [77]. The graphs with the empty markers in Fig. 3.25(c) show that indeed the full depletion voltage can be reduced by around 60 V and 110 V for the sensors with active thicknesses of 75 μm and 150 μm, respectively.

The second irradiation run contained 16 strip sensors with 80 μm pitch. Eight of these were irradiated to $3 \cdot 10^{15}\,\mathrm{n_{eq}/cm^2}$, while the other eight received an integrated fluence of $10^{16}\,\mathrm{n_{eq}/cm^2}$, i.e. the value expected to be reached in the innermost pixel layer at the sLHC. These sensors will primarily be used for CCE measurements, but were also electrically characterized before, to assert their functioning after the irradiation. Figures 3.26(a) to 3.26(d) show the leakage currents of the irradiated devices. The graphs with the open markers represent the leakage currents of some of the sensors after the beneficial annealing. As expected, the current levels strongly increase after the received fluences. The sensors irradiated to $3 \cdot 10^{15}\,\mathrm{n_{eq}/cm^2}$ were measurable up to high voltages, showing that U_{bd} for these exceeds 800V. Higher voltages were not tried, since at these high current levels and voltages a junction break-down could lead to irreversible damage of the sensors and the setup. The leakage current reaches on average around $0.14\,\mathrm{mA/cm^2}$ for the 75 μm and $0.19\,\mathrm{mA/cm^2}$ for the 150 μm thick sensors at 500 V. For the sensors irradiated to $10^{16}\,\mathrm{n_{eq}/cm^2}$ the current increases by more than a factor of 10^4, compared to the not irradiated sensors (Fig. 3.20), reaching the current limit of 0.5 mA ($0.67\,\mathrm{mA/cm^2}$) of the measurement setup at around $(300 - 600)$ V.

After annealing, the sensor with an active thickness of 150 μm irradiated to $3 \cdot 10^{15}\,\mathrm{n_{eq}/cm^2}$ shows a decrease of the leakage current by a factor of about two. Similarly, the annealed sensor with an active thickness of 75 μm irradiated to $10^{16}\,\mathrm{n_{eq}/cm^2}$ has around 30% lower leakage current. The sensor with the higher active thickness irradiated to the sLHC fluence does not show an improvement after the annealing but rather a slight increase of the leakage currents. This is unexpected but could be caused by a mechanical damage during the handling or a permanent damage due to the high leakage currents during the measurements.

Figure 3.26(e) shows the full depletion voltage of the irradiated strip sensors before and after the annealing. Only for the sensors with an active thickness of 75 μm irradiated to $3 \cdot 10^{15}\,\mathrm{n_{eq}/cm^2}$, an annealing was not performed since all of these sensors will first be used for CCE measurements. From $\Phi_{\mathrm{eq}} = 3 \cdot 10^{15}\,\mathrm{n_{eq}/cm^2}$ to $\Phi_{\mathrm{eq}} = 10^{16}\,\mathrm{n_{eq}/cm^2}$, U_{fd} increases from 480 V to 520 V for the sensors with an active thickness of 150 μm. Even though being much higher than before irradiation, especially the value at the higher fluence turned out to be surprisingly low. After the annealing these values decrease to 350 V and 480 V, respectively, showing just a minor improvement for the latter of the two. The sensors with an active thickness of 75 μm yield $U_{\mathrm{fd}} = 250$ V after $\Phi_{\mathrm{eq}} = 3 \cdot 10^{15}\,\mathrm{n_{eq}/cm^2}$ and $U_{\mathrm{fd}} = 420$ V after $\Phi_{\mathrm{eq}} = 10^{16}\,\mathrm{n_{eq}/cm^2}$. After the annealing of the sensor irradiated to the higher fluence, U_{fd} decreases to 300 V.

The interpretation of these results is difficult since the measurements of U_{fd} of the irradiated patterned strip sensors involves larger uncertainties than measurements performed on unstructured diodes. Furthermore, after the irradiation, low temperatures of

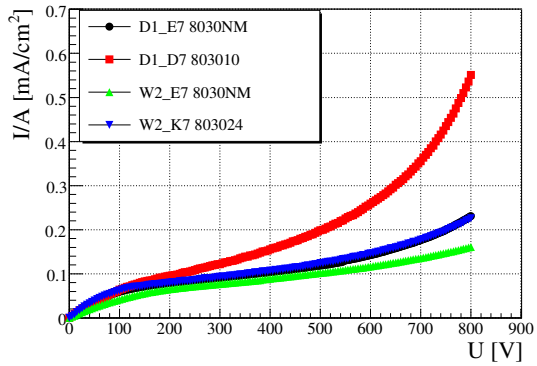

(a) Strip sensors, 75 μm, $3 \cdot 10^{15}$ n_{eq}/cm^2

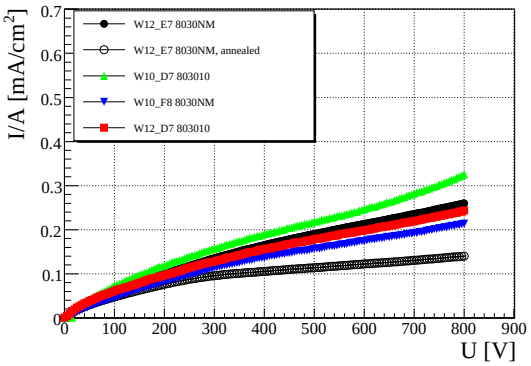

(b) Strip sensors, 150 μm, $3 \cdot 10^{15}$ n_{eq}/cm^2

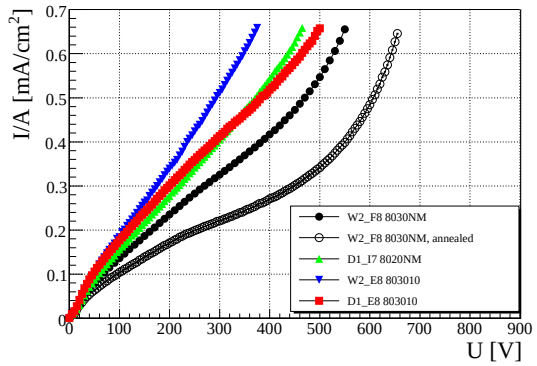

(c) Strip sensors, 75 μm, 10^{16} n_{eq}/cm^2

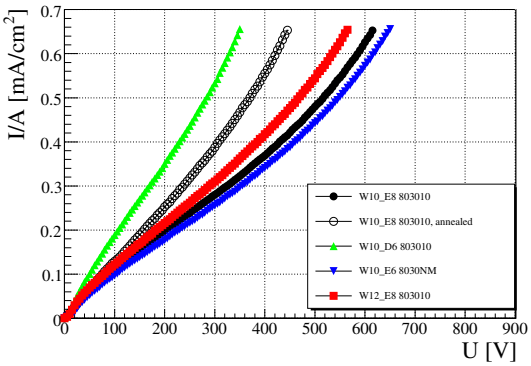

(d) Strip sensors, 150 μm, 10^{16} n_{eq}/cm^2

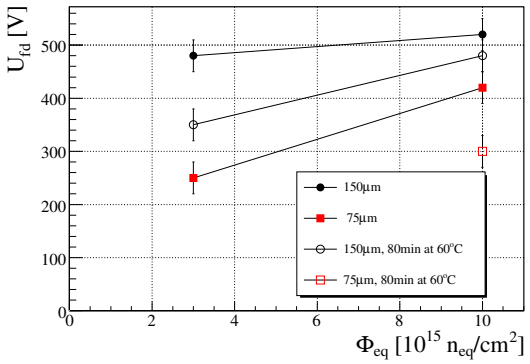

(e) U_{fd} of diodes

Figure 3.26: Current voltage characteristics of strip sensors at a temperature of $-10°C$ are shown in (a) to (d). The full depletion voltages as a function of the received integrated fluence are shown in (e). They were measured from the $1/C^2$ vs. U characteristics at a frequency 3 kHz and a temperature of $-10°C$.

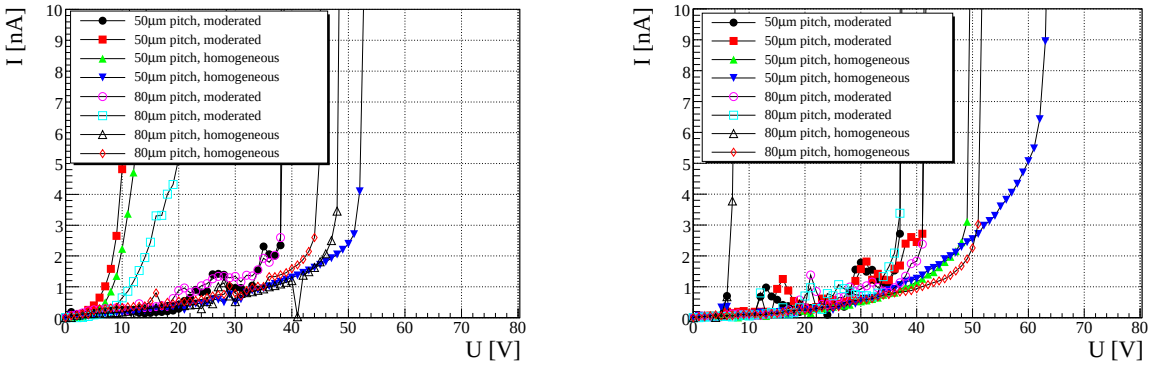

(a) Epitaxial strip sensors, $d = 50\,\mu$m (b) Epitaxial strip sensors, $d = 75\,\mu$m

Figure 3.27: Leakage current characteristics of epitaxial strip sensors with different thicknesses and pitches.

-10°C are needed to reduce the leakage current. At this temperature the capacitance should be measured with a frequency of 450 Hz [127]. However, the measurement setup did not allow to decrease the frequency below 3 kHz, introducing an additional, but hard to estimate, uncertainty.

Obviously, the full depletion voltage does not scale with the square of the thickness and the annealing does not show significant improvement for the 150 μm sensor after the sLHC irradiation. The small beneficial effect of the annealing could again be explained by a damage during the handling or from the large leakage currents during the measurements. The dependence of U_{fd} on the sensor thickness, not being quadratic anymore, can be related to the change of the electric field configuration after the irradiation. The electric field values are believed to be much higher close to the pn-junction in thin sensors. Consequently, the potential drop occurs mainly in this region, leading to low potential differences further away from the junction.

Apart from these measurements, it is more important to directly measure the charge collection efficiency, since the depletion depth does not give a reliable estimate for this after high irradiation doses.

3.4.4 Epitaxial sensors

Also the epitaxial sensors were electrically characterized after their production. The current voltage characteristics of representative subsets of sensors with active thicknesses of 50 μm and 75 μm are shown in Figs. 3.27(a) and 3.27(b). Both sets include strip sensors with 50 μm and 80 μm pitch and moderated as well as homogeneous p-spray implants. While the leakage currents of these sensors are in general very low with less than 4 nA/cm^2, they showed a very unstable high-voltage behavior contrary to the

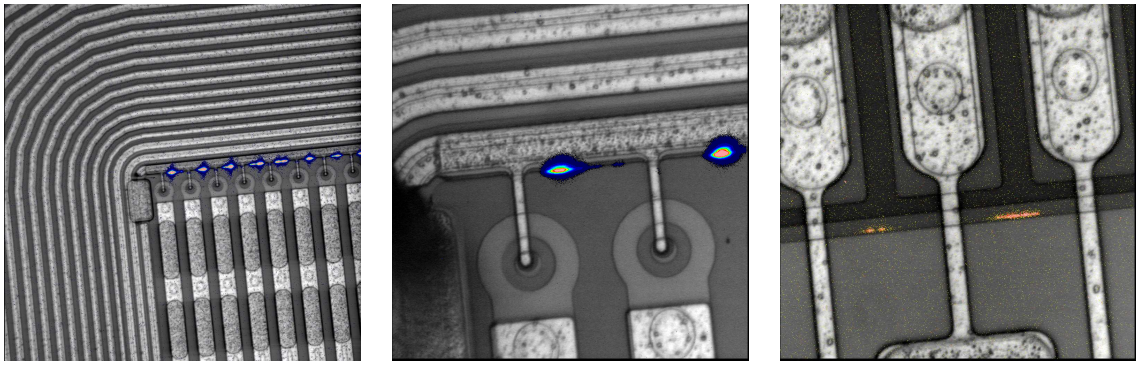

(a) $M = 20$ (b) As (a) but at $M = 100$ (c) $M = 100$

Figure 3.28: Infrared emission pictures of two sensors at different magnifications M.

sensors from the main production. In most cases U_{bd} is around 40 V to 50 V and hence lower than U_{fd} of 170 V for the 50 μm thick sensors and 190 V for the 75 μm thick sensors. Compared to the main thin sensor production U_{fd} of these sensors is much higher, since they were produced on wafers with a low resistivity of 150 Ωcm for the thinner and 300 Ωcm for the thicker of the epitaxial wafers.

To locate the cause for the early break down, the PHEMOS 1000 emission microscope was again used. A variety of strip sensors were examined with respect to their light emission in the break-down regime. Figure 3.28(a) depicts a part of a strip sensor with a pitch of 50 μm and a homogeneous p-spray implant. Clearly visible are the hot spots in the vicinity of the punch-through structures. The same area with a higher magnification (Fig. 3.28(b)), reveals that for these sensors the break-down does not occur in the punch-through structures but rather in-between them, close to the bias ring implant which is kept at ground potential. The same hot spots were also seen at the opposing side of the strip implants, where no punch-through structures are present (Fig. 3.28(c) using a moderated p-spray implant). This break down behavior was found on many of the strip sensors pointing to a general problem in the epitaxial sensor production.

The design of the epitaxial strip sensors within the area showing the hot spots, is identical to the one used in the main production, not revealing a break-down at this position. Therefore, a correlation to the difference in the sensor material is suspected. This difference is mainly manifested in the different effective doping concentrations in the sensor. While the wafers of the main production have a resistivity of about 3 kΩcm the epitaxial sensors of 50 μm thickness have only a resistivity of 150 Ωcm, due to the epitaxial production process. This corresponds to an increase in the effective doping concentration of a factor of 20 for the epitaxial sensors. Such high differences in doping concentrations lead to a considerable change of the potential distribution and the electric field within the sensor during operation. To have a qualitative confirmation that the

change of the potential distribution can lead to an early junction break-down at this position, further simulations with DIOS and TeSCA were carried out. A simulation of the exact region of the break-down was not possible with the 2D simulation, so that a simulation of a standard strip sensor with a pitch of 50 μm was carried out to extract a qualitative description of the problem.

Figures 3.29(a) and 3.29(b) show the hole concentration in a 50 μm thick n-in-p strip or pixel sensor at a bias voltage of 20 V for a high resistivity sensor material with 2 kΩcm and a low resistivity material with 150 Ωcm. Due to the lower resistivity the depletion, i.e. the removal of the majority carriers in the bulk, occurs at higher voltages and only a small volume around the n-type implants is depleted at 20 V. In contrast, the high resistivity sensor (Fig. 3.29(a)) is almost completely depleted.

The high hole concentration in the un-depleted volume leads to a constant potential, whereas in the depleted volume the potential has a parabolic behavior as shown in Fig. 3.29(c). For the sensor operation, the main difference between these two scenarios, caused by the larger U_{fd}, is the voltage at which the electrical connection between the back-side and the p-spray implant is pinched off by the depletion. While for the high resistivity material this happens at very low voltages, Fig. 3.29(b) shows that for the low resistivity material, there is still a bridge of a large concentration of holes between the back-side to the p-spray. In Fig. 3.29(d) the corresponding potential distribution is presented, revealing that the p-spray is drawn to the back-side potential. This leads to a very high potential difference between the p-spray and the neighboring n-type pixel or strip implants. For the simulation an additional 200 kV/cm was seen in the sensors made from the low resistivity epitaxial silicon.

Considering this qualitative outcome of the simulation, the position of the hot spots seen in Fig. 3.28 can be explained. The hot spots occur at the boundary of the largest continuous area of the p-spray isolation, i.e. where the n-type implants have the largest separation. The larger the distance between the n-type implants, the later the mentioned potential pinch-off occurs, and the potential differences of p-spray and n-type implants increase. Furthermore, since the bias-ring is on a higher potential of about 0 V compared to the strip implants on the punch-through potential with $U_{\mathrm{PT}} < 0\,\mathrm{V}$, the break-down is expected to commence in the vicinity of the bias ring as seen in the infrared measurements.

After exposing the sensors to particle irradiation, the accumulated positive charges at the surface are expected to lower the voltage, needed to pinch off the p-spray implant from the back-side potential. This is a consequence of the attraction of electrons and the resulting partial depletion of the p-type implant through these charges. The lateral depletion, starting from the n-type implants and growing towards the volume below the p-spray, can therefore extend further at the same applied bias voltage, leading to a lower pinch-off potential. The current-voltage characteristics of irradiated strip sensors, presented in Fig. 3.30, indeed shows this expected behavior. While U_{bd} was around 40V for the strips with an active thickness of 50 μm before irradiation, after an integrated

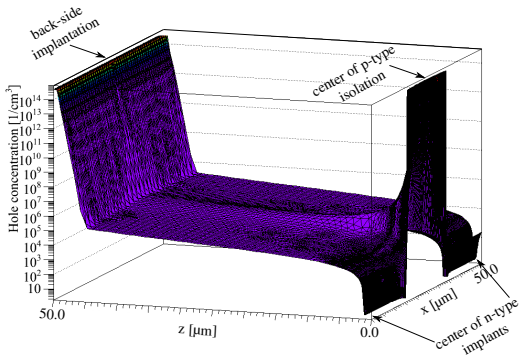

(a) $d = 50\,\mu$m, $\rho = 2\,$kΩcm

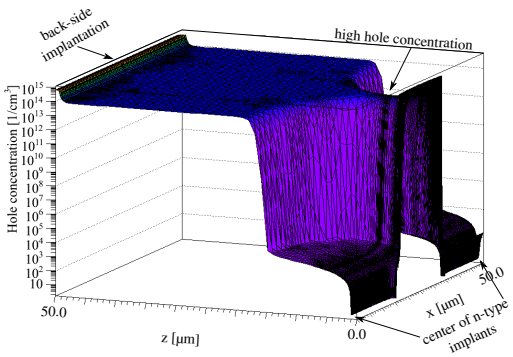

(b) $d = 50\,\mu$m, $\rho = 150\,\Omega$cm

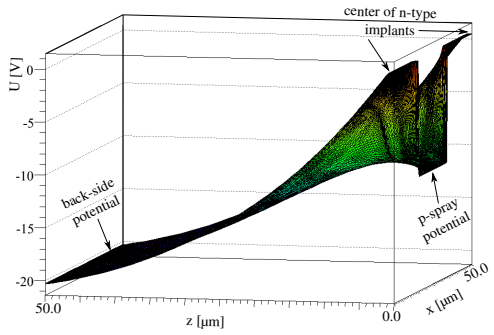

(c) $d = 50\,\mu$m, $\rho = 2\,$kΩcm

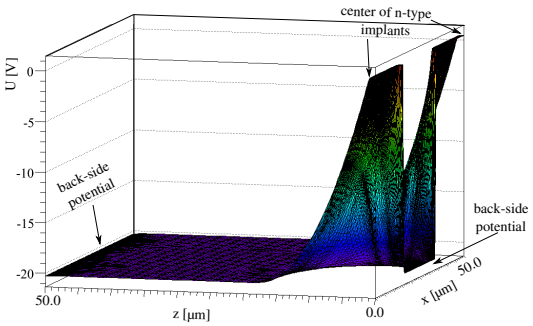

(d) $d = 50\,\mu$m, $\rho = 150\,\Omega$cm

Figure 3.29: Hole concentrations and potential distributions in high resistivity (a,c) and low resistivity (b,d) silicon at a bias voltage of 20 V.

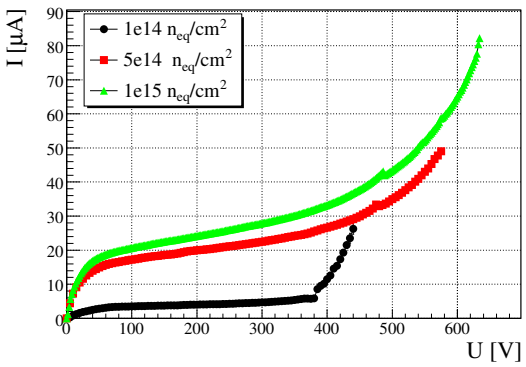

Figure 3.30: Improvement of U_{bd} during irradiation.

fluence of $10^{14}\,\mathrm{n_{eq}/cm^2}$, the break-down occurs at about 380V. For even higher fluences up to $10^{15}\,\mathrm{n_{eq}/cm^2}$, U_{bd} reaches around 500V.

Summarizing the results on the epitaxial sensors it has to be concluded that low resistivities of less than 300 Ωcm are not suited to produce strip and pixel sensors of the presented design. The low U_{bd} prohibits a thorough testing of the devices and therefore is not promising for prototype productions. In this respect, producing thin sensors from epitaxial wafers is only a promising solution if wafers of high resistivity can be produced. At present this is less common than for wafers produced with the float-zone or magnetic Czochralski techniques. Hence, the HLL production process represents a more suitable process for thin high resistivity sensors at present.

3.5 Charge collection efficiency - simulation and measurements

After high irradiation doses, the signal size, i.e. the amount of collected charge, of silicon sensors decreases while the noise due to a higher leakage current increases. These two quantities are the main sensor performance parameters for the ATLAS pixel detector upgrades. In this section, simulations are presented that were implemented to estimate the effect of radiation damage on the charge collection process in silicon sensors. Especially for sensors of the standard 250 μm thickness, they predict a strong decrease of the signal size after the fluence expected at the IBL and even more so at the sLHC. At this fluence, thinner sensors show larger signals.

Furthermore, the Alibava readout system [107] is introduced, which was used to measure the charge collection efficiency (CCE) of strip sensors from the main thin sensor production before and after irradiation. The CCE is defined as the collected charge of a given sensor, normalized to the collected charge of an identical sensor before irradiation.

The measurements of sensors irradiated up to $3 \cdot 10^{15}\,\mathrm{n_{eq}/cm^2}$ show larger signals than expected from the current radiation damage models. An interpretation of the results is given based on a comparison between the simulations and the measurements.

3.5.1 Charge collection efficiency simulation

To calculate the signal size of an irradiated sensor, a simple charge collection simulation (SCCS) was implemented. It is a Monte Carlo algorithm, based on the generation of electron-hole pairs along the trajectory of a particle penetrating the sensor, and the propagation of these in the electric field. Radiation damage is modeled in the form of charge trapping and the change of N_{eff}. The change of N_{eff} alters the electric field distribution and can cause high field regions, leading to charge multiplication. This is in SCCS accounted for by the avalanche multiplication model described by Eq. 2.4. Since the electric field distribution of large area diodes is significantly different from that of structured pixel- and strip sensors, the possibility to import 2-dimensional electric field configurations, e.g. the ones simulated by TeSCA, was implemented in addition. The x and z coordinates in this simulation are defined analog to the coordinate system of TeSCA.

A minimum ionizing particle (MIP) generates about 80 electron-hole pairs per micrometer of silicon penetrated. According to this, the SCCS algorithm creates one electron-hole pair every 12.5 nm along the incident particle trajectory. These electrons and holes are propagated by the electric field to the electrodes of the sensor, and the induced current is integrated over the propagation time. This allows to simulate the pulse shape and the total size of the signal that is integrated by the readout electronics.

The instantaneous current in the sensor is given by Ramo's theorem (Eq. 2.5), i.e. by the sum over the currents of the individual electrons and holes:

$$I_{\mathrm{e,h}}(t) = \sum_{\mathrm{e,h}} \mp q\, \vec{v}_{\mathrm{dr_{e,h}}}(\vec{x}_{\mathrm{e,h}}(t))\, \vec{\mathcal{E}}_{\mathrm{w}}(\vec{x}_{\mathrm{e,h}}(t)), \tag{3.6}$$

where the drift velocity $\vec{v}_{\mathrm{dr_{e,h}}}$ is defined by Eq. 2.7. The charge carriers are propagated in small time steps of Δt according to

$$\vec{x}_{\mathrm{e,h}}(t + \Delta t) = \vec{x}_{\mathrm{e,h}}(t) + \vec{v}_{\mathrm{dr_{e,h}}}(\vec{x}_{\mathrm{e,h}}(t))\Delta t. \tag{3.7}$$

In the case of an unstructured diode of infinite area, the electric field $\vec{\mathcal{E}}(\vec{x}_{\mathrm{e,h}}(t))$ in Eq. 2.7 and the Ramo field $\vec{\mathcal{E}}_{\mathrm{w}}(\vec{x}_{\mathrm{e,h}}(t))$ can be calculated. For $U < U_{\mathrm{fd}}$, the linear field distribution

$$\vec{\mathcal{E}}(\vec{x}) = \begin{pmatrix} 0 \\ \frac{qN_{\mathrm{eff}}}{\epsilon\epsilon_0}(\vec{x}\vec{e}_z - w) \end{pmatrix} \tag{3.8}$$

is assumed. Above U_{fd}, where $w = d$, a homogeneous constant field is added:

$$\vec{\mathcal{E}}(\vec{x}) = \begin{pmatrix} 0 \\ \frac{qN_{\mathrm{eff}}}{\epsilon\epsilon_0}(\vec{x}\vec{e}_z - d) + \frac{U_{\mathrm{fd}} - U}{d} \end{pmatrix}. \tag{3.9}$$

Only depending on the sensor geometry, the weighting field in the case of an large area diode before irradiation is merely the inverse of the depletion depth of the diode

$$\vec{\mathcal{E}}_{\mathrm{w}}(\vec{x}) = \begin{pmatrix} 0 \\ \frac{1}{w} \end{pmatrix}. \tag{3.10}$$

In irradiated, partially depleted sensors w has to be replaced by d since the effective detector geometry is different due to radiation damage which manifests as a decrease of the silicon conductivity [128]. For a partially depleted sensor before irradiation the back-side potential is forwarded into the un-depleted volume of the sensor, i.e. the potential at the depletion boundary can be assumed to be close to the back-side potential. Hence, the effective geometry of the partially depleted diode of thickness d is the same as for a fully depleted diode of thickness w. The low conductivity of irradiated silicon impedes the forwarding of the back-side potential to the depletion boundary. In this case the weighting field corresponds to the one of a fully depleted diode of thickness d.

For the simulation of the signal generation in the strip sensors, 2-dimensional field distributions for the electric and the weighting field are imported into SCCS. While the first are simulated for each N_{eff} and U with TeSCA, the weighting field was provided by a TCAD simulation [129] of a more extended sensor geometry including two complete readout cells.

To account for the change of the effective bulk doping concentration, a simplified version of Eq. 2.18 was used, which is valid before irradiation and for high integrated fluences:

$$N_{\mathrm{eff}}(\Phi_{\mathrm{eq}}) = \begin{cases} N_0 & : \Phi_{\mathrm{eq}} = 0 \\ -\beta\Phi_{\mathrm{eq}} & : \Phi_{\mathrm{eq}} \gg 0 \end{cases}, \tag{3.11}$$

where $\beta = 0.0071$ [128] and $N_0 = 6.5 \cdot 10^{12}/\mathrm{cm}^3$, similar to the initial doping concentration of the p-type sensors of the main production. Trapping is included according to Eq. 2.17. The relation $R < 1 - \exp(-\Delta t/\tau_{\mathrm{eff}_{\mathrm{e,h}}})$ for a random number $R \in [0, 1)$ is used to decide, if a charge carrier is removed from the collection of carriers. In a similar way, the avalanche process is included. Via Eq. 2.4 for each step Δt, the amount of newly created electron-hole pairs is calculated. If the result is a fractional number a comparison of the fractional part with the next R decides if a new electron-hole pair is created.

3.5.2 Simulation results

The damage models for the change of the bulk doping and the trapping probabilities have been established in the past with sensors irradiated to moderate particle doses compared to what is expected at the sLHC. The values for β and $\tau_{\mathrm{eff}_{\mathrm{e,h}}}$ used in this simulation are based on measurements [84] of diodes irradiated up to $\Phi_{\mathrm{eq}} = 2.4 \cdot 10^{14}\,\mathrm{n_{eq}}/\mathrm{cm}^2$. With the SCCS program it was investigated, if an extrapolation of these current radiation damage models to sLHC fluences is in agreement with measurements.

Figure 3.31 shows the results from a simulation of diodes with thicknesses of 75 μm, 150 μm, and 250 μm. The time step Δt is chosen to be 1 ps, the integration time t_{max} is 25 ns - identical to the LHC bunch-crossing time, and the particle trajectories are perpendicular to the sensor surface. In Figs. 3.31(a) and 3.31(b), the CCE of the 75 μm and 150 μm thick diodes are shown as a function of the bias voltage for different fluences. The normalization factors for the CCE are 6 ke and 12 ke, respectively. Clearly the full charge can be collected before irradiation, as soon as $U_{\mathrm{fd}}(75\,\mu\mathrm{m}) \approx 30\,\mathrm{V}$ or $U_{\mathrm{fd}}(150\,\mu\mathrm{m}) \approx 110\,\mathrm{V}$ is reached. For the irradiated diodes the CCE drops down to around 30% and 15% at 1000 V after $\Phi_{\mathrm{eq}} = 10^{16}\,\mathrm{n_{eq}/cm^2}$ for the 75 μm and 150 μm thick diodes due to charge trapping and higher U_{fd}. From the figures it becomes apparent that the 75 μm diodes can be fully depleted at around 350 V after this fluence, visible through the formation of a plateau, while the 150 μm diodes are fully depleted only at around 1400 V. This is far above the present maximum operating voltage of 600 V for the pixel detector modules. Starting at around 1100 V for the 75 μm thick diodes and at 1700 V for the 150 μm thick diodes, multiplication of charge carriers starts to dominate the signal and leads to an exponential increase of the CCE to values larger than 100%.

Figure 3.31(c) compares the absolute signal size of diodes with different thicknesses and different received fluences as a function of the bias voltage. At $\Phi_{\mathrm{eq}} = 10^{15}\,\mathrm{n_{eq}/cm^2}$ the 150 μm thick diode gives a larger signal than the 75 μm thick version. However it becomes evident, that at $\Phi_{\mathrm{eq}} = 10^{16}\,\mathrm{n_{eq}/cm^2}$, i.e. the sLHC fluence, the signal size of the 75 μm thick sensor is the highest. Especially in comparison to the signal of a diode with a thickness of 250 μm, i.e. the thickness of the present ATLAS pixel sensors, a factor of around two in the signal size is seen up to around 850 V. One of the reasons for the increased signal of sensors with a smaller thickness is the lower trapping probability, as a consequence of the higher drift velocities due to the higher electric field in thin diodes. In addition, the smaller weighting field in the thick diodes after high irradiation doses leads to a decrease of the signal size.

Figure 3.32 shows simulations of irradiated sensors with a strip geometry. At each step during the SCCS simulation, every electron and hole has to query the electric field object for the field vector at the current position. This involves a search through the many thousand elements of the finite element grid and thus, takes a considerably longer time. Therefore the time-step was initially chosen to be 20 ps and t_{max} was again set to 25 ns.

In Fig. 3.32(a) a comparison of diodes and strip sensors with a thickness of 75 μm is presented for $\Phi_{\mathrm{eq}} = 10^{15}\,\mathrm{n_{eq}/cm^2}$ and $\Phi_{\mathrm{eq}} = 10^{16}\,\mathrm{n_{eq}/cm^2}$. In both cases the electron-hole pairs are created along a particle trajectory perpendicular to the sensor surface below the n-type implant, i.e. the readout electrode. Here, the CCE of the strip sensors is similar to that of the diodes. The increase due to the different electric and weighting field distribution is only about 5%. However, it is expected that this difference is larger for 3-dimensional pixel sensors, since the weighting field is higher in the vicinity of the electrodes [128]. Figure 3.32(b) compares the dependence of the CCE on the position of

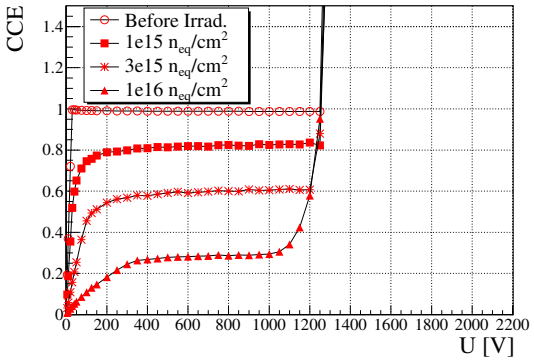

(a) diode, $d = 75\,\mu$m

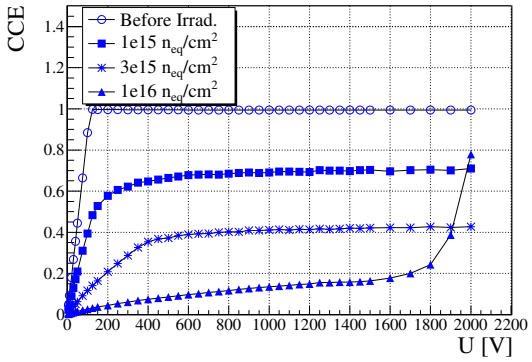

(b) diode, $d = 150\,\mu$m

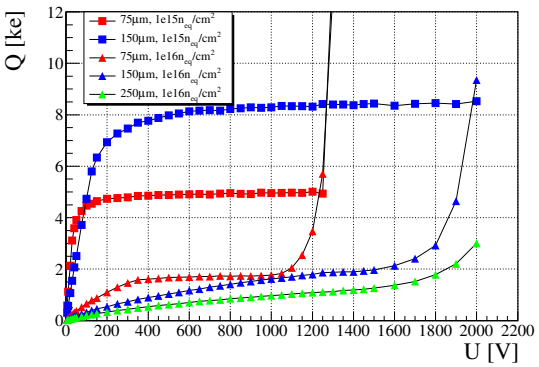

(c) diodes, $d = 75\,\mu$m, $d = 150\,\mu$m, and $d = 250\,\mu$m

Figure 3.31: Charge collection of diodes as a function of the bias voltage for different thicknesses and received irradiation doses. The efficiencies are normalized to 6 ke for the 75 μm and to 12 ke for the 150 μm diodes.

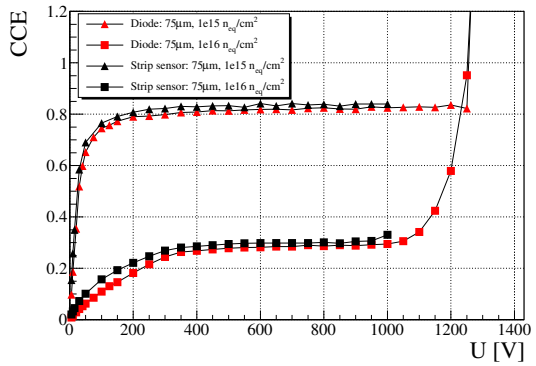

(a) Comparison between a 75 μm thick diode and a strip sensor.

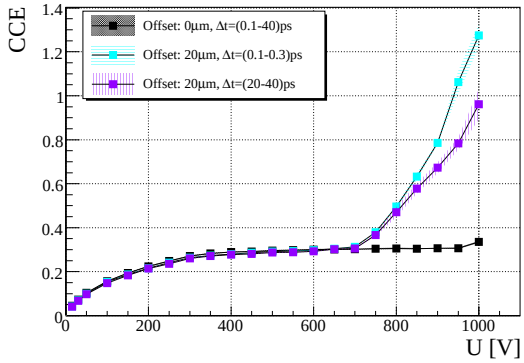

(b) Comparison of different injection positions with respect to the electrode implant.

Figure 3.32: CCE simulated for a diode and a strip sensor with an 80 μm pitch and 30 μm wide n-type electrode implants.

the charge injection into a strip sensor of 75 μm thickness and a homogeneous p-spray implant after a received dose of $10^{16}\,\mathrm{n_{eq}/cm^2}$. One of the incident particles was again penetrating the sensor vertically through the center of the 30 μm wide n-type implant (black squares), while the other (purple and cyan squares) was displaced by 20 μm so that it penetrates through the p-spray implant. Each of the simulation runs was carried out for six different time-step sizes Δt of 0.1 ps, 0.2 ps, 0.3 ps, 20 ps, 30 ps, and 40 ps to simulate different mean free path lengths of the charge carriers. For the central injection, the mean CCE of the 6 simulation runs is given with an according band of uncertainty denoting the standard deviation. For the injection with the offset of 20 μm, the simulations using the three smaller Δts are averaged and shown in the cyan curve, whereas the ones with the three larger Δts are drawn in purple with corresponding uncertainties.

For bias voltages below 700 V, the signal size is almost independent of the injection position, showing just a minor reduction for the simulation with the displaced particle track. In contrast, above this voltage a strong increase of the signal size can be seen up to 1000 V. This increase has an almost linear behavior using the larger time-steps and is approaching an accelerated increase using the smaller ones. However, both are not as steep as the increase due to multiplication seen in the simulation of diodes.

Both effects can be explained by the electric field configuration and the resulting paths of electrons created at different depths. In the case of the displaced track, the electrons in a depth of $z \gtrsim 5\,\mu$m drift directly to the n-implants, inducing a similar current like the electrons that are created by the central injection. Those electrons, created close to the surface first drift towards the $\mathrm{Si} - \mathrm{SiO_2}$-interface, and are then propagated by the lateral field component towards the n-implant. The longitudinal

field component below the surface and the lateral field component at the pn-junction (cf. Fig. 3.10(a)) are very inhomogeneous with sharp peaks at the $Si-SiO_2$-interface and the border between the n-type and the p-type implant. The slightly smaller signal size below 700 V can be explained by an increased trapping probability of those electrons and holes propagating through the low field regions below the p-spray implant. The increase above 700 V is due to charge multiplication in the high field regions. The different slopes of the CCE above the multiplication threshold for the different Δts can be explained by the different corresponding mean free path lengths of the electrons and holes. Assuming a saturation of the drift velocity of the electrons in the high field regions, a time step Δt of 1 ps corresponds to a mean free path of

$$\Delta x \approx 10^7 \,\mathrm{cm/s} \cdot 1 \,\mathrm{ps} = 0.1 \,\mu\mathrm{m} \tag{3.12}$$

between two possible interactions of the electrons with the crystal lattice. The lateral Gaussian width of the high field region that can cause charge multiplication in the simulated sensor is $(0.16 \pm 0.02)\,\mu$m. Hence, when using time-steps of $(20 - 40)$ ps only few of the electrons moving through the high field region are interacting and create new electron-hole pairs. From these newly created charge carriers, even less are causing multiplications themselves. This leads to a more linear increase of the CCE since only a certain fraction of charge carriers is multiplied and the multiplication cannot sustain itself. For the smaller step-sizes of $(0.1 - 0.3)$ ps the chance for multiplication is higher for the initial electrons as well as the electron-hole pairs newly created. Therefore, an faster increase of the CCE with higher U is seen.

In highly doped silicon the mean free path length of electrons is in the order of $(30 - 50)$ nm [130]. This is similar to the second set of simulations and also to the width of the high field regions. Hence, also in a real sensor a linear increase of the CCE above 100%, as seen by other groups, could be explained by the small multiplication probability in the narrow high electric field regions of the sensors. This however should depend much on the actual sensor and implant geometry and is expected to depend on the incident position of the ionizing particle. In conclusion, the detection efficiency of charged particles will critically depend on the exact trajectory they follow. It remains to be seen, whether this property can be accounted for in the data analysis or whether it renders the device not usable as a particle detector.

3.5.3 Charge collection measurements

The charge collection measurement setup was assembled to measure the signal size of irradiated strip sensors from the main sensor production. It is based on the Alibava readout system [107], combined with a ^{90}Sr source and a scintillator trigger system, and is partially installed in a climate chamber to allow for dark and cool operation down to about -40°C. The Alibava readout system was specifically designed and built by

the RD50 [94] institutes from Liverpool [131], Barcelona [132], and Valencia [133] to readout strip test sensors with a pitch of 80 μm. The two main electronics components of the Alibava system are the daughter board located within the climate chamber to read out the signals from the attached sensor, and the mother board installed outside of the climate chamber, processing the data and communicating with a data acquisition PC. Figure 3.33(a) shows the different parts of the setup. Within the climate chamber a mounting rack is installed which holds the shielded radioactive ^{90}Sr electron source, the sensor with the analog readout electronics, and one or two plastic scintillators with attached photo-multiplier tubes (PMTs) Hamamatsu H6780 for triggering. If two trigger units are used they can be logically connected with an OR or an AND operator to allow for coincident triggering. For the measurements presented, only one trigger unit below the sensor is used.

The source is equipped with a movable exit window to control the illumination of the sensor below. The sensor is glued onto the detector board (Fig. 3.33(b)) which has an aperture below the active area of the sensor. Both are placed on an aluminum plate which also has an aperture in the same region and can be fixed to a position under the exit window of the source. Below the aluminum plate the scintillator and the PMT are located. Due to the sensor-aligned aperture in the aluminum plate, the PMT will only register signals created by electrons from the source, which are passing through the active area of the sensor.

The individual strips of the sensor are wire-bonded to a pitch-adapter with an 80 μm pitch on the same board. Hence, only sensors with this pitch can be used for the charge collection studies. The pitch-adapter is bonded to another pitch-adapter on the Alibava daughter board also mounted onto the aluminum plate. Both pitch-adapters have multiple bonding pads per channel, to allow for exchanging and re-bonding detector boards without damaging the sensor or readout chip contact pads. On the daughter board, an analog Beetle readout chip [67] is attached to the pitch-adapter to read out the signals from the sensor. A second Beetle chip on the same board can be used to connect a second sensor via a separate pitch-adapter system. For the presented measurements, only one sensor at a time was attached. In addition to the wire bonds, two cables connect the daughter board to the sensor to supply the high voltage.

A flatband cable for analog data transmission and a high voltage cable for sensor biasing connect the daughter board to the Alibava mother board and a HV power supply outside of the climate chamber. The PMT, providing the trigger signals, is also connected to the mother board via a coaxial cable. The USB output of the mother board allows for controlling the system and reading out the collected data by an attached PC.

3.5.4 The Alibava readout chain

The key components of the Alibava electronics boards are the two Beetle chips on the daughter board (Fig. 3.34(a)), reading the signals from the attached sensor and the

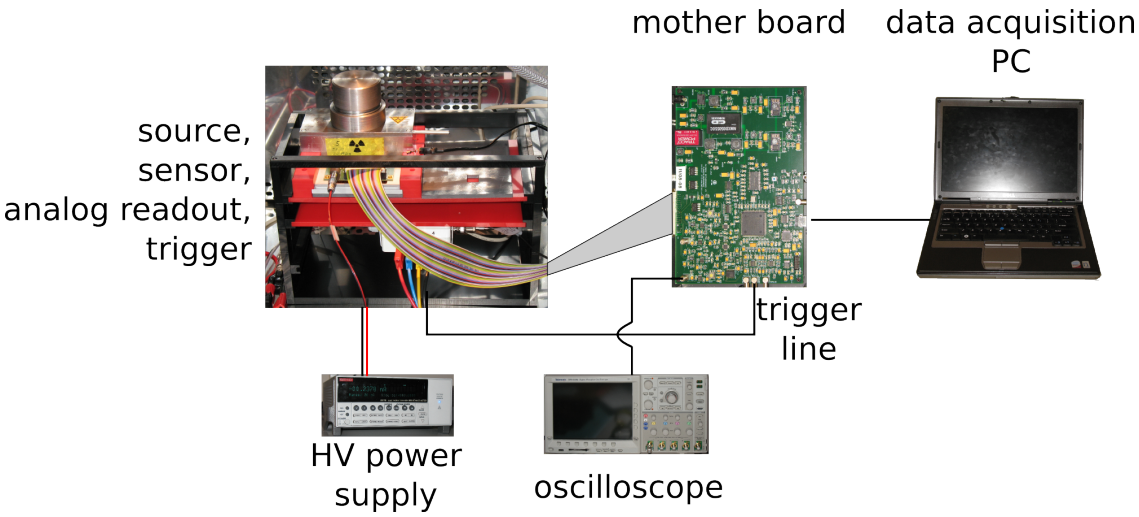

(a) The measurement setup

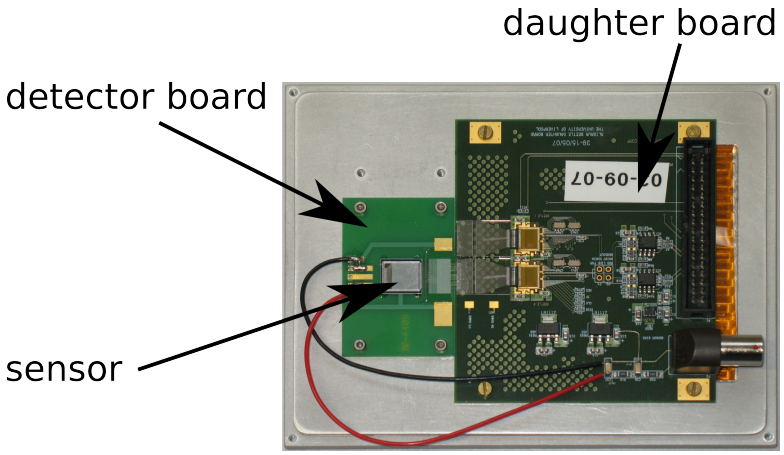

(b) The Alibava daughter board.

Figure 3.33: Components of the Alibava readout system. The source, sensor, analog readout, and scintillator triggers are installed in a climate chamber, the other components are located outside.

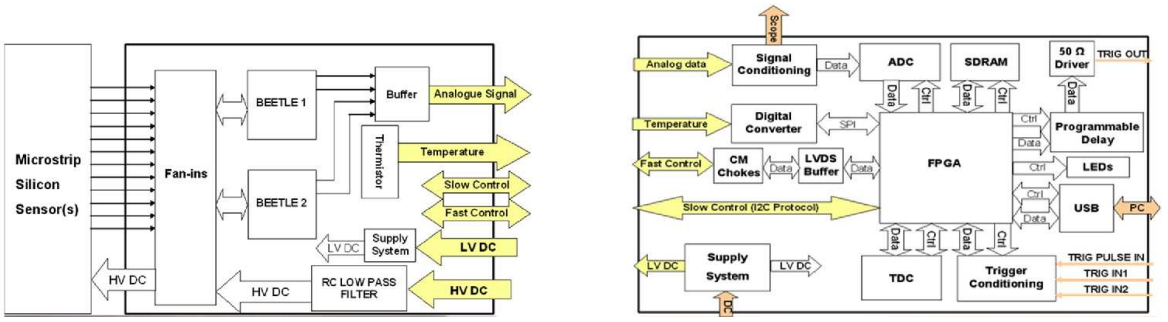

(a) Daughter board. (b) Mother board.

Figure 3.34: The two Alibava readout boards [107]. The daughter board (a) submits the analog signals from the beetle chips to the mother board (b) where they are digitized and transmitted to the PC.

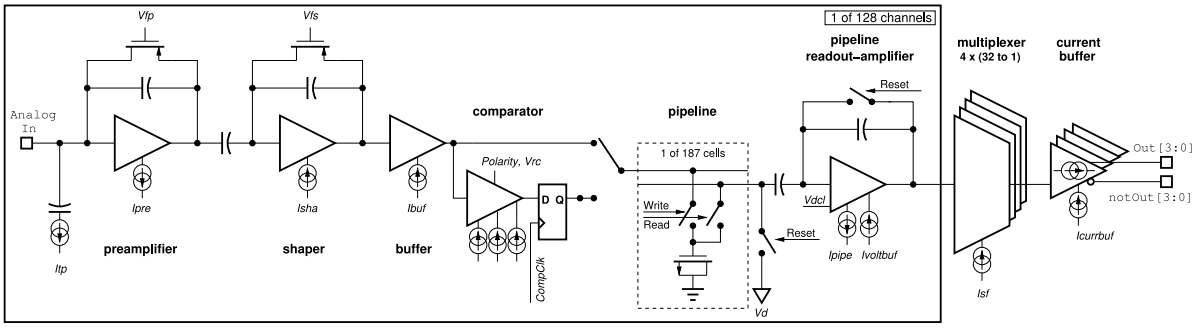

Figure 3.35: Schematics of a single Beetle readout channel [67].

programmed FPGA, steering the mother board (Fig. 3.34(b)) operation.

The Beetle chip, designed for reading out strip sensors of the LHCb experiment at the LHC, has 128 input channels (Fig. 3.35) which measure an input signal from the attached sensor strip or an internal pulse generator (*Itp*) that is used for chip calibration. Each of the analog channels consists of a low-noise charge-sensitive pre-amplifier, a pulse shaper and a buffer. The typical rise-time of the signal pulse, i.e. the time on the rising edge between 10% and 90% of the peak voltage U_{peak}, is around 25 ns. The voltage level 25 ns after the peak is adjusted to be below 30% of U_{peak}. A typical signal pulse length is around $(60 - 70)$ ns. Depending on the operation mode, a comparator can be used to discriminate the signal and to obtain a binary readout. In the Alibava setup, the comparator is not used and the pulse shape is directly sampled into an analog pipeline with a sample rate of 40 MHz, i.e. a sample time of 25 ns. The depth of the pipeline is fixed to 128 cells, corresponding to a delay of 3.2 μs. In case of an external trigger signal

(TRIGGER) to the Beetle chip, a multiplexer system serializes a time slices of 25 ns of the 128 pipelines and sends it off the chip with only one of four implemented current buffers (Fig. 3.35). The transmission time for the 128 analog channel readings and a preceding 16bit digital header is $(128 + 16) \cdot 25\,\text{ns} = 3.6\,\mu\text{s}$, during which no further trigger is accepted.

The FPGA in the mother board (Fig. 3.34(b)) controls the data flow of the Alibava system, i.e. it accepts the trigger signals, queries corresponding time-stamps, digitizes the data and transfers them to the PC. If an electron from the radioactive source penetrates the sensor and generates light in the scintillator, a trigger signal (e.g. TRIG IN1) is generated in the Trigger Conditioning block of the mother board. For this trigger a starting time-stamp is acquired from the TDC with a precision of 0.6 ns. A second, stopping time-stamp is independently created by a pulse which is periodically generated every 100 ns. Exactly 128 clock cycles after the second time-stamp, the readout of both Beetle chips is started with the TRIG_R signal of the TDC invoking the TRIGGER signal of the Beetle chips. At this point in time, the signal from the sensor has been propagated through the Beetle pipeline and can be sent off the chip. This is done by serializing the 25 ns time slice containing the data of all 256 pipelines of the two chips as described above. The selected time slice reflects a random 25 ns wide time window of the signal pulse. Its starting time relative to the event time is known to a precision of 0.6 ns. Collecting many of these time slices from different events, an average pulse shape can be reconstructed with a time resolution much below the sampling time of 25 ns.

The analog data from the Beetle chips is transmitted to the Signal Conditioning block of the mother board which has two outputs. One can be connected to an oscilloscope for monitoring while the other is connected to a 10-bit ADC which digitizes the 256 signals of the acquired time slice. Together with the correct time-stamp the digital data is forwarded to the PC.

The Alibava readout system is operated in three different running modes: the pedestal mode, the calibration mode, and the data taking mode. They differ in the trigger setup of the mother board and the signal input to the Beetle chip channels.

- **Pedestal mode:** The trigger is not given by the PMT but by an internal random trigger logic. With this the random signal of individual Beetle chip channels can be measured.

- **Calibration mode:** The signal input from the Beetle chip is not provided by the sensor but by the internal pulse generator of each Beetle channel which can inject signals from 0 to about 100 ke, spanning the total dynamic range of the chip. The trigger signal is given such that the data is read out from the Beetle chips when U_{peak} has propagated to the end of the internal pipelines.

- **Data taking mode:** The trigger is given by the PMT signal and the signal from the strip sensor is read out, using the mechanism described above. This is the

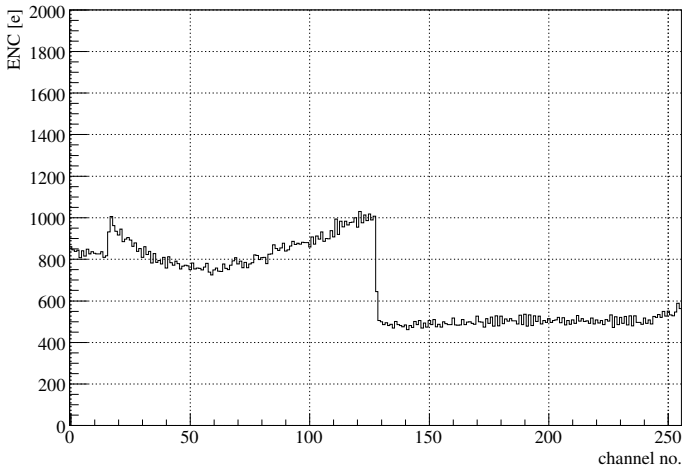

Figure 3.36: Sample noise spectrum of a 150 μm thick sensor before irradiation, biased at 100 V and operated at -30°C. Only the channels 16 to 111 are connected.

regular operation mode to collect the signals generated by the ^{90}Sr source.

3.5.5 The data taking procedure

To measure the signal size of a sensor at a given voltage, several measurements were carried out consecutively. Since the leakage currents from the irradiated sensors are very high, all measurements were performed at -30°C or -40°C. In a first step a pedestal run was carried out to determine the pedestal and noise of all channels. For this 20000 random triggers are generated and all 256 strips are read out. For each strip, the average signal is the pedestal that will later be subtracted from the signal events, and the standard deviation of the pedestal distribution of each channel defines the noise. Figure 3.36 shows a typical noise distribution for randomly triggered events of the 256 channels. In the presented case, chip 0 (channels 0-127) has a strip sensor attached. Since the strip sensors with a pitch of 80 μm only have 96 strip implants, strips 0-15 and 112-127 are not connected and show different noise values. From this measurement, strips with a broken connection or unusual high noise values can be identified and masked for the readout, i.e. excluded from the further analysis.

In the presented measurements, the typical noise in the Alibava system corresponds to an equivalent noise charge (ENC) of 800-900 electrons. Calculating the exact ENC expected from strip sensors is very difficult since it depends strongly on the implant geometry. For small sensors approximated as a single capacitance, the two main contributions stem, as already shown in Eqs. 2.10 and 2.11, from the input capacitance to the pre-amplifier and the leakage current of the sensor. The contribution from the input

capacitance (serial noise) is the dominating factor and is parameterized by

$$ENC_{\text{serial}} = a + b \cdot C, \tag{3.13}$$

where C is the capacitance, $a = 497\,\text{e}$ and $b = 48.3\,\text{e/pF}$. Therefore, in the case $C \sim 0$, i.e. when no sensor is attached, the ENC is around 500 e as seen in Fig. 3.36 for the channel numbers above 127. The contribution from the leakage current (shot noise) is parameterized with

$$ENC_{\text{shot}} = \sqrt{B \cdot I}, \tag{3.14}$$

with $B = 169\,\text{e}^2/\text{nA}$. The input capacitance is dominated by the inter-strip capacitance (cf. Fig. 3.15) and has further contributions from the capacitance of the sensor bulk, and the capacitance of the attached wire-bonds. Assuming a total input capacitance of 2.5 pF for the strip sensors used for these measurements and a total leakage current of 300 nA spread over the 96 strips of the attached sensor, this leads to an equivalent noise charge of

$$ENC = \sqrt{ENC_{\text{serial}}^2 + ENC_{\text{shot}}^2} = \sqrt{(618\,\text{e})^2 + (23\,\text{e})^2} \approx 618\,\text{e}. \tag{3.15}$$

In the case of heavily irradiated sensors with leakage currents up to 10 μA, this only slightly changes to

$$ENC = \sqrt{(618\,\text{e})^2 + (133\,\text{e})^2} \approx 632\,\text{e}. \tag{3.16}$$

The discrepancy between these approximative calculations for a single capacitance and the expected and measured values can be explained by the much more complex electrical characteristics of the strip sensors. For these, the simple equations presented above do not give accurate results.

After the pedestal run, a calibration of the beetle chip is carried out. At a frequency of around 50 Hz, signals are injected into each channel by the internal pulse generator. Since the beetle chip accepts positive as well as negative signals, both polarities are injected alternatingly. To avoid a global offset of the channels, neighboring channels are always supplied with opposite polarities. During the calibration run, each fixed amount of charge is injected multiple times to get a stable measurement before switching to the next charge value. In the analysis software a linear fit to the known injected charge as a function of the measured ADC value of the mother board, gives a calibration of the gain factor for each channel.

During the actual data run the readout of the sensors is triggered by the scintillator trigger system according to the procedure mentioned in the previous section. For each triggered event the 256 channels are read out and the raw data, i.e. the ADC values, are stored on the computer together with the corresponding time-stamp of the event. The analysis of the data is done in software. In a first step each event is processed, by the subtraction of the pedestals and common mode offsets, which might be introduced

during the analog signal transfer between the daughter- and the mother board, as well as the application of the gain factors measured in the calibration run. From this point on, a signal normalized to the electron charge is associated to each readout channel of each event.

In the next step a cluster finding algorithm is used to group neighboring channels belonging to the same incident particle. The cluster finding is based on two requirements that are adjusted the measurable signal size, the signal to noise requirement *sn* and the signal to noise requirement of the neighboring strips *snn*. Starting from the highest signal in one event, it is tested if it fulfills the *sn* requirement. If this is the case a new search is started from this position to both directions, adding the neighboring strips on each side until one falls below the *snn* requirement. The signal from the group of strips is summed, forwarded to the analysis, and the group is removed from the search. After this, the second iteration starts to find the next possible signal in the event with the same algorithm. This procedure is repeated until no channel is left that fulfills the *sn* requirement.

To reconstruct the average pulse shape, all signals that were found by the clustering algorithm are binned in time and for each time bin the average signal size is plotted. Since the data is taken at random times up to 100 ns after the physical event, each time bin should on average have the same number of entries but a characteristic signal size. Figure 3.37 shows a typical average pulse shape reconstructed from a number of events collected. The maximum of the pulse height is reached at the peak time t_{peak} of around 20 ns. At times later than 60 ns after the trigger, the pulse height approaches the noise level.

Based on the pulse shape, time requirements are used to select those signals that correspond to U_{peak} of the pulse which is proportional to the signal size. To find the correct time window, a fit with a Gaussian and a constant

$$Q(t) = -c \cdot \exp\left(-\frac{1}{2}\left(\frac{t-\mu}{\sigma}\right)^2\right) + d \tag{3.17}$$

is carried out. Beginning and end of the time window are defined as $\mu \pm \sigma/4$, leading to a good noise reduction. A typical charge spectrum of a 150 μm thick strip sensor before irradiation biased at 100 V is shown in Fig. 3.38. A clear signal spectrum is visible which resembles a Landau distribution convoluted with a Gaussian. The Gaussian part accounts for the smearing of the spectrum due to the noise contribution. In Fig. 3.38, the most probable value is labeled as "MPV", the width parameter of the Landau as "Scale", the width of the Gaussian as "Sigma", and the total integral is labeled as "Norm". This signal is well separated from the noise contribution that starts to rise at charges below 5 ke.

After high integrated fluences or for low bias voltages the signal spectrum is shifted towards smaller charges. In extreme cases, the MPV of the measured charge is domi-

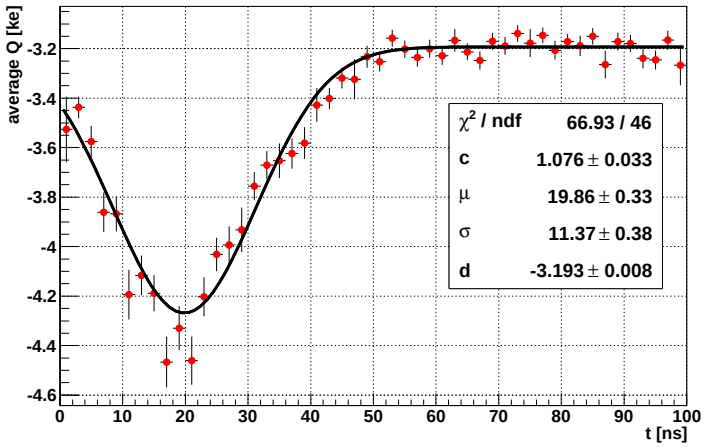

Figure 3.37: Average pulse shape of a 150 μm thick sensor before irradiation, biased at 100 V and operated at −30°C. The points denote the mean values, the bars give the standard deviation of the events in each bin. The signal to noise requirements are $sn = 4.5$ and $snn = 3.5$. The fit parameters and uncertainties are calculated with Minuit [134]

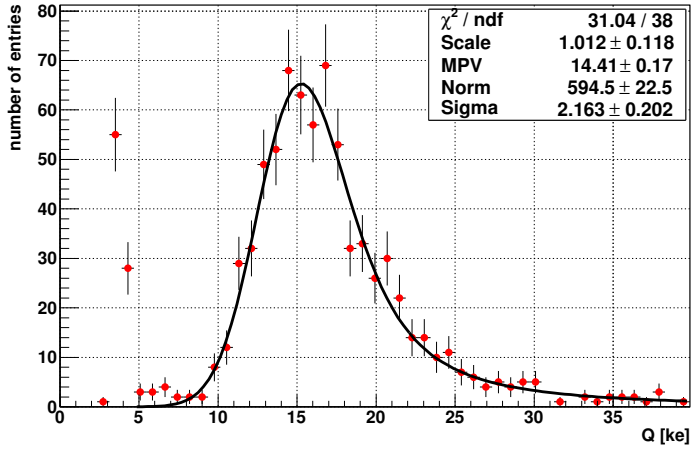

Figure 3.38: Spectrum of a 150 μm thick sensor before irradiation, biased at 100 V and operated at −30°C. The points in this an the following spectra denote the number of entries, the bars give the purely statistical uncertainty. The signal to noise requirements are $sn = 4.5$ and $snn = 3.5$.

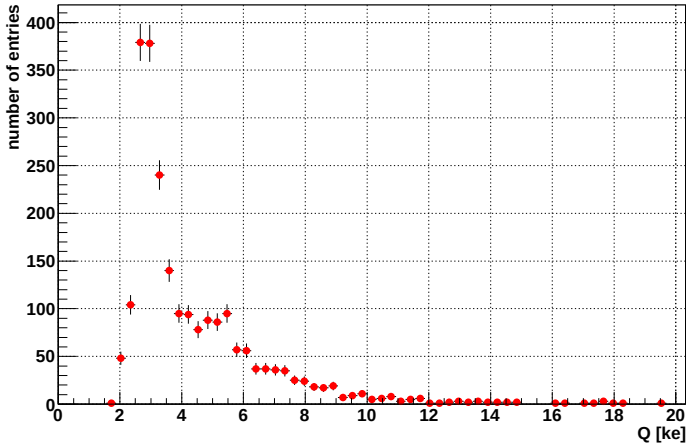

Figure 3.39: Charge spectrum of an irradiated sensor of 150 μm thickness, biased at 200 V and operated at -30°C. The signal to noise requirements are $sn = 3.0$ and $snn = 2.0$. The average noise is 760 e.

nated by noise so that a direct measurement of the charge spectrum is not possible. In Fig. 3.39 the spectrum of a 150 μm thick sensor irradiated to $10^{15}\,\mathrm{n_{eq}/cm^2}$ and biased at 200 V exhibits a large noise peak at $Q \approx 3$ ke To reconstruct the signal spectrum, an algorithm has been developed to estimate the noise contribution to the total spectrum for subtraction. For this a second spectrum is created from events of a different time window, i.e. between 60 ns and 90 ns after the trigger, strongly dominated by random events. To subtract the noise histogram from the signal histogram the correct normalization has to be found. This is achieved if the signal spectrum after the noise subtraction has a baseline compatible with 0 for low and high charges. A method to find a suitable normalization factor was developed, which integrates both histograms up to a charge q_{max} and uses the ratio of the integrals for the normalization. The charge q_{max} is chosen as the product of the sn requirement and the maximum noise charge of all channels of the readout chip that are included in the analysis. This value is motivated by trying to preserve all signals that would have passed the sn requirement of all channels, whereas those signals that only pass the sn requirement of low noise channels are subtracted. This reduces the noise especially in the case of large noise fluctuations (e.g. Fig. 3.36). The result of this subtraction (Fig. 3.40) reveals that indeed the signal to noise ratio can be much improved.

3.5.6 Results of the charge collection measurements

The above mentioned data taking procedure was performed on several strip sensors from the main sensor production. Two sensors that were not irradiated were used to obtain a

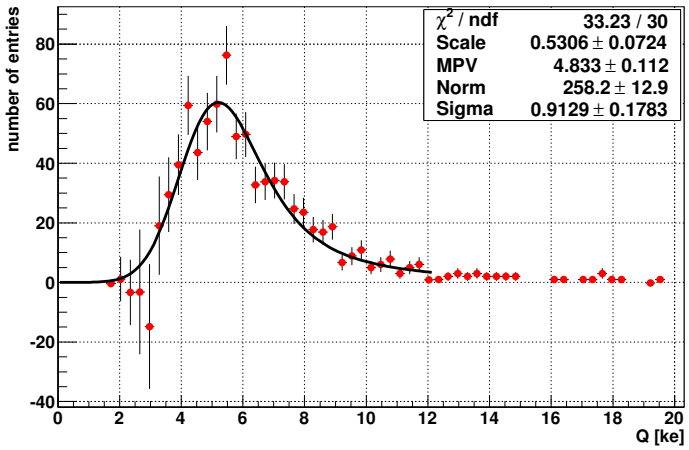

Figure 3.40: Spectrum of Fig. 3.39 after the noise subtraction.

Name	thickness [μm]	received fluence [10^{15} n_{eq}/cm^2]	temperature [°C]
W2D7	75	-	-30
D1E6	75	1	-30
W2E7	75	3	-40
W10D6	150	-	-30
W12E5	150	1	-30

Table 3.11: List of sensors used for the CCE measurements. Listed are the thicknesses the received fluences and the temperature during the measurements.

calibration for the expected signal of 75 μm and 150 μm thick sensors before irradiation. To measure the signal size of irradiated devices, three sensors of different thicknesses and for fluences up to $3 \cdot 10^{15}$ n_{eq}/cm^2 were chosen (Tab. 3.11). Measurements of sensors which were irradiated up to 10^{16} n_{eq}/cm^2 were so far not exhaustively carried out, since the large leakage currents of these DC coupled sensors might lead to permanent damage of the Beetle chips. To avoid these high leakage currents a decoupling capacitor array is going to be used which is placed between the sensor and the Beetle readout chip.

Table 3.12 lists the charge collection measurements performed on the not irradiated sensors. For both thicknesses the charge Q_0 was measured in the plateau region, i.e. at full depletion, were the full signal size can be measured. In the case of the 75 μm thick sensor, four measurements were carried out at voltages between 50 V and 60 V, while for the 150 μm thick sensor only two measurements could be carried out at 100 V and 120 V. A junction break-down was observed above 120 V, inhibiting further measurements. For each measurement the uncertainty was assumed to be ΔQ is 0.5 ke. This value is

Name	thickness [μm]	Q_0[ke]
W2D7	75	7.44 ± 0.5
W10D6	150	14.12 ± 0.5

Table 3.12: Measured maximum signals from the sensors before irradiation.

estimated by various repetitions of the same measurement using different fit parameters, *sn* requirements, and temperatures. The uncertainty is mostly of systematic nature and hence will be propagated linearly.

The CCE of the three irradiated sensors is calculated from the collected charge Q by

$$CCE = \frac{Q}{Q_0} \tag{3.18}$$

with the appropriate Q_0, and the uncertainty is calculated by

$$\Delta CCE = \left|\frac{1}{Q_0}\Delta Q\right| + \left|-\frac{Q}{Q_0^2}\Delta Q_0\right|. \tag{3.19}$$

The result of the CCE measurements for the three irradiated sensors are given in Fig. 3.41(a). The sensors with an active thickness of 75 μm show a CCE of up to almost 100% for the integrated fluences of $10^{15}\,\mathrm{n_{eq}/cm^2}$ and $3 \cdot 10^{15}\,\mathrm{n_{eq}/cm^2}$ at 400 V and 650 V, respectively. For the sensor with a thickness of 150 μm and a received fluence of $10^{15}\,\mathrm{n_{eq}/cm^2}$ a CCE of almost 90% was observed at 500 V. The noise is calculated from the average of all channels that were not masked (Fig. 3.41(b)). The band indicates the standard deviation of the noise distribution. In all three cases the observed noise agrees with the expected value from the Alibava specification, and is constant over the measured bias voltage range. A slightly lower noise can be seen for the sensor with a thickness of 150 μm. A slight increase of the noise can be seen for the 75 μm thick sensor irradiated to $10^{15}\,\mathrm{n_{eq}/cm^2}$ below 100 V. Both these effects are likely correlated to the change of the input capacitance caused by the different depletion depths (cf. Eq. 3.13).

In Figs. 3.42(a) to 3.42(e) the signal spectra of the five sensors at their individual maximum bias voltage are presented. For all sensors a well defined spectrum with acceptable fit quality can be recovered by the noise subtraction algorithm. For the 75 μm thick sensors all three spectra look similar and the irradiated sensors reproduce the charge collected from the not irradiated sensor within the measurement uncertainty. The 150 μm thick sensor irradiated to $10^{15}\,\mathrm{n_{eq}/cm^2}$ exhibits only a slight decrease of the MPV with respect to the not irradiated sensor. In addition, the measurements do not show a strong increase in the width of the spectra, indicating that the noise does not significantly change and contribution from avalanche multiplication to the signal is not dominating.

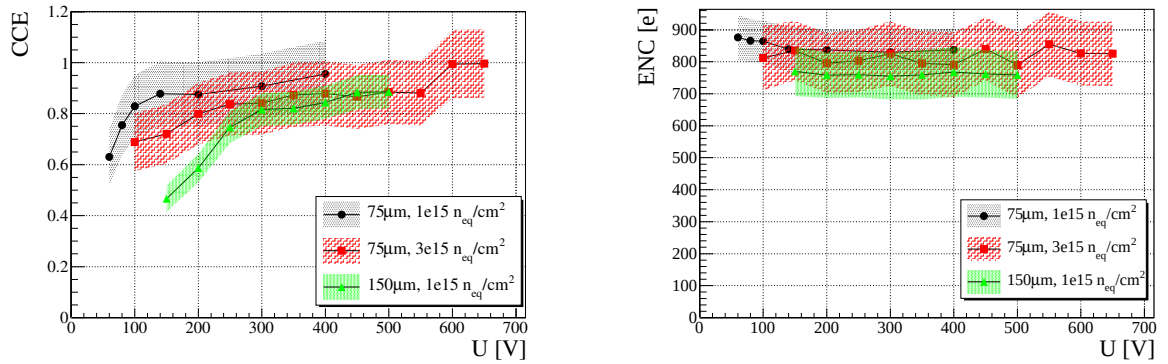

(a) CCE (b) ENC

Figure 3.41: Charge collection efficiency and noise as a function of the bias voltage for three sensors. For the noise distribution, the mean ENC is averaged over all strip channels that are used in the analysis. The bars denote the standard deviation of the mean.

3.5.7 Interpretation of the results

Comparing the measurements with the simulation results, two observations can be made:

- At the same integrated fluence for any voltage, the charge collection efficiency in the 75 μm thick sensors is higher than in the 150 μm thick sensors.
- The signals are larger than expected from the calculations based on the current radiation damage models.

The first observation is not unexpected and was also seen in the simulation (Fig. 3.31). Two reasons were already named that cause this behavior. The first is the electric field strength which is higher in thin sensors at the same applied bias voltages. Hence, especially in the low electric field regions the drift velocity in the thin sensors can increase and the trapping probability is lower. Consequently, on average more of the initially created free charge carriers are collected before they are being trapped. The second reason is the different shape of the weighting potential, which couples the movement of the charge carriers to the signal induced in the readout electronics. Even though the weighting potential only depends on the geometry of the sensors, i.e. the relative position of the electrodes, an effective geometry change can be provoked by radiation damage. This leads to a decrease of the weighting field in partially depleted sensors and consequently, to lower signals. Therefore, the benefit of thin over thick sensors develops only after high irradiation fluences.

The second observation was not expected from the simulation. While for the measured 150 μm thick sensors the CCE reaches almost 90% after $10^{15}\,\mathrm{n_{eq}/cm^2}$, the 75 μm

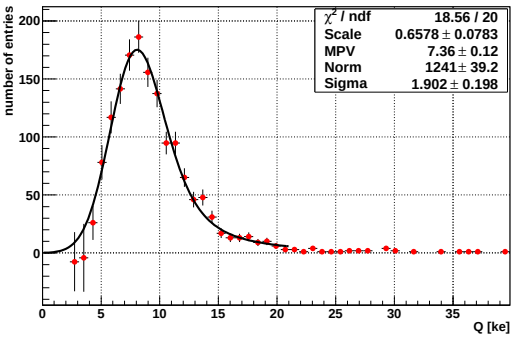

(a) $d = 75\,\mu$m, not irradiated

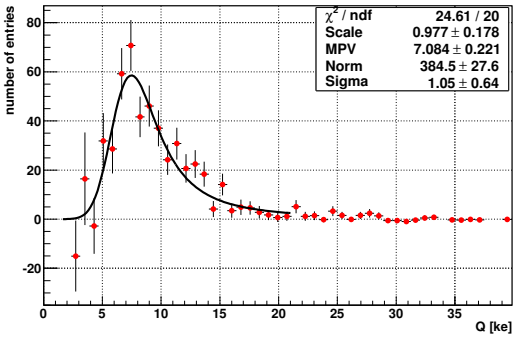

(b) $d = 75\,\mu$m, $\Phi = 10^{15}\,\mathrm{n_{eq}/cm^2}$

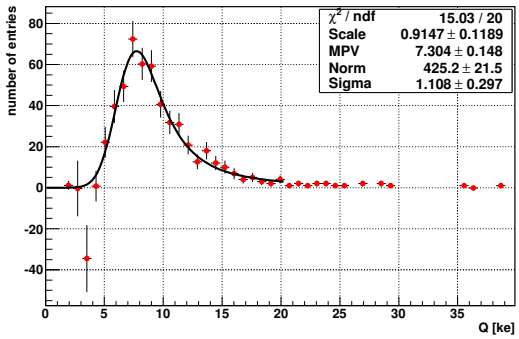

(c) $d = 75\,\mu$m, $\Phi = 3 \cdot 10^{15}\,\mathrm{n_{eq}/cm^2}$

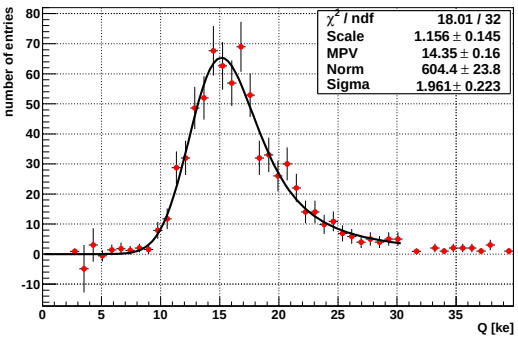

(d) $d = 150\,\mu$m, not irradiated

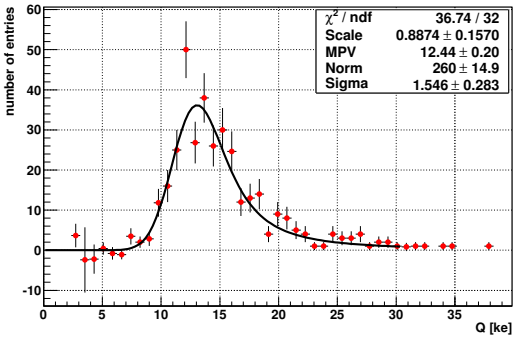

(e) $d = 150\,\mu$m, $\Phi = 10^{15}\,\mathrm{n_{eq}/cm^2}$

Figure 3.42: Charge spectra of the five sensors under test at their respective maximum applied bias voltage.

thick sensors reproduce the full charge, compared to not irradiated sensors. Especially for the 75 μm thick sensors, a saturation of the CCE is not suggested by the measurements up to the highest voltages.

A similar observation has been made earlier by other groups that compared sensors of standard thickness to thinned ones, e.g. [105]. In some cases even a linear increase of the CCE values beyond 100% at very high voltages was observed. The interpretation of these results is more difficult. Two theoretical models can be considered to explain this unexpected increase in the CCE. The first one is the Poole-Frenkel effect [135], a detrapping effect which assumes that the time t_i during which the charge carriers are immobile, decreases for increasing electric field strengths predicted after high irradiation fluences. If t_i reduces to values much below the integration time, a considerable amount of the trapped charges can again contribute to the signal size. In the limit of $t_i \rightarrow 0$ this could lead to the full charge collection at high voltages. However, this model would predict a saturation towards the full CCE which was confuted by measurements [105]. The explanation currently discussed, is charge multiplication in high electric field regions of the sensors. As shown in the simulation this could lead to a very high number of collected charges. However, assuming that all charge carriers are multiplied, this should lead to a very steep exponential increase of the CCE which has not been observed for planar sensors. Instead the CCE rises almost linearly with the applied bias voltage. A possible explanation for this observations is motivated by the field distribution in the sensor. Already shown in the simulation above, in planar sensors the highest electric field values are found at the $Si - SiO_2$-interface and the transition from the n-type electrode implants to the p-spray implant. Hence, at a large range of bias voltages only those particles are multiplied which propagate through these local high field regions. This was seen in the simulation through the strong difference of the CCE for different injection positions. Also recent measurements [106], measuring the dependence of the CCE on the generation depth, show that multiplication is most likely to occur close to the surface of the sensors. To test this hypothesis a new experimental setup can be designed to measure the CCE as a function of the position of the injected charge. For this either a very fine focussed particle source or a laser setup would be needed with a focus diameter of around 10 μm and a positioning accuracy of the same size.

3.6 Conclusions

The HLL thinning process allows to produce thin sensors from silicon wafers of standard thickness without degrading the properties of the silicon material. It was used to produce the first pixel and strip sensors with active thicknesses of 75 μm and 150 μm. To ensure successful operation before and during irradiation a preceding simulation of different p-spray implant options and measurements of the inter-strip isolation after X-ray irradiation were carried out to define the isolation implant parameters. After suc-

cessfully finishing the main thin sensor production, the electrical characterization of the sensors proved that the thinning process can be used for pixel and strip sensors without degrading their functioning. The sensors showed low leakage currents, break-down voltages well above the full depletion voltage, and a device yield of over 98% for the pixel sensors. In particular, the measurements also demonstrated that the simulation of the p-spray implant parameters led to a well performing p-spray isolation for the thin strip and pixel sensors.

Measurements of the leakage current and break-down voltage of diodes with a slim guard-ring structure proved that it is possible to increase the active area of the thin sensors. Together with a reduction of the safety margin to the cutting edge of the sensors an inactive edge of less than 500 μm is well within reach. With this and the new 3D-integration technology presented in the next chapter, the live-fraction of the pixel sensor modules can be increased from 71% to 90% to meet the requirements for the IBL upgrade of the pixel detector.

Some of the thin sensors were irradiated with protons up to the integrated fluence expected at the sLHC. The leakage currents of the sensors increase proportional to the fluence received. This and the accompanying increase of the full depletion voltage due to irradiation damage were expected and could be partially decreased by a controlled annealing procedure.

A comparison between a simulation and measurements of the charge collection efficiency of irradiated strip sensors revealed that the signals of thin sensors do not decrease as strong as expected from the current damage models. For the sensor with a thickness of 150 μm a CCE of almost 90% was measured after an integrated fluence of $10^{15}\,\mathrm{n_{eq}/cm^2}$ while for the 75 μm thick sensors, irradiated up to $\Phi = 3 \cdot 10^{15}\,\mathrm{n_{eq}/cm^2}$, a CCE compatible with 100% was found. This very encouraging result could be explained by the electric and weighting field distributions in thin sensors which might lead to a detrapping mechanism in high electric field regions (Poole-Frenkel effect) or to avalanche charge carrier multiplication. Similar measurements of other groups also have shown increased signal sizes from thin sensors compared to sensors of standard thicknesses after irradiation. Reaching CCEs above 100%, they strongly suggest that an avalanche multiplication process contributes to the signal.

Considering the success of the thin sensor production and the encouraging results from the CCE measurements of irradiated thin sensors it can be concluded that thin sensors present a promising technology for the upgrades of the ATLAS pixel detector. Furthermore, they are produced mainly with standard processing tools, leading to much lower production costs and a considerably higher device yield than competing approaches like diamond- or 3D-sensors.

Chapter 4

3D-integration technology for future pixel modules

In the field of semiconductor manufacturing, the term 3D-integration refers to a vertical packaging of two or more layers of Integrated Circuits (ICs) with electrical interconnections between them [136]. During the last years, the research on different techniques towards the 3D-integration of ICs is strongly being pursued since the expansion into the third dimension offers various performance improvements [137, 138]. These include a higher compactness of the ICs, higher speed due to shorter electrical paths, lower power consumption, new possible design concepts, and also the ability to combine ICs that are individually optimized. To vertically integrate several layers of ICs from standard silicon wafer processing lines two additional technologies are needed. The first is an interconnection technology between the layers which has to contain a patterned structure of electrical contacts. The second is the formation of Inter-Chip Vias (ICV) in each layer to form a conducting vertical path through the silicon substrate.

In most current high-energy physics experiments at particle colliders high-granularity semiconductor pixel sensors are used as the innermost active detector components. To instrument the small volume around the interaction-point most efficiently a compact design of the pixel detector system is needed. In view of the foreseen upgrades of the present ATLAS pixel detector, one of the research goals presented within this work is 3D-integration applied to the heterogeneous combination of silicon sensors and readout electronics and its potential to further increase the compactness of future pixel detectors. The integration technology ICV-SLID, used for this research, was developed by the Fraunhofer-Institut für Zuverlässigkeit und Mikrointegration (IZM) München [139]. As the name implies, Inter-Chip Vias are used for the vertical signal transport through the silicon layers. For the interconnection between the sensor and readout electronics a copper-tin-copper soldering technology called Solid-Liquid InterDiffusion (SLID) is employed.

A description of ICV-SLID and a comparison to the bump-bonding technology used

in the present ATLAS pixel detector are given in Sec. 4.1. Since the SLID interconnection contains copper it is crucial to have a diffusion barrier to protect the sensor from the metalization. Otherwise, the introduction of copper atoms into the silicon would lead to large leakage currents during operation. To confirm the functioning of the diffusion barriers, measurements of leakage currents of diodes with the SLID metalization applied were carried out and are presented in Sec. 4.2.

Two key ingredients for a high SLID interconnection efficiency are the relative alignment of the devices to be connected and the surface planarity over the full area of all devices. To evaluate these and the resulting interconnection efficiency, a production of test wafers containing several SLID daisy chains (see below) and structures for alignment measurements was carried out. First, two wafers were interconnected in a wafer-to-wafer process while in a second step the SLID connections were performed in a chip-to-wafer process. The results of the SLID efficiency measurements are presented in Sec. 4.3. In Sec. 4.4 the plans and preparations for the application of the ICV-SLID technology to the present ATLAS readout electronics chip to construct single-chip demonstrator modules are summarized.

4.1 Solid-Liquid InterDiffusion and Inter-Chip Vias

In Sec. 1.4 it was described how the 3D-integration of a silicon sensor and readout electronics is planned to be used to build more compact pixel detector modules. The possibility to route signals vertically to the back-side of the readout electronics is employed to produce four-side buttable devices, reaching a higher fraction of active area. However, not all 3D-integration technologies are suitable to be used in a future ATLAS pixel detector.

At present, several 3D-integration technologies are developed and investigated in industry and public research institutes. They differ in the wafer interconnection technology, the filling material of the ICVs, and the order of the processing steps [140]. The interconnection technologies are usually based on polymer glues [141], bump-balls [139, 142], or copper-copper respectively copper-tin-copper (SLID) soldering [139, 143]. Materials used for the ICVs mainly comprise polysilicon, copper or tungsten, and the vias can be introduced before or after individual interconnection steps. The interconnection processes can be performed on three different scales: wafer-to-wafer, chip-to-wafer, and chip-to-chip. In any case the production of the devices to be interconnected is performed at wafer-level, however the singularization and connection steps are done in a different order.

The wafer-to-wafer process connects all layers at the full wafer scale. Only after the complete stack of wafers is interconnected, the 3D-packages are singularized. The advantage is that only one alignment step has to be carried out per connection between two layers, but naturally, if there is a remaining misalignment, all devices are affected.

Furthermore, no selection of devices can be carried out before the integration. This can drastically decrease the package yield, i.e. the percentage of working integrated packages, being the product of the yields of the individual devices.

For the chip-to-wafer process, the devices of one of the wafers are singularized before the 3D-integration, allowing to chose a subset of devices to be interconnected. This increases the package yield, since only devices which are verified to work are connected. Also, single devices from shared wafer productions can be used. However, the individual handling of the singularized devices is a potential source for an additional misalignment. The connection of the singularized devices and the wafer is usually done with an additional handle-wafer onto which the devices are mounted. Therefore, the total misalignment depends on the alignment precision of the individual devices on the handle-wafer as well as the wafer-to-wafer alignment, usually dominated by the former.

The chip-to-chip 3D-integration is mainly used for prototype production. Here, devices from both wafers are singularized before the vertical integration. This is reasonable if individual device yields are very low, or only little quantities are produced.

For the presented work, the ICV-SLID 3D-integration technology of the IZM is explored, presenting a good candidate for compact pixel sensor modules to be used in environments exposed to large irradiation fluences. It is based on an interdiffusion of tin and copper and hence, is expected to be radiation hard in contrast to polymer glues. The ICVs are etched via Deep Reactive Ion Etching (DRIE) and are filled with tungsten.

4.1.1 Solid-Liquid InterDiffusion

The SLID interconnection technology (Fig. 4.1) is characterized by a very thin system of metal layers. To prepare the sensors and the readout chips for the SLID metalization, a 100 nm thin TiW diffusion barrier is applied onto the aluminum pads of the devices to be connected. This prevents the diffusion of copper atoms into the silicon, originating from the 5 μm Cu-layer, which is electroplated in a second step on both devices. Copper atoms in the silicon bulk would lead to defects causing high leakage currents, rendering the sensors useless. In a third step, on one of the two devices a 3 μm layer of tin (Sn) is applied on-top of the structured Cu-layer.

To form the connection, the two devices are aligned, brought in contact, pressed together with a force[1] of $(2.5 - 5)$ kN, and heated to a temperature of around $(240 - 320)$°C. At these temperatures the tin melts and diffuses into the copper to form an eutectic Cu_3Sn alloy. The alloy has a melting point of around 600°C and hence, does not melt during the SLID interconnections of subsequent layers. This allows for many-layer stacking. Although more than two layers are not planned for the proposed pixel module, it might well present the technology of choice for future, even more integrated, detector concepts [52].

[1] The value of $(2.5 - 5)$ kN applies to 6-inch wafers and depends on the area filled with SLID pads.

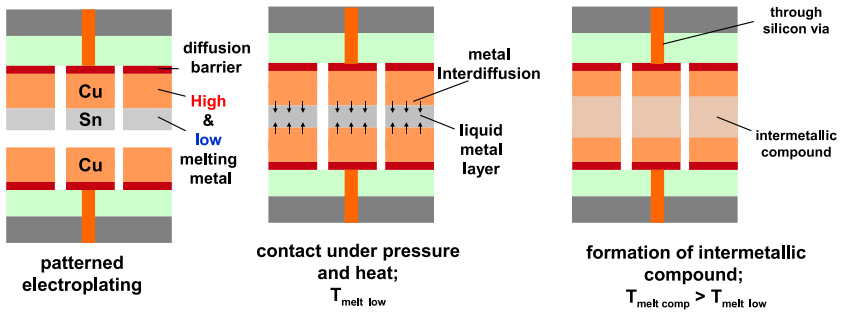

(a) Schematic representation of the SLID process

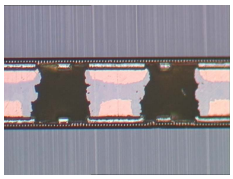

(b) SLID connection cross-section

Figure 4.1: The SLID interconnection based on Sn diffusing into Cu to form an eutectic Cu_3Sn alloy with a high melting point. Figures adapted from [139].

The SLID interconnection has several advantages compared to the bump-bonding [39] technology used in the present ATLAS pixel detector. For the bump-bonding, a similar surface metalization of Cu on top of TiW is electroplated on the aluminum contact pads of the sensors and readout electronics. On top of the Cu pads of the readout electronics, an additional $(20-25)\,\mu$m thick layer of a PbSn soldering alloy is electroplated[2] (1st step in Fig. 4.2). As a second step, at a temperature above the melting point of the PbSn alloy, the so-called reflow-process is used to form the solder into a ball-like shape via the surface tension, and to clean the solder ball [145]. The next step is the chip-to-wafer pick-and-place process to position single readout electronics chips face-to-face to the side with the bump-balls. In a last step the soldering is carried out, forming a Cu-PbSn alloy similar to the Cu-Sn alloy in the SLID interconnection, but only in a small volume around the interfaces between Cu and PbSn(4th step in Fig. 4.2). Bump-bonding cannot connect more than two layers of silicon devices. The PbSn of the bump-balls would melt during the consecutive connections of layers and the already existing connections would be destroyed.

As shown in the step-by-step comparison of both technologies in Fig. 4.2, the reflow-process is not needed for the SLID interconnection. Therefore, it is expected that the cost with respect to bump-bonding is lower, once it is used in larger scale productions. Furthermore, without the reflow-process various shapes and sizes of the contact pads are possible since the height of all contacts is uniform in the SLID technology (3rd step in Fig. 4.2). To establish a successful SLID connection between the contacts of two devices, an area of at least $5 \times 5\,\mu$m^2 has to be connected. Thus, reaching a sufficient alignment precision allows for smaller pixel sizes which is beneficial for the spatial resolution and

[2] A part of the pixel modules is connected with a similar indium bump-bonding process discussed e.g. in [144].

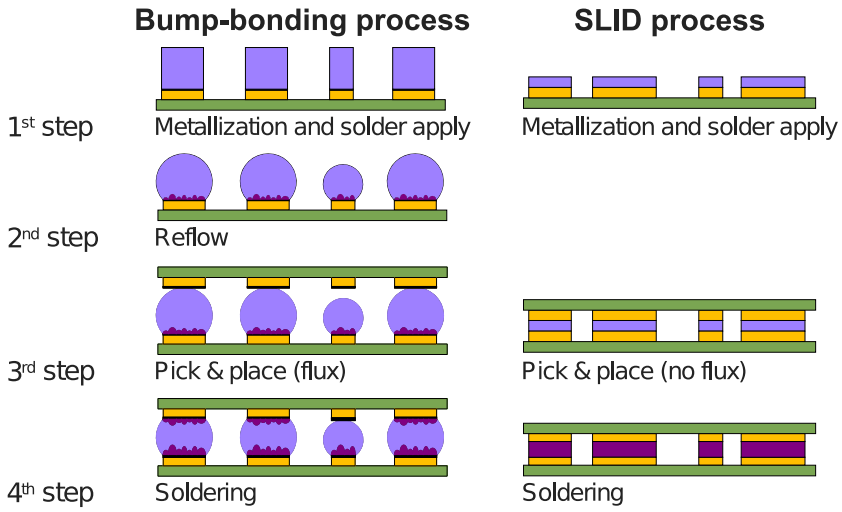

Figure 4.2: Step-by-step comparison of the bump-bonding and SLID interconnection technologies [139].

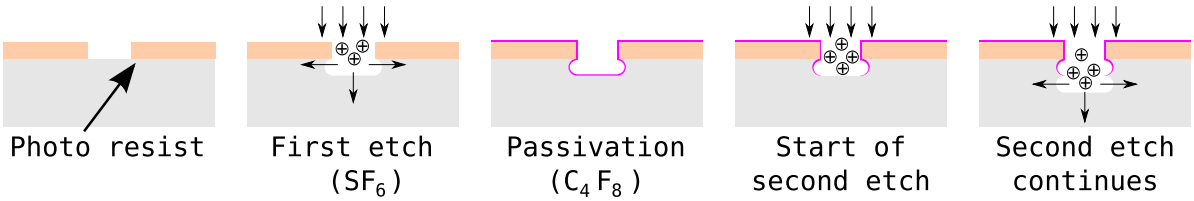

Figure 4.3: Schematic representation of the Bosch process.

also leads to a lower occupancy.

A challenge imposed by the SLID interconnection technology is, that reworking of connected layers is not possible. While for the bump-bonding technology, modules with an insufficient amount of working connections could be heated up, disassembled, and re-attached, the SLID interconnection cannot be undone, once it is formed.

4.1.2 IZM Inter-Chip Vias

ICVs allow for a vertical signal transport through silicon devices. They are formed in two consecutive processing steps, namely via-etching with the DRIE process (also called the Bosch process [146]) and via-filling with tungsten. The DRIE process is visualized in Fig. 4.3 and is a sequel of alternating, often repeated etching and passivation steps. In a first step an etch-resistant photo-resist is patterned onto the device surface to define the via positions. In the following etching step the devices are treated with SF_6 ions being

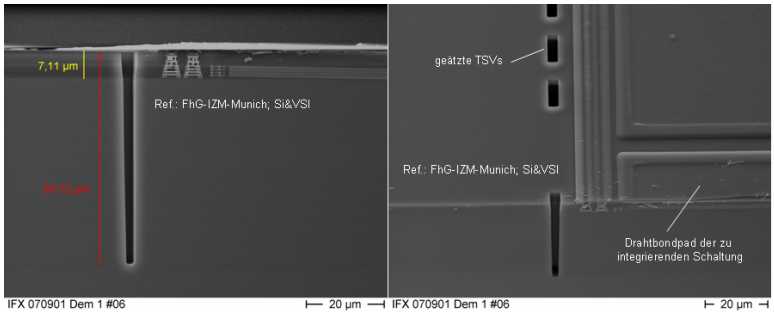

(a) Cross-sections of etched vias without filling.

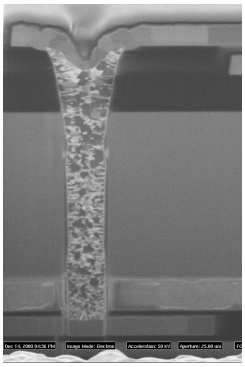

(b) An ICV filled with a tungsten plug.

Figure 4.4: Scanning electron microscope images of empty and filled ICVs [139]. In (a) a side view and an inclined view of empty vias are shown, in (b) a side view of a filled via is given.

accelerated perpendicular towards the surface of the device. This leads to an anisotropic etching which mainly progresses vertically into the silicon. Due to diffusion and reflection of the incident ions, also some etching in the horizontal directions is taking place which is retarded by the passivation steps. For the passivation the devices are covered with a layer of C_4F_8 which also coats the inside of the etched hole and acts as a short-term etch resist for the SF_6. Under the head-on bombardment during the following etching step, the C_4F_8 forming the bottom layer of the hole will be etched away first, allowing for the hole to grow deeper. However, due to the anisotropic etching, the passivation of the side walls will persist until the end of the etching step. This can be repeated many times to arrive at deep, but slim tunnels within the silicon.

With the IZM via-formation process, vias with a cross-section of $3 \times 10\,\mu\text{m}^2$ and a depth of $60\,\mu$m can be etched into silicon devices (Fig. 4.4(a)). They are passivated with tetraethyl orthosilicate and afterwards filled with tungsten in a chemical vapor deposition (CVD) process (Fig. 4.4(b)). The pixel module introduced in Sec. 1.4 will use such ICV etched from the front-side to route the signals from the front-side to the back-side of the ATLAS pixel readout chip. As these chips have an initial thickness of around $650\,\mu$m they have to be thinned down from the back-side after the via filling until the vias are exposed. After the thinning, an additional processing step is needed to form the metal contact pads on the back-side.

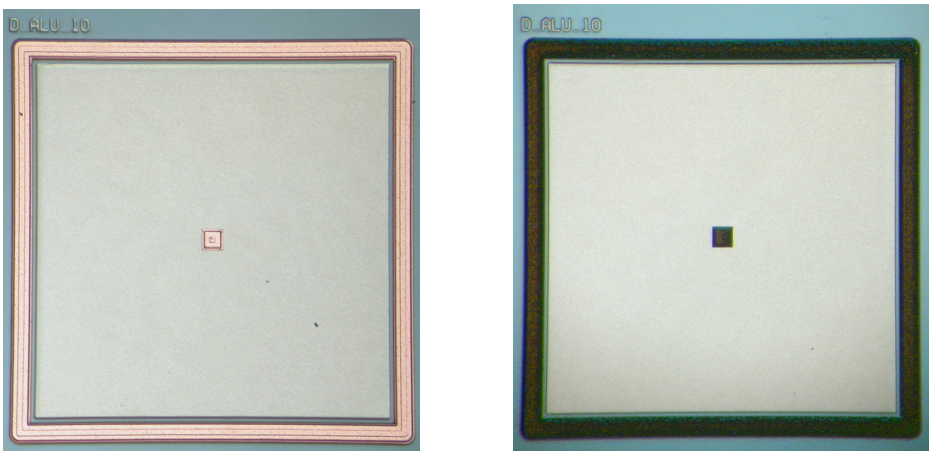

(a) Wafer 1: Cu as top layer (b) Wafer 2: Sn on top of Cu

Figure 4.5: Images of thin p-in-n diodes used to test the performance of the TiW diffusion barrier. The Cu can be seen as a pale orange surface while the Sn appears black under the coaxial illumination.

4.2 Influence of the SLID process on silicon sensors

A first prototype production of diodes subjected to the SLID metalization and temperature treatment was carried out to verify the functionality of the TiW diffusion barriers on thin silicon sensors. This was advisable, since the SLID interconnection was only known to work with IC devices. Compared to these, the performance of sensors, usually made from high resistivity silicon, is much more sensitive to high leakage currents caused by an introduction of copper atoms.

To model both sides of the SLID metalization, two 6-inch wafers with various thin p-in-n diodes were produced. The p-in-n option was chosen since no difference in the sensitivity of p-in-n and n-in-p sensors towards copper atoms is expected and the n-type wafers were easily procurable. The implemented diodes have an area of $10\,\mathrm{mm}^2$ with different guard-ring designs and are thinned down with the HLL thinning technology to an active thickness of $50\,\mu\mathrm{m}$. Together with the handle wafer, the total thickness of the wafers is $500\,\mu\mathrm{m}$. On both wafers, a 100 nm thin layer of TiW was applied to the aluminum contact pads of all diodes, followed by an electroplating of Cu. For the first wafer the thickness of the Cu is around $1\,\mu\mathrm{m}$ and no further layers are applied (Fig. 4.5(a)). The second wafer was equipped with $5\,\mu\mathrm{m}$ of Cu and $1\,\mu\mathrm{m}$ of Sn (Fig. 4.5(b)). Hence, both sides of the SLID metalization are replicated separately. A connection between the wafers was not performed. The reduced thickness of the Cu layer on the first wafer of $1\,\mu\mathrm{m}$, compared to the $5\,\mu\mathrm{m}$ used in the SLID connection, should be enough to investigate the full impact of a possible copper diffusion. For the second wafer, the thickness of

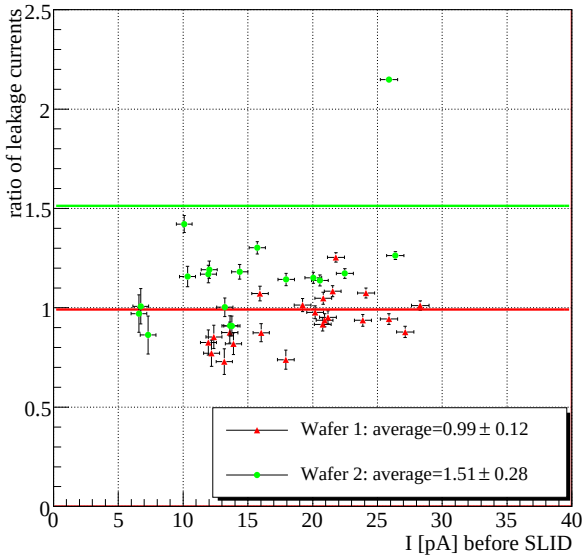

Figure 4.6: Ratio of leakage currents of the thin p-in-n diodes as a function of the leakage current after the application of the SLID metalization.

the Sn was chosen to be a little less than half of the 3 μm used in the SLID process. This ensures, that the Sn can be completely absorbed by the single Cu layer of the wafer.

In a first step the leakage currents of the diodes were measured before the application of any SLID metal layers. The same diodes were measured after the application of the TiW and Cu for the first wafer and TiW, Cu, and Sn for the second wafer. Shown in Fig. 4.6 is the ratio of the leakage currents of the measured diodes of both wafers at 50 V. The currents were determined by a linear fit in the plateau region of the leakage current characteristics. The bars given, denote the standard deviation and were calculated from the measurement uncertainties of the Keithley 487 picoamperemeter [147] and the fit uncertainties. The diagrams show that the leakage currents of the diodes on both wafers do not increase dramatically. On wafer 1, the average current of the diodes at 50 V is unchanged while on wafer 2, it increases by about 51%. However, a large contribution to the increase is given by one single diode which revealed a processing fault when investigated under a microscope. The fault itself is likely not correlated to the SLID processing but the measurable effect of it changed during the processing. Removing this diode from the analysis an average increase of only 18% is seen. These measurements show, that during the application of the SLID metalization no copper diffuses into the sensor, since this would lead to an increase of the leakage current by several orders of magnitude.

In a next step, both wafers were heated at the IZM in the standard processing

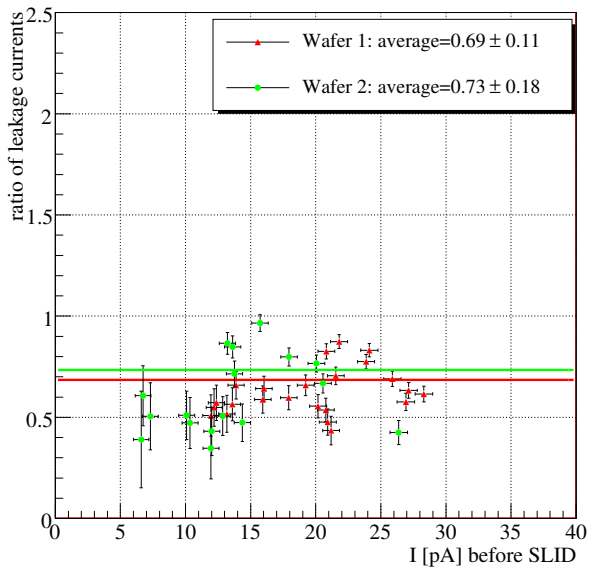

Figure 4.7: Ratio of leakage currents of the thin p-in-n diodes as a function of the leakage current after the SLID temperature treatment with respect to the untreated diodes.

atmosphere to 320°C for 15 minutes to simulate the SLID temperature treatment, and to start the solid-liquid interdiffusion of the Sn into the Cu. An actual connection of the wafers was not performed. After the temperature treatment, the leakage currents of the diodes showed a slight decrease (Fig. 4.7). Compared to the measurements before any SLID processing steps, the currents are only 69% and 73% of the initial values for wafer 1 and 2, respectively.

This can be explained by a beneficial annealing of defects during the heating phase of the SLID processing (cf. Sec. 2.2.4). Such defects can be introduced during the wafer fabrication and processing but usually do not severely affect the sensor performance. The diode exhibiting the increased leakage current in Fig. 4.6, had to be removed for the last set of measurements, since it showed an early junction break-down.

Summarizing the presented measurement of the thin p-in-n SLID prototype diodes, the TiW diffusion barrier presents an effective means to prevent the introduction of copper atoms into the silicon sensor. The leakage currents, after the application of the materials needed for the SLID connection, only slightly increase and show that no copper has diffused into the sensor. After the SLID temperature treatment the leakage currents even decrease below those of the untreated diodes. Hence, the SLID interconnection does not pose a threat to the performance of thin sensors and can be used for the production of the first demonstrator modules.

4.3 Efficiency and alignment precision of the SLID interconnection

One of the key performance parameters to judge the applicability of the SLID interconnection technology for a future ATLAS pixel module is its connection efficiency p. It is defined as the probability that a given single SLID connection is successful. The corresponding inefficiency, i.e. the probability $p_{\text{not}} = 1 - p$ of a fault of a given connection, is the figure of merit commonly used and given in the results below. To calculate the inefficiency from measurements of structures with a group of serial SLID connections, a binomial probability distribution can be assumed. From the number n of SLID connections per group and the fraction P of groups with all connections working,

$$p_{\text{not}} = 1 - P^{1/n} \tag{4.1}$$

is derived. The inefficiency should be as low as possible and was required to be smaller than 10^{-4} for the present ATLAS pixel modules [39].

To measure p_{not} of the SLID interconnection, its dependency on the alignment precision, and the sensitivity to disturbances of the device planarity, a second SLID prototype production was carried out. For this, a 6-inch wafer layout was designed at the MPP which includes a total of 152 test devices. The design of the wafer (Fig. 4.8(a)) does not use implants but just contains a structured metalization on top of the SiO_2 passivation. The SLID contact positions are symmetric with respect to the x-axis and hence, two of these wafers can be connected by rotating one around its symmetry axis by 180° and placing it onto the other. Through this, the 76 devices in the northern half of one wafer, which are referred to as sensor devices, are connected to the 76 chip devices of the southern part the other wafer.

A large fraction of the area of each device is filled with daisy chains which are a serial wiring scheme of a large group of SLID connections in a row with alternating aluminum traces on the sensor- and chip-side (Fig. 4.8(c)). If a potential difference is applied to the ends of a daisy chain, a current can only flow provided all SLID connections are functional. Hence, a large number of SLID connections is tested at the same time. The daisy chains of the 76 devices of the sensor side are equipped with aluminum traces leading to contact pads for needle probes at the ends of the daisy chains (Fig. 4.8(b)). On the chip devices, there are no traces since this part of the devices is cut off during the singularization to enable access to the contact pads of the sensor devices. Hence, after connecting two wafers only those 76 interconnected packages can be used where the sensor devices are on the lower wafer which is not cut.

Rows 1 and 2 of larger devices above the horizontal wafer axis contain daisy chains which have the same geometry as an ATLAS pixel sensor. This means that the metal traces occupy the same areas as the pixel implants do in the sensors. In addition, aluminum lines are implemented to connect every second pair of traces to form an open

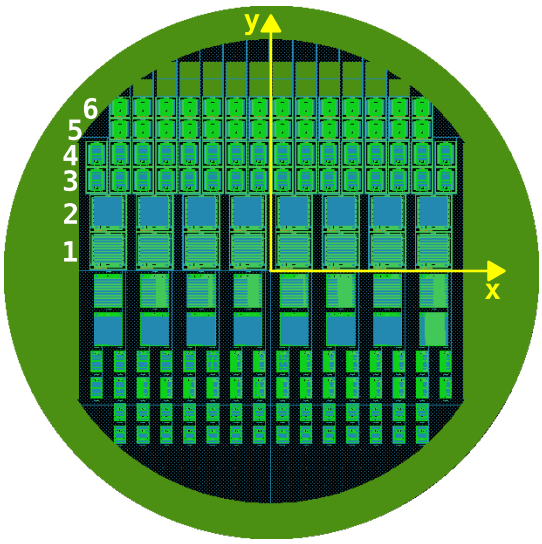

(a) Wafer map of the SLID dummy devices.

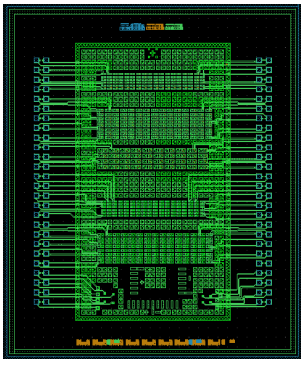

(b) A sensor device with contact pads.

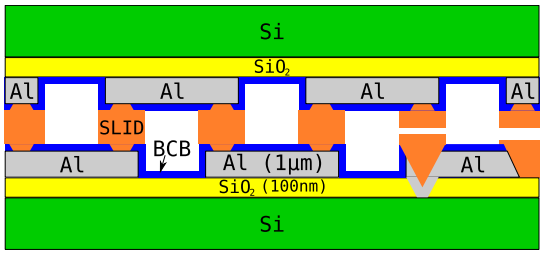

(c) Schematics of a daisy chain.

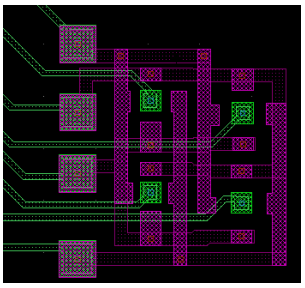

(d) An electrical alignment structure.

Figure 4.8: An overview and detailed schematics of the SLID prototype production.

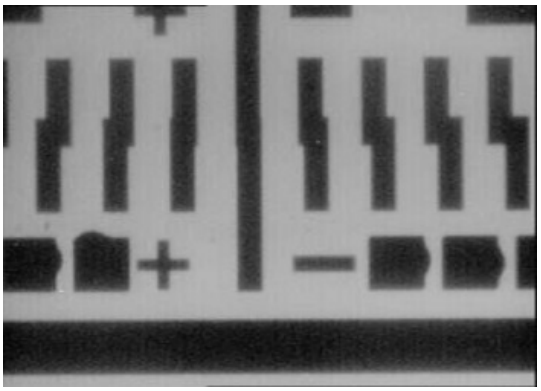

Figure 4.9: Infrared image of a well aligned vertical alignment vernier scale. A perfect alignment is reached if only the central long aluminum lines of both wafers completely overlap. For each 6 μm of misalignment, the lines that completely overlap are shifted by one to the left or right.

chain. The SLID connection of open chains from chip and sensor devices leads to closed, i.e. conducting chains (Fig. 4.8(c))). In row 1, the SLID pad size is $27 \times 58\,\mu\text{m}^2$ with a small pitch of 50 μm and a large pitch of 400 μm. They correspond to the foreseen SLID connection pads for the single chip demonstrator modules. The chains of row 2 have identical pitches but the SLID pads are of similar size as the n-type implants in the ATLAS pixel sensors, i.e. $27 \times 360\,\mu\text{m}^2$. Within the smaller devices in rows 3 to 6 of the wafer, a variety of SLID pad sizes and pitches are implemented in different daisy chains. They range from $30 \times 30\,\mu\text{m}^2$ with a pitch of 60 μm to $80 \times 80\,\mu\text{m}^2$ with a pitch of 115 μm. In addition, in rows 3 and 4 there are chains implemented which have a deliberately introduced area, where either the SiO_2 or the aluminum layer is missing. This leads to a lowering of the SLID pads by 100 nm and 1 μm, respectively (cf. right side of Fig. 4.8(c)). With these degradations of the device planarity the sensitivity of the SLID interconnection to surface imperfections is investigated.

Next to the different daisy chains, optical and electrical alignment structures are introduced in the devices. The optical alignment structures are aluminum vernier scales that are implemented partly on the sensor- and partly on the chip side of the packages (Fig. 4.9). They are evaluated with an infrared microscope which allows to look through the silicon wafer package but not through the aluminum scales. With the implemented design of the scales, the relative misalignment between the devices can be measured to an accuracy of 3 μm. The electrical alignment structures consist of SLID pads that are only connected, if the devices are misaligned. A section of the wafer map containing one of the alignment structures which measures a misalignment of $(2.5 - 15)\,\mu$m is shown in Fig. 4.8(d). Further alignment structures on each device allow for measuring

a misalignment of up to 30 μm. The structures shown in green are located on the sensor wafer and consist of eight metalized squares, four small ones and four larger ones covered by the red squares. On the left, eight aluminum traces lead to pads for needle contacting (not shown). The structures drawn in red are on the chip side and also contain four large square contact pads and several more SLID pads connected to the large squares with aluminum lines. In the presented case of perfect alignment, the four large square contacts of both sides are connected while the small green square contacts have no counter part on the chip side. If a misalignment of e.g. 3 μm is introduced, the lower left SLID pad in Fig. 4.8(d) can contact one or two of the surrounding red structures of the chip side. This forms a conducting channel which can be identified by contacting the corresponding needle probing pads. Hence, not only the magnitude but also the different directions of the misalignment can be identified since the sensor side contact squares will connect to different counterparts.

4.3.1 Wafer-to-wafer interconnection

A first wafer-to-wafer SLID interconnection with thinned chip devices has been carried out on two pairs of wafers to evaluate the connection inefficiency, the wafer-to-wafer alignment, and the sensitivity to surface imperfections. For this, both wafers were first equipped with the corresponding SLID metalizations. The wafers, which supply the chip devices are furthermore thinned down to 200 μm to test the chip-thinning process of the IZM. In this process, the wafers are glued face-down to a UV-release tape as a handling substrate and thinned down from their back-side. Then the back-side is glued to a silicon handling wafer with a polymer glue, and the UV-release tape is removed after submitting it to ultraviolet light. While glued to the silicon handle wafer the devices are singularized with a standard diamond saw. With this procedure a thinning and dicing of the chips is possible without loosing the relative alignment of the devices of this wafer.

The wafer-to-wafer connection is carried out as explained before and in a last step the handling wafer is removed with a chemical solvent. The singularized chip devices are now SLID connected to the sensor devices of the full wafer, while the intermediate silicon pieces are not connected and can be removed. This reveals the openings needed to contact the needle probe pads of the various test structures of the sensor devices. Because the dicing was performed with a standard diamond saw, only straight cuts could be performed. As a consequence, only the sensor devices from rows 1 and 2 or rows 3 to 6 of the lower wafer can be measured, since it was not possible to open the access to all needle probe pads without sawing through the chip devices. This motivated to interconnect two pairs of wafers. In the first pair, the dicing is performed to access the small devices in rows 3 to 6 while in the other pair, the large devices in row 1 and 2 with the pixel sensor like daisy chains can be tested.

The measurements of the SLID daisy chains were carried out with a Keithley 6517A electrometer [147], supplying a small voltage to the ends of the chains and measuring the

Pad size [μm^2]	Pitch [μm]	Aplanarity [μm]	Connections measured	Inefficiency $p_{\text{not}}[10^{-3}]$
30×30	60	–	8288	< 0.36
80×80	115	–	1120	< 2.7
80×80	100	–	1288	< 2.3
27×60	$50, 400$	–	24160	0.5 ± 0.1
30×30	60	0.1	5400	1.0 ± 0.4
30×30	60	1.0	5400	0.4 ± 0.3

Table 4.1: Geometrical parameters and performance of various SLID connection options.

current. Through this, also the resistance of the chains can be measured and a mean resistance per SLID connection can be determined. For most of the chains all SLID connections were functioning resulting in finite resistances ranging from $(0.25 \pm 0.12)\,\Omega$ to $(1.5 \pm 1.7)\,\Omega$ per SLID connection, where the uncertainties are given by the standard deviation of measurements from various equivalent chains. The chain resistances do not directly correlate to the size of the SLID pads but rather to the number of SLID connections per row ranging from 46 to 302 connections. This leads to the conclusion that the dominating contribution to the resistance is not caused by the SLID metal layers, but rather by the contact between them and the aluminum traces. This contact is made by creating an opening in the BCB passivation layer covering the whole wafer (Fig. 4.8(c)) and has the same diameter for all pads of all chains.

Table 4.1 summarizes the results of all daisy chain measurements and includes the total number of SLID connections tested. The SLID inefficiency is less than 10^{-3} for most of the chain types. In those cases, where no interrupted contacts were found, an upper limit at a 90% confidence level is reported. This was the case for almost all daisy chains types without the variations in the SLID pad height, due to missing aluminum or SiO_2. Only in the case of the structures of row 1 where 24160 contacts were measured, 10 out of 80 chains with 302 connections each were interrupted. Those chains which have a variation of the SLID pad height also show small inefficiencies comparable to the other chains. Even the chains with the missing aluminum below the SLID pads result in a connection inefficiency of $(0.4 \pm 0.3) \cdot 10^{-3}$, clearly showing that the SLID interconnection is not severely affected by variations of the surface planarity up to $1\,\mu$m.

The optical inspections of the vernier scales as well as the measurements of the electrical alignment structures showed a very good alignment accuracy of better than $5\,\mu$m for the first and about $(5 - 10)\,\mu$m for the second pair of interconnected wafers.

4.3.2 Chip-to-wafer interconnection

A second interconnection test of the SLID wafers was carried out in a chip-to-wafer process. For this, the wafers supplying the chip devices were cut before the placement onto the handle wafer. The chip placement is done with a pick-and-place machine that positions the single devices on the handle wafer where they are glued to the desired positions. This is done row by row, and every two rows a different pick-and-place tool had to be used, since each tool only fits one size and for this R&D project the device sizes vary. Finally, also here the handle wafer is rotated and placed onto the wafer with the sensor devices. The SLID connection is formed and the handle wafer is removed by a chemical solvent.

Due to two problematic steps during the processing, the success of this SLID interconnection test was not as good as expected. The first problem was caused by the exchange of the pick-and-place tool which had to be done to pick up the chip devices of different sizes. During this exchange, an offset of the calibration of the pick-and-place machine was introduced which could not be retracted. Since this was known before the interconnection process, one of the three pairs of rows were selected to be used for the alignment. For this, rows 1 and 2 were chosen because they contain the most interesting daisy chains which resemble the ATLAS pixel geometry. The second problem was due to the loss of two complete SLID test wafers. As a consequence, the last sensor wafer which was not cut yet had to be equipped with singularized chip devices of three different already thinned wafers. Even though the thickness of each wafer after the thinning is very homogeneous, variations between the wafers can reach several micrometer. Hence, next to the large misalignments also large variations in the thickness of the chips are created.

Figure 4.10(a) depicts the vertical and horizontal misalignment of all structures after the SLID interconnection, measured at the IZM with infrared cameras and a pattern recognition software. The row numbering corresponds to the one in Fig. 4.8(a). Considering all devices, the average misalignment is $(-17.9 \pm 13.5)\,\mu$m in the x-direction and $(10.3 \pm 7.8)\,\mu$m in the y-direction, where the uncertainties denote the standard deviation of all device measurements. Since the alignment was performed on the basis of the alignment marks in row 1, this row showed the smallest deviations from the ideal position of all rows. However, the average misalignment of row 1 of $(-2.8 \pm 3.0)\,\mu$m in x and in $(12.6 \pm 2.9)\,\mu$m y shows that the alignment in the y-direction is much worse than in the x-direction and not compatible with zero. For rows 3 and 4, as well as rows 5 and 6 a pairwise similar distribution of the misalignments is visible. This is likely correlated to the exchange of the pick-and-place tool after the assembly of rows 2 and 4. The linear correlation between the misalignment in x and y for these four rows, hints to a rotation of these rows with respect to row 1. But, evaluating the change of the misalignment within this rows clearly disproves this. However, there are some single devices which showed a rotational misalignment. In Fig. 4.10(b) two infrared pictures from the two

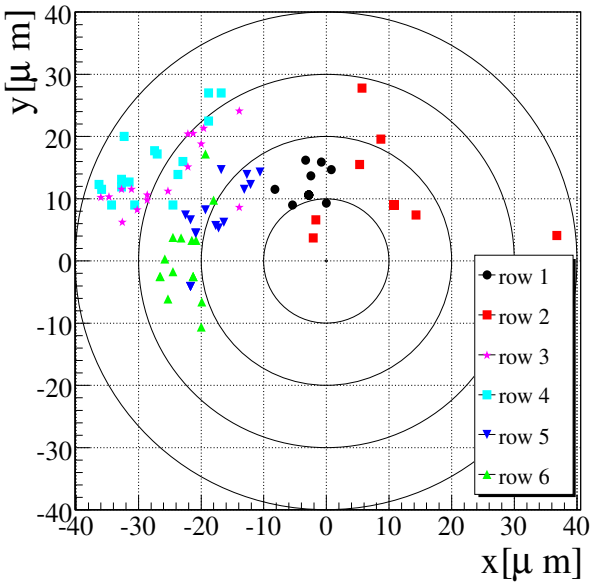

(a)

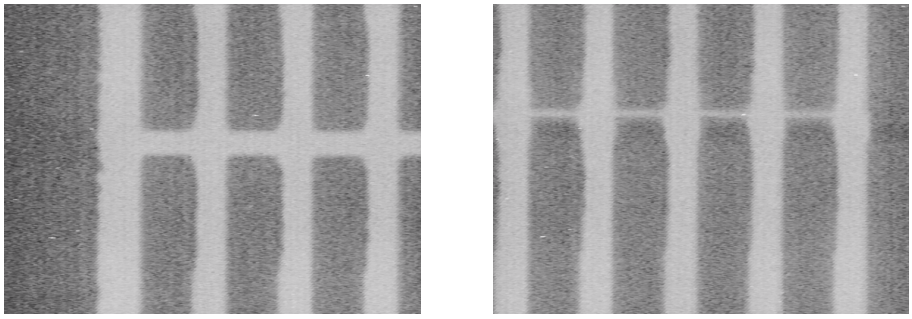

(b)

Figure 4.10: Summary of the alignment precision of the chip-to-wafer interconnection. The vertical and horizontal misalignment of all devices after the chip-to-wafer interconnection are shown in (a). In (b) two horizontally opposing sides of the same device package are depicted and indicate a rotational misalignment of the connected devices.

ends of the same daisy chain, located in row 1, are presented. The different gap widths reveal a change in the alignment of the SLID pads within the chain, being a clear sign for a device rotation which was estimated to be 0.3°.

Given the large misalignments and the large variations of the chip thickness, naturally many of the daisy chains do not function correctly. This includes all chains of rows 3 to 6 with a pad size of $30\times30\,\mu\text{m}^2$ and 25 of 60 measured chains with a pad size of $50\times50\,\mu\text{m}^2$. From another 60 chains with a pad size of $80\times80\,\mu\text{m}^2$ nine do not function. In rows 1 and 2 out of 16 devices with chains comprising pad sizes of $27\times58\,\mu\text{m}^2$ and $27\times360\,\mu\text{m}^2$, eleven are not connected properly. With such a high number of non-functioning chains, where probably none of the SLID connections is working, a calculation of the SLID connection efficiency on the basis of a binomial distribution is not meaningful.

In summary, the results obtained from the measurements of the chip-to-wafer SLID test devices leave much room for improvement. Especially the alignment precision of the single devices on the handle wafer was lower than expected, and led to problems in many of the daisy chains. However, these problems are not tied to the SLID interconnection process itself but rather to the tool exchange of the pick-and-place machine. In the future production of pixel modules this will not be needed, since all readout chips have the same dimensions. Also the problems caused by the different thicknesses of the chip devices are not expected since the readout chips will be thinned to a uniform thickness before they are connected to the sensors. Hence, these results do not disqualify the SLID interconnection technology for the use in a future ATLAS pixel module.

4.4 ICV-SLID for a single-chip demonstrator module

To give a proof of principle for pixel modules, successfully using thin sensors and the novel 3D-Integration technology, two different options of a single-chip demonstrator module are being pursued. Both options will use thin pixel sensors from the main production, connected with the SLID technology to an ATLAS FE-I2 readout chip[3]. For the extraction of the digitized output of the FE-I2 chip, option A (Fig. 4.11) will use a fan-out structure on the sensor side. This fan-out can be connected with wire bonds to a pixel readout system. Since no ICV are needed, the FE-I2 chips are not thinned. In option B, the signals will be routed through ICVs which will be integrated into the FE-I2 readout chips. As explained before, the dimensions of the vias are $3\times10\times60\,\mu\text{m}^3$. Therefore, the chips are thinned down after the via formation to a thickness of around $50\,\mu$m. In this way the vias are accessible from the back-side and the wire bonds can be connected to aluminum pads that will be electroplated onto the via openings.

The footprint of the sensor for the FE-I2 readout chip is depicted in Fig. 4.12(a).

[3]The ATLAS FE-I2 chip is very similar to the FE-I3 chip presently used in the ATLAS pixel detector, but for minor internal differences. However, it is much easier available at wafer scale than the precious FE-I3 wafers that are kept for possible repairs.

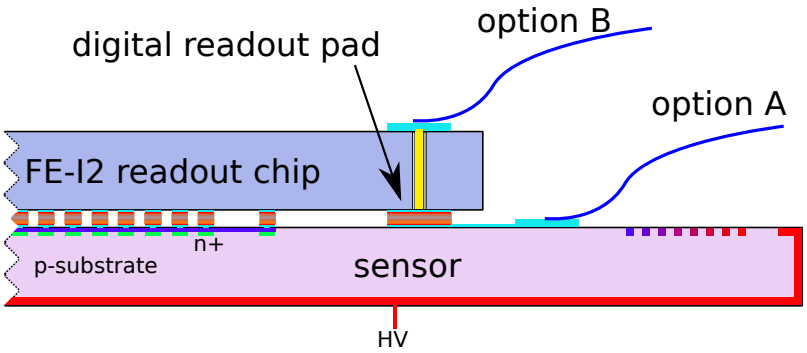

Figure 4.11: Schematics of the two options for the single-chip demonstrator module under production. Option B uses an ICV, whereas option A uses a fan-out structure on the sensor side to transmit the digital signals from the readout chip to the data acquisition system.

Each pixel channel will receive a SLID pad of $27 \times 58\,\mu\text{m}^2$, and the pixel cells of the readout chip will have a corresponding counterpart resulting in a total of 2880 SLID connections to read out the pixel cells. In addition, 47 SLID pads are used to connect the FE-I2 digital readout pads (bottom part of Fig. 4.12(a)). Further SLID connections are placed in the area of the end of column region of the chip (Fig. 4.12(b)). They are needed to evenly distribute the pressure over the whole chip and sensor area during the SLID interconnection process and are not electrically connected to either of them. In this way a total fraction of 14% of the whole chip area will be covered with SLID pads.

To ensure a good electrical connection to the back-side of the readout chips, several ICVs will be placed in the area of each digital contact pad. Figure 4.12(c) shows, how these vias will be arranged. A $(2.4-3)\,\mu$m wide trench surrounding the ICVs, etched and filled using the same technology as for the ICVs, will be used as an additional isolation of the group of vias towards the rest of the chip.

4.5 Conclusions

During the last years, the novel 3D-integration technologies are gaining popularity in the field of semiconductor manufacturing since they offer a variety of functional benefits. Some of these benefits like an increased compactness of multi-layer packages and the ability to connect devices optimized for different tasks, can also be exploited for the construction of pixel detector modules.

A first prototype production of thin p-in-n diodes was carried out to verify that the ICV-SLID technology can be applied to high resistivity sensors without deteriorating their performance. A second prototype production was carried out to produce wafers

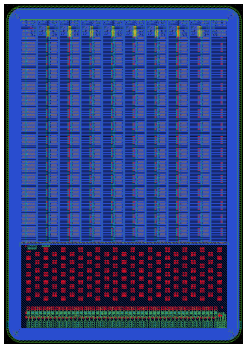

(a) Full size pixel sensor with SLID pads.

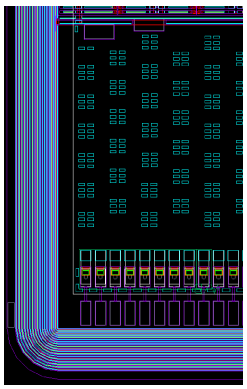

(b) Close-up of the mechanical support structures.

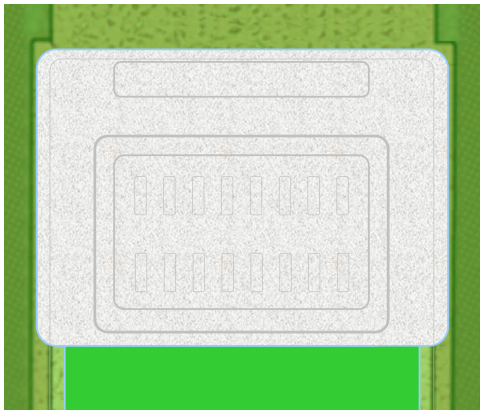

(c) Planned positions for the ICV on the FE-I2 chip readout pads.

Figure 4.12: Three schematics of the projected SLID connection pads (a,b) and ICV (c). SLID interconnections are used for each pixel cell, for the digital readout pads, and also as mechanical support structures. Several ICV will be placed in the volume below the digital readout pads (c).

with various devices to evaluate the connection efficiency of the SLID technology and the alignment precision of the interconnection process. The devices that were connected with a wafer-to-wafer process showed a good alignment precision of better than $10\,\mu$m and a connection inefficiency of 10^{-4} to 10^{-3} or less for the chains where no interrupted contacts were found. In this respect, given the promising results at this early stage of the investigations, the SLID connection can be regarded as a possible alternative to the present bump-bonding technology. The devices connected in a chip-to-wafer process showed large misalignments of mostly $(20-30)\,\mu$m caused by exchanging the pick-and-place tool between assembling different rows on the handle wafer. Furthermore, the variation of the thickness of the individual chips lead to a poor performance of the SLID interconnection. However, both these problems are not expected to be present in the currently ongoing and future pixel module productions, since equally sized readout chips from the same wafer will be thinned to a common thickness before they are connected to the sensors.

Chapter 5

Optimization of the ATLAS FE-I3 readout chip for small signals

In the present ATLAS pixel detector each of the 1744 pixel modules contains 16 FE-I3 readout chips [51]. They measure the signal size of the penetrating particles in each pixel cell at a rate of 40 MHz and transmit the data to the Module Control Chip (MCC) [148] that sends it to the data acquisition system. For the upgrades of the ATLAS pixel detector a successor of the FE-I3 readout chip, the FE-I4, has been designed. This readout chip will be used for the pixel sensors of the IBL upgrade as well as for the pixel sensors in the outer layers of the future ATLAS pixel detector at the sLHC. In both cases, due to the radiation damage, the signal size which can be extracted from the attached sensors is going to decrease. Even exploiting the beneficial properties of thin sensors that show large charge collection efficiencies after high irradiation doses, the initial signal size decreases proportional to the sensor thickness. Hence, using sensors of 150 μm thickness a signal reduction of 40% is expected before irradiation compared the the present sensors of 250 μm thickness. The present discriminator threshold of the FE-I3 chip is 4 ke for the 250 μm thick sensor. Pessimistically assuming a signal size reduction by a factor of two, a target threshold of around 2 ke is needed to reach the same detection efficiency than in the present ATLAS pixel detector.

The FE-I3 and similarly the FE-I4 readout chip can be tuned for different working conditions with a set of internal configuration parameters, controlled by digital to analog converters (DACs). In this chapter, for the first time a systematic investigation of lowering the FE-I3 discriminator threshold is carried out and the standard tuning algorithm is optimized to reach a threshold of 2 ke, while maintaining the performance with respect to measured signal sizes, noise, and crosstalk. The results of this investigation are planned to be migrated to the tuning of the future FE-I4 chip which will have similar tuning options.

Section 5.1 gives an overview of the experimental setup and the FE-I3 readout chip. In Sec. 5.2, the threshold tuning procedure is introduced and an optimization of the

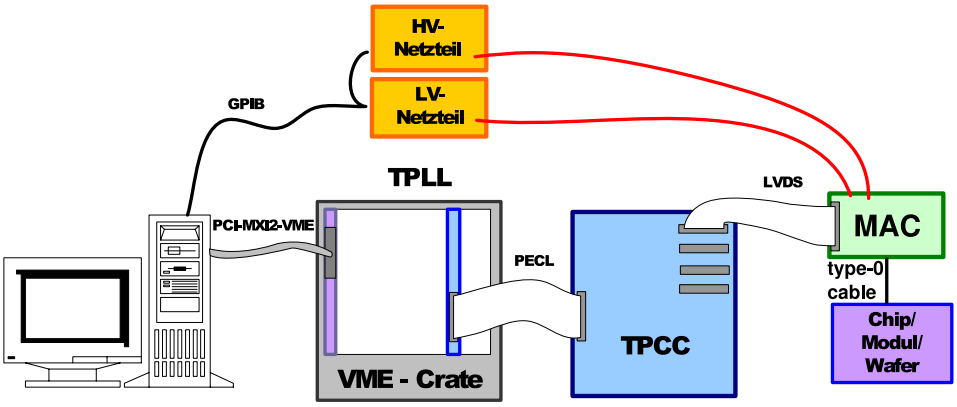

Figure 5.1: Schematics of the TurboDAQ pixel module readout setup [153].

procedure for small signal sizes is presented. The results of the threshold tuning of a full ATLAS pixel module with 16 FE-I3 chips is presented in Sec. 5.3, followed by the conclusions in Sec. 5.4.

5.1 Operation of the FE-I3

To operate the pixel module and the contained readout chips, the TurboDAQ readout system was used (Fig. 5.1), being the standard ATLAS pixel module testing equipment[1]. A detailed description of the system can be found in [151], a short overview is given here. The setup consists of the pixel module under test, which is connected with an ATLAS pixel type-0 cable [152] to a module adapter card (MAC). Via the type-0 cable the high and low voltage are supplied to the module, and the data between the module and the readout system is transmitted. The MAC is connected with a flatband cable to the Turbo Pixel Control Card (TPCC), and the high voltage (Keithley 487) and low voltage (Agilent E3646A) power supplies. Via a second flatband cable the TPCC transmits data to the Turbo Pixel Low Level (TPLL) card within a VME-Crate. A central steering PC that runs the LabWindows TurboDAQ software [153] in version 6.6, controls the TPLL card in the VME crate via a PCI-MXI2-VME interface card and the power supplies via the GPIB protocol. The software contains routines largely identical to those of the ATLAS pixel detector data acquisition system. They are used for basic operations, e.g. to read and set the control registers of the FE-I3 chips, as well as for completely automatized data-taking and chip testing. A description of the ATLAS pixel

[1]The TurboDAQ system and one ATLAS pixel module was made available by the Institute of Physics of the University of Dortmund [149]. Two further modules were supplied by the Lawrence Berkeley National Laboratory [150].

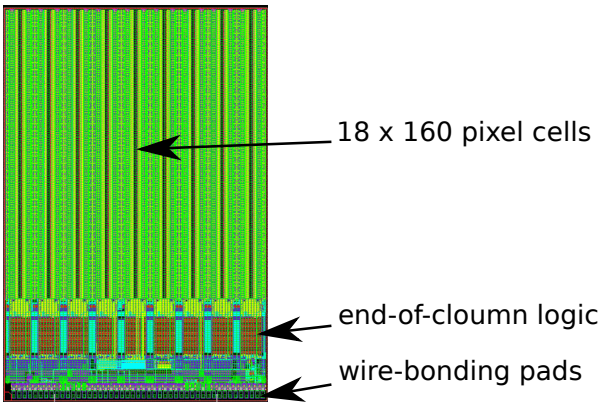

Figure 5.2: Footprint of the present FE-I3 readout chip with the pixel cells in the upper region and the end-of-column (EOC) logic block below [51].

module tests that can be performed with the TurboDAQ system is given in [154]. The tuning procedures used for the investigations presented will be outlined below.

5.1.1 The FE-I3 readout chip

The ATLAS FE-I3 readout chip (Fig. 5.2) has an area of 81.4 mm^2 and contains 2880 pixel cells which are arranged in 9 double-columns with 160 rows. Each pixel cell has a size of $(50 \times 400)\,\mu$m^2, corresponding to the size of the pixel cells of the attached sensor, and contains an analog and a digital readout block. They can be configured for different working conditions with several local DACs in each cell. In the lower region of Fig. 5.2, the end-of-column (EOC) region is shown. It contains global configuration DACs, EOC buffers to store the data collected from the pixel cells, and control blocks that accept trigger signals and transmit the data to the MCC. This is done through the 47 wire-bonding pads at the bottom of the figure.

Figure 5.3 displays the readout architecture of a single pixel channel. Arrows between the components symbolize the data flow direction. The three white triangles in the center are the first and second stage analog amplifier and the discriminator, which decides whether an input signal is above a certain threshold. The analog circuits are shown upstream of the discriminator (left side), while on the downstream side the digital components are located (right side). The blue circle marks the input connection from the pixel sensor. Two injection capacitors C_{lo} and C_{hi} in the left center are used to inject signal charges into the analog pre-amplifier for calibration and testing purposes. The signal size is controlled by the 10-bit VCal DAC that can produce 1024 different voltages which are converted to different charges Q with the injection capacitors according to

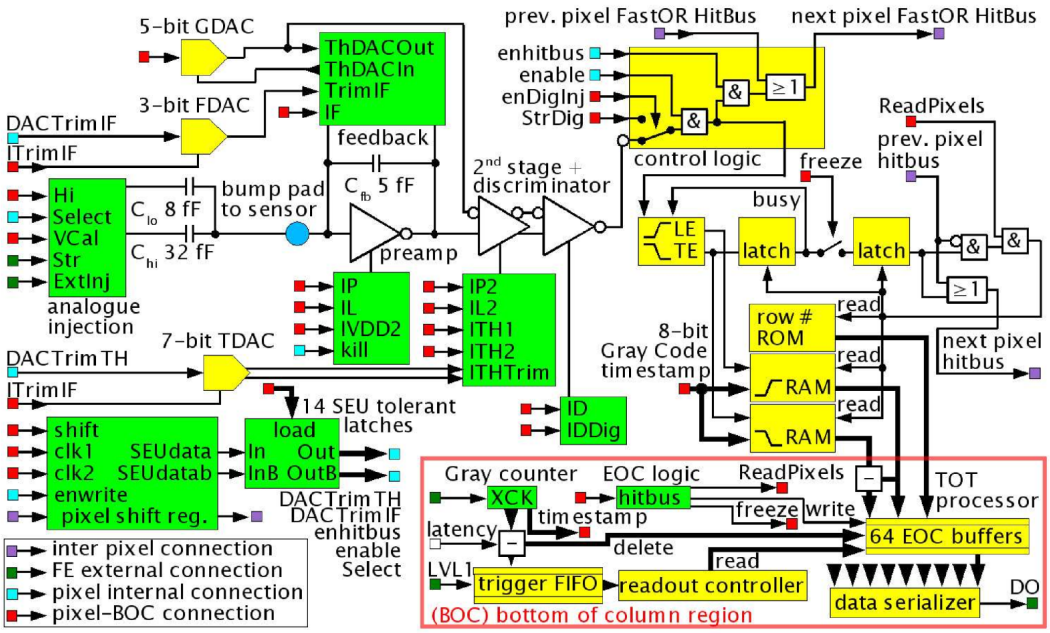

Figure 5.3: Schematics of the pixel readout architecture [151].

the equation

$$Q = C \cdot U. \tag{5.1}$$

The target capacity C can either be $C_{\mathrm{lo}} = 8\,\mathrm{fF}$ or $C_{\mathrm{lo}}+C_{\mathrm{hi}} = 40\,\mathrm{fF}$. A conversion between the VCal DAC value and the number of electrons injected can thus be calculated with

$$Q[\mathrm{e}] = \frac{C[\mathrm{F}] \cdot U_{\mathrm{conv}}[\mathrm{V/DACval}]}{q[\mathrm{C}]} \cdot \mathrm{VCal[DACval]}. \tag{5.2}$$

Here U_{conv} is the conversion factor between the DAC value and the VCal voltage. The actual parameters C_{lo}, C_{hi} and U_{conv} are determined for each channel before the module assembly and are loaded into the TurboDAQ software.

The input signals, stemming either from the capacitors or the sensor, are amplified in the charge-sensitive pre-amplifier and fed back through a feedback loop. A digital time-stamp is issued as soon as the rising edge at the discriminator input is above a predefined threshold. When most of the signal is integrated, the feedback current causes a reduction of the signal at the output of the pre-amplifier. At a certain point the trailing edge of the signal is lower than the threshold of the discriminator. This is again associated to a time-stamp in the digital electronics which measures the time over threshold (TOT) in units of 25 ns. During the data analysis the TOT value is converted back to a signal size in the data acquisition system. The left part of Fig. 5.4 shows the

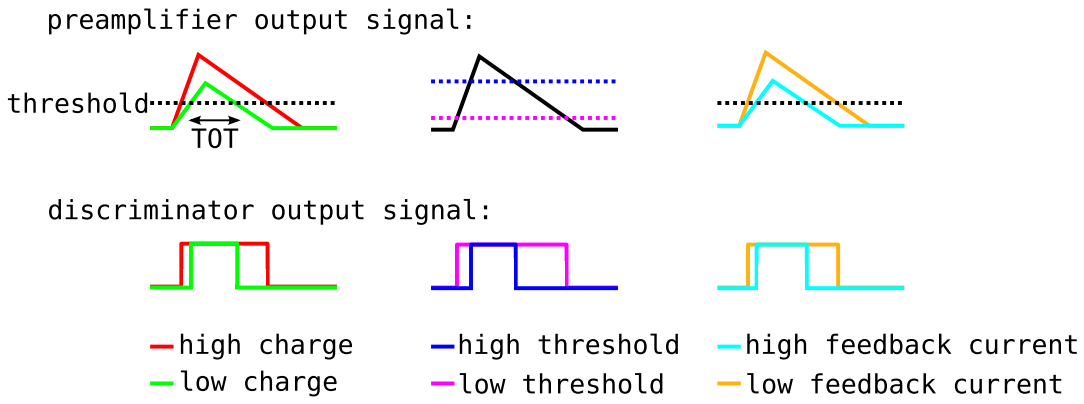

Figure 5.4: Influence of tuning parameters and input charge on the time over threshold (TOT).

	threshold	feedback current
global DAC	GDAC (5-bit)	IF DAC (8-bit)
local DAC	TDAC (7-bit)	FDAC (3-bit)

Table 5.1: Digital to analog converters to control the TOT response.

behavior of the TOT for different signal sizes. Larger signals have a steeper rising edge, i.e. an earlier first time-stamp, and stay longer above threshold than smaller ones.

There are two parameters that control how a signal is converted into a TOT: the discriminator threshold and the feedback current. The threshold of the discriminator can be varied with a 7-bit DAC (TDAC) in each pixel cell, and a 5-bit DAC (GDAC), acting globally on all pixel cells. The higher the threshold, the shorter the TOT (middle section of Fig. 5.4). The feedback current can be controlled with a local 3-bit DAC (FDAC) in each pixel cell and a global 8-bit DAC (IF DAC). A higher feedback current leads to a shorter TOT since the leading edge time-stamp is issued later and the trailing edge time-stamp sooner (right section of Fig. 5.4). In summary, Tab. 5.1 lists the different DACs used for controlling the digital signal generation.

The threshold of a pixel channel is defined as the charge that leads to a detection probability of 50% (Fig. 5.5). It is determined by the TurboDAQ threshold scan routine which uses the VCal DAC to inject a number of signals with charges in the range from 0 to 9 ke in 200 steps, where at each step 100 pulses are generated. For each of the charges Q the detection probability $r(Q)$ is measured. Signals below the threshold charge Q_{th} are rarely detected, and signals above the threshold are detected almost certainly. Since the analog amplifier and the discriminator are not ideal components, and noise from the sensor is influencing the threshold scan, the transition between $r(Q) = 0$ and $r(Q) = 1$

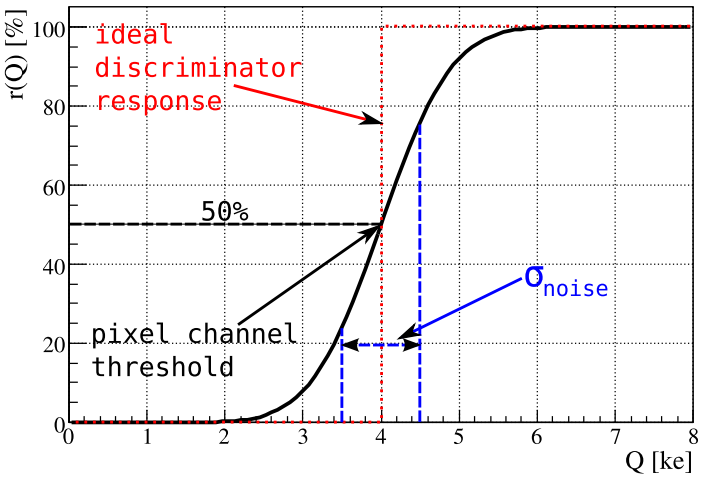

Figure 5.5: The response function, i.e. the detection probability of the ATLAS pixel discriminator for a threshold of $Q_{\mathrm{th}} = 4\,\mathrm{ke}$.

is not a Heaviside function, but an error function being the convolution ($\otimes$ operator) of a Heaviside function Θ and a Gaussian [155]

$$r(Q) = \Theta(Q - Q_{\mathrm{th}}) \otimes \left(\frac{1}{\sqrt{2\pi}\sigma_{\mathrm{noise}}} e^{-\frac{1}{2}Q^2/\sigma^2_{\mathrm{noise}}} \right). \tag{5.3}$$

Fitting the error function to the detection probability, the charge Q_{th} of the step of Θ defines the threshold, whereas the width of the Gaussian σ_{noise} gives the noise of a pixel.

The relation between the TOT and the injected charge $t(Q)$ is measured with the TurboDAQ TOT scan routine. For this several different signals of known size are injected into each pixel channel using the C_{low} capacitance. The TOT values are measured for each injection and averaged over the whole module. The heuristic function

$$t(Q) = a + \frac{b}{c + Q} \tag{5.4}$$

is used to fit the TOT dependence on the injected charge. The inverse function is later used to calculate the signal sizes from measured TOT values.

5.2 The FE-I3 tuning procedure

For the tuning of the FE-I3 chips, a target threshold Q_{T} and a target TOT t_{T} (in units of 25 ns) for a given sample charge Q_{s} are defined in the TurboDAQ software. Typical values for the standard ATLAS pixel configuration are $Q_{\mathrm{T}} = 4\,\mathrm{ke}$ and $t_{\mathrm{T}} = 30$

for $Q_s = 20\,\text{ke}$, i.e. the expected charge for a $250\,\mu\text{m}$ thick sensor. The predefined TurboDAQ tuning routines iteratively change the different DACs settings (Tab. 5.1) to approach these target values. This is done following the standard "IF DAC - GDAC - TDAC - FDAC - TDAC" tuning cycle. First the global DACs are optimized, followed by the local DACs, used for fine tuning. Since the TDAC and FDAC tunings can influence each other, an iterative tuning optimizes the results. In the following the individual tuning steps are briefly described:

- **IF DAC tuning:** The sample charge Q_s is injected multiple times for three different IF DAC settings (16, 32, 48) and the mean TOT of all channels and injections is measured for each of the three settings. In a next step an exponential function is used to fit these three data points. From the inverse fit function the IF DAC setting that will produce TOT values closest to t_T (here, $t_T = 30$) is calculated.

- **GDAC tuning:** All TDACs are set to their median value of 64, and threshold scans are performed using 5 different GDAC values (11, 14, 20, 26, 31). A mean threshold Q_{th} is measured for each value. These are fitted with the heuristic function:
$$Q_{th} = a + \frac{b}{c + GDAC}. \tag{5.5}$$
The inverse fit function approximates the GDAC setting that will produce thresholds closest to the desired Q_T.

  If in the standard tuning procedure, the final GDAC value is below 10, the tuning is considered unsuccessful, and the GDAC is set to the standard value of 16. Similarly, if a threshold of less than 1.9 ke is measured during the tuning procedure, this tuning step is discarded. These internal software limits are suitable for the standard target threshold of 4 ke, but lead to unwanted behavior when tuning for lower target thresholds Q_T.

- **TDAC tuning:** The TDAC tuning is similar to the GDAC tuning. Instead of a fit to only some of the possible values, for each of the 128 TDAC values a threshold scan is performed. The value leading to a Q_{th} closest to Q_T is used as the final setting.

- **FDAC tuning:** The FDAC tuning is used to adjust the TOT behavior of every pixel channel to the mean TOT value of the front end chip. For this, every possible FDAC value is tested for the injection of Q_s and the one leading to a result closest to the average TOT of the whole chip, is chosen as the final setting of the FDAC. Using the average value of the chip as a target value instead of t_T is supposed to lead to a more uniform behavior of the TOT within the chip.

5.2.1 The modified tuning procedure

The standard TOT tuning does not perform well for $Q_{\mathrm{T}} \ll 4\,\mathrm{ke}$ as shown below. Therefore for the presented investigations, slight but important modifications were made to the tuning procedure to arrive at lower thresholds while retaining a stable TOT behavior.

To increase the fit stability for the global IF DAC tuning, nine DAC values were chosen for the exponential fit instead of three, albeit within the same range as in the original tuning. Furthermore, the FDAC local tuning was not used to tune each pixel to the average value of the chips but rather to the target t_{T} used for the IF DAC global tuning. On top of this, the lower limits for the GDAC was reduced to 6 and the minimum valid threshold was reduced to 1 ke to allow for tunings to lower thresholds.

5.3 Tuning results

Tunings were carried out for thresholds between 4 ke and 1.7 ke with different Q_{s} settings, using the standard as well as the modified tuning algorithm. For the TOT behavior the standard ($t_{\mathrm{T}} = 30$ for $Q_{\mathrm{s}} = 20\,\mathrm{ke}$) and a low feedback current ($t_{\mathrm{T}} = 30$ for $Q_{\mathrm{s}} = 10\,\mathrm{ke}$) were chosen. The latter was motivated by reproducing the same time behavior but for the expected signal decrease of a factor of around two. The tunings were conducted with the ATLAS pixel module No. 512451, the only one available for most of the time. For the last measurements presented, two more modules (No. 511351 and No. 513092) were also used for comparing the noise behavior at very low discriminator thresholds.

Several observables were measured after each tuning, from which the most important are presented in this section. These include the discriminator threshold and noise, the TOT characteristics and the crosstalk.

5.3.1 Discriminator threshold and noise

After each tuning cycle the discriminator threshold and the threshold noise were measured by the threshold scan routine described above. Figure 5.6(a) shows the measured discriminator threshold Q_{th} as a function of the target threshold Q_{T} for the different tuning parameters of the module. The green triangles represent the standard tuning procedure with the standard feedback current, the other two represent low feedback current tunings. Of those two, the black circles show the results of the modified tuning procedure as introduced in Sec. 5.2.1 and the red squares denote the standard tuning, however, with the low feedback current. In this and the following figures the markers of the three different tuning procedures are artificially shifted on the Q_{T}-axis by $\pm 20\,\mathrm{e}$ to allow for an easier distinction between them.

In general the three different tuning procedures did not show significant differences for the measured thresholds down to around 2 ke. The bars in Fig. 5.6(a), denote

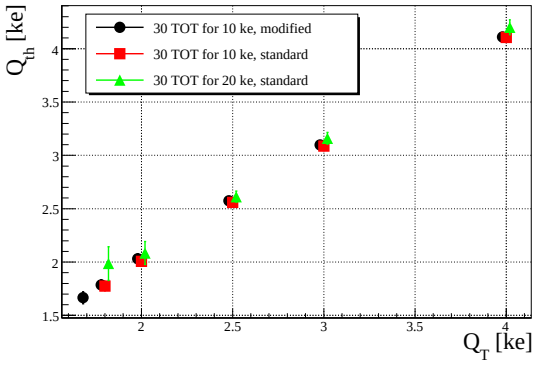

(a) Measured discriminator threshold.

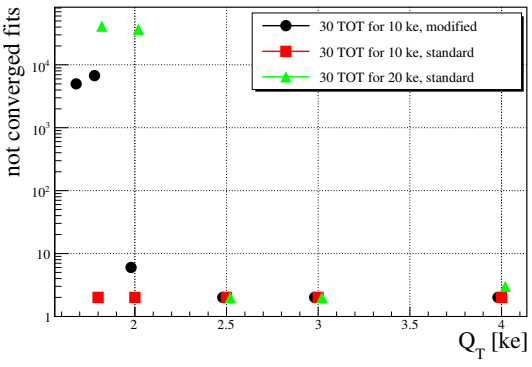

(b) Numbers of not converged fits.

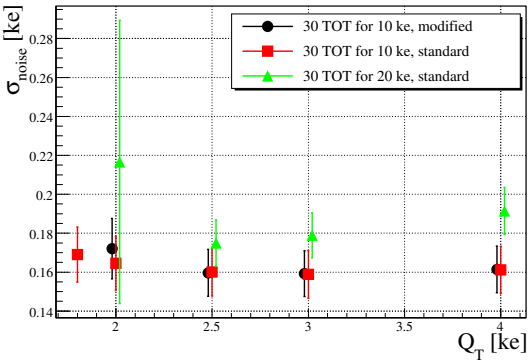

(c) Noise of the pixels.

Figure 5.6: Threshold, fit convergence, and noise performance of different tunings as functions of the target threshold Q_{T}. The bars in (a) and (c) denote the standard deviation of the distribution containing all pixel channels.

t_T[25 ns]	Q_s[ke]	procedure	average overdrive [ke]
30	20	standard	$1.4 \pm .1$
30	10	standard	$1.8 \pm .1$
30	10	modified	$1.7 \pm .2$

Table 5.2: Average overdrives of the different tunings.

the Gaussian width of the Q_{th} distribution over the whole module, indicating that the threshold of the pixel channels was very uniform, varying mostly less than 50 e.

At a threshold of around 2 ke the noise contribution to the threshold scan started to deteriorate the fit of the discriminator response so that the threshold could not be measured for some pixel channels. Figure 5.6(b) shows the number of fits which did not converge due to this for the three tuning procedures. Here it is evident that most of the 46080 fits (16 chips, each having 2880 pixel cells) for the standard feedback current failed below 2.5 ke, while for the tunings with the low feedback current a threshold of 2 ke still led to a fit success of more than 99.98%

The threshold noise σ_{noise} (Fig. 5.6(c)) was not significantly affected by the different target threshold settings. However, for the tunings with the low feedback current, the noise values were in general lower than for the standard feedback current. Due to the large number of not converging fits the fluctuations seen for the standard feedback current were much higher for $Q_T = 2$ ke.

As presented in Fig. 5.4, a small signal leads to a later crossing of the rising edge over the discriminator threshold. Below a certain signal size this delay becomes as large as the time between two bunch crossings, and the signal will be associated to the wrong time bin within the pixel detector. Depending on the operation mode, these late signals can be shifted to the correct time bin, so that the discriminator threshold yields the effective threshold. However, this signal transfer is likely not used in the regular operation mode, shifting the effective threshold to a higher value which is called the in-time threshold [62, 156]. To determine the in-time threshold, a large reference signal is injected to measure the leading edge time-stamp t_0 for all pixels. As a safety margin, this value is increased by 5 ns. Afterwards differently sized signals are injected together with an internal trigger every 25 ns. Hence, small signals with a delay of more than 20 ns compared to the reference pulse are not associated to the correct trigger and lost. The size of the smallest signal that is collected in time corresponds to the in-time threshold.

The magnitude of the threshold increase due to the late arrival of small signals, the so called overdrive, is given in Tab. 5.2 for the different tuning procedures. It shows, that the tunings using the low feedback current exhibit a larger increase of the threshold by around 400 e. Hence, the in-time threshold for the tuning to 2 ke with the low feedback current is similar to the tuning to 2.5 ke with the standard feedback current.

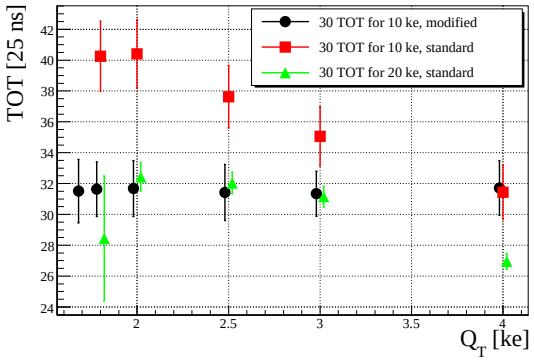

Figure 5.7: Time over threshold as a function of the target threshold for the three different tuning options.

5.3.2 Time over threshold

Figure 5.7 depicts the TOT for the injected sample charges $Q_s = 10\,\text{ke}$ or $Q_s = 20\,\text{ke}$, calculated with Eq. 5.4 and using the parameters obtained form the TurboDAQ TOT scan routine. Since $t_\text{T} = 30$ was the target of all tunings, a similar TOT is expected for each data point. However, the standard tuning procedure reveals a strong dependence of the TOT on Q_T. The reason for this is the coarse IF DAC variation in the standard tuning procedure, together with the interdependence of the following TDAC and FDAC tunings. With the modified TOT tuning described above, this dependency is not visible, since for the tuning of each FDAC t_T is used as a target value, instead of the mean TOT from the coarse IF DAC tuning. Still a constant offset of about 1.5 TOT units is seen, but this could be reduced by further iterative TDAC and FDAC tunings.

5.3.3 Crosstalk

Lowering the discriminator threshold increases the probability for crosstalk and thus, can lead to more false signals, deteriorating the pixel detector resolution and increasing the channel occupancy. The crosstalk can be measured by the TurboDAQ setup by reading out a certain pixel cell while injecting charges into the neighboring cells. For pixel cell i the crosstalk is then defined as the measured signal Q_i divided by the charge $Q_{i\pm1}$ injected in the two neighboring pixel channels:

$$X_\text{talk} = \frac{Q_i}{Q_{i\pm1}} \tag{5.6}$$

The maximum allowed average value for X_talk to qualify a pixel module for the present ATLAS pixel detector was 5% [155].

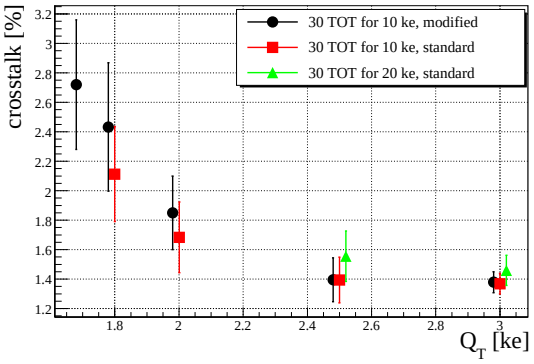

Figure 5.8: Average crosstalk measured as a function of the target threshold for the different tuning procedures.

Figure 5.8 shows the average crosstalk for those pixel channels where Q_i was above the discriminator threshold. Since for the tunings with $Q_\mathrm{T} = 4\,\mathrm{ke}$ none of the measured values was above the threshold for the tunings with the low feedback current and only one for the standard feedback current, these values are not given. Due to the large number of not converged fits at $Q_\mathrm{T} = 2\,\mathrm{ke}$ for the tuning with the standard feedback current also here a meaningful value for X_talk could not be obtained. Even though the crosstalk is increasing for decreasing thresholds, it never reaches 5% on average. Hence for each of the tuning procedures, the module met the crosstalk requirements of the present ATLAS pixel detector.

5.3.4 Investigations of correlated noise patterns at low thresholds

In the preceding measurements it was shown that a tuning of the ATLAS pixel module to discriminator thresholds down to 2 ke is possible. Below this value, noise starts to dominate and a number of pixel cells cannot be used for signal detection. The positions of the pixel cells that start to malfunction are not randomly spread over the whole module area, and also not confined to certain readout chips. They rather show a module-wide geometric pattern. To investigate the origin of this pattern, two other ATLAS pixel modules were acquired to compare their spatial noise distributions. All modules were tuned with the modified tuning algorithm with the low feedback current until the noise started to increase. This is reached at $Q_\mathrm{T} = 1.8\,\mathrm{ke}$ for modules No. 512451 and No. 513092 and at $Q_\mathrm{T} = 2\,\mathrm{ke}$ for module No. 511351. The χ^2 values of the fits to the discriminator response at these Q_T are becoming far larger than one, indicating that the measured signals are dominated by noise which alters the shape of the response function. Figure 5.9 shows the three noise maps, indicating in which regions of the module the

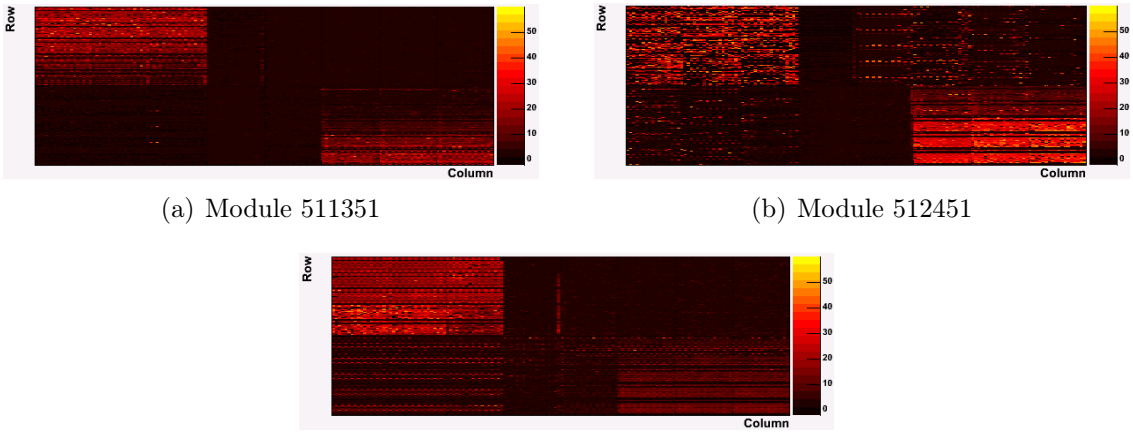

(a) Module 511351

(b) Module 512451

(c) Module 513092

Figure 5.9: Maps of the χ^2 values of the fits to the discriminator response for three different ATLAS pixel modules. Each module has a matrix of 8×2 ATLAS FE-I3 readout chips.

noise increases to high values. Even though the reason could not be linked to certain components of the pixel modules, it can clearly be seen that for all three modules the noise develops in the same regions of the module. This clearly suggests, that the lower limit for a successful threshold tuning is not given by the FE-I3 chip, but rather by some components of the assembled modules. Hence, even lower thresholds might be reachable for single FE-I3 chips, as well as for the modules of the upgraded ATLAS pixel detector which will use independent FE-I4 readout chips.

5.4 Conclusion

The result of the low threshold tuning performed is, that the threshold of the ATLAS FE-I3 readout chip can be lowered to 2 ke without negative impacts on the noise, the TOT measurements, or the crosstalk. This was reached by modifying the TurboDAQ threshold tuning procedure and by developing a more refined TOT tuning algorithm to allow smaller discriminator thresholds with a more stable TOT behavior. Setting thresholds of less than 2 ke, the noise of many pixel cells starts to increase and impedes a successful module operation. Comparing the geometrical areas where the noise starts to set in for three different modules it was shown that the cause of the noise cannot be routed to the FE-I3 chip but has to originate from other components of the module assembly. Hence, it is expected that single FE-I3 chips can be tuned to even lower thresholds.

Assuming that the successor of the FE-I3 readout chip, i.e. the FE-I4, performs similar in terms of the discriminator threshold and noise it seems well possible to use this readout chip in combination with thin pixel sensors. Especially after irradiation to high fluences it can be expected, that thin sensors will perform better with the FE-I4 readout chip than sensors of standard thicknesses.

Recently, thin sensors were attached to FE-I3 readout chips with the bump-bonding technology and attached to single-chip readout cards. With these single chip modules further laboratory measurements and test-beam operation are imminent to verify the successful operation of thin sensors with the present ATLAS readout electronics. Assemblies of thin sensors and the new FE-I4 readout chips are foreseen to be produced until the end of this year.

Chapter 6

Conclusion and outlook

Within this thesis a novel module concept was evaluated for the operation in the ATLAS pixel detector after the foreseen luminosity upgrades of the LHC. It comprises thin n-in-p pixel sensors and a new 3D-integration technology to connect the sensors to low threshold readout chips. The usage of thin sensors increases the radiation tolerance of the sensors while the n-in-p design with reduced guard-ring structures and the 3D-integration result in very compact as well as cost-efficient pixel modules. In the work presented, the components for a demonstrator module were produced and investigated for their applicability to the ATLAS pixel detector upgrades.

Before the main production of the first twelve wafers with thin pixel and strip sensors could be carried out, the parameters of the boron implantation for the inter-electrode isolation had to be defined. The simulation programs DIOS and TeSCA were used to model different homogeneous and moderated p-spray implantations and to simulate the resulting potential and electric field distributions before and after irradiation. On the basis of the simulation results, the implantation parameters for six of the twelve wafers were chosen to be 100 keV for the boron implant energy and $3.2 \cdot 10^{12}/\,\mathrm{cm}^2$ for the area dose. For the second half of the wafers a more aggressive implant option, using an implant energy of 140 keV and an implant area dose of $1.4 \cdot 10^{12}/\,\mathrm{cm}^2$, was chosen motivated by inter-strip resistance measurements of sensors irradiated with X-rays. This implant option leads to a low electric field strength and was proven to maintain a sufficient inter-strip isolation even after saturated interface damage. With these two sets of parameters, the main production of thin sensors was performed.

The characterization of the thin n-in-p sensors showed low leakage currents of $(1.6 \pm 0.2)\,\mathrm{nA/cm}^2$ and $(2.8 \pm 0.3)\,\mathrm{nA/cm}^2$ for the 75 μm and 150 μm thick diodes and full depletion voltages of $(18 \pm 5)\,\mathrm{V}$ and $(82 \pm 6)\,\mathrm{V}$, respectively, where the uncertainties are only statistical. Measurements of the thin pixel sensors showed a very good device yield of more than 98% and low leakage currents of mostly less than $10\,\mathrm{nA/cm}^2$. The break-down voltages were usually much above the full depletion voltage demonstrating that the sensors deliver the maximum signal size before irradiation. Also the thin strip

sensors can be fully depleted and therefore used for charge collection measurements. This revealed that the novel thin sensor production process does not have a negative effect on the silicon properties of the pixel and strip sensors.

The leakage currents and break-down voltages observed for the diodes with a reduced number of guard-rings, occupying only around one third of the area of the standard guard-rings, proved that an increase of the active area of the sensors is possible. Combining this observation with the results of collaborating groups that reduced the safety margin to the cutting lines of the sensors without deteriorating the U_{bd}, it is possible to reduce the width of the inactive edges to less than 500 μm. This reduction is needed to fulfill the requirements for the IBL and will likely also be required for the sLHC upgrade of the pixel detector sensors.

A subset of the thin sensors was irradiated with protons up to an integrated fluence of $10^{16}\,\mathrm{n_{eq}/cm^2}$, corresponding to the expectation for the sLHC operation. The electrical characterization showed a linear increase of the leakage current with the fluence. Even though the full depletion voltage increases to several 100 V, the thin sensors can be fully depleted at least up to a fluence of $3 \cdot 10^{15}\,\mathrm{n_{eq}/cm^2}$. However, at these fluences, not the full depletion voltage, but charge carrier trapping is the main process limiting the signal size.

A second shared production of thin sensors, produced by CiS with the epitaxial silicon growing technology, showed low break-down voltages before irradiation. Simulations with DIOS and TeSCA were carried out to identify possible causes. The simulation results clearly suggest, that the low resistivity of the epitaxial sensors leads to very high electric field strengths at the sensor surface causing the unfavorable break-down behavior. This shows one advantage of the HLL production process which can be used to produce thin sensors of high resistivity.

The main figures of merit for irradiated sensors are the charge collection efficiency (CCE) and the noise. Simulations of the CCE, were carried out with a Monte Carlo algorithm developed within this work that includes models for charge carrier trapping and avalanche multiplication. They affirm the beneficial properties of thin sensors compared to those of standard thicknesses and show that according to the present damage models the CCE is expected to decrease to 30% and 15% in the 75 μm and 150 μm thick sensors after $\Phi_{\mathrm{eq}} = 10^{16}\,\mathrm{n_{eq}/cm^2}$. The measurements of irradiated strip sensors with the Alibava readout system using a newly developed noise subtraction method have shown a higher CCE than expected from the standard irradiation damage models. A CCE of almost 90% was found for the 150 μm thick sensors after $\Phi_{\mathrm{eq}} = 10^{15}\,\mathrm{n_{eq}/cm^2}$, and values compatible with 100% were measured for the 75 μm thick sensors up to a fluence of $\Phi_{\mathrm{eq}} = 3 \cdot 10^{15}\,\mathrm{n_{eq}/cm^2}$. Likely, these high CCEs are a consequence of the high electric field strengths in the thin irradiated sensors which could lead to both, a field enhanced de-trapping of the charge carriers (e.g. the Poole-Frenkel effect) and an avalanche multiplication process. However, the avalanche multiplication has to be quenched by another process since the increase of the CCE with the applied bias voltage is not very steep. A

possible interpretation of this behavior was qualitatively given by the simulation, predicting that only in a very restricted volume the electric field is high enough such that multiplication can take place. Nevertheless, a quantitative agreement with the measurements could not be reached and therefore further modeling is needed to understand the high CCE after irradiation. The measured noise values are dominated by the noise of the analog readout chips and the input capacitance provided by the attached sensors. A dependence on the higher leakage currents present in irradiated sensors is not visible.

Regarding the 3D-interconnection technology, the SLID metalization was for the first time tested on thin pad sensors. The measurement of the leakage currents after the metalization and the SLID temperature treatment demonstrated that no Cu diffuses through the TiW diffusion barrier. Therefore, the compatibility of the SLID interconnection and high resistivity thin silicon sensors was proven.

At the IZM, first SLID interconnections were performed at wafer-to-wafer level. The wafers contained a variety of daisy chains with different pad sizes and distances as well as structures to measure the relative wafer alignment. In addition, modulations of the surface planarity up to 1 μm were introduced to test the SLID sensitivity to imperfect wafer surfaces. The inefficiencies of the initial interconnection tests were on the order of 10^{-4} to 10^{-3}. For three chains only upper limits for the inefficiency could be given since none of the more than ten thousand interconnections were found to be broken. The effect of the imperfect surface planarity did not result in significant changes of the interconnection efficiency. The relative alignment accuracy of the wafers was measured to be between 5 μm and 10 μm. A second interconnection was carried out at chip-to-wafer level. Due to several tool changes during the pick-and-place process and the selection of chips from different wafers with different thicknesses, the misalignment was mostly between 20 μm and 30 μm and the connection efficiency was low. However, for the final module production the chips will have identical sizes avoiding tool changes and will stem from the same wafer. Both problems discovered in this R&D run are therefore not expected.

A first systematic tuning series of the 16 ATLAS FE-I3 chips of a complete pixel module showed that the discriminator threshold can be lowered from the standard 4 ke down to 2 ke without deteriorating the module performance with respect to noise, crosstalk, or timing parameters. This was possible by optimizing the standard tuning algorithm to also cope with small signal sizes. Below a threshold of around 2 ke a module-wide noise pattern developed for all three modules investigated. This indicated that the limiting factor of the discriminator threshold is not given by the FE-I3 chip but rather by other components of the module. The results of the tuning procedure are planned to be transferred to the successor of the FE-I3 chip, the FE-I4, to allow for a similar low threshold optimization.

In summary thin sensors and the 3D-integration technology present a very promising and competitive concept for the pixel modules in the framework of the ATLAS detector upgrades. The high CCE after irradiation and the 3D-integration allow for efficiently

instrumenting even the innermost pixel layer very close to the interaction point while the standard cost-effective n-in-p sensor design offers the possibility for a large volume pixel detector.

At the time of writing, the measurements of the strip sensors irradiated to $10^{16}\,\mathrm{n_{eq}/cm^2}$ are carried out using a decoupling pitch adapter to suppress the large leakage currents. First results of the sensors with an active thickness of $75\,\mu$m still show a large CCE compatible with 100% at 750 V. Measurements of the sensors with an active thickness of $150\,\mu$m are anticipated in the near future.

A second production of five 6-inch wafers containing thin n-in-p sensors with an active thickness of $150\,\mu$m and the favorable low homogeneous p-spray isolation option developed within this thesis, has been started to supply sensor candidates for the upcoming IBL pixel sensor qualification. The main structures of this production are pixel sensors with a pixel cell size of $50 \times 250\,\mu\mathrm{m}^2$ which are designed to be connected to the FE-I4 readout chip. Most of the sensors use the slim guard-ring design evaluated in this thesis and a reduced safety-margin to the cutting line to arrive at an inactive edge with a total width of $450\,\mu$m as needed for the IBL upgrade. In addition, the sensors from this production will also be used to further investigate the use of thin n-in-p pixel sensors for the sLHC ATLAS pixel detector upgrade.

With an upgraded pixel detector employing radiation hard sensors with smaller pixel cell sizes, a very compact module design, and a dense module arrangement it is possible to efficiently and reliably reconstruct the particle trajectories within the ATLAS detector at a ten-fold luminosity with respect to the nominal one at the LHC. This is indispensable for extending the discovery reach of the ATLAS experiment at the sLHC as well as for improving the measurement precision of rare processes and new physics potentially discovered at the LHC. Especially if the Higgs boson is realized in nature and discovered at the LHC, the measurements at the sLHC are inevitable to fully prove or disprove the Higgs mechanism.

List of Figures

List of Tables

Bibliography

[1] S. Hawking, *The Universe in a nutshell*, Bentam, 2001.

[2] Conseil Européen pour la Recherche Nucléaire (CERN), `http://cern.ch`.

[3] The Relativistic Heavy Ion Collider (RHIC) of the Brookhaven National Laboratory, `http://www.bnl.gov/rhic`.

[4] M. Krämer et al., *Large Hadron Collider Phenomenology*, Inst. of Physics Publishing, Bristol and Philadelphia, 2004.

[5] G. Kane et al., *Perspectives on LHC Physics*, World Scientific Publishing Co. Pte. Ltd., Singapore, 2008.

[6] R. S. Moore, Performance and Future of the Tevatron, Nucl. Phys. B Proc. Suppl. **177 - 178**, 5 (2008).

[7] P. Sicho, SLHC upgrade plans for the ATLAS pixel detector, Nucl. Instrum. Methods Phys. Res., Sect. A **607**, 31 – 34 (2009).

[8] The Tevatron Luminosity monitor, `http://www.fnal.gov/pub/now/tevlum.html`.

[9] A. Tricomi, SLHC: The LHC luminosity upgrade, Nucl. Instrum. Methods Phys. Res., Sect. A **596**, 43 – 47 (2008).

[10] F. Englert et al., Broken Symmetry and the Mass of Gauge Vector Mesons, Phys. Rev. Lett. **13**, 321 – 323 (1964).

[11] P. W. Higgs, Broken Symmetries, massless particles and gauge fields, Phys. Lett. **12**, 132 – 133 (1964).

[12] P. W. Higgs, Broken Symmetries and the Masses of Gauge Bosons, Phys. Rev. Lett. **13**, 508 – 509 (1964).

[13] The Collaborations ALEPH, CDF, D0, DELPHI, L3, OPAL, SLD, the LEP Electroweak Working Group, the Tevatron Electroweak Working Group, and the SLD electroweak and heavy flavour groups, Precision Electroweak Measurements and Constraints on the Standard Model, arXiv.org (arXiv:0911.2604v2 [hep-ex]) (2009).

[14] The CDF Collaboration, the D0 Collaboration, the Tevatron New Physics, Higgs Working Group, Combined CDF and D0 Upper Limits on Standard Model Higgs-Boson Production with 2.1 - 5.4 fb-1 of Data, arXiv.org (arXiv:0911.3930v1 [hep-ex]), 1 – 30 (2009).

[15] The ATLAS Collaboration, The ATLAS Experiment at the CERN Large Hadron Collider , J. Instrum. **S08003**(3), 1 – 438 (2008).

[16] The ATLAS Collaboration, `http://atlas.web.cern.ch/Atlas/Collaboration`.

[17] The CMS Collaboration, `http://cms.web.cern.ch/cms/Collaboration`.

[18] The ATLAS Collaboration, Expected Performance of the ATLAS experiment - Detector, Trigger and Physics, arXiv.org (arXiv:0901.0512 [hep-ex]) (2009).

[19] The CMS Collaboration, CMS Physics Technical Design Report Vol II, J. Phys. G: Nucl. Part. Phys. **34**, 995 – 1579 (2006).

[20] K. Jakobs, Higgs bosons at the LHC , Eur. Phys. J. C **59**(2), 463 – 495 (2008).

[21] M. Dührssen et al., Extracting Higgs boson couplings from CERN LHC data, Phys. Rev. D **70**(11), 113009 (2004).

[22] F. Gianotti, Physics potential and experimental challenges of the LHC luminosity upgrade, Eur. Phys. J. C **39**, 293 – 333 (2005).

[23] U. Baur, Probing the Higgs self-coupling at hadron colliders using rare decays, Phys. Rev. D **69**(5), 053004 (2004).

[24] J. G. Taylor, A review of supersymmetry and supergravity, Prog. Part. Nucl. Phys. **12**, 1 – 101 (1984).

[25] N. Arkani-Hamed et al., Phenomenology, astrophysics, and cosmology of theories with submillimeter dimensions and TeV scale quantum gravity, Phys. Rev. D **59**(8), 086004 (1999).

[26] C. T. Hill et al., Strong dynamics and electroweak symmetry breaking, Phys. Rep. **381**(4 - 6), 235 – 402 (2003).

[27] P. F. Perez et al., Leptoquarks and neutrino masses at the LHC, Nucl. Phys. B **819**(1 - 2), 139 – 176 (2009).

[28] The ALICE Collaboration, `http://aliceinfo.cern.ch`.

[29] The Large Hadron Collider beauty experiment, `http://lhcb.web.cern.ch`.

[30] F. Zimmermann, Update on LHC Upgrade Plans, Talk at the ATLAS Upgrade Week, CERN, November 2009.

[31] E. Courant et al., Theory of the Alternating-Gradient Synchrotron, Ann. Phys. **3**(1), 1 – 48 (1958).

[32] L. Arnaudon, Linac4 Technical Design Report L., Technical Report CERN-AB-2006-084 ABP/RF, CERN, 2006.

[33] The LINAC4 Project, `http://linac4.web.cern.ch/linac4`.

[34] K. Oide et al., Beam-beam collision scheme for storage-ring colliders, Phys. Rev. A **40**(1), 315 – 316 (1989).

[35] K. Akai et al., RF systems for the KEK B-Factory, Nucl. Instrum. Methods Phys. Res., Sect. A **499**, 45 – 65 (2003).

[36] A. D. Ciaccio, Status and commissioning of the ATLAS experiment at the LHC, Nucl. Instrum. Methods Phys. Res., Sect. A **602**, 682 – 686 (2009).

[37] The ATLAS Collaboration, ATLAS inner detector: technical design report vol.1, Technical Report CERN-LHCC-97-16, CERN, Geneva, 1997.

[38] The ATLAS Collaboration, ATLAS inner detector: technical design report vol.2, Technical Report CERN-LHCC-97-17, CERN, Geneva, 1997.

[39] G. Hallewel et al., Pixel Detector Technical Design Report, `http://atlas.web.cern.ch/Atlas/GROUPS/INNER_DETECTOR/PIXELS/tdr.html`.

[40] A. Ahmad et al., The silicon microstrip sensors of the ATLAS semiconductor tracker, Nucl. Instrum. Methods Phys. Res., Sect. A **578**(1), 98 – 118 (2007).

[41] M. Newcomer, Design and implementation of the ATLAS TRT front end electronics, Nucl. Instrum. Methods Phys. Res., Sect. A **563**(2), 306 – 309 (2006).

[42] Review of the ATLAS Calorimetry TDR, Technical Report CERN-LHCC-97-027, CERN, Geneva, 1997.

[43] The ATLAS Collaboration, Review of the ATLAS Muon TDR, Technical Report CERN-LHCC-97-047, CERN, Geneva, 1997.

[44] B. Bittner et al., Development of muon drift-tube detectors for high-luminosity upgrades of the Large Hadron Collider, Nucl. Instrum. Methods Phys. Res., Sect. A (2009), In Press, Corrected Proof.

[45] H. Oberlack et al., Upgrade of the Cold Electronics of the ATLAS HEC Calorimeter for sLHC, Technical Report ATL-COM-LARG-2009-049, Max-Planck-Institut für Physik, München, 2009.

[46] F. G. Oakham, Temperature rise in the FCal at 10 times design luminosity, Talk at the ATLAS LArg calorimeter upgrade workshop, CERN, December 2006.

[47] J. Tseng, ATLAS Upgrade Plans for the SLHC, Nucl. Phys. B Proc. Suppl. **177 - 178**, 212 – 216 (2008).

[48] The ATLAS Upgrade Steering Group (USG), `http://atlas.web.cern.ch/Atlas/GROUPS/UPGRADES`.

[49] D. Giugni et al., The ATLAS Insertable B-Layer Detector (IBL), Talk on the 11th ICATPP Conference on Astroparticle, Particle, Space Physics, Detectors and Medical Physics Applications, Como, Italy, Oct 2009.

[50] T. Flick, IBL - ATLAS Pixel Upgrade, Technical Report ATL-INDET-PROC-2010-001, CERN, Geneva, Jan 2010.

[51] K. Einsweiler, ATLAS On-detector Electronics Architecture, Technical report, LBNL, 2003.

[52] R. Nisius et al., R&D on a novel interconnection technology for 3D integration of sensors and electronics and on thin pixel sensors, CERN Engeneering & Equipment Data Management Service , 1 – 11 (2007), ATL-P-MN-0019.

[53] MPI Halbleiterlabor, `http://www.hll.mpg.de`.

[54] A. Macchiolo et al., Development of thin pixel sensors and a novel interconnection technology for the SLHC , Nucl. Instrum. Methods Phys. Res., Sect. A **591**, 229 – 232 (2008).

[55] R. Dyck et al., Integrated arrays of silicon photodetectors for image sensing, IEEE Trans. Electron Devices **ED-15**(4), 196 – 201 (1968).

[56] P. J. W. Noble, Self-Scanned Silicon Image Detector Arrays, IEEE Trans. Electron Devices **ED-15**, 202 – 209 (1968).

[57] M. F. Tompsett et al., Charge Coupled 8-bit Shift Register, Appl. Phys. Lett. **17**, 111 – 115 (1970).

[58] C. Kittel, *Introduction to Solid State Physics*, John Wiley & Sons, 2005.

[59] L. Ma et al., Holes in Hall Effect, Lat. Am. J. Phys. Educ. **3**(1), 48 – 51 (2009).

[60] H. Moser, Silicon Detector Szstems in high energy physics, Nucl. Instrum. Methods Phys. Res., Sect. A **63**, 186 – 237 (2009).

[61] R. van Overstraeten et al., Measurement of the ionization rates in diffused silicon p-n junctions , Solid-State Electron. **13**, 583 – 608 (1970).

[62] G. Aad et al., ATLAS pixel detector electronics and sensors, J. Instrum. **P07007**(3), 1 – 80 (2008).

[63] R. H. Richter et al., Strip detector design for ATLAS and HERA-B using two-dimensional device simulation, Nucl. Instrum. Methods Phys. Res., Sect. A **377**, 412 – 421 (1996).

[64] S. Ramo, Currents Induced by Electron Motion, Proceedings of the I.R.E **27**, 584 – 585 (1939).

[65] C. Jacoboni et al., A review of some charge transport properties of silicon, Solid-State Electron. **20**(2), 77 – 89 (1977).

[66] V. Barzdenas et al., Leakage Current Compensation for the 0.13 μm CMOS Charge Sensitive Preamplifier, Elektronika ir elektrotechnika **5**(77), 33 – 36 (2007).

[67] D. Baumeister, The Beetle Reference Manual, Chip version 1.3 , Technical Report LHCb Note, LHCb-2005-105, April 2004.

[68] S. Köstner et al., Noise considerations of the Beetle amplifier used with long silicon strip detectors, Technical Report LHCb Note, LHCb-2005-029, 2005.

[69] J. Wüstenfeld, *Characterization of Ionization-Induced Surface Effects for the Optimization of Silicon-Detectors for Particle Physics Applications*, PhD thesis, Universität Dortmund, 2001.

[70] K. L. Brower, Kinetics of H2 passivation of Pb centers at the (111) Si-SiO2 interface, Phys. Rev. B **38**, 9657 – 9666 (1988).

[71] C. T. Sah, Origin of Interface States and Oxide Charges Generated by Ionizing Radiation, IEEE Trans. Nucl. Sci. **NS-23**(6), 1565 – 1568 (1976).

[72] D. L. Griscom, Hydrogen Model for Radiation-Induced Interface States in SiO2-on-Si Structures: A Review of the Evidence, J. Electron. Mater. **21**, 763 – 767 (1992).

[73] D. B. Brown et al., Time dependence of radiation-induced interface trap formation in metal-oxide-semiconductor devices as a function of oxide thickness and applied field, J. Appl. Phys. **70**, 3734 – 3747 (1991).

[74] S. Rashkeev et al., Defect Generation by Hydrogen at the Si-SiO2 Interface, Phys. Rev. Lett. **87**, 165506 (2001).

[75] V. van Lint et al., *Mechanisms of Radiation Effects in Electronic Materials*, John Wiley & Sons, 1980.

[76] J. R. Srour et al., Review of Displacement Damage Effects in Silicon Devices, IEEE Trans. Nucl. Sci. **50**, 653 – 670 (2003).

[77] M. Moll, *Radiation Damage in Silicon Particle Detectors*, PhD thesis, Universität Hamburg, 1999.

[78] B. Gossick, Disordered regions in semiconductors bombarded by fast neurons, J. Appl. Phys. **30**, 1214 – 1218 (1959).

[79] O. L. Curtis et al., Effect of Irradiation on the Hole Lifetime of N-Type Germanium, J. Appl. Phys. **28**, 1161 – 1165 (1957).

[80] O. L. Curtis et al., Recombination within disordered regions: Influence of barrier height on recombination rate and injection level effects, IEEE Trans. Nucl. Sci. **20**, 196 – 203 (1973).

[81] B. G. Svensson et al., Divacancy acceptor levels in ion-irradiated silicon, Phys. Rev. B **43**(3), 2292 – 2298 (1991).

[82] S. Watts et al., A new model for generation-recombination in silicon depletion regions after neutron irradiation, IEEE Trans. Nucl. Sci. **43**, 2587 – 2594 (1996).

[83] M. Huhtinen, Simulation of non-ionising energy loss and defect formation in silicon, Nucl. Instrum. Methods Phys. Res., Sect. A **491**, 194 – 215 (2002).

[84] G. Kramberger et al., Effective trapping time of electrons and holes in different silicon materials irradiated with neutrons, protons and pions, Nucl. Instrum. Methods Phys. Res., Sect. A **481**, 297 – 305 (2002).

[85] R. Wunstorf, *Systematische Untersuchungen zur Strahlenresistenz von Silizium-Detektoren für die Verwendung in Hochenergiephysik-Experimenten*, PhD thesis, Universität Hamburg, 1992.

[86] R. Wunstorf et al., Radiation tolerant sensors for the ATLAS pixel detector, Nucl. Instrum. Methods Phys. Res., Sect. A **466**, 327 – 334 (2001).

[87] J. Frenkel, On Pre-Breakdown Phenomena in Insulators and Electronic Semi-Conductors, Phys. Rev. **54**, 647 – 648 (1938).

[88] J. Lindhard et al., Range concepts and heavy ion ranges, Danske Vidensk. Selsk. Mat.-Fys. Medd. **33**(14), 1 – 42 (1963).

[89] I. Lazanu et al., Theoretical calculation of diamond damage by π^+/π^- mesons in the Δ_{33} resonance energy range, Nucl. Instrum. Methods Phys. Res., Sect. A **406**, 259 – 266 (1998).

[90] J. Morin et al., Widening The Range in Measuring Neutron Fluences with PIN Silicon Diodes, Radiation and its Effects on Components and Systems **95**, 476 – 480 (1995).

[91] A. Vasilescu, The NIEL scaling hypothesis applied to neutron spectra of irradiation facilities and in the ATLAS and CMS SCT, Technical Report ROSE RD-48 internal Note, ROSE/TN/97-2, CERN, 1999.

[92] M. Moll, Radiation Damage in Silicon Particle Detectors, Talk about The Radiation effects on electronic components and systems for LHC - CERN Technical Training, CERN, April 2000.

[93] J. Lange, Radiation Damage in Proton - Irradiated Epitaxial Silicon Detectors, 2008, Diploma thesis, Universität Hamburg.

[94] RD50 - Radiation hard semiconductor devices for very high luminosity colliders, `http://rd50.web.cern.ch/rd50/`.

[95] E. Fretwurst et al., Bulk damage effects in standard and oxygen-enriched silicon detectors induced by 60Co-gamma radiation, Nucl. Instrum. Methods Phys. Res., Sect. A **514**, 1 – 8 (2003).

[96] G. Kramberger, Recent Results from the CERN RD50 collaboration, Nucl. Instrum. Methods Phys. Res., Sect. A **583**, 49 – 57 (2007).

[97] E. Fretwurst et al., Radiation damage studies on MCz and standard and oxygen enriched epitaxial silicon devices, Nucl. Instrum. Methods Phys. Res., Sect. A **583**, 58 – 63 (2007).

[98] RD42 - Development of Diamond Tracking Detectors for High Luminosity Experiments at the LHC, `http://rd42.web.cern.ch/rd42/`.

[99] G. Lutz, *Semiconductor Radiation Detectors*, Springer-Verlag Berlin, Heidelberg, New York, 1999.

[100] R. Wallny et al., Status of diamond detectors and their high energy physics application, Nucl. Instrum. Methods Phys. Res., Sect. A **582**, 824 – 828 (2007).

[101] S. Parker et al., 3D - A proposed new architecture for solid-state radiation detectors, Nucl. Instrum. Methods Phys. Res., Sect. A **395**, 328 – 343 (1997).

[102] C. D. Via et al., 3D active edge silicon sensors with different electrode configurations: Radiation hardness and noise performance, Nucl. Instrum. Methods Phys. Res., Sect. A **604**, 505 – 511 (2009).

[103] G. Kramberger et al., Signals in non-irradiated and irradiated single-sided silicon detectors, Nucl. Instrum. Methods Phys. Res., Sect. A **457**, 550 – 557 (2001).

[104] M. Rogalla et al., Analysis of trapping and detrapping in semi-insulating GaAs detectors, Nucl. Instrum. Methods Phys. Res., Sect. A **395**, 49 – 53 (1997).

[105] A. Affolder et al., Collected charge of planar silicon detectors after pion and proton irradiations up to $2.2 \cdot 10^{16} \mathrm{n_{eq}cm^{-2}}$, Nucl. Instrum. Methods Phys. Res., Sect. A (2010), In Press, Corrected Proof.

[106] G. Kramberger, Investigation of electric field and evidence of charge multiplication by Edge-TCT, Talk on the ATLAS Upgrade Week, CERN, November 2009.

[107] R. Marco-Hernendez, A Portable Readout System for Microstrip Silicon Sensors (ALIBAVA), IEEE Trans. Nucl. Sci. **56**(3), 1 – 8 (2009).

[108] L. Andricek et al., Processing of Ultra-Thin Silicon Sensors for Future e+ e- Linear Collider Experiments, IEEE Trans. Nucl. Sci. **51**(3), 1117 – 1120 (2004).

[109] U. Gösele et al., Semiconductor wafer bonding, Annu. Rev. Mater. Sci. **28**, 215 – 241 (1998).

[110] Tracit Technologies, Division of the Soitec Group, `http://www.soitec.com/en/products/tracit-services.php`.

[111] Soitec S.A., `http://www.soitec.com`.

[112] L. Rossi, Pixel detectors hybridisation, Nucl. Instrum. Methods Phys. Res., Sect. A **501**, 239 – 244 (2003).

[113] T. Rohe, *Planung, Bau und Test des Sensor-Bausteins für einen hybriden Silizium-Pixel-Detektor zum Einsatz unter den extremen Strahlenbelastungen am LHC*, PhD thesis, Ludwig-Maximilian-Universität München, 1999.

[114] CiS Forschungsinstitut für Mikrosensorik und Photovoltaik GmbH, `http://www.cismst.de`.

[115] R. Hünlich, Der 2D-Technologiesimulator DIOS, page 169, 1990, Proceedings of the VI. Symposium Physikalische Grundlagen zu Bauelementetechnologien der Mikroelektronik, Frankfurt/Oder.

[116] Personal communication with R.A. Richter, HLL-München.

[117] H. Gajewski, *TOSCA- Two Dimensional Semi Conductor Analysis Package, Handbuch*, Karl-Weierstraß-Institut, Berlin, Germany, 1992.

[118] B. Heinemann, *GridGen, ein Programm zur Erzeugung von Dreieckgittern für Simulationsrechnungen mit ToSCA*, Institut für Halbleiterphysik, Frankfurt an der Oder, 1994.

[119] B. Delaunay, Sur la sphere vide, Bulletin of Academy of Sciences of the USSR **7**(6), 793 – 800 (1934).

[120] W. van Roosbroeck, The Transport of Added Current Carriers in a Homogeneous Semiconductor, Phys. Rev. **91**(2), 282 – 289 (1953).

[121] Irradiation Center Karlsruhe, `http://www-ekp.physik.uni-karlsruhe.de`.

[122] R. Wunstorf et al., Damage-induced surface effects in silicon detectors, Nucl. Instrum. Methods Phys. Res., Sect. A **377**, 290 – 297 (1996).

[123] Hamamatsu Photonics, `http://www.hamamatsu.com`.

[124] The ATLAS Upgrade Planar Pixel Sensor R&D , `https://twiki.cern.ch/twiki/bin/view/Atlas/PlanarPixelUpgrade`.

[125] M. Beimforde, The Planar Pixel Project, Nucl. Instrum. Methods Phys. Res., Sect. A (2010), In Press, Uncorrected Proof.

[126] ZAG Zyklotron AG, `http://www.zyklotron-ag.de`.

[127] M. Petterson et al., Charge collection and capacitance-voltage analysis in irradiated n-type magnetic Czochralski silicon detectors, Nucl. Instrum. Methods Phys. Res., Sect. A **583**, 189 – 194 (2007).

[128] G. Kramberger et al., Simulation of signal in irradiated silicon pixel detectors, Nucl. Instrum. Methods Phys. Res., Sect. A **511**, 82 – 87 (2003).

[129] Simulated by M. Benoit, Universite de Paris-Sud (Paris XI), with the SILVACO TCAD simulation suite.

[130] L. Weber et al., Transport Properties of Silicon, Appl. Phys. A **53**, 136 – 140 (1991).

[131] Institute of Physics, University of Liverpool, England, `http://www.liv.ac.uk/physics/hep/index.html`.

[132] Instituto de Microelectronica de Barcelona, Centro Nacional de Microelectronica, IMB-CNM, Barcelona, Spain, `http://www.imb-cnm.csic.es`.

[133] Instituto De Fisicia Corpuscular, IFIC, Valencia, Spain, `http://ific.uv.es`.

[134] MINUIT Function Minimization and Error Analysis, `http://wwwasdoc.web.cern.ch/wwwasdoc/minuit/minmain.html`.

[135] S. Sze, *Physics of semiconductor devices*, John Wiley & Sons, 1981.

[136] P. Garrou et al., *Handbook of 3D Integration*, Wiley-VCH, 2008.

[137] A. W. Topol et al., Three-dimensional integrated circuits, IBM J. Res. Dev. **50**(4/5), 491 – 506 (2006).

[138] K. Puttaswamy, Implementing Caches in a 3D Technology for High Performance Processors, pages 1 – 8, 2005, Proceedings of the 2005 International Conference on Computer Design, ICCD'05.

[139] Fraunhofer-Institut für Zuverlässigkeit und Mikrointegration, `http://www.pb.izm.fhg.de/izm/index.html`.

[140] A. Klumpp, Chip-to-Wafer Stacking by using Through Silicon Vias and Solid Liquid Diffusion, Talk at the IEEE-International Workshop on 3D System Integration, Munich, October 2007.

[141] Rochester Institute of Technology Semiconductor & Microsystems Fabrication Laboratory, `http://www.smfl.rit.edu`.

[142] Toshiba Corporation, `http://www.toshiba.com`.

[143] Infineon Technologies, `http://www.infineon.com`.

[144] C. Gemme et al., Study of indium bumps for the ATLAS pixel detector, Nucl. Instrum. Methods Phys. Res., Sect. A **465**, 200 – 203 (2001).

[145] J. Helneder et al., Evaluation of lead-free SnAg solder ball deposition and reflow processes for flip chip applications , Microelectron. Eng. **82**(3 - 4), 581 – 586 (2005).

[146] F. Laermer, Verfahren zum anisotropen Ätzen von Silizium, Patentschrift DE 4241045 C1, Technical report, Rober Bosch GmbH, 1994.

[147] Keithley Instruments, Inc., Product support, `http://www.keithley.com/support`.

[148] R. Beccherle et al., MCC: the Module Controller Chip for the ATLAS Pixel Detector, Nucl. Instrum. Methods Phys. Res., Sect. A **492**(1 - 2), 117 – 133 (2002).

[149] Fakultät Physik, Technische Universität Dortmund, `http://www.physik.uni-dortmund.de`.

[150] Lawrence Berkeley National Laboratory, University of California, Berkeley, USA, `http://www.lbl.gov`.

[151] D. Dobos, Production accompanying testing of the ATLAS Pixel module, 2004, Diploma thesis, Universität Dortmund.

[152] K. Reeves, System Tests of the ATLAS Pixel Detector, arXiv.org (arXiv:physics/0601031v1 [physics.ins-det]), 1 – 5 (2006).

[153] The TurboDAQ software, `http://physik2.uni-goettingen.de/~jgrosse/TurboDAQ`.

[154] A. Andreazza, ATLAS Pixel Module Electrical Tests Description, Technical Report ATL-IP-QP-0144, CERN, January 2004.

[155] T. Stockmanns, *Multi-Chip-Modul-Entwicklung für den ATLAS-Pixeldetektor*, PhD thesis, Universität Bonn, 2004.

[156] J. Grosse-Knetter, The ATLAS pixel detector, Nucl. Instrum. Methods Phys. Res., Sect. A **568**, 252 – 257 (2006).

Abbreviations

Abbreviation	Explanation
ATLAS	A Toroidal LHC AparatuS
CCE	Charge Collection Efficiency
DAC	Digital to Analog Converter
DRIE	Deep Reactive Ion Etching
DUT	Device Under Test
ENC	Equivalent Noise Charge
HLL	HalbLeiterLabor
ICV	Inter-Chip Via
LHC	Large Hadron Collider
MCC	Module Control Chip
MIP	Minimum Ionizing Particle
MOSFET	Metal-Oxide-Semiconductor Field-Effect Transistor
MPP	Max-Planck-Institut für Physik
NIEL	NonIonizing Energy Loss
PKA	Primary Knock-on Atom
PMT	PhotoMultiplier Tube
SCCS	Simple Charge Collection Simulation
sLHC	super Large Hadron Collider
SLID	Solid-Liquid InterDiffusion
TDC	Time to Digital Converter
TeSCA	Two- and three-dimensional SemiConductor Analysis
ToSCA	Two-dimensional SemiConductor Analysis

Acknowledgments

The final words of this thesis are dedicated to those that supported me during the past years at the Max-Planck-Institute.

First of all, I want to thank Professor Bethke for giving me the opportunity to join the ATLAS SCT group at the MPP and to work towards the upgrade of one of the most complex and fascinating experiments ever build. Thank you also very much for the constructive input during the advisory panel meetings that paved the way for my work within this project. The same gratitude I wish to express to Richard Nisius who, as my supervisor, was always deeply involved in my work, asked challenging questions at the right time, and provided advice whenever needed. I am also very thankful for entrusting me with presenting our work on the many workshops and conferences I was allowed to attend. And of course, thank you very much for all the input that you patiently supplied for finishing this thesis.

To Anna Macchiolo I have to express much gratitude for everything and especially for sharing your knowledge about so many technical details of, as well as social entanglements within the semiconductor sensor business. Also for the many discussions, the good ideas, and your ability to remember almost everything I am very thankful. It was a great experience to work with you, and I very much enjoyed the activities during the spare time on the many business trips.

Many thanks also go to Rainer Richter who seems to know every electron and electron-hole by its first name. Thank you for introducing me to the simulation programs and for sharing your expert knowledge about the many sensor related topics without any reluctance. Furthermore, I want to thank Daniel Münstermann from the University of Dortmund for his support and enthusiastic planning as well as for promoting me to represent the ATLAS PPS project in Japan.

My former office mates Sophio and Roland always were in for quick and entertaining chats, sometimes extending to long exhaustive discussions about physics and naturally also topics beyond objective reasoning. Especially the latter were highly enjoyable and it was a great pleasure to share this time with you. Of course I am also very grateful to

all my other colleagues for the time we spent together during and after work. Thank you Tobias for organizing the many social activities and keeping the calendars up to date. Thank you Philipp, Giorgio, Petra, Silke, Jochen and Anja for the many interesting topics covered especially over lunch and coffee. Good luck to all of you!

And of course I want to express my greatest gratitude to my whole family, supporting me in every aspect I can imagine not only during the last years but always. A special thank - which I cannot express in words - goes to you, Vivi, living through this and many other adventures together with me.